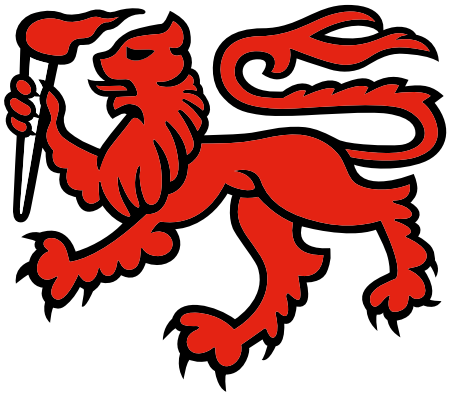

UNIVERSITY*of*
TASMANIA

AUSTRALIA

School of Natural Sciences

Geoelectric Structure of the Tasmanian Lithosphere from Multi-Scale Magnetotelluric Data

Thomas Charles Hughes Ostersen
B.Sc. (Hons)

Supervisor: Prof. Anya M. Reading
Co-Supervisor: Dr. Matthew J. Cracknell

April 2021

Submitted in fulfilment of the requirements for the Degree of Doctor of Philosophy

Abstract

The magnetotelluric (MT) method is a powerful geophysical technique capable of imaging geoelectric structure at depths ranging from the uppermost crust to the asthenospheric mantle. It exploits electrical resistivity as a key physical property that varies over several orders of magnitude in Earth materials and is dependent upon mineralogical and textural phenomena. Three dimensional (3D) resistivity models and two dimensional (2D) resistivity sections therefore yield geological information that would otherwise be inaccessible. This thesis presents an investigation of the geoelectric structure of the Tasmanian lithosphere driven by three separate newly collected or newly compiled MT data sets. While some of the first geoelectric studies in Australia took place in Tasmania, this is the first study that covers the entire island state. Tasmania has a plate tectonic history that brings together contrasting terrains with subsequent orogenesis, volcanism, sedimentation and intrusive events. The new geoelectric data sets therefore have the potential to advance knowledge of these diverse influences to benefit of both the fundamental understanding of tectonic evolution and practical, pre-competitive resources exploration.

Long period MT data were collected in the course of a major field program across Tasmania, and on Flinders Island in Bass Strait, as part of the national Australian Lithospheric Architecture Magnetotelluric Project (AusLAMP) initiative. This deployment yielded a regionally spaced data set with periods ranging 5 s to 16 000 s. Induction arrow patterns in AusLAMP data agree with earlier MT studies in highlighting a region of low resistivity coincident with, and extending southward from the Tamar River in northern Tasmania. Phase tensor ellipses plotted for the MT sites reveal stark contrasts in geoelectric structure between East Tasmania terrain (ETT) and West Tasmania terrain (WTT), with the ETT giving low minimum phase angles indicative of higher resistivities throughout the lithosphere. By contrast, the WTT is characterised by highly variable phase angles reflecting a heterogeneous resistivity structure.

Three dimensional inverse modelling of the AusLAMP data set yielded a regional-scale 3D resistivity model spanning the upper-crust through to lithospheric mantle depth range ($\sim$10 km to $\sim$100 km). The model reveals anomalously low resistivities along major terrain boundaries in the mid- to upper-crust likely resulting from conductive phases and pore fluids in shear zones. Highly resistive zones in the upper-crust correlate with the distribution of voluminous Devonian and Cambrian granitoid intrusive rocks. At deeper levels in the model, in the mid- to lower-crust, clear differences in the electrical structure of the geologically distinct ETT and older WTT emerge. The ETT is uniformly resistive, likely reflecting depletion of conductive phases following voluminous granitic melt extraction, while the WTT is electrically heterogeneous. Elevated resistivity in the ETT continues to the lithospheric mantle and is interpreted as the result of mantle geochemistry depleted of volatiles through similar processes. Elevated lithospheric mantle conductivities imaged beneath central and northwestern Tasmania in the WTT are

interpreted as being due to subduction-related mantle metasomatism potentially associated with intrusion of ubiquitous Jurassic dolerites.

In addition to the long period MT surveys, two broadband MT traverses were acquired for shallower investigations of the lithosphere beneath western and north western Tasmania. These surveys transected major crustal boundaries between Precambrian Tyennan basement and the highly metalliferous Cambrian to Devonian Dundas-Fossey Trough. Two dimensional inverse modelling of the traverses broadly agree with regional 3D modelling derived from AusLAMP MT data, and bring the geoelectric structure of the upper crust in these regions into sharper focus. In the west transect, upper crustal rocks within the Precambrian basement are considerably less resistive than younger Dundas-Fossey rocks and preserve internal heterogeneity potentially imaging relict metamorphic fluid pathways. The highly resistive Dundas-Fossey Trough contains small-scale low resistivity structure coincident with crustal-scale faults observed at surface. Low resistivities in the western part of the west transect are interpreted to image serpentinised Cambrian ultramafic rocks. Inverse modelling of the north transect was ultimately not carried out due to the severity of power line noise and consequent insensitivity of the data to upper crustal structure.

Six of the AusLAMP long period MT sites were deployed in central eastern Tasmania surrounding the Lemont geothermal prospect, a region of anomalously high surface heat flow that was the subject of exploration for geothermal energy by KUTh Energy Ltd between 2007 and 2011. A 255-site broadband MT data set was acquired by KUTh Energy Ltd at Lemont between 2008 and 2010 which culminated in the inversion of a 3D resistivity model of the area. The newly acquired long period MT data, together with the existing broadband data, presented an opportunity to re-model the Lemont MT data set. This modelling exercise improved on the previous 3D resistivity model by increasing the horizontal resolution of the model space, and incorporating the AusLAMP 3D model as *a priori* model structure. Together with different inversion approaches to static shift effects in the data, these improvements yielded significant differences in subsurface resistivity structure relative to the previous model, with the updated model containing more detail. The distribution of low resistivity zones in the updated model agrees with inferred subsurface fault structures thought to represent porous conduits for fluids radiogenically heated by underlying Devonian granitoids. The updated model fits and improves the conceptual model of the Lemont geothermal resource, with the ability to target exploration drill holes with greater confidence.

Statement of Originality

This thesis contains no material which has been accepted for a degree or diploma by the University or any other institution, except by way of background information and duly acknowledged in the thesis, and to the best of my knowledge and belief no material previously published or written by another person except where due acknowledgement is made in the text of the thesis, nor does the thesis contain any material that infringes copyright.

This thesis may be made available for loan and limited copying and communication in accordance with the Copyright Act 1968. The author also gives permission for the digital version of this thesis to be made available on the web via the University's digital research repository.

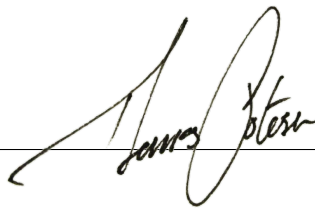

Signed

28 / 04 / 2021

Date

Acknowledgements

I would like to sincerely thank my supervisor Prof. Anya Reading for introducing me to the wonderful world of magnetotellurics and taking me on as her PhD student. It wasn't easy, and I am exceedingly grateful for her patience, encouragement, providing conference opportunities and sacrificing her summer holidays to make fieldwork a possibility. This thesis simply would not have come together were it not for her generous support. Many thanks also to Matt Cracknell, Mark Duffett and John Bishop for their expert councel in linking geophysics and geology, and again to John for making available data from Kuth Energy Ltd to the project.

I must also thank the project sponsors Geoscience Australia, Mineral Resources Tasmania and the University of Adelaide for making the project possible and providing practical support. Special thanks are due to Goran for sharing his magnetotelluric instrument knowledge, taking troubleshooting calls at odd hours and his exemplary in-the-field enthusiasm. To Jingming, Dennis, Joseph, Esi, Nick, Tanya, Matt, Yohannes and Ben; thanks a million for your sterling field work effort despite the rain, hail, snow, bush fires, flies and leeches.

To Kate and Stephan, thanks for flying all the way down to snowy Hobart for my mid-term review meeting and helping me out with magnetotelluric geophysics's steep learning curve. To my office mates Angela, Torsten, Brian, Tristan, (young) Tom and Jennifer; thanks for putting up with my jet engine of a PC, afternoon brews and being a great bunch of lads.

Thank-you to my parents, Jan and Holger, for all the hard work, support and encouragement throughout my education. To my brother Kristoffer, thanks for the campfire discussions, crayfish dives and hunting trips. Lastly I would like to thank my partner Lyndsay for her love, support and keeping me (relatively) sane - you are a gem.

Contents

List of Figures

List of Tables

Chapter 1

Introduction

Electrical resistivity is a fundamental property of matter that quantifies its ability to resist the flow of an electric current. In Earth materials this property varies over many orders of magnitude due to variation in temperature and composition relating to the presence or absence of melts, aqueous fluids or electrically conductive mineral phases [Chave et al., 2012]. Imaging the resistivity structure of the lithosphere can therefore provide insights into the temperature and compositional structure which, together with other geologic and geophysical information, reveals aspects of the lithosphere's tectonic history. The research project documented in this thesis was motivated by a desire to systematically characterise the geoelectric structure of the Tasmanian lithosphere at a number of scales using the magnetotelluric (MT) geophysical method.

MT is a passive geophysical technique that relies on the measurement of natural, time-varying electric and magnetic fields over a large frequency range on the Earth's surface. Fluctuations in the Earth's magnetic field incident on the surface from distant lightning strikes and solar wind activity are exploited as a source signal, while eddy currents induced in subsurface geologic structures are measured as the response. Described by Maxwell's equations, governing electromagnetic phenomena, the MT method applies a quasi-static approximation in order to convert the measured fields to subsurface apparent resistivity and phase [Cagniard, 1953, Tikhonov, 1950]. Depth of investigation of the MT method is governed by the skin depth effect, where low resistivities retard signal penetration and longer period signals penetrate deeper into the Earth.

Imaging subsurface resistivity structure using MT is commonly performed with linear or grid-like arrays of MT sites from which two dimensional (2D) and three dimensional (3D) models are derived. Up until the early 1990s, modelling MT data typically involved laborious forward modelling of relatively small numbers of sites [Cull, 1985, Jupp et al., 1979, Tammemagi and Lilley, 1973]. Improvements in computer power has since enabled the development of 2D [Constable et al., 1987, DeGroot-Hedlin and Constable, 1990] and 3D [Kelbert et al., 2014, Siripunvaraporn et al., 2005] inverse modelling algorithms, which are capable of deriving re-

sistivity structure from tens to hundreds of MT sites. This thesis documents the acquisition, processing and inverse modelling of Tasmanian MT data sets from which 2D and 3D models of subsurface resistivity, and their likely geological interpretation, are the ultimate product.

1.1 AusLAMP

The research presented herein was made possible by the formation of the Australian Lithospheric Architecture Magnetotelluric Project (AusLAMP). Established in 2013, AusLAMP is a decade-long national MT survey led by Geoscience Australia with the collaboration of state and territory geoscience agencies, universities and other research organisations. The survey aims for long period MT data at a half degree site spacing with the ultimate goal of imaging the lithospheric resistivity structure of the entire continent.

A key motivation for the creation of AusLAMP relates to the UNCOVER initiative, a industry and government collaboration that seeks to address diminishing mineral exploration success rates in Australia (Australian Academy of Science, 2012). Specifically, AusLAMP addresses UNCOVER theme 2 by investigating geoelectric structure as part of a larger investigation of lithospheric framework for mineral systems exploration. Figure 1.1 below illustrates AusLAMP data acquisition progress achieved between 2013 and mid-2018.

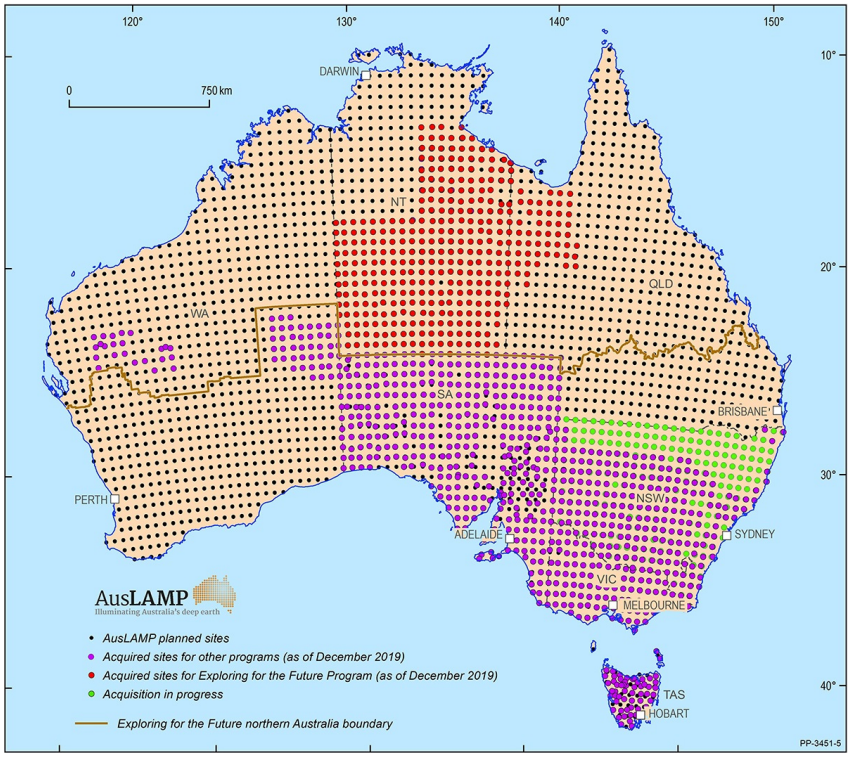

Figure 1.1: AusLAMP MT array data acquisition status as of December 2019. At the time of writing New South Wales is now complete, with acquisition currently focusing on northern Queensland and the Northern Territory. Source: Geoscience Australia [2021].

1.2 AusLAMP in Tasmania

Acquisition of AusLAMP MT data in Tasmania was conducted with the collaboration of the University of Tasmania, the University of Adelaide, Mineral Resources Tasmania and Geoscience Australia. The acquisition of long period AusLAMP data also presented an opportunity to jointly acquire broadband MT data in the same field season across key crustal element boundaries in western and northwestern Tasmania, and are discussed in a separate chapter to AusLAMP.

In keeping with UNCOVER theme 2, the 2D and 3D resistivity models derived from broadband traverses and AusLAMP surveys presented herein form a pre-competitive body of work with important implications for explorers. Chapter 6 presents a case study in which AusLAMP MT data and model outputs are integrated into a 3D inverse modelling exercise over a geothermal prospect in central eastern Tasmania. This example shows how the inclusion of AusLAMP-derived regional resistivity data as *a priori* model structure could be used to improve shallow surface resistivity investigations. Figure 1.2 below presents a map of Tasmania plotting the spatial distribution of AusLAMP and transect MT sites acquired in 2016, as well as legacy MT data sets acquired over the Lemont geothermal prospect by KUTh energy.

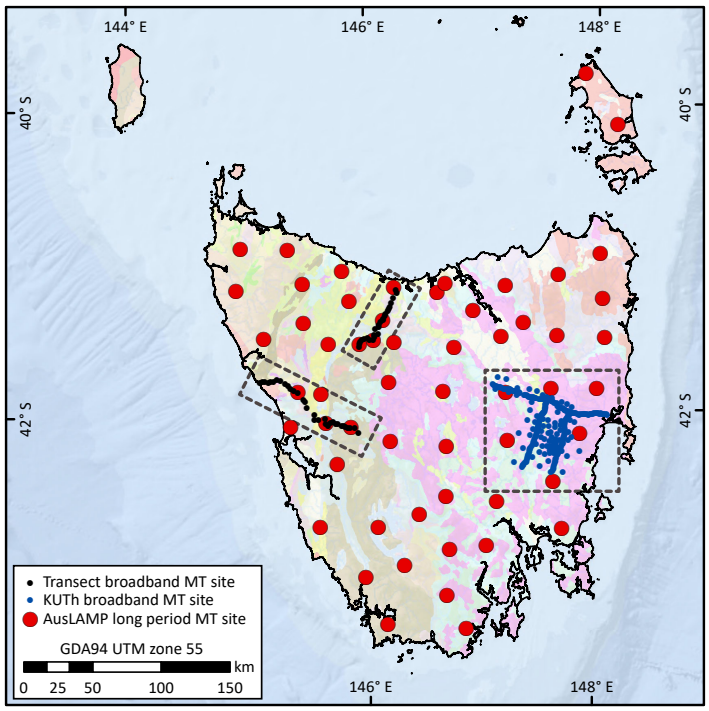

Figure 1.2: Tasmanian MT data sets overlain on a 1:5M scale Australian Geology map. Grey dashed rectangles highlight the area of interest for the western and northwestern broadband transects discussed in Chapter 5, and the KUTh integrated modelling case study discussed in Chapter 6. The AusLAMP data set is discussed in Chapter 4.

1.3 Aims

Aims are listed below and include an overarching, state-scale investigation as well as detailed regional-scale studies:

1. Acquire and process a Tasmania-wide AusLAMP long period MT data set for regional geoelectric structure characterisation.
2. Investigate the state-scale geoelectric structure of Tasmania by:
   (a) Geophysical inversion of the MT data set to generate a 3D resistivity model of the Tasmanian lithosphere, and;
   (b) Joint interpretation of 3D resistivity models with existing geophysical and geological information.
3. Acquire and process two broadband MT transect data sets for shallow-surface geoelectric investigations across key tectonic boundaries in northwestern and western Tasmania.
4. Investigate the upper- to mid-crustal geoelectric structure along these transects by:
   (a) Conducting geophysical inverse modelling of the transects so as to generate high resolution 2D geoelectric models of the subsurface, and;
   (b) Interpreting models in conjunction with existing geologic and geophysical information.
5. Evaluate legacy MT data acquired by KUTh Energy in central eastern Tasmania for subsequent joint 3D inversion with a subset of the newly acquired long period MT data set.
6. Investigate the upper- to lower-crustal structure by:
   (a) Performing high resolution 3D inverse modelling of the KUTh Energy data set and long period MT data, and;
   (b) Interpreting the geoelectric structure of the Lemont geothermal resource at higher spatial resolution than previously.

1.4 Thesis Structure

This thesis consists of eight chapters. Chapter 1 introduces the context and overarching aims of the study and outlines the structure of the thesis. Chapter 2 presents background information pertaining to the geological structure and tectonic history of Tasmania, provides a review of previous geoelectric studies in mainland Australia, discusses existing geophysical data sets for Tasmania as well as a background to the MT method and inverse modelling schemes. Chapter 3 provides a full account of the newly undertaken MT field campaign for Tasmania.

The core of this thesis comprises three chapters in which the aims outlined in the previous section are addressed. Chapter 4 addresses aims 1 and 2; and outlines the steps taken in processing raw AusLAMP time series data to derive the final MT data set. Regional geoelectric structure observed in phase tensor ellipses [Caldwell et al., 2004], and induction arrows [Parkinson, 1962] are discussed, with the latter compared to legacy data of Parkinson et al. [1988], and steps taken in 3D inverse modelling are covered in depth. The chapter then presents 3D inverse modelling results and an interpretation of observed model features derived from the integration of the model with available data sets. The understanding of the influences of tectonic history on the Tasmanian lithosphere is advanced through the new models and interpretation.

Aims 3 and 4 are addressed in Chapter 5, which discusses processing steps used to derive final broadband transect MT data from electric and magnetic field measurements, as well as the kinds of noise observed in the data. Full further analysis for the west transect is presented, while the north transect proved to be severely impacted by power line noise. Analyses of the geoelectric strike for the west transect data set is presented prior to the presentation of 2D inverse modelling results. The chapter culminates in geologic interpretations of the inverse modelling results enabled by integration with existing geologic models and geophysical data sets across a region known for its rich mineralisation. The new interpretations aim to assist further pre-competitive minerals exploration.

Aims 5 and 6 are addressed in Chapter 6, which presents the steps taken in collating existing KUTh Energy broadband MT data sets in preparation for joint inversion with existing AusLAMP MT data. This is followed by a presentation of distinct model results from two different starting models; one with a homogeneous half-space resistivity and another incorporating regional resistivity structure derived from model results presented in Chapter 4. The two distinct models are compared and contrasted with previous inverse modelling and the case is made for a preferred model incorporating regional resistivity structure from AusLAMP. Finally, integrated interpretations of the local resistivity structure are presented with images taken from 3D viewing software with the aim to assist geothermal resource exploration.

Chapter 7 synthesises the results of core Chapters 4, 5 and 6, and summarises recommendations. Finally, Chapter 8 summarises the outcomes of the research project and concludes the thesis.

Chapter 2

Geological and Geophysical Background

This chapter covers geological and geophysical background information relevant to the magnetotelluric (MT) investigations carried out over the course of this research project. Section 2.1 presents a broad overview of Tasmania's tectonic structure and geological evolution, while section 2.2 reviews the resistivity properties of Earth materials, the history of Australian geoelectric research, previous Tasmanian geophysical studies and existing geophysical data sets. Section 2.3 discusses the theoretical basis for the MT geophysical method with an overview of the source signal, induction arrow methods, theoretical examples for 2D and 3D geoelectric environments, and a discussion of both 2D and 3D inverse modelling algorithms.

2.1 Geological Background

2.1.1 Terrain Framework

The island of Tasmania in southeastern Australia has an enigmatic geological history with rocks ranging in age from the Mesoproterozoic to the Cenozoic. Pre-Carboniferous basement rocks are typically separated into two domains on the basis of age, lithology and deformation history: the West Tasmania Terrain (WTT), and the East Tasmania Terrain (ETT) [Baillie, 1986]. The WTT records substantial Proterozoic geological history, with much of the terrain comprising shallow-marine metasedimentary rocks deposited in the Mesoproterozoic with a distinct Laurentian provenance [Halpin et al., 2014, Mulder et al., 2015]. Younger Neoproterozoic metasediments in the WTT have been correlated to rocks of the Transantarctic Mountains, placing proto-Tasmania on the eastern margin of East Antarctica prior to the break-up of Rodinia [Berry et al., 2008]. In the Cambrian, tectonic collision between the proto-Tasmanian passive margin and an oceanic island arc to the east impacted the WTT. The collision initiated the Tyennan Orogeny resulting in the westward emplacement of mafic-ultramafic allocthonous

blocks followed by voluminous post-collisional felsic and andesitic volcanism in the Dundas-Fossey Trough [Berry and Bull, 2012].

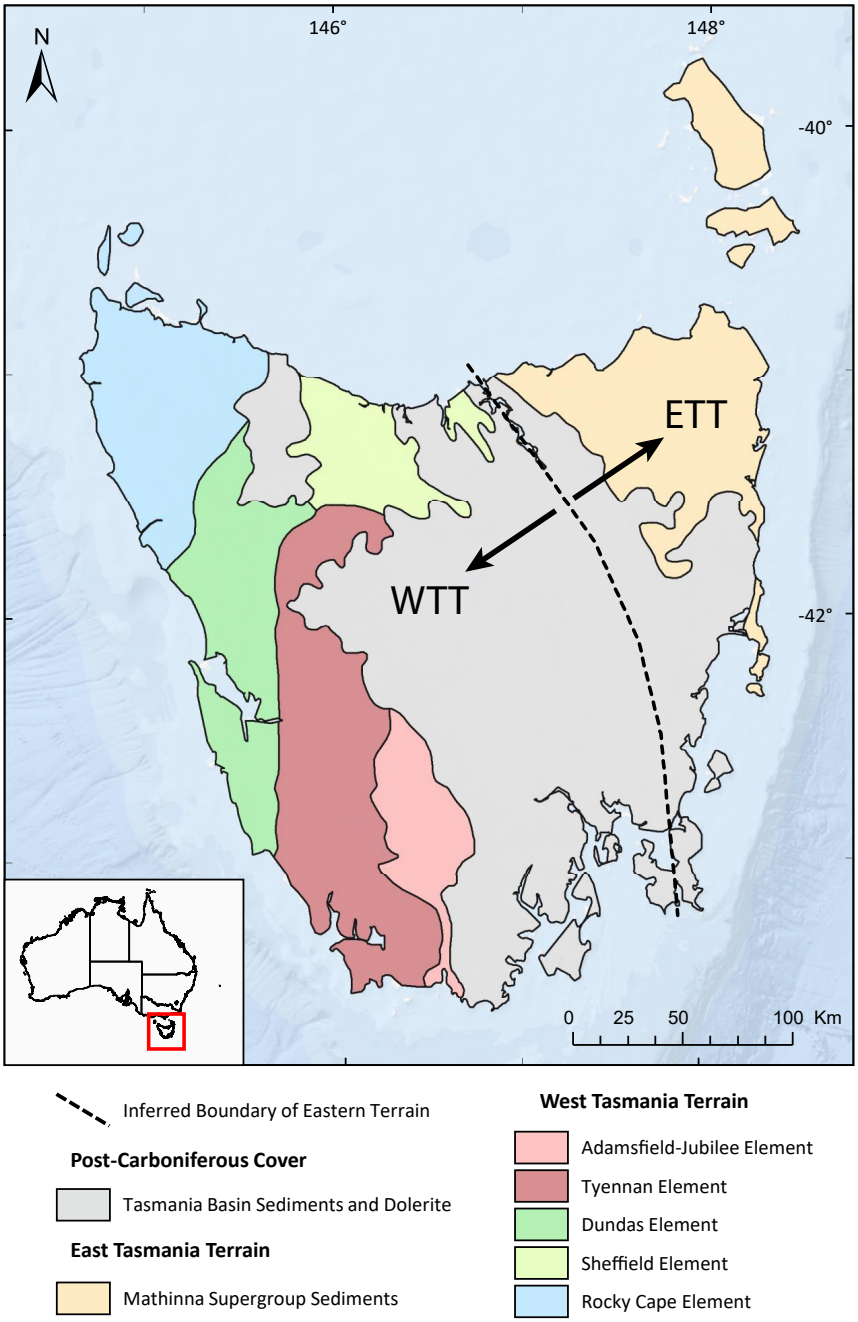

Figure 2.1: Tectonic elements map of Tasmania highlighting major crustal blocks with inferred boundary between WTT and ETT (modified from Seymour and Calver [1995]). Map projection: GDA94 UTM zone 55.

In contrast to the WTT, the ETT is dominated by Paleozoic rocks and exhibits no evidence of Proterozoic outcrop. The oldest rocks in the ETT belong to the Mathinna Supergroup, a thick sequence of Siluro-Devonian deep marine turbidites with strong similarities to the lower-Paleozoic turbidites of the Lachlan Fold Belt in Victoria [Calver et al., 2014a]. Both the ETT

and WTT were deformed and intruded by granites in the Devonian, the most voluminous of which are slightly older batholiths in the ETT [Seymour et al., 2014].

The nature of the boundary between the ETT and the WTT is controversial, with interpretations ranging from crustal-scale shear (the Tamar Fracture System, TFS [Williams, 1989]) to passive margin [Rawlinson et al., 2006, Reed, 2001]. This is in part due to its total concealment by younger Permian-Triassic sedimentary rocks of the Tasmania Basin (Fig. 2.1).

2.1.2 Tectonic Evolution

The tectonic evolution of Tasmania records three major orogenic events punctuating prolonged periods of sedimentation; the Wickham Orogeny at 750–780 Ma [Calver et al., 2014b], the Tyennan Orogeny at 520–490 Ma [Berry and Crawford, 1988, Crawford and Berry, 1992, Meffre et al., 2000], and the Tabberabberan Orogeny at 390 Ma [Black et al., 2005]. The Wickham Orogeny was preceded by a prolonged period of shallow marine continental shelf deposition (>10 km thick Rocky Cape Group and correlates) on the eastern margin of East Antarctica [Berry et al., 2008]. Deposition was suspended by orogensis at ∼760 Ma linked to deformation and granite intrusion on King Island, and inferred elsewhere as shallow angle unconformities separating the Rocky Cape Group from overlying Togari Group (and correlates). It should be noted that the Wickham Orogeny occurred during an extensional event associated with the breakup of Rodinia, leading to the potential attribution of low-angle unconformities at this time to rift-related erosion of uplifted horst blocks [Everard et al., 2007].

Following the Wickham Orogeny, sedimentation resumed with the deposition of the Togari group and its correlates. The basal units of this group suggest widespread shallow marine sedimentation in the Tonian to late Cryogenian and are immediately overlain by rift-phase mafic lavas and volcaniclastics in the late Cryogenian to Ediacaran. Rift phase sediments and lavas are overlain by upper Ediacaran shallow marine carbonate sediments transitioning to deep marine siliciclastics in the Cambrian, where deposition was suspended by continent-arc collision associated with the Tyennan Orogeny. For a comprehensive review of pre-Tyennan Orogeny Tasmanian geology, the reader is referred to Mulder et al. [2019].

The Cambrian was a very eventful time for proto-Tasmania, and produced rock sequences, structures and metamorphic complexes of great significance to the WTT despite its relatively short duration. Beginning in the the late Early Cambrian, a tectonic collision between an east-facing Tasmanian passive margin with an ocean island arc, the Tyennan Orogeny, resulted in the obduction of mafic-ultramafic complexes (now pervasively serpentinised) across much of western and northern Tasmania [Berry and Crawford, 1988, Crawford and Berry, 1992]. The emplacement age of these complexes is constrained by a minor felsic phase yielding a crystallisation age of 513.6 ± 5.0 Ma [Black, 1997], and the presence of ultramafic material in the basal beds of the overlying fossiliferous Middle Cambrian Dundas Group.

In a possible second stage to the obduction process, fault-bounded Proterozoic units with

anomalous metamorphic grades are also thought to have been emplaced in the WTT. These metamorphic complexes are believed to have been derived from distal parts of the passive margin that became deeply buried or partially subducted during collision before being emplaced at high crustal levels among relatively unmetamorphosed successions [Holm and Berry, 2002, Meffre et al., 2000, Mulder et al., 2019]. Cambrian metamorphic complexes occur as isolated packages on the western and northern boundary of the Proterozoic Tyennan element and along a 110 km long N-S trending belt (the Arthur Lineament) bounding the Dundas and Rocky Cape elements. The Tyennan Orogeny is broadly coincident with the Delamerian Orogeny in South Australia and the Ross Orogeny in Antarctica.

The Middle Cambrian saw an extensional phase of the Tyennan Orogeny following the cessation of subduction. This resulted in rapid subsidence and voluminous felsic volcanism. Extension saw the opening of the Dundas-Fossey Trough, an arcuate Middle Cambrian to Lower Devonian marine trough bounded to the west by Proterozoic rocks of the Rocky Cape element, and curving around Proterozoic rocks of the Tyennan element to the east, forming a significant crustal element within the WTT. Post-collisional volcanism and deposition in the trough over a period of ∼5 Myr formed the Mt Read Volcanics, a belt of mostly felsic volcanic, volcanosedimentary and minor intrusive rocks that host world-class polymetallic massive sulfide deposits [Crawford and Berry, 1992, Crawford et al., 1992].

The third and final phase of the Tyennan Orogeny in the Late Cambrian to Early Ordovician saw rapid uplift of Proterozoic basement and a return to clastic sedimentation in Tasmania. This phase is dominated by siliceous sandstones and conglomerate of the Owen Group and its correlates, which conformably and unconformably overlie Middle Cambrian rocks of the Dundas-Fossey Trough. Owen Group sediments are mostly fluvial, deltaic and shallow marine, with minor siltstone, suggesting high rates of erosion associated with rapid uplift of the Proterozoic Tyennan source region.

Coarse, post-collisional Owen Group sediments in the WTT are conformably overlain by shallow marine carbonate and siliciclastic rocks of the Gordon and Eldon Groups. The Middle to Late Ordovician Gordon Group and correlates are dominated by carbonate rocks, with minor sandstone, suggesting a shallow marine depositional environment. Gordon Group limestones are conformably overlain by the shallow marine siliciclastic succession of the Eldon Group deposited in the Early Silurian to Early Devonian. The shallow marine, continental shelf-like sediments of the Gordon and Eldon groups exposed in the WTT stand in stark contrast to deep marine sedimentation in the ETT at this time.

Ordovician to Early Devonian sedimentary rocks in the ETT present a thick sequence of deep-marine sandy turbidites known as the Mathinna Supergroup. This sedimentary succession has strong similarities to the lower Paleozoic turbidites of the Lachlan Fold Belt of Victoria, especially the Melbourne Trough [Cayley, 2011]. The basement to the Mathinna Supergroup and ETT is poorly defined as it does not outcrop, however, stark differences in inherited zircon

spectra from Devonian granites intruding both the WTT and ETT indicate the basement to the ETT is probably late Neoproterozoic to Cambrian oceanic crust [Black et al., 2010]. A mafic lower crust consistent with oceanic basement is also supported by high shear wave velocities in the ETT [Pilia et al., 2015].

Both the WTT and ETT were deformed during the Tabberabberan Orogeny (∼389 Ma; Black et al. [2005]), a collisional event that probably resulted in the juxtaposition of the two terrains. Characterised by regional-scale folding within the ETT, the Tabberabberan Orogeny produced complex fold structures in the WTT largely explained by reactivation of older Cambrian structures. Both the WTT and ETT were intruded by voluminous granite at this time, most of which were emplaced after the main phase of Tabberabberan deformation from the Middle Devonian to the Early Carboniferous [Seymour et al., 2014]. Tasmanian Devonian granites intruded at high crustal levels and record an irregular temporal distribution across Tasmania, with granites in the ETT typically returning older crystallisation ages (400–374 Ma) than those intruding the WTT (373–351 Ma). Figure 2.2 depicts a schematic model showing the geodynamic evolution of the WTT and ETT during the Tabberabberan Orogeny.

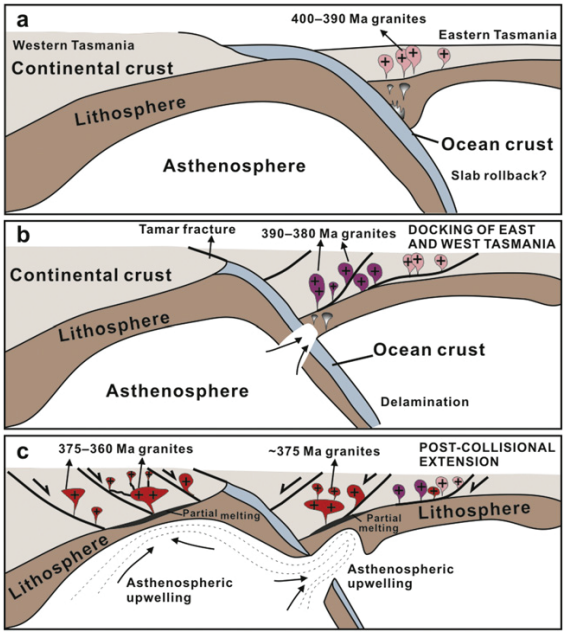

Figure 2.2: Cross sections of the WTT and ETT during various stages of the Tabberabberan Orogeny (from Hong et al. [2017]).

Unconformably overlaying the Devonian granites and older folded rocks, relatively flat-lying sedimentary rocks from the Tasmania Basin. Deposited in a foreland basin and now extensively eroded, Tasmania Basin sediments grade from glaciomarine in lower parts of the succession to fluvial and lacustrine with deposition spanning a long period of slow sedimentation from the Late Carboniferous to Late Triassic. Large volumes of tholeiitic dolerite intruded the Tasmanian crust in the Middle Jurassic, the majority of which was emplaced as thick sills within Tasmania

Basin. Dolerite intrusion in Tasmania represents an isolated fragment of the vast Karro-Ferrar large igneous province, the result of a cryptic thermal anomaly that afflicted Southern Gondwana in the Jurassic and heralded the breakup of the supercontinent [Ivanov et al., 2017].

The breakup of Gondwana in the Late Jurassic to Early Cretaceous saw rifting between Australia and Antarctica, initiating the opening of the Bass and Sorrell Basins to the north and west of Tasmania, respectively. By the Late Cretaceous, rifting gave way to ocean spreading and is coincident with a Tasmania-wide thermal anomaly also recognised in other formerly adjacent parts of Antarctica and New Zealand [Veevers, 2000]. Thermal anomalism is associated with minor onshore syenite intrusion in the southeast and far northeast [Seymour et al., 2006].

Cenozoic volcanic rocks, mainly basaltic lavas, crop out widely throughout the ETT and WTT, with the exception of the southwest, and extend into Bass Strait, the South Tasman Rise and East Tasman Plateau. Radiometric ages for Tasmanian Cenozoic basalt emplacement range from 8.5 Ma [Baillie, 1986] to 64 Ma and do not show a clear temporospatial relationship [Everard et al., 2004]. Cenozoic basalts in Tasmania being related to the impact of a fixed mantle hotspot beneath a northward moving Australian plate is therefore unlikely, and some other mechanism for lithospheric partial melting may be at play (e.g. edge-driven convection [King and Anderson, 1998]). For a comprehensive discussion of Cenozoic basalts, and Tasmanian geology more broadly, the reader is directed to Seymour et al. [2014].

It is generally understood that stable continental lithosphere is resistive, and anomalous conductive structures within it are often attributed to tectonic processes that have altered its geochemical or physical state. Above the brittle-ductile transition zone, increased porosity around major fault structures are often imaged as zones of elevated conductivity in otherwise resistive lithosphere. A Tasmanian example of such a structure includes the Tamar Conductivity Anomaly thought to represent a fracture system juxtaposing the WTT and ETT [Hermanto, 1992, Lilley, 1976, Parkinson et al., 1988]. Elevated conductivities at deeper levels in the lithosphere, where pore spaces are physically unlikely, are attributed to compositional alteration such as hydration of nominally anhydrous mineral phases and deposition of graphite along grain boundaries. These alterations are likely the result of fluid migration driven by tectonic events [Selway, 2014]. Given Tasmania's complex geological history of overlapping orogenic events and several episodes of intrusive magmatism, geoelectric imaging of the Tasmanian lithosphere is likely to yield similarly complex resistivity structure.

2.2 Geophysical Background

2.2.1 Resistivity of Earth Materials

Earth materials vary in resistivity by many orders of magnitude (Fig. 2.3), and can be classed as; *i*) conductors ($10^{-8}\,\Omega\,\mathrm{m}$ to $10^{-5}\,\Omega\,\mathrm{m}$), *ii*) semi-conductors ($10^{-5}\,\Omega\,\mathrm{m}$ to $10^{7}\,\Omega\,\mathrm{m}$), *iii*) or insulators ($>10^{7}\,\Omega\,\mathrm{m}$). As resistivity is the inverse of conductivity these terms are used in-

terchangeably in this thesis, with the term 'conductive' preferred for low resistivity regions of geoelectric models and the term 'resistive' preferred for high resistivity regions.

In typical geological settings the bulk resistivity of a volume of rock can be influenced by many factors, such as temperature, porosity and permeability, as well as the presence of volumetrically minor but conductive minerals (e.g. sulfide minerals, iron oxide minerals & graphite). The depth-dependence of porosity and temperature in the Earth influence the extent to which difference factors contribute to bulk resistivity at different depths.

At the Earth's surface, where temperature and pressures are relatively low, resistivity is primarily governed by the porosity and permeability of the substrate. Here, electrical currents are carried by ionic charge carriers in solution. Sedimentary basins and the regolith are typically highly porous and permeable, often containing saline pore space fluids which yield low bulk resistivities in the range of $1\,\Omega\,\mathrm{m}$ to $100\,\Omega\,\mathrm{m}$.

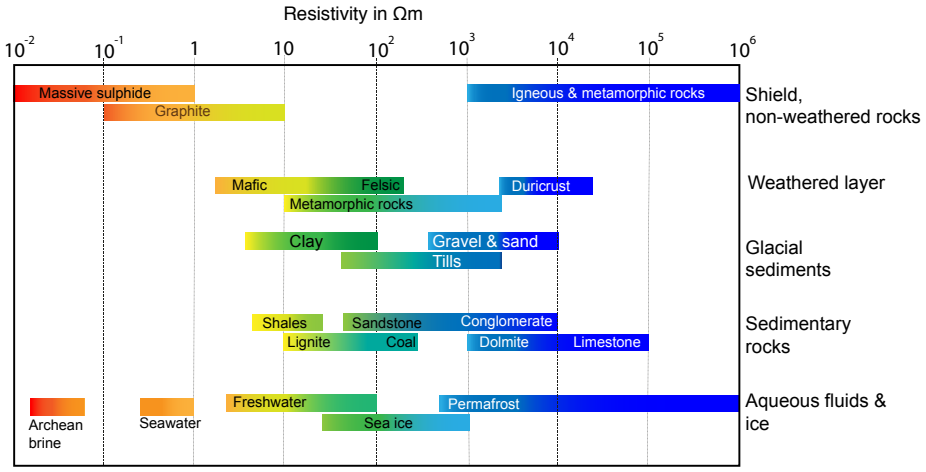

Figure 2.3: Electrical resistivity ranges for common Earth materials including aqueous phases. Image from Beka [2016], modified from Palacky [1988].

At deeper levels in the Earth, within the brittle upper crust, electrical studies of continental crust tend to return high resistivities in the order of $10^3\,\Omega\,\mathrm{m}$ to $10^5\,\Omega\,\mathrm{m}$ [Gough, 1986]. Discreet regions of low resistivity, referred to as conductivity anomalies, are often coincident with crustal-scale fault structures. Here, shearing has increased porosity and permeability enabling ionic conduction within pore fluids resulting in observed resistivities as low as $0.1\,\Omega\,\mathrm{m}$ to $1\,\Omega\,\mathrm{m}$.

Carbon is often used to explain high conductivities in upper-crustal to lithospheric mantle depths, particularly in highly sheared regions. Laboratory studies have shown carbon to be stable as grain boundary graphite films at temperatures below $\sim 900\,^{\circ}\mathrm{C}$ and, due to graphite's very high conductivity, has been shown to reduce bulk rock resistivity by up to two orders of magnitude even at concentrations of a few ppm [Yoshino and Noritake, 2011]. In the upper crust, grain boundary graphite may occur within carbonaceous black shales exposed to moderately high temperatures ($300\,^{\circ}\mathrm{C}$ to $400\,^{\circ}\mathrm{C}$) typical of the lower crust [Duba et al., 1988, Duba and

Shankland, 1982].

Below the brittle-ductile transition zone, in the lower crust, resistivities have been observed to vary substantially. In general the resistivity of the lower crust is lower than that of the upper crust, with resistivities up to two orders of magnitude lower than predicted by laboratory measurements on common lower-crustal minerals such as orthopyroxene and plagioclase [Hyndman et al., 1993, Yang et al., 2012]. In regions undergoing active tectonism low resistivities in the lower crust have been attributed to high degrees of partial melt [Unsworth, 2010]. In stable lithosphere where, by definition, melts are not present; low resistivity lower crustal zones are often attributed to the presence of conductive mineral phases such as iron oxide in serpentinite [Robertson et al., 2015], or graphite deposited by CO_2-rich fluids [Selway, 2014].

At lower-crustal depths and extending into the mantle, high temperatures and pressures increase the extent to which hydrogen can dissolve into nominally anhydrous minerals such as olivine and pyroxene. Laboratory studies indicate elevated hydrogen content in these minerals result in lower resistivities at lower-crustal and mantle conditions [Karato, 1990]. Recent reviews of electrical conduction mechanisms within continental lithosphere can be found in Jones et al. [2012] and Selway [2014].

2.2.2 Geoelectric Studies in Australia

The earliest geoelectric investigations on the Australian continent took the form of geomagnetic studies pioneered by the University of Tasmania's own Prof. Wilfred 'Dudley' Parkinson [Parkinson, 1959, 1962, 1964]. Using analogue 3-component data from fixed magnetic observatories, Parkinson devised a method of plotting the vector change in the Earth's magnetic field over periods of approximately 30 minutes he termed 'induction arrows' (see section 2.3.9). Such arrows typically have large magnitudes near the coast and invariably point toward deep offshore basins, a manifestation of the geomagnetic coast effect discussed in detail in Parkinson and Jones [1979]. For magnetic field data acquired sufficiently far away from the coast to be unaffected by it, induction arrows were found to point toward crustal-scale conductivity structures; and led to the discovery of several 'conductivity anomalies' including the Tamar Conductivity Anomaly in NE Tasmania by Lilley [1976]. A comprehensive summary of Australian conductivity anomalies identified using induction arrows is presented in Wang et al. [1997].

The development of digital acquisition systems in the late 1960s, such as that of Everett and Hyndman [1967a], rapidly advanced geoelectric research through Fourier analysis of magnetic and electric field data. With digital electric and magnetic field records, researchers including Everett and Hyndman [1967b] and Tammemagi and Lilley [1971] were able to derive the magnetotelluric impedance tensor from which apparent resistivity and phase curves could be plotted, and simplistic 1-dimensional (1D) forward models of subsurface geoelectric structure computed.

The increasing availability of computers in the 1970s led to the development of automated MT inverse modelling techniques. For numerical simplicity and tractability, these early inverse

methods dealt with 1D inversions; iteratively manipulating resistivity as a function of depth via deterministic algorithms. For example, Jupp and Vozoff [1975] and Larsen [1981] developed stable algorithms capable of modelling the resistivity and thickness of a few layers by minimising the discrepancy between the observed and predicted MT responses using a least-squares approach. Later, the introduction of regularised smooth model schemes for 1D inversions by Constable et al. [1987] and Smith and Booker [1988] represented a major leap forward in MT inverse modelling. These schemes laid the theoretical groundwork for regularised 2D inversion approaches developed soon afterwards [DeGroot-Hedlin and Constable, 1990, Smith and Booker, 1991, Uchida, 1993].

In the early 1990s, 2D resistivity modelling of MT data was limited to forward modelling approaches (see Gray and Cull [1990], Hermanto [1992]). These methods relied on 1D forward solvers to estimate the MT response from simplistic 2D models of subsurface resistivity, a tedious process with inherent dimensionality limitations. A landmark study by Wang and Chamalaun [1995] compared relatively new regularised smooth model inversion schemes (RRI of Smith and Booker [1991] and OCCAM2D of DeGroot-Hedlin and Constable [1990]) to older 1D forward model techniques for a 15-site traverse across the Adelaide Geosyncline. Although broadly consistent, 2D inversion methods were better able to account for complex subsurface conductivity distributions inherent in the data and became standard practice in MT surveying through to the 2000s. In this time, several large scale MT traverses were conducted across Australia with the aim of delineating the geoelectric structure of major crustal contacts and conductivity anomalies identified in geomagnetic surveys (see Fig. 2.4).

With increases in computing power, 2D models of ever increasing resolution inverted from larger data sets became the norm in the 2000s. 2D conductivity models from large-scale MT traverses in central and South Australia contributed to a new understanding of subduction polarity in Proterozoic Australia reconstructions [Selway et al., 2009a]. MT transects inferred the presence of a deep crustal mineralising system beneath the Olympic Dam iron oxide copper-gold deposit [Heinson et al., 2006], and imaged the conductivity structure of the western edge of the Gawler Craton [Thiel and Heinson, 2010]. In Victoria, three east-west MT traverses across rocks of the Lachlan Orogen are presented in Dennis et al. [2012], with 2D models clearly delineating new mid-crustal fault systems of potential gold exploration significance. A MT traverse further to the west, over rocks within the Delamerian Orogen, identified a deep crustal conductor coincident with a seismic reflector package interpreted to represent mafic/ultramafic rocks serpentinised during west-dipping Cambrian subduction (Fig. 2.5).

As with the transition from 1D to 2D modelling techniques, advances in computing power, and parallel computing in particular, have enabled the recent development of true 3D inversion algorithms for MT data [Egbert and Kelbert, 2012, Kelbert et al., 2014, Siripunvaraporn et al., 2005]. The availability of 3D inversion schemes coupled with the discovery of conductivity structures linking anomalous upper mantle conductivity with iron oxide copper-gold (IOCG)

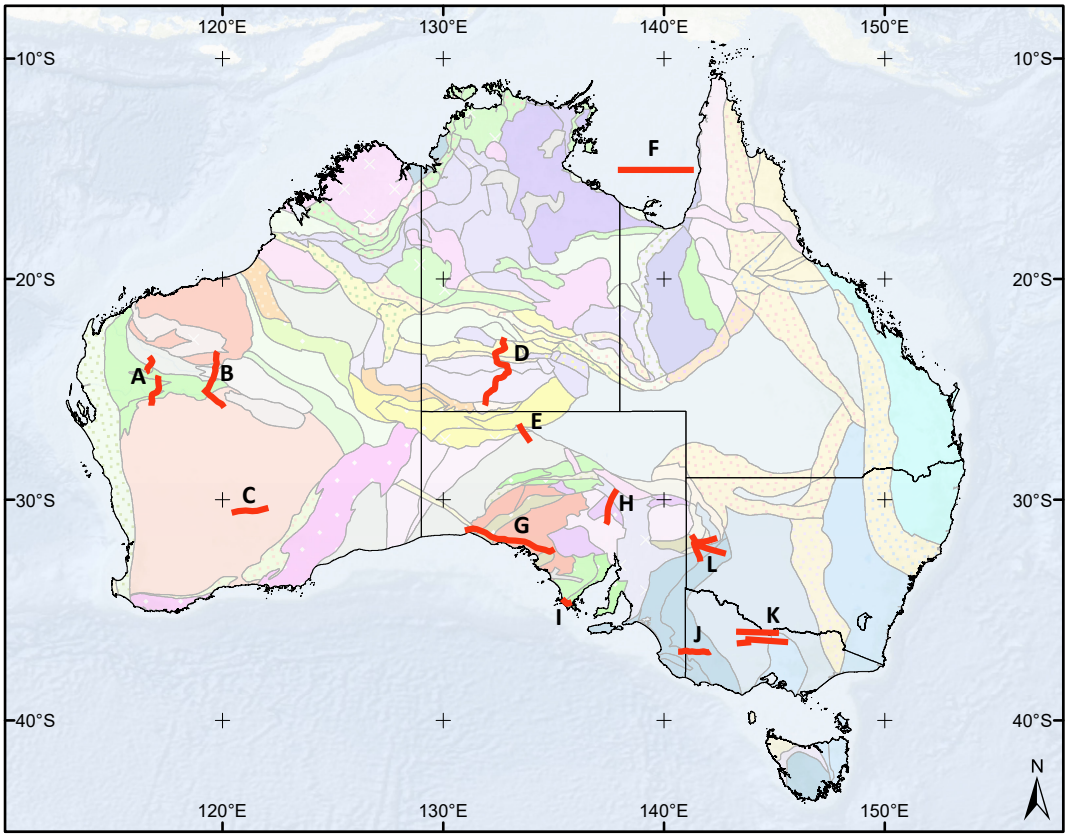

Figure 2.4: Large scale Australian MT transect locations superimposed on crustal elements map of Shaw et al. [1996]. Modelling and interpretations for **A** are reported in Selway et al. [2009b]; **B** in Dentith et al. [2014]; **C** in Blewett et al. [2010]; **D** in Selway et al. [2009a], **E** in Selway et al. [2011]; **F** in Heinson and White [2005]; **G** in Thiel and Heinson [2010]; **H** in Heinson et al. [2006]; **I** in Thiel et al. [2005]; **J** in Robertson et al. [2015], **K** in Dennis et al. [2012], and **L** in Gray and Cull [1990].

deposits in South Australia [Heinson et al., 2006] provided motivation for the Australian Lithospheric Architecture Magnetotelluric Project (AusLAMP). This collaborative national survey seeks to acquire long period MT data at half-degree site spacing (∼50 km) across the continent (Fig. 1.1). Commencing in 2013 with the acquisition of MT sites across the Flinders Ranges in South Australia, acquisition across South Australia, New South Wales, Victoria and Tasmania (as described in this thesis) is complete; with field deployments at the time of writing focusing on northern Australia.

While modelling and interpretation of AusLAMP MT data are ongoing for Victorian and New South Wales data sets, results from South Australia have yielded important insights into the nature of the lithosphere. Robertson et al. [2016] presented full 3D inverse resistivity models from eastern South Australia, at the transition from Proterozoic to Phanerozoic Australia, and identified high conductivities within the Proterozoic Curnamona Province at lower crustal depths indicative of subduction-related volatile enrichment. These 3D results also illuminated the complex structure of the Flinders Conductivity Anomaly identified previously by induction

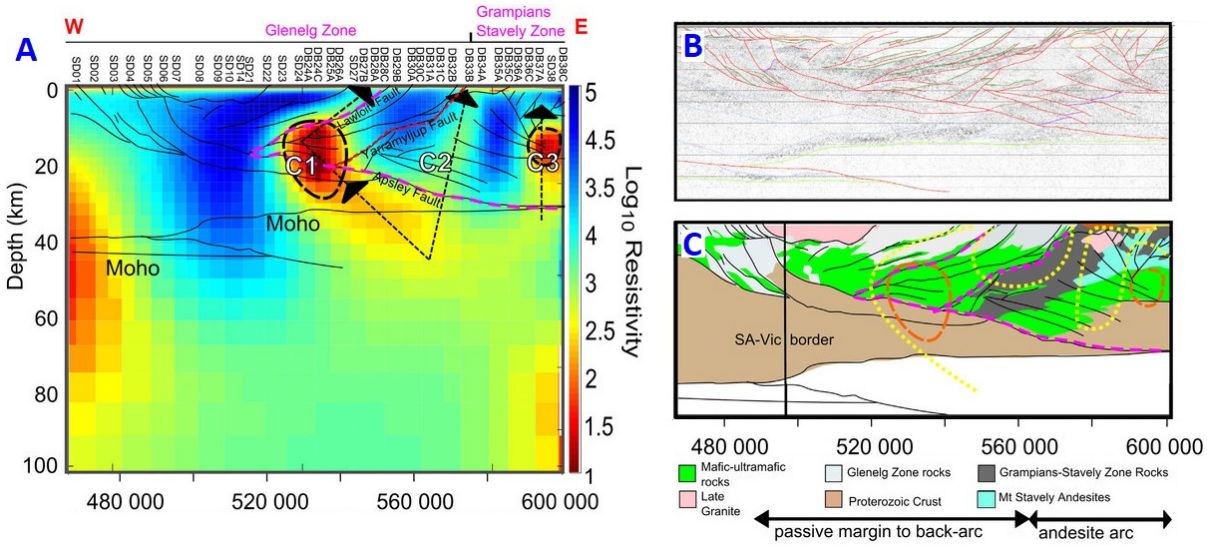

Figure 2.5: Smooth resistivity model from OCCAM2D inversion of MT data acquired across the Delamerian Orogen in southeastern Australia modified from Robertson et al. [2015]. **A**) presents an inverted resistivity model result, **B**) presents a reflected seismic section of the study area and **C**) presents an interpreted geologic section. Conductors C1 and C2 are coincident with seismic reflectors and are interpreted as serpentinised ultramafic rocks.

arrow patterns [Gough et al., 1972]. In high resolution 3D models this structure presents as three discontiguous conductive regions within the Nackara Arc and Curnamona Province.

AusLAMP MT 3D resistivity models from central South Australia have detailed the resistivity structure of the Gawler Craton and surrounding rocks [Thiel et al., 2016a]. The highly prospective IOCG belt on the eastern margin of the craton appears highly conductive, and is connected to a mantle conductivity anomaly beneath the craton. This finding agrees with earlier 2D MT profiles across the Olympic Dam deposit, and contributes to a mantle-source model of mineralisation with implications for future exploration in the region.

2.2.3 Tasmanian Geophysical Studies

Tasmania has a wealth of geophysical data available at a range of resolutions, with much of it acquired after the mid-1960s. The state's gravity coverage resolution varies considerably, with areas of economic interest in the Dundas-Fossey Trough surveyed at grid spacings of 100s of metres, while more remote parts of the state, such as the Southwest National Park and Tarkine region, are limited to helicopter-borne surveys with ∼7 km data spacing. Recent data acquisition has increased gravity coverage in the NW of the state (the Rocky Cape region), and updated terrain correction methods have improved the accuracy of gravity data in more mountainous areas of the island [Duffett, 2016]. At the state-scale, the Tasmanian gravity field is dominated by prominent low Bouguer gravity regions associated with voluminous Devonian and Cambrian granite intrusions (see Fig. 2.6.A). Metamorphic rocks in the Arthur Lineament and regions

with thick Jurassic dolerite cover in the central south of the state give rise to anomalously high Bouguer gravity signatures.

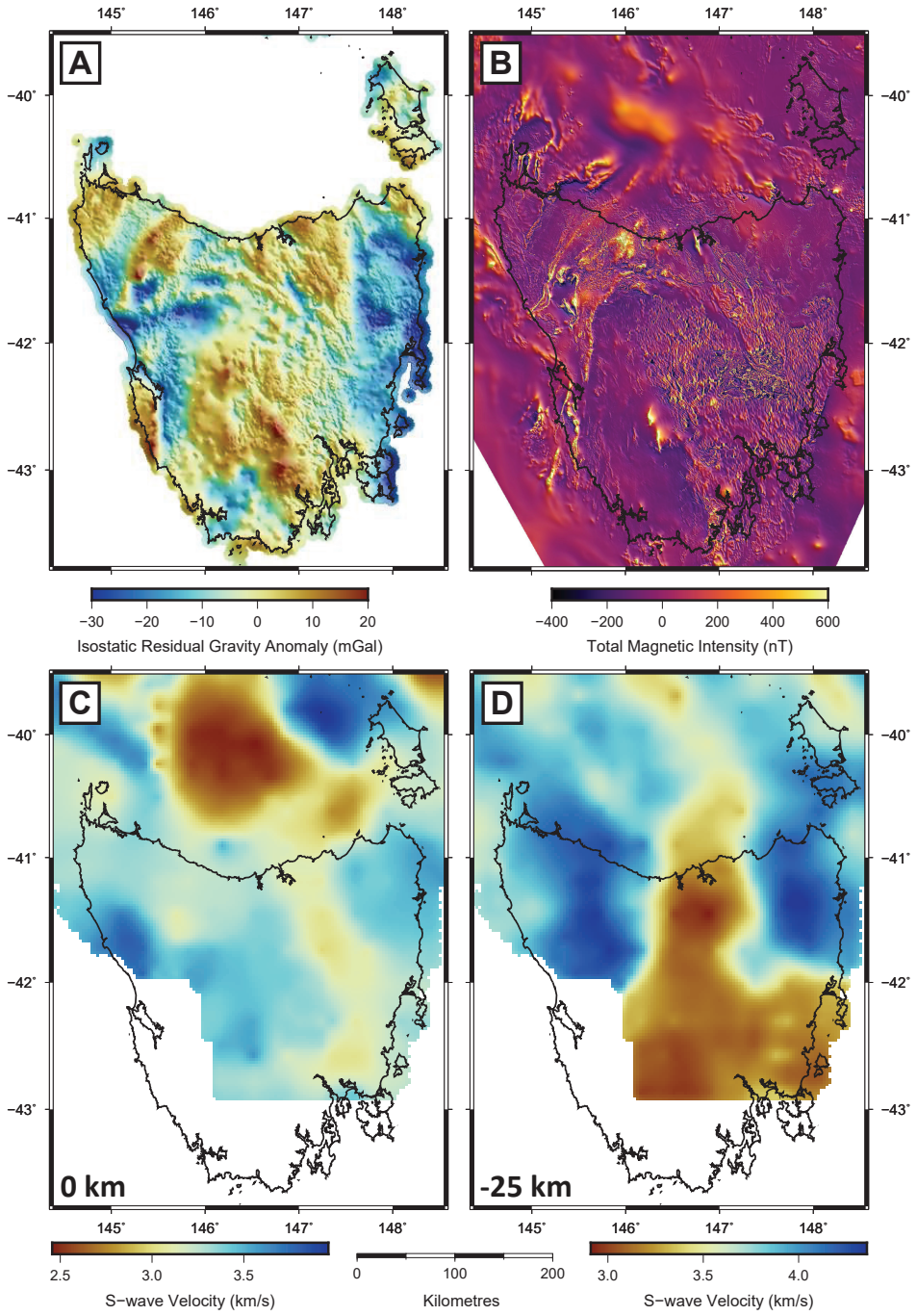

Figure 2.6: State-scale geophysical data sets. Panels **A** and **B** depict Tasmanian onshore isostatic residual Bouguer gravity anomaly and magnetic intensity, respectively. Panels **C** and **D** present depth slices through a shear wave velocity model inverted for s-wave group velocities from the WOMBAT transportable seismic array of Pilia et al. [2015].

Magnetic data coverage is similar to the state's gravity data set in that high resolution ($\leq$200 m flight line spacing) data is mostly restricted to the Dundas-Fossey Trough, parts of the

northeast and central Tasmania. Magnetic coverage for the remainder of the island is restricted to relatively low resolution (1500 m flight line spacing) data acquired by Geoscience Australia as part of a state-wide aeromagnetic survey in 1985 [Leaman and Richardson, 2014]. Tasmania's magnetic character, presented in Figure 2.6.B), is highly variable across geologic terrains. In the WTT, high total magnetic intensities coincident with serpentinised Cambrian ultramafic rocks are observed within and at the boundaries of the Dundas element. The ETT, by contrast, is magnetically quiet. Central and southern Tasmania are dominated by highly irregular magnetic signatures associated with Jurassic dolerite intrusion into Permo-Triassic sediments of Tasmania Basin.

Numerous seismic surveys employing differing methods have taken place in Tasmania since the 1960s. Major offshore and onshore seismic surveys were completed as part of the TASGO project: a circum-Tasmania seismic reflection survey coupled with numerous onshore seismic stations in an effort to map the topography of the Tasmanian Moho [Drummond et al., 2000, Hill and Yeates, 1995, Rawlinson et al., 2001]. More recent surveys have focused on passive seismic methods, with the deployment of the TIGGER and SETA passive seismic arrays across north and eastern Tasmania yielding insights into the deep structure of the Tasmanian lithosphere [Rawlinson et al., 2006, 2010]. Recent work on the WOMBAT seismic array in southeast Australia, which includes the TIGGER and SETA arrays, has shed light on the seismic structure of the southern Tasmanides, providing new geophysical evidence for Victoria-Tasmania crustal block correlations [Pilia et al., 2016, 2015].

Depth slices through a shear wave velocity model of Pilia et al. [2015] are presented in Figure 2.6.C) and D). Coverage of the south west of the island is incomplete, however models spanning northern and eastern Tasmania depict highly variable shear wave velocity structure in the mid- to lower-crust. The lower crust beneath the ETT returns a high shear wave velocity coincident with dense, possibly mafic material. Western Tasmania also returns high shear wave velocities typical of old Proterozoic crust. A zone of low shear wave speed between western and eastern Tasmania, roughly coincident with the Tamar Fracture System is also observed at mid-crustal depths and may represent younger accreted material against Precambrian crust to the west.

Geoelectric studies have a long history in Tasmania as noted previously. Pioneering work by Parkinson [1964] and Lewis [1965] investigated the coast effect and crustal conductivity structure in the Hobart area. Interesting anomalous results near the Tamar River valley in northern Tasmania were encountered by Lilley [1976] using magnetovariational (MV; induction arrows) techniques, the discovery of which led to intensive MT and MV surveys in this part of Tasmania. Buyung [1980] carried out MV investigations south of Launceston and noted the anomalously high conductivity zone continued beneath the Tamar River. Hermanto [1992] and Parkinson et al. [1988] further confined the extent of the anomaly, extending it to the southeast and named it the Tamar Conductivity Anomaly. Other early MT and MV studies were carried out in southeastern Tasmania by Dwipa [1992].

Wang et al. [2014] developed a continent-scale conductivity model from magnetic field data recorded at 57 magnetic base stations distributed across the Australian continent over the course of the Australia Wide Airborne Geophysical Survey (AWAGS). This low resolution model (55 x 55 km cells) was derived from geophysical inversion of vertical magnetic field transfer functions, and did not include data from sites in Tasmania. The model delineates major crustal block conductivities on the Australian continent, but does not show conductivity structure in Tasmania.

Detailed geoelectric studies were conducted between 2008 and 2010 in eastern and northern Tasmania as part of a KUTh Energy Ltd geothermal exploration program. Two high-frequency MT data sets were acquired; a 37-site, 1 km spaced high frequency MT transect across the Tamar river valley north of Launceston, and a 244-site high frequency MT gridded survey near Lemont in central eastern Tasmania to image conductivity structure over a zone of high surface heat flow coincident with the Tamar Conductivity Anomaly [Battaglini et al., 2010, Holgate et al., 2010].

More detailed geoelectric surveys have been conducted at prospect scale in parts of western Tasmania, mostly in connection with volcanic-hosted massive sulfide and tin skarn ore deposit exploration within the Dundas-Fossey Trough (e.g. example data in Asten et al. [2005]). These very high frequency MT surveys largely target the top $\sim$1 km of the crust, which is of most interest to the mining company operating in the locality.

2.3 The Magnetotelluric Method

The MT method is a passive electromagnetic (EM) geophysical technique for which time-varying electric (**E**) and magnetic (**B**) fields are recorded on the Earth's surface over a large frequency range. The inductive relationship between magnetic source signals and electric field responses observed at surface enables the determination of subsurface conductivity structure on depth scales ranging from hundreds of metres to hundreds of kilometres.

Geophysical tradition holds that MT theory was developed simultaneously and independently by Tikhonov [1950] in the USSR, Rikitake [1951] in Japan and Cagniard [1953] in France; and hinges on the assumption that magnetic source signals behave as plane waves and are uniform over any horizontal plane. This assumption drew criticism in the 1960s, but was defended by later numerical studies [Madden and Nelson, 1964] which have stood the test of time. These early researchers laid a mathematically correct foundation that formed a basis for subsequent MT studies. Chave et al. [2012] provides a complete account of the MT method in its modern form.

2.3.1 MT Source Signals

The Earth's magnetic field is primarily the result of dynamic processes in the liquid outer core, the geodynamo. Variations in the field due to these processes are of high amplitude and occur over time scales far greater than those relevant to the MT method. The MT method is reliant on geomagnetic field variation that occurs at much shorter time scales and originates from phenomena external to the Earth.

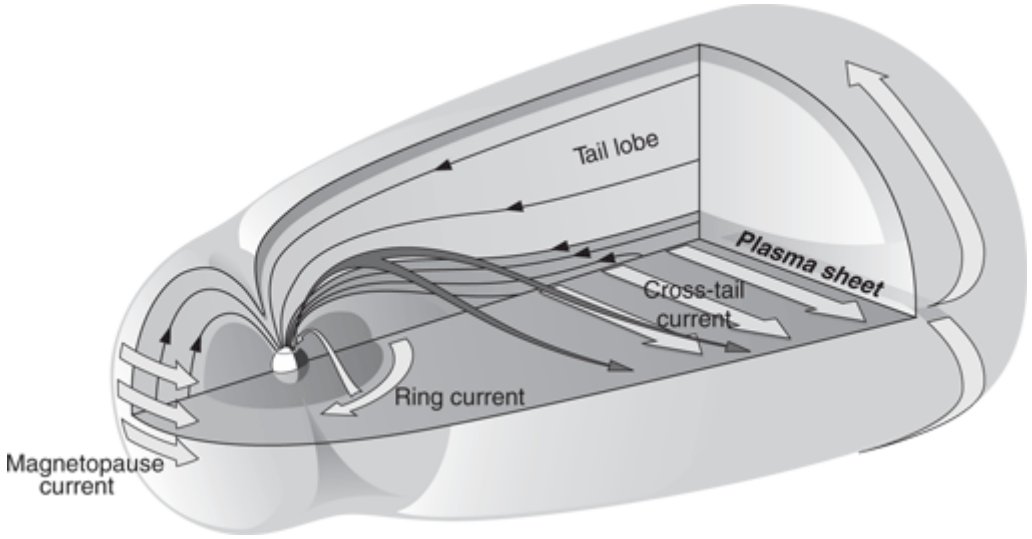

Figure 2.7: Sketch of the magnetosphere surrounding the Earth. The Sun and day side of the Earth are to the left. Illustration by Teemu Mäkinen from Chave et al. [2012].

Geomagnetic field fluctuations suitable for analysis using the MT method range in period-

icity from 10^{-3} s and 10^{5} s (or between frequencies of 10^{3} Hz and 10^{-5} Hz). Electromagnetic signals with periods shorter than one second are the result of meteorological activity in the neutral atmosphere. Here, lightning strikes result in high frequency (1 Hz to 10 kHz) electromagnetic signals that propagate within the Earth-ionosphere waveguide and are of particular use in shallow imaging broadband MT investigations. Weak signal intensities within the range 0.5 Hz to 5 Hz constitute the 'dead band' in the MT frequency range, and typically result in less robust estimations of the MT transfer function at these frequencies. This band is thus especially sensitive to industrial electromagnetic noise [Chave et al., 2012].

Long-period electromagnetic signals, with periods greater than 1 s, are produced by interactions between solar wind and the Earth's magnetosphere and ionosphere. The solar wind is a constant stream of charged particles that compresses the Earth's magnetic field on the day side. Variation in the solar wind's density and velocity result in field distortions with varying periodicity. Thermal heating of charged particles in the ionosphere on the daylight side results in large convection cells generating broad time-varying electric currents, thereby inducing time-varying magnetic source fields (Fig. 2.7). Variation in magnetic source field intensity results in geomagnetic pulsations with periods up to 600 s.

Longer period variations result from lunar distortions and solar flare effects, which dominate on solar quiet days where solar wind activity is relatively stable. During solar storms, where the solar wind is more intense and variable, long period high amplitude geomagnetic fluctuations result from strong ring currents and bay anomalies in the magnetosphere. Further discussion of MT source fields is given by Chave et al. [2012].

2.3.2 Electromagnetic Field Behaviour

The theoretical basis for the magnetotelluric method can be derived from Maxwell's equations, which taken together are a complete description of the relationships between electric and magnetic fields in any medium. These equations written in SI form are expressed as follows:

$$\nabla \times \mathbf{H} = \frac{\partial \mathbf{D}}{\partial t} + \mathbf{J}, \qquad \textit{[Ampère's Law]} \tag{2.1a}$$

$$\nabla \times \mathbf{E} = -\frac{\partial \mathbf{B}}{\partial t}, \qquad \textit{[Faraday's Law]} \tag{2.1b}$$

$$\nabla \cdot \mathbf{D} = q, \qquad \textit{[Gauss's law]} \tag{2.1c}$$

$$\nabla \cdot \mathbf{B} = 0, \qquad \textit{[Gauss's Law for magnetism]} \tag{2.1d}$$

where **E** is the electric field strength (V/m), **B** is the magnetic induction (T), **H** is the magnetic field strength (A/m), **D** is electric displacement (C/m^2), **J** is the current density (A/m^2), and q is the electric charge density (C/m^3). In linear, isotropic media with electric conductivity σ (S/m), Maxwell's equations yield three further relationships:

$$\mathbf{B} = \mu\mathbf{H}, \tag{2.2a}$$

$$\mathbf{D} = \varepsilon\mathbf{E}, \tag{2.2b}$$

$$\mathbf{J} = \sigma\mathbf{E}. \qquad \textit{[Ohm's Law]} \tag{2.2c}$$

Here, $\mu = \mu_0\mu_r$ and $\varepsilon = \varepsilon_0\varepsilon_r$ describe the magnetic permeability and electric permittivity of the medium, respectively, from the magnetic permeability of free space ($\mu_0 = 4\pi \times 10^{-7}$ H/m) and the electric permittivity of free space ($\varepsilon_0 = 8.85 \times 10^{-12}$ F/m). Given the wide variation in conductivities observed in Earth materials, variations in both μ_r and ε_r are assumed to be negligible. With Equations 2.2a, 2.2b and 2.2c, Ampère's Law (Equ. 2.1a) and Gauss's Law (Equ. 2.1c) can be re-written as:

$$\nabla \times \mathbf{B} = \mu\varepsilon\frac{\partial \mathbf{E}}{\partial t} + \mu\sigma\mathbf{E}, \tag{2.3a}$$

$$\nabla \cdot \mathbf{E} = \frac{q}{\varepsilon}. \tag{2.3b}$$

2.3.3 Physical Assumptions of the MT Method

Derivation of the MT method requires a number of key assumptions regarding the physics of the source signal and the nature of electrical conduction in the Earth. These are;

1. Electromagnetic signals utilised by the MT method are assumed to be generated by magnetic source fields located at a distance approximating infinity. As a consequence, electromagnetic signals can be treated as uniform plane waves propagating vertically downward onto the Earth's surface. A plane electromagnetic wave with **E** and **B** fields with amplitude $\mathbf{E}_0$ and $\mathbf{E}_0$ at origin, and angular frequency ω takes the mathematical form:

$$\mathbf{E} = \mathbf{E}_0 e^{i\omega t}, \tag{2.4a}$$

$$\mathbf{B} = \mathbf{B}_0 e^{i\omega t}. \tag{2.4b}$$

2. In Earth-like materials, the relatively low frequencies of electromagnetic fields utilised by the MT method do not induce significant displacement currents relative to conduction currents. Displacement currents are assumed to be quasi-static. Thus, in Equation 2.3a, the displacement current term $\mu\varepsilon\frac{\partial \mathbf{E}}{\partial t} \approx 0$, and so

$$\nabla \times \mathbf{B} = \mu\sigma\mathbf{E}. \tag{2.5a}$$

3. Charges do not accumulate in the horizontally layered Earth. However, charges can accumulate within a multi-dimensional Earth at conductivity gradients. This is referred to as the galvanic effect, and can be expressed as the following equation derived by taking the divergence of Ohm's Law (Equ. 2.2c) and solving for electric charge density q using Equation 2.3b;

$$q = -\varepsilon(\nabla\sigma) \cdot \frac{\mathbf{E}}{\sigma}. \tag{2.6a}$$

This effect, also referred to as current channelling or current deflection, can be visualised by considering the electric field strength in a media with conductivity σ_0 containing a distinct zone with different conductivity σ_1 (Fig. 2.8). Charge accumulation at the edges (a conductivity gradient) of the body in the media result in differing total electric field strengths depending on the nature of the resistivity contrast. Shallow, local scale conductivity contrasts producing this effect can introduce frequency independent distortions to electric field observations relevant to MT and must be accounted for in data interpretation.

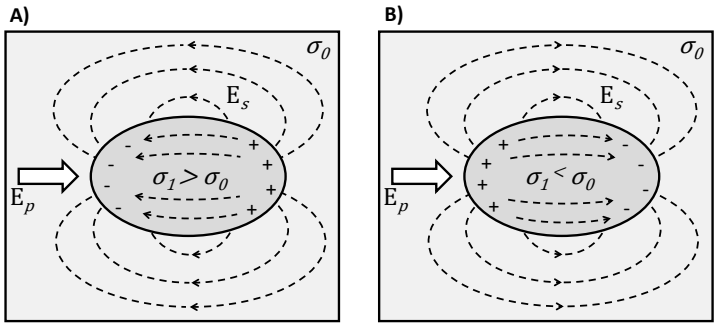

Figure 2.8: Illustration of the galvanic effect in two different media: A) where a conductive body is encased in a resistive medium, and B) where a resistive body is encased in a conductive medium. In the presence of a primary electric field $\mathbf{E}_p$, electric charges accumulate at conductivity contrasts resulting in a secondary electric field $\mathbf{E}_s$. In case A), the total electric field ($\mathbf{E}_T = \mathbf{E}_p + \mathbf{E}_s$) is reduced directly over the body, enhanced at the ends and diminished along the sides. In case B), the total field is enhanced over the top of the body, diminished at the ends and amplified at the sides. Figure modified from Jiracek [1990].

2.3.4 Depth of Penetration and Skin Depth

For a homogeneous and isotropic medium with non-zero conductivity ($\sigma > 0$), and assuming a time variation of the form $e^{\mathrm{i}\omega t}$ (where $\omega = 2\pi f$ the angular frequency in Hz, and $\mathrm{i} = \sqrt{-1}$ the imaginary unit), Maxwell's equations yield Helmholtz equations for the electric ($\mathbf{E}$) and magnetic ($\mathbf{B}$) fields;

$$(\nabla^2 - \gamma^2)\mathbf{E} = 0, \tag{2.7a}$$

$$(\nabla^2 - \gamma^2)\mathbf{B} = 0, \tag{2.7b}$$

where γ denotes the complex wave number described by

$$\gamma^2 = \mathrm{i}\omega\mu\sigma - \omega^2\mu\varepsilon = \boldsymbol{k}^2 - \kappa^2. \tag{2.8}$$

Here, κ describes the undamped part of the electromagnetic wave travelling at speed of $c = \frac{1}{\sqrt{\mu\varepsilon}}$ with wavelength $\lambda = \frac{2\pi}{\kappa} = \frac{2\pi}{\omega\sqrt{\mu\varepsilon}} = \frac{c}{f}$. Given the quasi-static assumption, where displacement currents are assumed to be static, the propagation constant $\boldsymbol{k}$ (m^{-1}) plays a far greater role relative to κ as $\sigma >> \varepsilon\omega$. Thus, the Helmholtz equations 2.7a and 2.7b can be re-written as;

$$(\nabla^2 - \boldsymbol{k}^2)\mathbf{B} = 0, \tag{2.9a}$$

$$(\nabla^2 - \boldsymbol{k}^2)\mathbf{E} = 0 \tag{2.9b}$$

where $\boldsymbol{k}^2 = \mathrm{i}\omega\mu\sigma$, and so

$$\boldsymbol{k} = \sqrt{\mathrm{i}\omega\mu\sigma} = \sqrt{\mathrm{i}}\sqrt{\omega\mu\sigma} = \frac{1+\mathrm{i}}{\sqrt{2}}\sqrt{\omega\mu\sigma} = (1+\mathrm{i})\sqrt{\frac{\omega\mu\sigma}{2}}. \tag{2.10}$$

The propagation constant $\boldsymbol{k}$ described in Equation 2.6a has real and imaginary components. The real component can be written as

$$\delta = \frac{1}{\Re\boldsymbol{k}} = \sqrt{\frac{2}{\omega\mu\sigma}} \tag{2.11}$$

where δ is known as the *skin depth* (in m). This describes the depth at which a signal is attenuated to $1/e$ of its amplitude at the surface, and is often used as an estimate of penetration depth for electromagnetic signals in MT. Given that the magnetic permeability of Earth

materials in most geologic environments is equivalent to that of free space ($\mu \approx \mu_0 = 4\pi \times 10^{-7}$ Vs/Am), the skin depth (m) equation is often approximated to

$$\delta \approx 500\sqrt{\frac{T}{\sigma}} = 500\sqrt{T\rho} \tag{2.12}$$

where $T = 2\pi/\omega$ is the period of the electromagnetic signal in seconds and ρ is the apparent resistivity (Ωm) of the medium. This is a critical approximation in MT, as the depth of electromagnetic signal penetration is determined by only two factors; the resistivity of overlying material and the periodicity of the signal.

2.3.5 The MT Impedance Tensor

Expanding the curl operator in Faraday's Law (Equ. 2.1b) for 3-dimensional cartesian coordinates yield the following relationship between electric (**E**) and magnetic (**B**) fields;

$$\frac{\partial \mathbf{E}_z}{\partial_y} - \frac{\partial \mathbf{E}_y}{\partial_z} = \text{-i}\omega\mathbf{B}_x, \tag{2.13a}$$

$$\frac{\partial \mathbf{E}_x}{\partial_z} - \frac{\partial \mathbf{E}_z}{\partial_x} = \text{-i}\omega\mathbf{B}_y, \tag{2.13b}$$

$$\frac{\partial \mathbf{E}_y}{\partial_x} - \frac{\partial \mathbf{E}_x}{\partial_y} = \text{-i}\omega\mathbf{B}_z. \tag{2.13c}$$

As noted above, key assumptions of the MT method state that the Earth can be approximated by a conducting half space with a plane surface, and magnetic source fields are of infinite dimensions located at a distance approximating infinity. These assumptions yield a situation in which magnetic source signals behave as plane waves vertically incident on the Earth's surface. Since this **B**-field signal propagates vertically downward, induced **E**-field signals do not have a vertical component ($\mathbf{E}_z = 0$). Another implication of the plane wave assumption is that the **B**-field does not have vertical components ($\mathbf{B}_z = 0$), and so $\frac{\partial \mathbf{E}x}{\partial y} = \frac{\partial \mathbf{E}y}{\partial x} = 0$. Applying these assumptions to Equations 2.8 and 2.9a yield these relationships;

$$\frac{\partial \mathbf{E}_y}{\partial_z} = \text{i}\omega\mathbf{B}_x, \tag{2.14a}$$

$$\frac{\partial \mathbf{E}_x}{\partial_z} = \text{-i}\omega\mathbf{B}_y, \tag{2.14b}$$

$$\mathbf{Z}(\omega) = \frac{\mathbf{E}_{y_0}}{\mathbf{B}_{x_0}} = -\frac{\mathrm{i}\omega}{\boldsymbol{k}} = -\frac{\mathrm{i}\omega}{\sqrt{\mathrm{i}\omega\mu\sigma}} = -\sqrt{\frac{\omega}{\mu\sigma}}\sqrt{\mathrm{i}} \tag{2.15}$$

where $\mathbf{Z}$ is the magnetotelluric impedance, a complex function relating the electric and magnetic fields. From the impedance tensor the apparent resistivity ρ of the half space at a given angular frequency ω can be derived by rearranging Equation 2.15 as follows;

$$\rho = \frac{\mu}{\omega}|\mathbf{Z}|^2. \tag{2.16}$$

In the frequency domain $\mathbf{Z}(\omega)$ is a complex number and has an associated phase ϕ;

$$\phi = \arg \mathbf{Z} = \arg \sqrt{\frac{\omega}{\mu\sigma}}\sqrt{\mathrm{i}} = \arg \sqrt{\frac{\omega}{\mu\sigma}} e^{\frac{\mathrm{i}\pi}{4}} = \frac{\pi}{4} = 45°. \tag{2.17}$$

The phase of the impedance tensor is therefore a constant 45° with the electric field leading the magnetic field, independent of the resistivity of the uniformly resistive halfspace.

2.3.6 MT in 3-Dimensional Environments

The homogeneous half space approach to investigating the impedance tensor described above can be extended to arbitrary 3D subsurface resistivity distributions. In such situations, all components of the **B**-field and **E**-field are coupled, and the MT impedance is now expressed as a tensor:

$$\begin{bmatrix} \mathbf{E}_x \\ \mathbf{E}_y \end{bmatrix} = \begin{bmatrix} \mathbf{Z}_{xx} & \mathbf{Z}_{xy} \\ \mathbf{Z}_{yx} & \mathbf{Z}_{yy} \end{bmatrix} \begin{bmatrix} \mathbf{B}_x \\ \mathbf{B}_y \end{bmatrix}. \tag{2.18}$$

Here, each component of the impedance tensor has apparent resistivity ρ and phase ϕ given by;

$$\rho_{a_{ij}}(\omega) = \frac{1}{\mu_0\omega}|\mathbf{Z}_{ij}(\omega)|^2, \tag{2.19a}$$

$$\phi_{ij} = \arctan\left(\frac{\Im\mathbf{Z}_{ij}}{\Re\mathbf{Z}_{ij}}\right), \tag{2.19b}$$

where the subscripts i and j are indices for the rows and columns of the impedance tensor.

2.3.7 MT in 2-Dimensional Environments

The impedance tensor derived for 3D environments can be simplified greatly in 2D geoelectric environments, with important implications for MT modelling and interpretation. Figure 2.9 presents an idealised case in which two geologic units with differing resistivities are separated by a vertical interface. It is assumed that all quantities are constant along the x-direction, i.e. $\frac{\partial}{\partial_x} = 0$, and the geologic units are significantly greater in extent than the skin depth δ (Equ. 2.12).

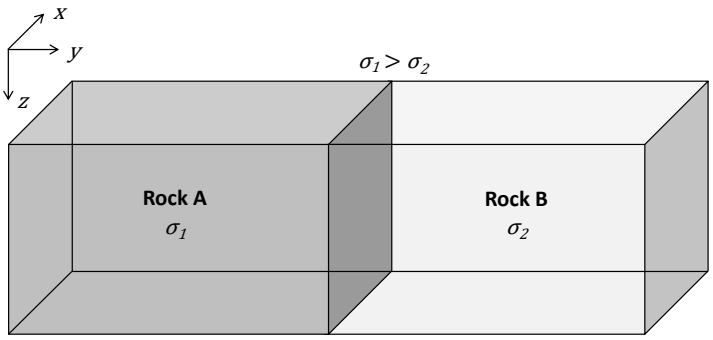

Figure 2.9: 2D model with vertical interface between conductive rock A and resistive rock B striking in the x-direction.

In this 2D case electric and magnetic fields are orthogonal and can be decoupled into a component with the **E**-field parallel to the conductivity contrast strike direction, and a component with the **B**-field parallel to strike. In such a situation, the impedance tensor is simplified as $\mathbf{Z}_{xx} = \mathbf{Z}_{yy} = 0$ and $\mathbf{Z}_{xy} \neq \mathbf{Z}_{yx}$.

In practice, 2D geoelectric structures are rarely parallel to **B**-field or **E**-field measurement directions. As a result, the measured MT impedance tensor $\mathbf{Z}'$ contains non-zero components unless it is rotated by an angle α to be parallel with the strike of the resistivity boundary. This is implimented by

$$\mathbf{Z}' = \begin{bmatrix} \mathbf{Z}'_{xx} & \mathbf{Z}'_{xy} \\ \mathbf{Z}'_{yx} & \mathbf{Z}'_{yy} \end{bmatrix} = \mathbf{R} \begin{bmatrix} 0 & \mathbf{Z}_{xy} \\ \mathbf{Z}_{yx} & 0 \end{bmatrix} \mathbf{R}^T = \mathbf{R}\mathbf{Z}_{2D}\mathbf{R}^T, \tag{2.20}$$

where

$$\mathbf{R} = \begin{bmatrix} \cos\alpha & \sin\alpha \\ -\sin\alpha & \cos\alpha \end{bmatrix}. \tag{2.21}$$

2.3.8 The MT Phase Tensor

The MT phase tensor is a second rank tensor in the impedance tensor that describes the phase relationships between the electrical and magnetic fields. It is particularly useful in interpreting MT data sets as it is unaffected by galvanic distortion and does not require *a priori* knowledge of the local geoelectric structure to interpret [Bibby et al., 2005, Booker, 2014, Caldwell et al., 2004]. The phase tensor Φ is given by the equation

$$\Phi = \mathbf{X}^{-1}\mathbf{Y}, \tag{2.22}$$

where $\mathbf{X}$ and $\mathbf{Y}$ are the real and imaginary components of the impedance tensor $\mathbf{Z}$. The coordinate invariants of the phase tensor are the minimum and maximum phases and the skew angle β. The parameters are related to the dimensionality of the geoelectric environment, with simplistic 1D geoelectric environments giving rise to phase tensors with a single coordinate invariant equal to the corresponding impedance tensor phase.

In 2D geoelectric environments the phase tensor is symmetric with one of its principal axes aligned parrallel to the regional geoelectric strike, the preferred regional current flow direction. Geoelectric strike is given by either α or $\alpha + 90°$, as there is ambiguity between the two principal axes, and is given by

$$\alpha = \frac{1}{2}\arctan\frac{\Phi_{xy} + \Phi_{yx}}{\Phi_{xx} - \Phi_{yy}}, \tag{2.23}$$

$$\beta = \frac{1}{2}\arctan\frac{\Phi_{xy} - \Phi_{yx}}{\Phi_{xx} + \Phi_{yy}}. \tag{2.24}$$

The skew angle β describes the degree of asymmetry of the phase tensor, and is a critical in assessing the dimensionality of MT data sets. In ideal 1D and 2D environments $\beta = 0$ and the phase tensor is symmetrical, while in 3D environments $\beta \neq 0$. A key test for 2-dimensionality in MT data sets involves the derivation of the skew angle for each period, and periods where $-5° < \beta > 5°$ are typically rejected as they are excessively 3D and cannot be accurately modelled in 2D [Caldwell et al., 2004]. A critical review of this approach by Booker [2014] suggests $-6° < \beta > 6°$ are acceptable for treatment as 2D, however 2D inverse modelling workflows presented in this thesis use the β thresholds of Caldwell et al. [2004].

Qualitative analysis of the phase tensor is commonly conducted by way of the phase tensor ellipse plotting convention (Fig. 2.10). Phase tensor ellipse plots provide a visual means of assessing likely geoelectric strike direction as well as dimensionality when coloured by skew angle.

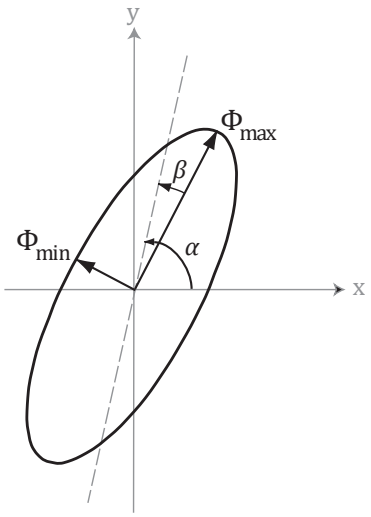

Figure 2.10: Graphical representation of the phase tensor ellipse derived from a 3D impedance tensor. Image modified from Caldwell et al. [2004].

2.3.9 Geomagnetic Depth Sounding and Induction Arrows

The ratio of vertical components to the horizontal components of the **B**-field can describe lateral resistivity boundaries. This relationship is employed through the Geomagnetic Depth Sounding (GDS) technique, where the GDS transfer function **T** (the 'tipper') is a complex vector that defines the amplitude and phase of the horizontal inducing field and vertical anomalous induced field at a frequency ω. This relationship is written as;

$$\mathbf{B}_z = \mathbf{T}_{zx}\mathbf{B}_x + \mathbf{T}_{zy}\mathbf{B}_y. \tag{2.25}$$

In the case of a laterally uniform resistive Earth (flat-lying sedimentary basins for example), with a horizontal source field, there is no anomalous vertical **B**-field and **T**=0. Close to a conductivity boundary such as that presented in Figure 2.9, there is a strong anomalous vertical component to the **B**-field and **T** is correspondingly large.

Induction arrows are a graphical representation of the GDS transfer function components $\mathbf{T}_{zx}$ and $\mathbf{T}_{zy}$. These have a real (in-phase) and quadrature (out-of-phase) part, with arrow lengths of the real ($\mathbf{M}_r$) and quadrature ($\mathbf{M}_q$) given by;

$$\mathbf{M}_r = \sqrt{(\Re\mathbf{T}_{zx}^2 + \Re\mathbf{T}_{zy}^2)}, \tag{2.26a}$$

$$\mathbf{M}_q = \sqrt{(\Im\mathbf{T}_{zx}^2 + \Im\mathbf{T}_{zy}^2)}. \tag{2.26b}$$

Induction arrow orientations are given by θ_r for the real, and θ_q for quadrature. These are plotted clockwise from the x-direction, usually geomagnetic north, and are determined as follows;

$$\theta_r = \arctan\left(\frac{\Re\mathbf{T}_{zy}}{\Re\mathbf{T}_{zx}}\right), \tag{2.27a}$$

$$\theta_r = \arctan\left(\frac{\Im\mathbf{T}_{zy}}{\Im\mathbf{T}_{zx}}\right). \tag{2.27b}$$

When plotted on a map, the magnitudes and directions of these arrows yield information about the lateral variation in subsurface conductivity. It should be noted that there are two different plotting conventions for induction arrows; the Weise convention after Wiese [1962] and the Parkinson convention after Parkinson [1962]. The Parkinson convention involves the reversal of the real component which results in arrows that point toward regions of high conductance and away from regions of low conductance. All induction arrows presented in this thesis use the Parkinson convention.

Induction arrows have no depth sensitivity, but are a useful means of investigating MT data in cases where 3-component magnetometer information is recorded. GDS tensor information can also be incorporated into 3D inversion algorithms as observed data additional to the impedance tensor.

2.3.10 2D Inversion Algorithms

Of the 2D inverse algorithms developed in the 1990s, OCCAM2D of DeGroot-Hedlin and Constable [1990] is perhaps the most commonly used algorithm in MT inversion. Although superseded by computationally less expense non-linear conjugate gradient (NLCG) inversion methods of Rodi and Mackie [2001], OCCAM2D remains something of a standard 2D inverse algorithm owing to its free availability. The algorithm is built on earlier work in smooth 1D inverse modelling of Constable et al. [1987], and similarly seeks to avoid over-fitting MT data by imposing a smoothness constraint so as to arrive at a regularised 2D model of subsurface resistivity with minimum structure. More recently the 2D inversion code MARE2DEM of Key [2016] has emerged as a competitor to OCCAM2D in the open source code space, the key point of difference being its approach to model space parameterisation as a finite element mesh with variable triangular polygon resolution for greater parameter efficiency. For a comprehensive overview of the 2D MT inverse problem see Rodi and Mackie [2012].

Of the MT transects presented in Figure 2.4, transects **F**) and **J**) utilised OCCAM2D code to derive 2D models, while the rest utilised NLCG 2D inversion methods implemented in MT software packages such as Winglink owned by the oil and gas services company Schlumberger. 2D modelling conducted as part of this study utilised open source OCCAM2D code.

2.3.11 3D Inversion Algorithms

The increasing availability of parallelised computing power has led to the recent development of full 3D inverse modelling algorithms for MT. As with 2D codes, 3D inversion codes come in a number of different implementations the details of which is beyond the scope of this chapter. Reviews of 3D inverse modelling methods are presented in Siripunvaraporn [2012] and Egbert and Kelbert [2012].

Examples of 3D inverse modelling codes suitable for application in this thesis include the adaptive finite element GoFEM code of Grayver [2015], the hexahedral finite element HexMT code of Kordy et al. [2016] and the rectangular element ModEM3DMT code of Kelbert et al. [2014]. All 3D inverse modelling presented in this thesis uses Mod3DMT, a freely available code that has resulted in at least 300 publications (as of August 2020) since its release, and has become the benchmark 3D inversion code within the broader MT community. All inverse models derived from the AusLAMP MT array have used the ModEM3DMT code, as have similar modelling studies using the USArray data set in the United States [Meqbel et al., 2014].

2.3.12 MT Summary

The MT method is a passive geophysical technique sensitive to subsurface resistivity. The method relies on time varying magnetic fields as a source signal and induced electric fields as a response signal. The depth of investigation of the method is dependent on the skin depth effect, which describes the depth of penetration of an electromagnetic signal as being dependent on the resistivity of the subsurface and frequency of signal.

Measurement of the electric and magnetic fields at the surface of the Earth enable the derivation of the MT impedance tensor, from which apparent resistivity and phase values can be calculated. Determination of the regional geoelectric strike and likely subsurface geoelectric dimensionality can be achieved by analysis of the phase tensor and its invariants. Dimensionality analysis of MT data is particularly important in the case where MT data is being modelled in 2D, where highly 3D data can introduce erroneous model structure.

Chapter 3

Magnetotelluric Data Acquisition

This chapter introduces the reader to the key motivations for the experiment, provides a background to the magnetotelluric (MT) survey design and describes data acquisition efforts in detail.

3.1 AusLAMP Long Period MT Data

Much of the Australian continent is obscured by young sedimentary cover of substantial thickness representing a major impediment to mineral exploration. Further exploration success depends on the development and application of geoscientific methods capable of extracting geological information about the older, often prospective basement to this sedimentary cover.

Recently, a greater understanding of lithospheric architecture controls on mineralised corridors [Griffin et al., 2013] has been made possible with advancements in deep probing geophysical techniques such as MT [Heinson et al., 2006, Thiel and Heinson, 2010] and seismic tomography [Fishwick and Rawlinson, 2012, Kennett et al., 2011, Rawlinson et al., 2006]. The potential for lithosphere-scale geophysical information to assist explorers with terrain-to-province target selection was a major impetus for the Australian Lithospheric Architecture Magnetotelluric Project (AusLAMP).

AusLAMP is a collaborative national MT survey led by researchers at Geoscience Australia and the University of Adelaide. With the involvement of State and Northern Territory geological surveys and universities, the multi-year project aims to acquire approximately 3000 long period MT measurements at half-degree spacing across the Australian continent. At the time of writing acquisition in Tasmania, Victoria, South Australia and New South Wales is largely complete, with current acquisition prioritising Northern Australia.

In the early planning stages of data acquisition for the Tasmanian AusLAMP field campaign, the decision was made to reduce the half-degree site spacing (equivalent to $\sim$55 km at the equator) to a 40 km by 40 km grid in order to achieve an even data spread across the island and increase the spatial resolution. Site locations generated at this spacing were snapped to the

nearest roadside locations in using Geographic Information Systems (GIS). An assessment of site suitability was then carried out on an individual basis. All sites were moved to the nearest clear area with minimal slope based on a subjective assessment of air photographs and digital elevation models. Site locations near the coast, pipelines or high voltage transmission lines were relocated to areas with an ∼8 km buffer around these potential sources of electromagnetic noise.

3.2 Broadband Transects

Cambrian volcanic and sedimentary rocks of the Dundas-Fossey Trough form a ∼30 km belt wrapping around the western and northern margins of the Neoproterozoic Tyennan Block [Seymour et al., 2006]. The western end of the trough consists of geological basement which is host to several Volcanic Hosted Massive Sulfide (VHMS) type deposits including the large Mt Lyell and Rosebery deposits. In the north, much of the trough basement rocks are obscured by younger sedimentary sequences as well as thin, remanently magnetised and geophysically opaque Cenozoic basalts Corbett et al. [2014].

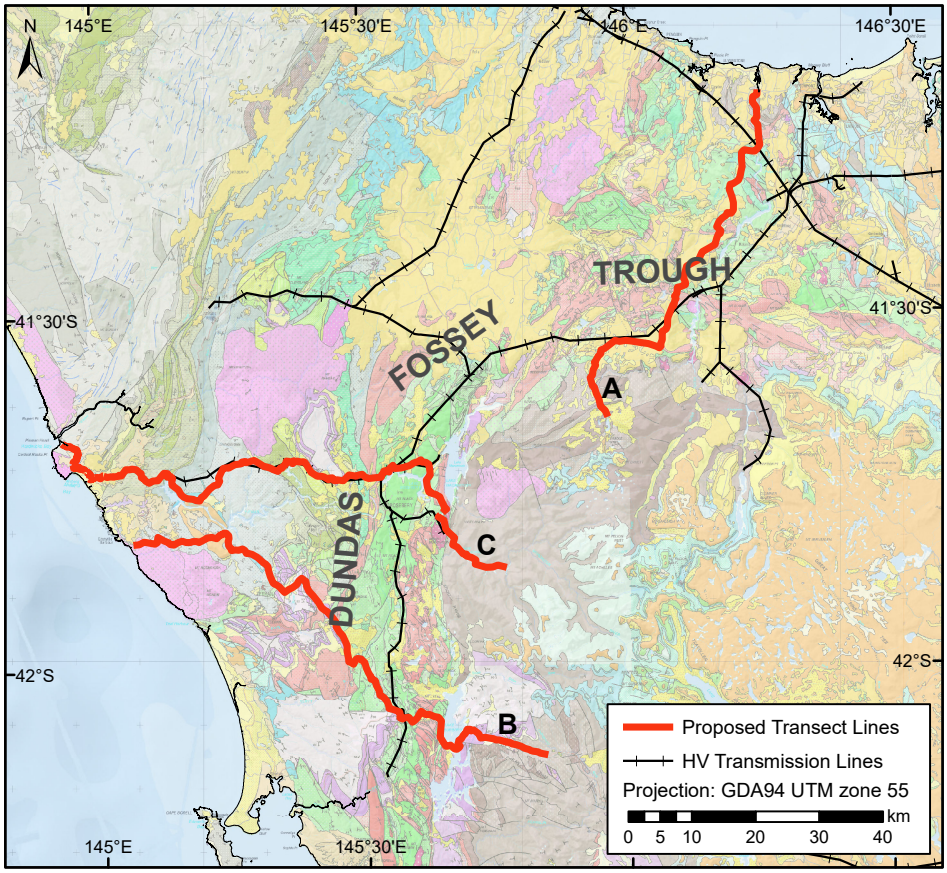

Figure 3.1: Location of proposed transect lines plotted on 1:250,000 scale surface geology [Mineral Resources Tasmania, 2011]. Transects **A** and **B** were carried out. **C** was not carried out due to noise from high voltage transmission lines.

A series of broadband MT transects across the Dundas-Fossey trough were proposed by Mineral Resources Tasmania with the aim of imaging the basement beneath the sedimentary and volcanic cover rocks. Three traverses were considered, each using existing road infrastructure to transect the trough; two in the west and another in the north. Of the three proposed transect lines, one western line was judged to be very problematic due to electromagnetic noise related to a high voltage transmission line running parallel to road access for a significant proportion of the transects length (line **C** in Fig. 3.1).

In order to image the complex geology of the Dundas-Fossey Trough, a relatively fine instrument spacing of 2 km was selected. Ever a compromise between maximising image resolution and field practicality, this choice in site spacing was informed by a similar survey interpreted by Robertson et al. [2015] in western Victoria where a spacing of 5 km was found to be inadequate for imaging complex geology in the shallow crust.

As with the initial AusLAMP sites discussed above, each proposed transect site was assessed individually and, where necessary, manually adjusted to the nearest suitable location. This process was particularly difficult for the northern transect, where high voltage transmission lines cross the transect at a number of locations, and run parallel to it for several kilometres. Proposed and final locations for the transect sites are presented in detail in Figures 3.3 and 3.4.

3.3 AuScope MT Instruments

MT instruments used for broadband transects and AusLAMP long period deployments were sourced through the Australian National Seismic Imaging Resource (ANSIR) national Earth sounding instrument pool. Co-funded by AuScope and maintained by the University of Adelaide, the instrumental capability results from a collaboration between the University of Adelaide and Geoscience Australia.

Each instrument consists of a 24-bit 6-channel PR6-24 Earth Data Logger housed in a reinforced Pelican case. The logger records GPS-synchronised time series electric field data from an array of three Petiau-type lead chloride non-polarisable electrodes. Magnetic field time series data are recorded from LEMI-120 induction coil output when in broadband survey mode, or a Bartington Mag-03 three-axis fluxgate magnetometer when in long period survey mode.

Powered by a 70 amp-hour 12 volt battery, the unit can log broadband data for $\sim$3 days without a recharge or battery replacement. When deployed in long period mode for upwards of 3 weeks, a 1 square metre solar panel (deployed some $\sim$15 metres from the magnetic field sensors to avoid cross talk noise) is employed to recharge the battery continuously and maintain voltage to the data logger.

3.4 Instrument Deployments

Data acquisition took place over several months across four deployment phases throughout 2016. The bulk of the acquisition, including all transect sites, was completed during phase 1 while phases 2, 3 and 4 deployed or redeployed remaining AusLAMP sites. Due to the challenging nature of deploying MT instruments in Tasmania, field operations are described in detail to assist any future surveys.

The author of this thesis took the role of field leader and was responsible for the successful execution of planning station deployment and data recovery. Field deployments took place between January and November 2016, with the need to work around summer bush fires and scheduling of other loans by the ANSIR equipment pool.

3.4.1 Land Access & Reconnaissance Trip

Land access negotiations and permitting for private and public land took place throughout December 2015 and January 2016. In the case of private land, considerable effort was made to contact all landholders by phone and meet them in person to discuss the project. After securing permission, a generic letter was either delivered in person or emailed to each landholder (see appendices A for long period and B for broadband sites). For sites located on public land, all of which were administered by the Tasmanian Parks and Wildlife Service and Forestry Tasmania, the permitting process begun in early December and was completed by mid-January.

A reconnaissance trip was completed in the second week of January 2016 to meet with landholders and ground truth the suitability of sites chosen on the basis of air photographs and digital elevation models. Most sites on the northern transect were favourable however it became apparent that a number of sites on western transect were inaccessible due to very dense vegetation and rugged terrain (Fig. 3.2).

3.4.2 Phase 1

Commencing on the 22nd of January, phase 1 involved an intensive 4 week round of data acquisition involving two 2-person rotating field crews staffed by students from the University of Tasmania and the University of Adelaide, as well as experienced staff from Geoscience Australia, the University of Adelaide and PassiveX Pty Ltd. With a pool of 24 MT instruments, crews began by deploying 10 northeastern AusLAMP sites in long period mode before advancing to broadband deployments on the western transect.

Based out of Queenstown, crews began broadband acquisition from the eastern end of the transect after establishing a remote reference site 5 km east of easternmost proposed transect site. Occupation time at each site was in the order of 36-48 hours with crews deploying and retrieving two sites per day. Acquisition of all western transect sites was completed by the 6th

of February, at which point field crews rotated staff and relocated to Gowrie Park in northern Tasmania to commence acquisition on the northern transect.

Data acquisition on the northern transect commenced on the 8th of February starting at the northernmost site near Forth following the establishment of a remote reference site some 4 km south of Beulah and 20 km east of the transect line. Less dense scrub and easier digging allowed for faster instrument deployments on the northern transect, with crews deploying and retrieving up to three instruments per day. Acquisition on the northern transect was hindered by wildlife chewing and severing electrode cables early in deployment at four sites, three requiring a single redeployment and one requiring two re-deployments with progressively deeper burial of cables, electrodes and magnetometers.

Figure 3.2: A typical western transect deployment location in buttongrass moorland beneath Mt Owen east of Queenstown.

Acquisition on the northern transect was completed on the 19th of February. Crews then converted all instruments used in broadband transect surveying to long period mode and deployed them to remaining AusLAMP locations in northern and eastern Tasmania. AusLAMP sites deployed at the start of phase 1 were retrieved after logging ∼28 days worth of data and deployed to new locations. Phase 1 AusLAMP deployment was completed on the 23rd of February.

All AusLAMP instruments were retrieved by a single 2-person crew over the course of a week between the 10th and 15th of March. All 23 AuScope instruments were returned to Adelaide before being sent onto Western Australia in line with ANSIR scheduling.

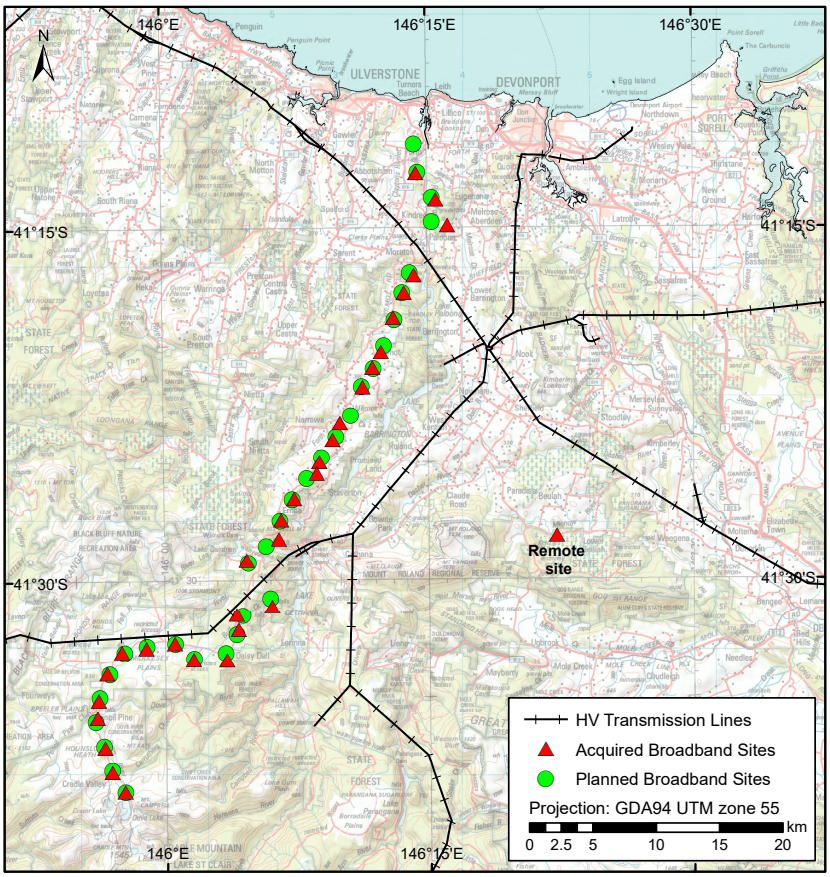

Figure 3.3: Distribution of broadband MT sites comprising the northern broadband transect.

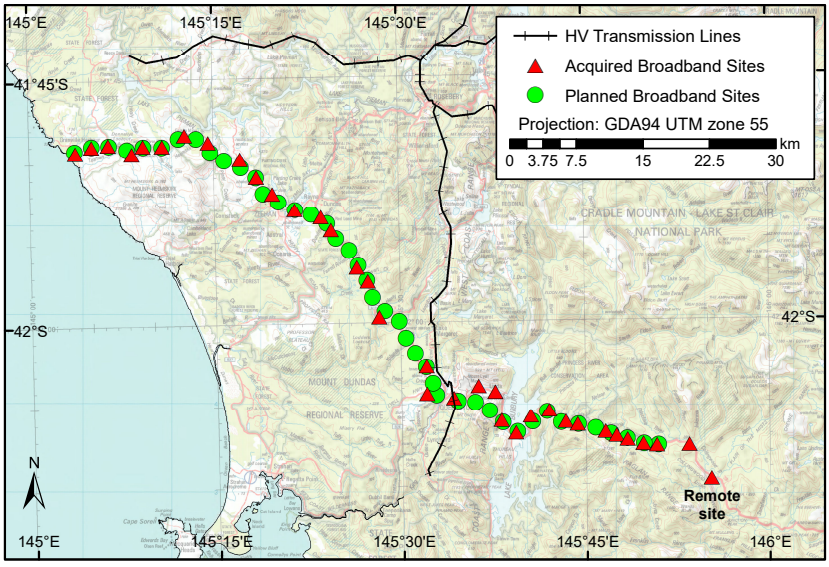

Figure 3.4: Distribution of broadband MT sites comprising the western broadband transect.

3.4.3 Phase 2

Phase 2 involved the deployment of AusLAMP long period MT instruments to remaining locations. This included sites previously inaccessible due to bush fires in northwestern Tasmania as well as remote sites requiring air transport to Flinders Island, and helicopter flights to the Southwest National Park.

These remote sites required a significant amount of planning. Flinders Island deployments involved the close collaboration of Parks and Wildlife Service officers for ground transport and site selection, and the organisation of light aircraft cargo flights from Bridport in northeast Tasmania. Helicopter flights to the Southwest National Park required separate landing permits and a degree of flexibility with dates due to the need for favourable weather conditions.

Data acquisition commenced on the 16th of July with a single, 2-person crew starting in the northwest of the state. The crew managed an average of two deployments per day in very cold, wet and sometimes snowy conditions. Two instruments were deployed on Flinders Island over the 27th and 28th of July. Helicopter-borne deployments in the southwest were scheduled for the 20th of July but took place on the 30th due to poor weather conditions.

Instrument pickups commenced on the 28th of August, again starting in the northwest of the state. Helicopter-accessed sites in the southwest were retrieved on the 1st of September and Flinders Island instruments, the last phase 2 instruments to be retrieved, were picked up on the 13th of September.

Despite the best efforts of the field crew to ensure magnetometer housings were watertight, four instruments deployed during phase 2 had waterlogged magnetometers upon retrieval. An analysis of the time series data revealed that these instruments logged enough **B**-field data to obtain a satisfactory result without the need to redeploy.

Some phase 2 deployments recorded incomplete time series records due to batteries not being sufficiently recharged by solar panels during short daylight hours. At one northwestern site the problem was compounded by trees obscuring some of the morning daylight, and necessitated redeployment at this location at a later date. All but two sites out of a deployed 23 recorded enough time series data (>2 weeks) to compute satisfactory impedance tensors.

3.4.4 Phases 3 & 4

Nineteen AuScope instruments used in phase 2 were returned to Adelaide immediately after retrieval to align with ANSIR scheduling. Four instrument sets were kept in Tasmania for the remainder of the University of Tasmania's ANSIR instrument loan duration. These instruments were deployed over phases 3 and 4 in order to re-acquire data at failed deployment locations from phase 2 as well as increase the spatial resolution of the data set by infilling at select locations.

New infill deployments were all located on Forestry Tasmania, and Parks and Wildlife Service

administered land for which survey permission had already been granted. Phase 3 deployments took place between the 19th and 21st of September, and focused on the deployment of three infill sites around the Tamar River Valley as well as the redeployment of a failed site in the northwest.

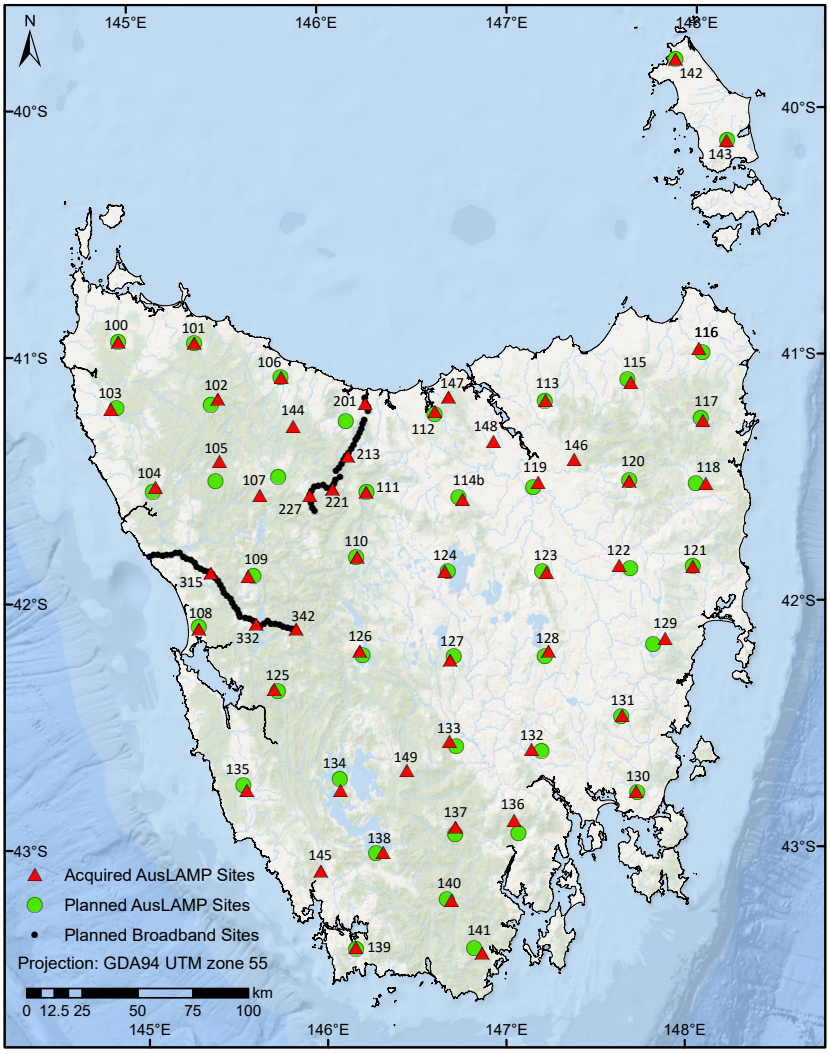

Figure 3.5: Distribution of planned and acquired long period AusLAMP sites in Tasmania after completion of data acquisition (with site numbers). A number of AusLAMP sites were deployed a significant distance from their planned deployment locations, especially in north west Tasmania. This is a consequence of planned site locations being unsuited to instrument deployment, requiring field teams to seek out the nearest accessible locations within Forestry Tasmania or Parks and Wildlife administered land for which instrument deployments were pre-approved.

Phase 3 instruments were picked up on the 17th of October and immediately redeployed the 4th and final phase of deployments. Phase 4 instrument deployments redeployed a failed phase 2 site in the southwest and infilled areas in the central east of the state, increasing the spatial resolution over the Tamar Fracture System. These instruments were retrieved on the 10th of November.

Chapter 4

AusLAMP Long Period 3D Resistivity Statewide Models for Tasmania

This chapter discusses the steps taken in processing and analysing long period MT data acquired as part of the Tasmanian component of the AusLAMP national survey. Sections 4.1 and 4.2 discuss the software packages and processing procedures used in raw data processing, as well as the types of noise encountered in the raw data and the procedures used to minimise their influence. The chapter then continues to show results and interpretation of geoelectric features discovered. The level of detail used throughout this thesis chapter aims to provide a record of utility to geophysicists planning future tectonic and exploration-related studies of Tasmania with higher station density.

Section 4.3 presents an analysis of phase tensor ellipses plotted for all sites on the island while section 4.4 presents an analysis of induction arrow relationships including legacy data from previous studies in northern Tasmania. Section 4.5 discusses 3D inversion including modelling techniques used, data preparation steps required and presents results in the form of depth slices through the preferred 3D inverse model. Section 4.6 presents an interpretation of the preferred resistivity model arising from the integration of the preferred model with available geological and geophysical data sets into 3D visualisation software packages. Finally, sections 4.7 and 4.8 conclude the chapter and present recommendations for future work.

4.1 Data Processing

For each of the 57 long period AusLAMP sites acquired, raw time series data were processed to output electronic data interchange (EDI) format files containing impedance tensor ($\mathbf{Z}$) and geomagnetic depth sounding (GDS) transfer function, or tipper ($\mathbf{T}$), information. These EDI

files formed the basis from which all further interpretation and modelling progressed.

4.1.1 Instrument Outputs

AuScope MT instruments in long period survey mode were used as AusLAMP stations, and recorded magnetic and electric field data with a sampling frequency of 10 Hz. Horizontal and vertical components of the magnetic field were recorded using a Bartington Mag-03 fluxgate magnetometer, while horizontal electric field components were recorded as electric potentials across two non-polarisable electrodes buried in the ground and separated by a known distance (one oriented N-S the other E-W). Both magnetometer and electrode outputs were digitised by a 24-bit PR6-24 Earth Data Logger and recorded in units of millivolts (mV) onto internal hard drives in ASCII format. Figure 4.1 presents a schematic diagram of a long period MT site.

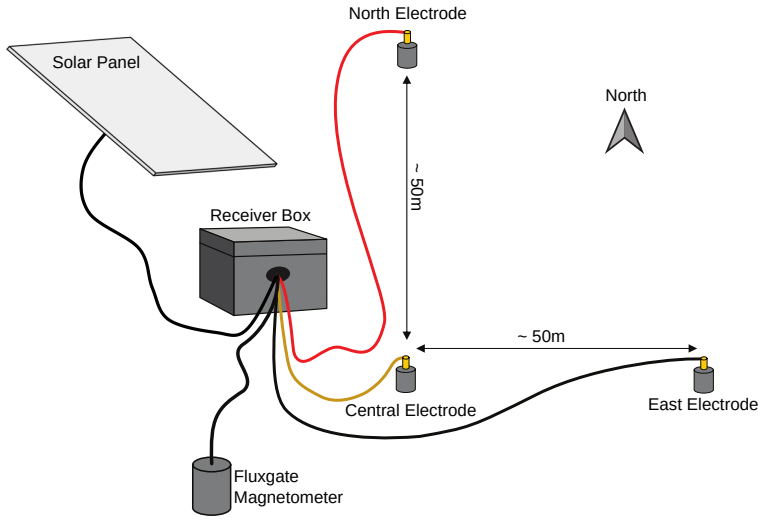

Figure 4.1: Schematic diagram of an AuScope MT instrument deployed in long period mode. Electrodes and magnetometer are buried to a depth of ∼0.5 m in order to ensure stability and good electrical contact.

4.1.2 Time Series Data Processing

Following data download and archive, initial time series data processing was carried out in step-by-step operations to;

1. convert millivolt magnetometer channel outputs to units of magnetic field strength (nT),
2. convert electric field channel millivolt outputs to units of electric field strength (µV/m),
3. rotate both electric and magnetic field data to geographic north,
4. down sample the time series by a factor of 10,
5. generate input files for impedance tensor and GDS transfer function computation with the Bounded Influence Remote Reference Processing (BIRRP), and,

6. plot time series data plots for subjective data quality inspection.

All of these steps were carried out using the LMTraw2ts code of Thiel [2008] developed in MATLAB specifically for use with AuScope MT instruments in long period mode. LMTraw2ts requires site-specific inputs for electrode orientation and dipole lengths (recorded in field deployment notes) in order to calculate the electric field strength and orientation, as well as the Earth's magnetic field declination at the site location for data rotation to geographic north. Declination inputs were calculated for the date of site deployment using the International Geomagnetic Reference Field 2012 (IGRF12).

After inputting site-specific electrode and declination information, LMTraw2ts down sampled the electric and magnetic field data by a factor of 10, generating final time series data files and a plot of each field component (Fig. 4.2). Inspecting time series plots for data quality at this point was a crucial step in data processing. Spurious signals, typically of high amplitude, from major rainfall events, wildlife disturbances or electrode contact degradation were easily identified and portions of time series data free of such problematic signals could be selected for final processing in BIRRP.

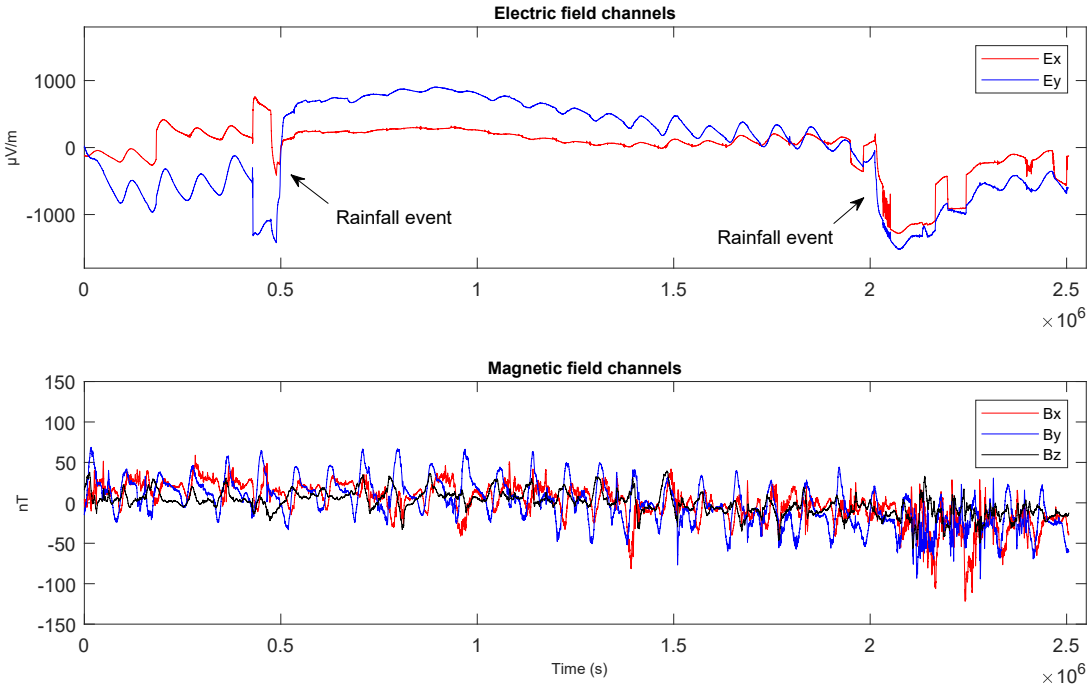

Figure 4.2: Time series plot output example from LMTraw2ts for **E**-field and **B**-field channels from long period site 100 deployed in NW Tasmania. Time series section between rainfall disturbances was selected for processing and yielded the best **Z** and **T** estimations.

The BIRRP program computes impedance tensor and GDS transfer functions from raw time series data using a bounded influence, remote reference method. Remote referencing is required to remove any uncorrelated magnetic field signals due to local sources as these can introduce significant error to the impedance tensor and GDS transfer function estimations, especially

at shorter periods. In order to use remote referencing, it is necessary to have simultaneously recorded, LMTraw2ts-processed magnetic field time series from another MT site to use as a reference field. This necessity was accounted for in field procedures by ensuring at least three MT instruments were deployed at any one time. This is the final step in raw time series processing, yielding an EDI file containing frequency domain impedance tensor and GDS transfer function information with associated error estimates.

4.2 Noise & Missing Data

AusLAMP MT data processing did not involve any systematic noise reduction processing steps other than selection of 'clean' data from visual inspection of time series. However, it is important to consider the kinds of noise that can introduce large errors into impedance tensor and GDS transfer function estimations. In this context, noise constitutes electromagnetic signals from nearby sources that do not fit the plane wave approximation.

Typical noise sources encountered in AusLAMP surveying include man-made signals, such as electric fence pulses and power line noise; or natural signals, such as those induced in instrument cables due to wind vibration. Several sites were also subject to wildlife and farm animal interference as well as issues with battery power shortages in low-light winter months, both of which resulted in shortened time series.

4.2.1 Power Line Noise

The most pervasive type of noise in MT surveys is 50 Hz noise from alternating current (AC) power line networks. As discussed in previous chapters, and in accordance with MT data acquisition best-practice, AusLAMP MT sites were deployed in excess of 1 km from high voltage electrical transmission lines in an effort to mitigate excessive noise of this nature. However, practical constraints on site accessibility resulted in a few instruments being deployed within 1 km of lower voltage domestic power infrastructure, and any noise that may result was to be dealt with in later processing.

Given that AusLAMP MT sites recorded field data at a 10 Hz sample rate, later decimated to 1 Hz in processing, any noise emanating from 50 Hz AC power lines is likely the result of spectral leakage and possibly subharmonics in the network. Figure 4.3 presents time series and estimates of the power spectral density (PSD) plots for magnetic field data collected at MT sites 119, deployed near Launceston, and 135 deployed in the southwest wilderness area. Despite being located within 400 m of domestic power lines, PSD estimates from site 119 indicate the majority of the signal is concentrated in the lower frequencies, and no obvious spectral peaks of the kind expected from subharmonic power line noise are observed. The same is true for site 135, which was deployed some 35 km away from any electrical infrastructure.

Noise resulting from spectral leakage was not directly detected in time series or spectral

density plots and, if present, was largely controlled by remote referencing in BIRRP. Where possible, reference sites deployed in remote and ostensibly power line noise-free areas were used.

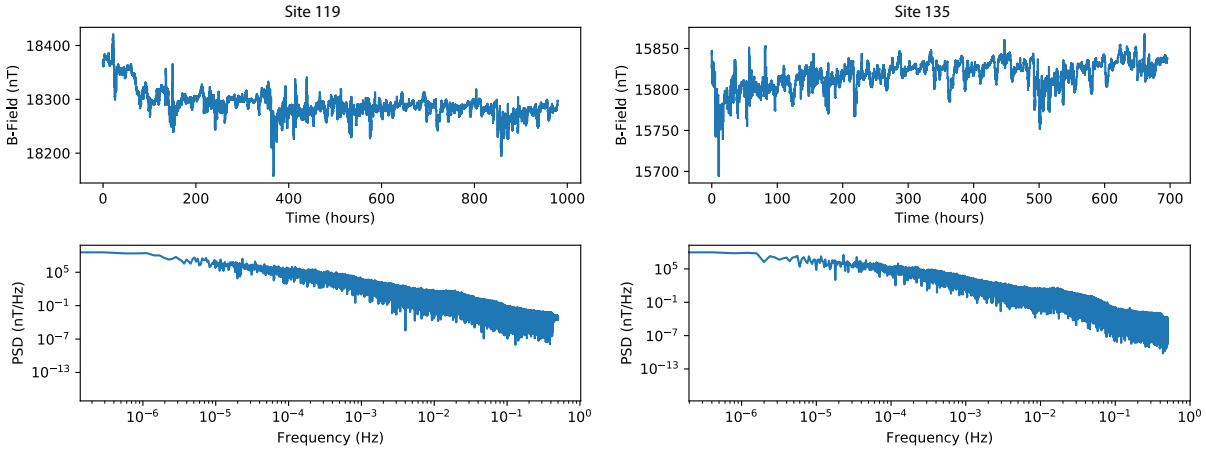

Figure 4.3: North-south oriented components of the **B**-field gathered over the deployment of sites 119 (left) and 135 (right). Data is presented as raw time series (top) and periodograms depicting estimated power spectral density (bottom). PSD was estimated using the Python SciPy library of codes.

4.2.2 Animal Interference & Winter Deployments

Incomplete time series data were recorded at a number of AusLAMP MT sites. The cases where this resulted from animal interference was often obvious on instrument retrieval where electrode and magnetometer cables were chewed through or electrodes dug up, most likely by common wombats (*Vombatus ursinus*). Inspection of time series for one such site indicated interference had occurred the day prior to retrieval, making re-deployment unnecessary.

Several wintertime deployments, and a few summertime deployments in shaded areas, were subject to power shortages that also resulted in incomplete data. In these cases, complete data existed for the first 8 to 12 days of the deployment, after which batteries would be expended and the charging rate from solar panels could not maintain constant data recording. Data recording once batteries reached this state was sporadic, with less than 1 h of data recorded in the late afternoon common, while some sites missed entire days of data altogether.

Data processing immediately following instrument retrieval was essential in determining whether re-deployment to the site was required in these cases. The majority of sites with missing data, whether due to animal interference or low battery, recorded enough time series to return adequate impedance tensor and GDS transfer function estimates, with only a few requiring re-deployment.

4.2.3 Waterlogged Magnetometers

Major rainfall events took place during winter deployments and affected several instruments in northern and central Tasmania. On retrieval, a number had waterlogged magnetometer

housings resulting in damaged magnetometers and incomplete magnetic field data for two sites. One site had very noisy electric field data and was re-deployed (site 138). Another (site 132) had good electric field data, and given limited instrument availability, was used for processing using magnetic data from a different site (131) some 40 km to the north west. Since the plane wave assumption holds true for periods up to 100 000 s, and field data is recorded relatively close together, this is a valid method of retrieving MT impedance tensor estimates from sites with electric field data only. Given that site 132's magnetic field data was not recorded, this site does not have any GDS, or tipper information.

4.3 Phase Tensor Analysis

The MT phase tensor, described in Equation 2.17 in Chapter 2, represents the phase difference between electric and magnetic fields from which the impedance tensor is calculated. This is a useful property of MT data as it presents a means of qualitatively analysing geoelectric structure while being unaffected by galvanic distortion [Bibby et al., 2005, Booker, 2014].

Phase tensor analysis typically involves plotting tensor properties as an ellipse [Caldwell et al., 2004]. The minor and major axes of the ellipse represent the principal axes of the tensor, and thus yield lateral geoelectric structure information with the preferred current flow direction or geoelectric strike angle represented by the major axes of the ellipse. The degree of preferential current flow along the geoelectric strike is indicated by the ellipticity of the ellipse. Vertical geoelectric structure information can be included in these phase visualisations by colouring ellipses by the phase angle. In the case of a uniformly resistive halfspace phase angles are 45°. Instances where phases are >45° indicate resistivity decreasing with depth, while phases <45° are indicative of resistivity increasing with depth.

The MT phase tensor does not contain depth information. However, skin depths for electromagnetic signals penetrating the Earth at the periods for which ellipses are calculated provide a means of inferring likely depth of investigation. In geoelectric environments typical of continental crust, periods ranging from 0.1 to 10 s are sensitive to shallow- to mid-crustal depths, periods around 100 s are sensitive to the lower crust, and periods exceeding 1000 s are sensitive to lithospheric mantle. These observations are highly generalised, and variation in resistivity structure can give rise to greater variability in depth of penetration.

Phase tensor ellipse plots from Tasmanian AusLAMP data for periods less than 10 s are dominated by shallow local-scale effects yielding non-coherent phase tensor plots. For periods greater than 50 s, phase tensor plots begin to reveal clear differences in geoelectric structure between the ETT and WTT. At 100 s, phase tensor ellipses from the ETT (including Flinders Island) are highly elliptical, tend to align east-west and have low (<45°) minimum phase angles indicating increasing resistivity with depth (Fig. 4.4). High ellipticity in the ETT suggests strong east-west preferential current flow at mid-crustal depths. In the west of the ETT, phase

tensor ellipses become highly skewed and align broadly parallel to the inferred boundary with the WTT. This is likely due to the influence of the Tamar Conductivity Anomaly, an upper- to mid-crustal zone of elevated conductivity [Hermanto, 1992].

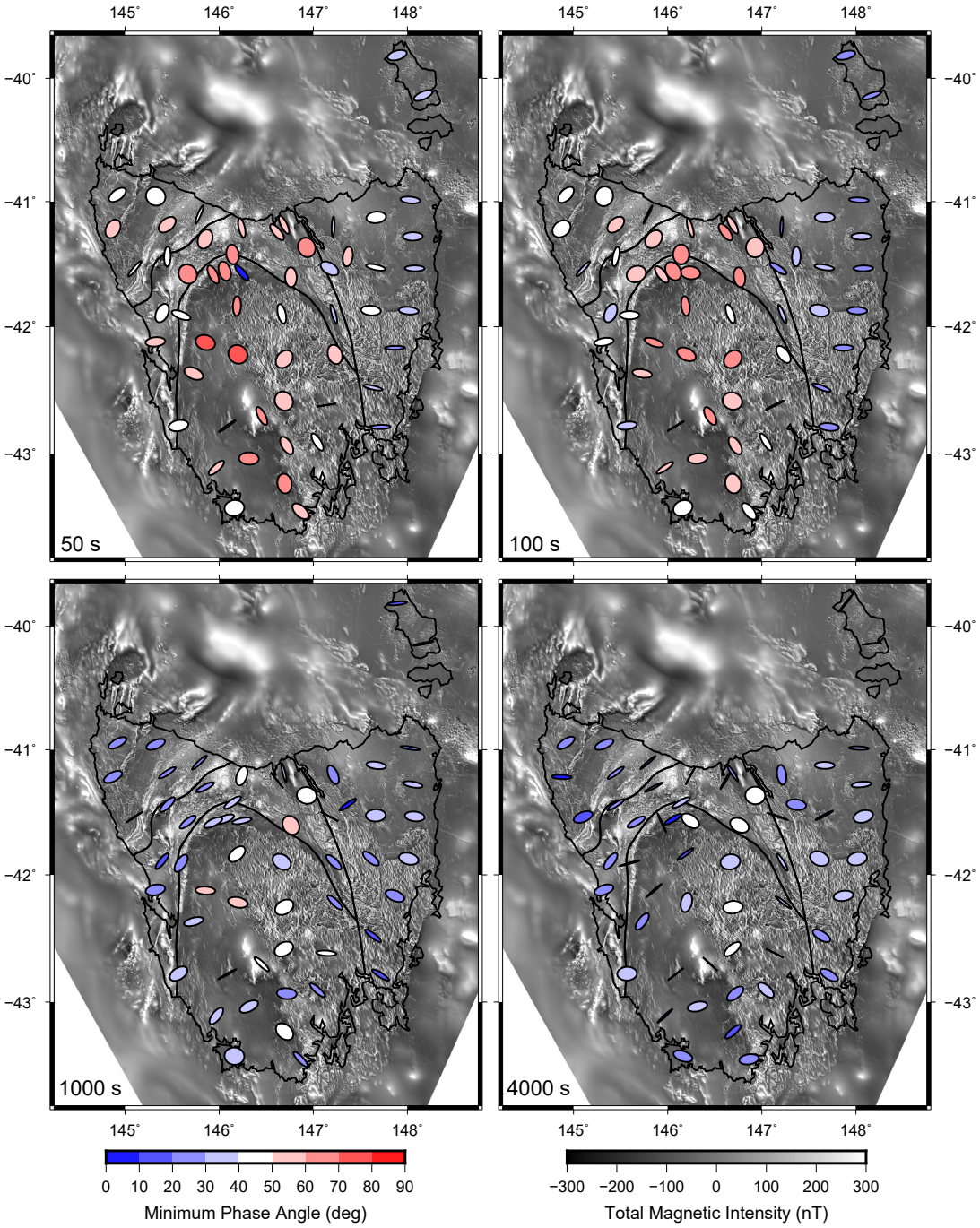

Figure 4.4: Phase tensor ellipses for 50 s, 100 s, 1000 s and 4000 s periods corresponding to mid-crustal through to upper-mantle depths over a sunshaded greyscale total magnetic intensity image. Black lines represent the Tasmanian coastline and major crustal boundaries from Shaw et al. [1996]. Ellipses are coloured by minimum phase angle, giving an indication of how resistivity changes with depth. Phase angles greater than 45°, shaded red, show conductivity is increasing with depth. Phase angles less than 45°, ellipses shaded blue, indicate conductivity is decreasing with depth.

At periods greater than 500 s, corresponding to lower crustal and lithospheric mantle depths, phase tensor ellipses for sites in the Rocky Cape and Dundas-Fossey Trough elements tend to align northeast-southwest with sites proximal with the boundary with the Tyennan Block tracing an arcuate geoelectric strike pattern parallel to the terrain boundary. At these depths, phase angles indicate conductivity is decreasing with depth in all geologic regions with the exception of the central Tyennan Element, where a complex internal geoelectric structure gives rise to variable ellipse orientation and phase angles.

4.4 Induction Arrow Analysis

Given that AusLAMP sites recorded the full magnetic tensor, it is possible to compute the GDS transfer function for sites with complete magnetic field recordings. This is a complex vector relating amplitude and phase of the horizontal inducing field to anomalous induced vertical fields for a given frequency.

In the case of a subsurface with 1D resistivity structure, there is no anomalous vertical magnetic field and the transfer function is zero. By contrast, close to boundaries between low and high resistivity structures, there is a large anomalous vertical field. Parkinson arrows, or more commonly, induction arrows are a graphical representation of the geomagnetic depth sounding transfer function developed by Parkinson [1962] while investigating the effect of the conductive ocean on magnetic field measurements at coastal observatories. For a given frequency or period, induction arrows are plotted for the real (in-phase) and imaginary (quadrature) components of the GDS transfer function, giving a sense of the relative magnitude and direction of each component. This contains qualitative information on the regional geoelectric structure, with the real component pointing toward conductive regions and relative size of the arrow indicative of the magnitude of the conductivity contrast.

Legacy GDS data from magneto-variational surveys of Parkinson et al. [1988] in NE Tasmania containing induction arrow information for 1000 s and 4000 s periods have been digitised and incorporated into plots of AusLAMP induction arrows presented in Figures 4.5 and 4.6. AusLAMP induction arrows are in agreement with legacy data, showing the strong influence of the Tamar Conductivity Anomaly (TCA) on mid- to lower-crustal current flow in eastern Tasmania.

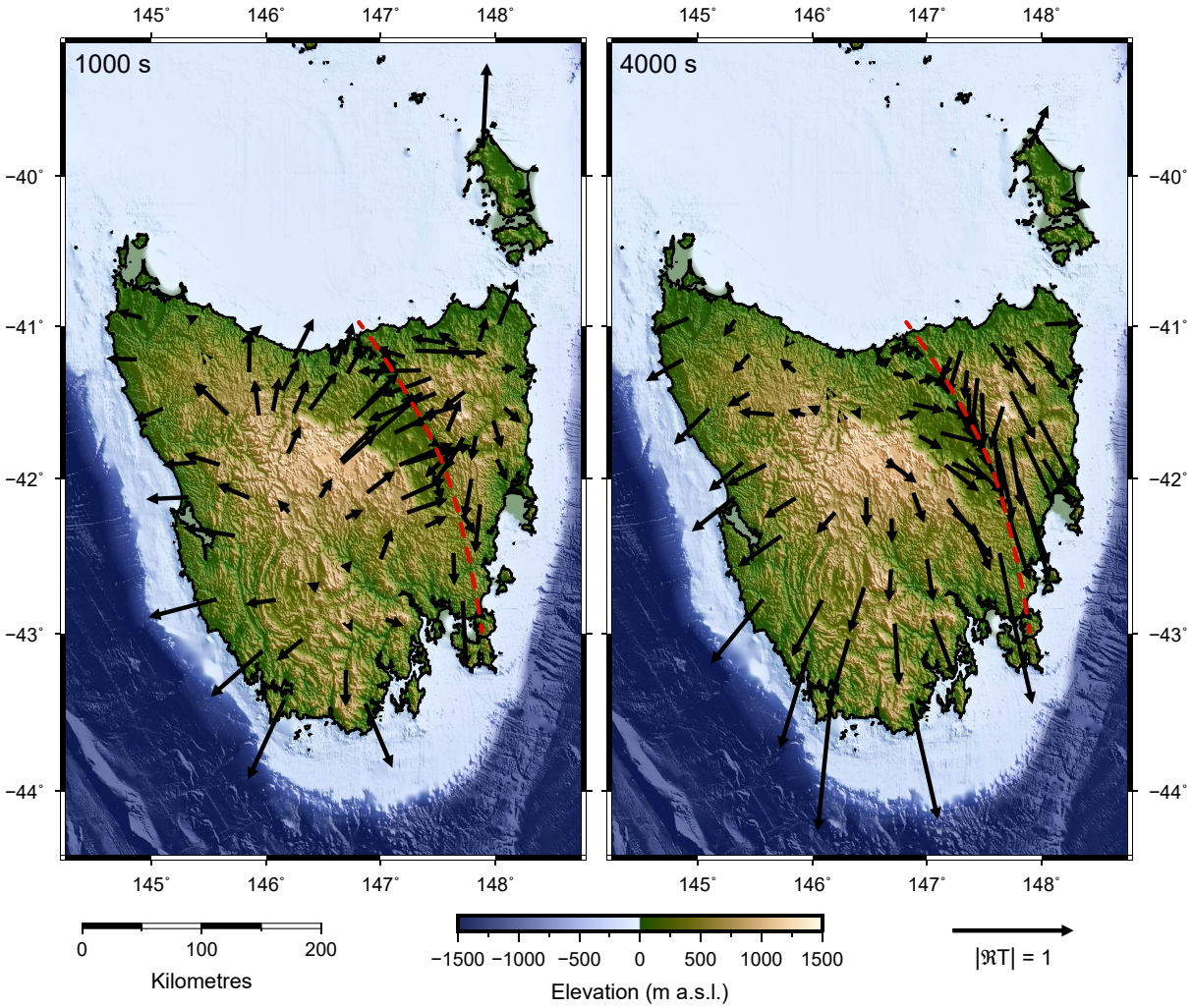

Figure 4.5: Real component induction arrows for 1000 and 4000 second periods from magnetic field observations at AusLAMP MT sites and legacy GDS sites of Parkinson et al. [1988] overlain onto a shaded digital elevation model. At 1000 seconds both AusLAMP and legacy GDS induction arrows highlight regional conductivity structure, with coastal sites strongly influenced by the coast effect [Parkinson and Jones, 1979] and most north eastern sites pointing toward the TCA (dashed red line). At 4000 seconds, most induction arrows are dominated by the coast effect with north eastern sites showing residual TCA influence.

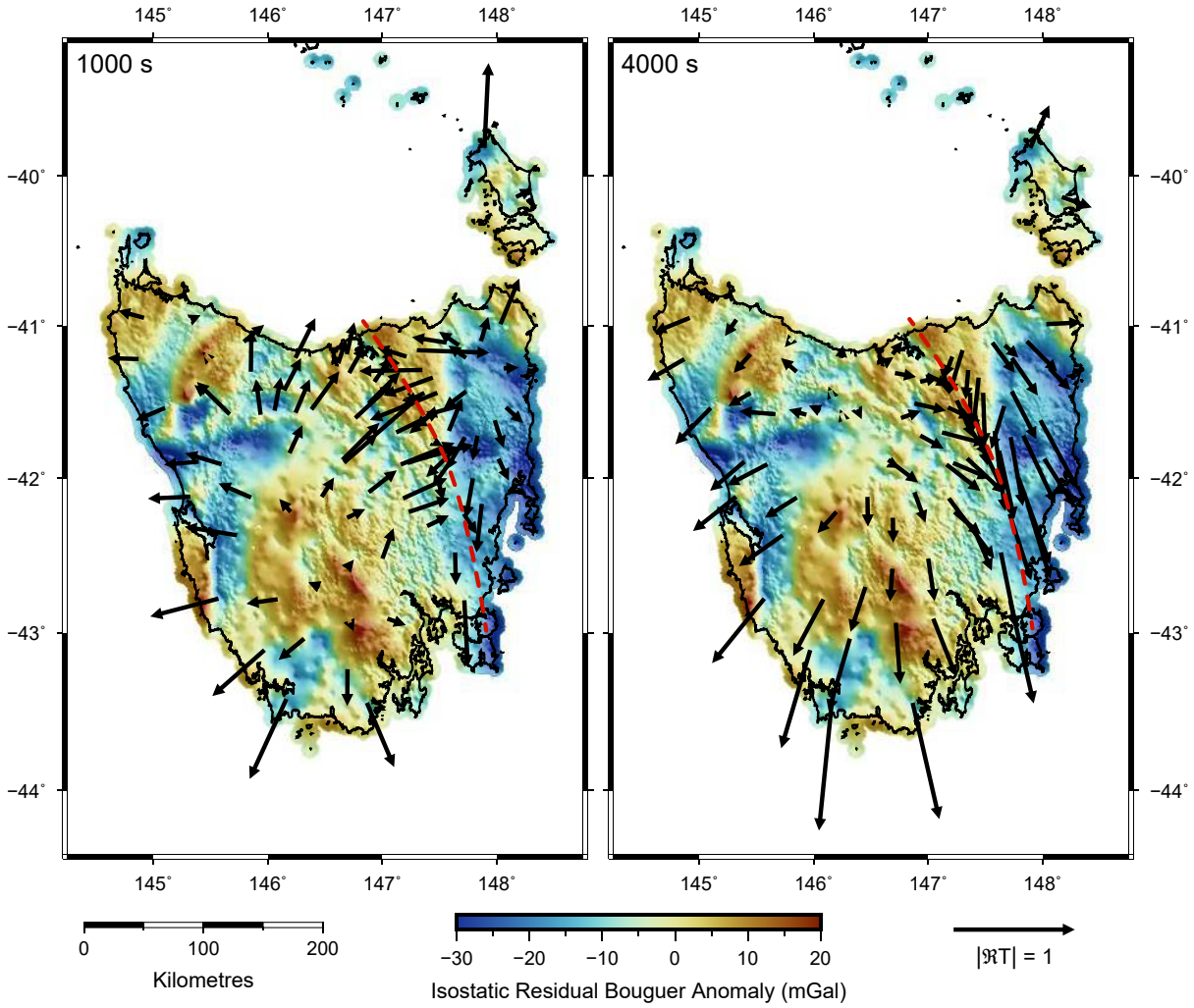

Figure 4.6: Real component induction arrows for 1000 and 4000 second periods from magnetic field observations at AusLAMP MT sites and legacy GDS sites of Parkinson et al. [1988] overlain onto gridded isostatic residual Bouguer anomaly gravity image.

4.5 3D Inversion

Since 2000, the ever increasing speed and memory capacity of computers has allowed for the development of true three dimensional (3D) inversion codes for frequency-domain electromagnetic data, including MT (e.g. Egbert and Kelbert [2012], Newman and Alumbaugh [2000], Siripunvaraporn et al. [2005]). All 3D inversions performed on Tasmanian AusLAMP MT data in this study utilised the ModEM3DMT inversion algorithm developed by Kelbert et al. [2014] at Oregon State University, part of the ModEM modular electromagnetic inversion system discussed in Egbert and Kelbert [2012]. Refer to Chapter 2 Section 3.11 for further background on ModEM.

4.5.1 ModEM Inversion Code

ModEM is a freely available software package developed in FORTRAN 90 that follows an object oriented programming philosophy. The package consists of several modules for 2D and 3D inverse and forward modelling, allowing interchangeability and re-use of basic inversion components including sensitivity computations, inversion search algorithms, model parameterisation and model regularisation.

Computational requirements for 3D inversion are considerable, necessitating parallel computing on high performance computing (HPC) clusters. Initially, 3D AusLAMP data inversion was performed on the Phoenix HPC cluster at the University of Adelaide. Further computation work was completed on the Vortex and Kunanyi clusters operated by the Tasmanian Partnership for Advanced Computing (TPAC) hosted at UTAS in Hobart.

4.5.2 Input Data Masking & Error Floors

Prior to inversion in ModEM3DMT, site-specific EDI data files were imported into 3DGrid model building software of Meqbel [2016] in order to generate ModEM3DMT format input data files. This involved a two step process to: 1) to remove or mask spurious apparent resistivity, phase and tipper data points; and 2), to apply error floors to the data. Figure 4.7 presents apparent resistivity, phase and tipper plots for a typical AusLAMP MT site before and after preparation for inverse modelling.

Data masking is a subjective process involving the removal of periods from an MT sounding where apparent resistivity, phase and tipper values plot outside the smooth curves required by the physics of the MT method. Tipper data for all sites at periods 8000 s and greater were also masked as these periods violate the quasi-stationary assumption, where source fields are treated as a quasi-stationary plane waves propagating vertically downward through the earth [Chave et al., 2012].

Calculated measurement errors for the impedance tensor are often quite small, especially for short periods. This presents a problem in inversion as periods with smaller calculated errors

are effectively weighted higher than those with larger errors, thereby forcing the inversion to fit shallow surface features preferentially over deeper structures. Error floors were added to impedance tensor and tipper data to avoid this effect. Tipper data error floors were defined as a simple percentage (i.e. 4% error floor gives an error of 0.04). Impedance tensor error floors were computed for individual periods and expressed as a percentage of $\sqrt{|\mathbf{Z}_{xy}\mathbf{Z}_{yx}|}$.

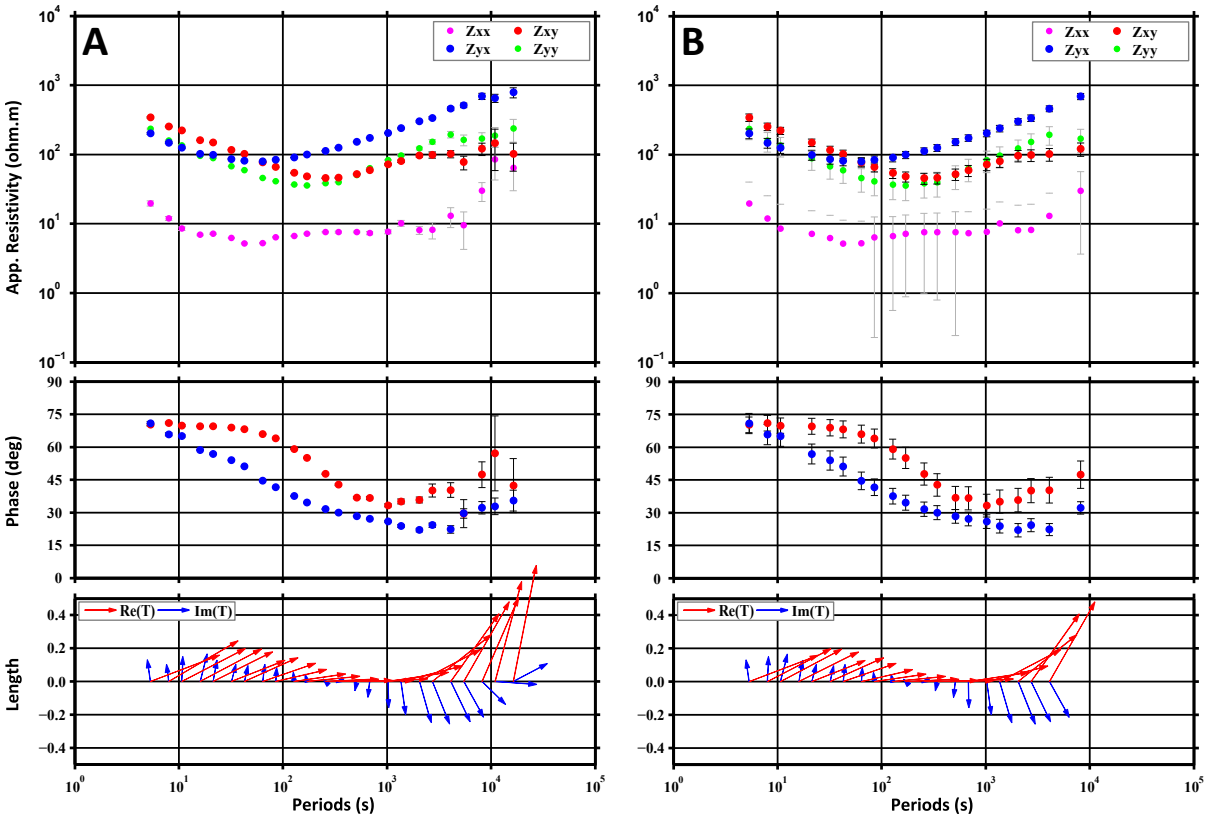

Figure 4.7: Apparent resistivity, phase and induction arrow (tipper) plots for AusLAMP MT site 108 from western Tasmania. Plot A) depicts the raw data prior to masking and error floor addition. Plot B) depicts data after masking and addition of error floors. Errors floors used were 10% for $\mathbf{Z}_{xy}$ and $\mathbf{Z}_{yx}$, 20% for $\mathbf{Z}_{xx}$ and $\mathbf{Z}_{yy}$; and 0.05 for tipper data. It should be noted that tipper error estimates cannot be represented in this induction arrow notation. Plots comparing observed and predicted data from inverse modelling presented later in this chapter show tipper data as $\mathbf{T}_x$ and $\mathbf{T}_y$ components with error estimates given as error bars in a similar fashion to apparent resistivity and phase data points (Figs. 4.14, 4.19 and 4.15).

4.5.3 Depth Sensitivity Analysis

An analysis of the depth sensitivity of the AusLAMP data set was conducted after preparation for inversion. This is an important consideration in modelling MT data as it provides a means of assessing the depth ranges for which data can reliably be used to infer geoelectric structure. Analysis relied on an application of the Niblett-Bostick transformation [Jones, 1983] where the impedance tensor is rotated to obtain minimum and maximum $\mathbf{Z}_{xy}$ and $\mathbf{Z}_{yx}$ for which lower

and upper bounds of apparent resistivity can be calculated. Computing the skin depth of the signal using these apparent resistivity values for the shortest and longest period for each site thus yields an estimate of the depth sensitivity range beneath the MT site.

Figure 4.8 presents a histogram plotting mean signal penetration depth for the shortest and longest periods computed using the Niblett-Bostick transformation for each site after data masking. The distribution of signal penetration depths for the shortest period of each site suggest data sensitivity beginning around 5 km, while geometric means indicate the entire data set is most sensitive to depths in the range 10 km to 200 km spanning upper-crust to lithospheric mantle.

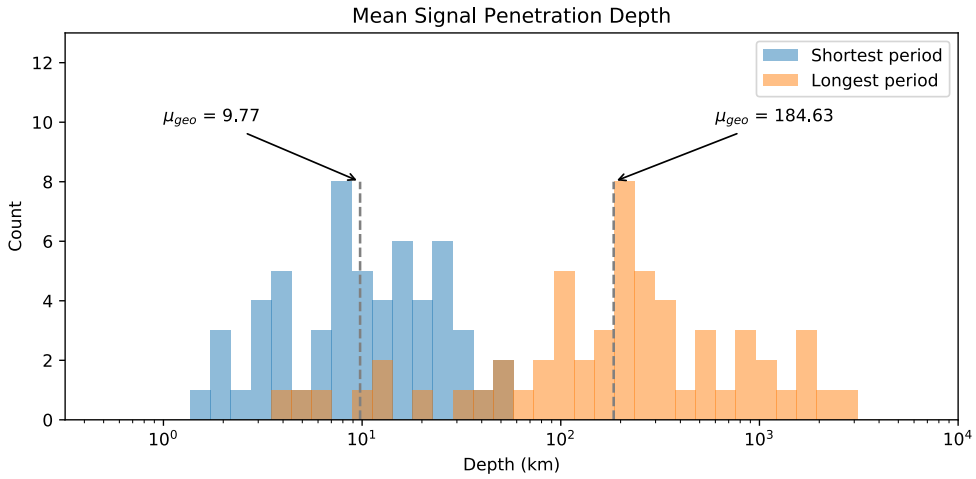

Figure 4.8: Histograms depicting mean depth of penetration for the shortest and longest period of each site in the inversion data set. Depth of penetration was calculated by averaging the minimum and maximum depths of penetration for each period computed by the Niblett-Bostick transformation.

The spatial distribution of mean minimum and mean maximum signal penetration depth is presented in Figure 4.9. Mean minimum signal penetration depths support a ∼5 km upper limit on depth sensitivity for most of the data set. Sites with the largest mean signal penetration depth between 30 km to 50 km are clustered in the central west of the data set. These correspond to sites with very high apparent resistivities (sites 107 and 332) or masked short periods (site 109). Other parts of the data set with deep upper limits on sensitivity include the northeast corner of Tasmania and Flinders Island where sites return similarly high apparent resistivities (sites 115, 116 and 117).

Mean depth of penetration for the longest period for each MT site in the data set spans a large range of depths (4.1 km for site 146, to 2550 km for site 143). This reflects a similarly large range of maximum period values from which skin depths were computed (170 to 16,000 s). All sites with mean penetration less than 50 km had very noisy longer periods that were masked out prior to inversion or returned very low apparent resistivities. In general, the depth sensitivity of the inversion data is acceptable for depths ranging from about 5 km to 500 km, with peak sensitivity in the range 10 km to 200 km.

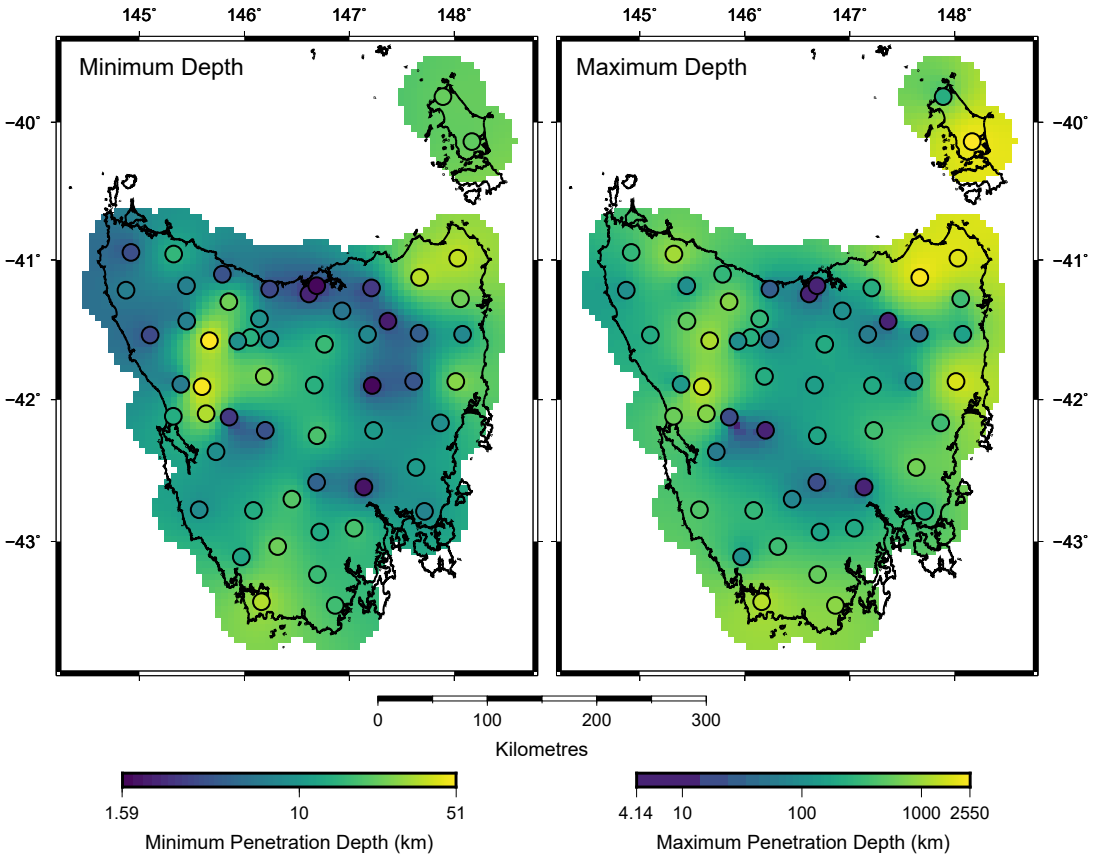

Figure 4.9: MT site locations coloured by their mean signal penetration depth for the shortest, left, and longest, right, periods. Sites are overlain onto a gridded image of the same data. This is a geographical representation of the data presented in Figure 4.8.

4.5.4 Starting Model Design

ModEM3DMT requires a prior or starting model from which to initiate data inversion. These models take the form of a rectangular mesh grids with user defined dimensions in a Mercator projection and resemble common mesh types used in potential field inversion systems such as UBC-GIF and VPMG (Li and Oldenburg [1998], and Fullagar et al. [2007], respectively). All mesh grids and starting models were built using the same 3DGrid software used for data masking and error floor addition.

Cell Size and Mesh Design

Selecting an appropriate cell size for 3D inversion involved balancing computational requirements with model resolution. Without a detailed understanding of the computational requirements for 3D inversion of a 57-site MT data set given the computing resources available, a decision was made to minimise computational intensity on the first modelling attempt by selecting a relatively large 7 km horizontal mesh size (∼1/4 the median site spacing). This yielded a horizontal mesh of 84 by 66 cells, including 9 padding cells at horizontal edges of the model

space.

Padding cells are required by the inversion algorithm to mitigate any errors incurred from model space boundary conditions. These cells increase in horizontal thickness from the core of the model outwards in order to place boundary conditions well outside the sensitivity range, or maximum skin depth, of the data being inverted. Given the maximum skin depth for the AusLAMP data set is ∼600 km, calculated for halfspace resistivity of 100 Ω m with a maximum data period of 16 000 s (Chapter 2, Eq. 2.12), 9 padding cells expanding in thickness by a factor of 1.5 was selected. These values place the model space boundary ∼800 km from the edge of the core of the model.

Vertical cell thicknesses increased exponentially in line with the diffusive nature of MT phenomena. From an uppermost cell thickness of 50 m, cells increased in vertical thickness by a factor of 1.1 over a total of 80 cells; yielding a total vertical extent of 1024 km. As with horizontal padding, placing the base of the model space well beyond the maximum skin depth of the data set ensured boundary conditions at the model base did not erroneously interfere with the inverse model result.

After the completion of a series of 7 km cell models, a decision was made to increase the horizontal resolution to 5 km for a second series of inverse models. The number and dimensions of horizontal padding cells were kept constant, as were vertical cell dimensions. This yielded much higher resolution models with 68% more cells requiring a commensurate increase in computational resources to invert (Table. 4.1).

Horizontal Resolution	N-S Cells	E-W Cells	Padding Cells	Z Cells	Total Cells	Max Depth
7 km	84	66	9	80	443,520	1023.7 km
5 km	108	82	9	80	708,480	1023.7 km

Table 4.1: Summary of low and high resolution AusLAMP ModEM3DMT inverse model mesh dimensions.

Prior Knowledge

Electrically conductive ocean and thick sedimentary sequences surrounding Tasmania exert a strong influence on observed MT responses, particularly for coastal sites, as evidenced by induction arrow plots (Figs. 4.5 and 4.6). This inductive effect can cause artefacts in inverse modelling if not properly accounted for. In order to do this, prior knowledge in the form of realistic volumes and resistivities for ocean water and sediments were included in starting models prior to ModEM3DMT inversion.

Ocean water volume was added to the model using bathymetry information taken from Geoscience Australia's AusBath 2009 data set. Bathymetry data were windowed to the model extents, converted to XYZ data format and imported into 3DGrid software where a cell-wise nearest-neighbour re-sampling operation was performed to define the volume of ocean water in

the model space. All cells above the 3D surface were assigned a resistivity value corresponding to that of sea water (0.3 Ω m).

A similar procedure was used to add a conductive sediment layer to starting models. This utilised a modified sediment thickness layer taken from the OZ SEEBASE v2 data set compiled by FrOG Tech [FrOGTech, 2006]. The choice of resistivity for ocean sediments, 10 Ω m, was informed by conductance forward modelling efforts in South Australia in which a sensitivity analysis of onshore long period MT data to variation in offshore sediment resistivity was performed [Thiel and Heinson, 2009].

Assigning constant sediment resistivity values is a simplification of more complex resistivity structure. In the typical case, sediment resistivity increases with depth due to compaction-related decreasing porosity. Given the complexity this would add to starting model design a constant value was preferred, however an accommodation was made whereby thick sedimentary piles were bathymetry-restricted to 2 km thickness. This method prevents unrealistic conductance values for thick sedimentary basins, such as the Bass Basin, while still accounting for the presence of the upper most conductive sediment in the model space. Figure 4.10 depicts the gridded data sets used in constructing the starting model shown in Figure 4.11.

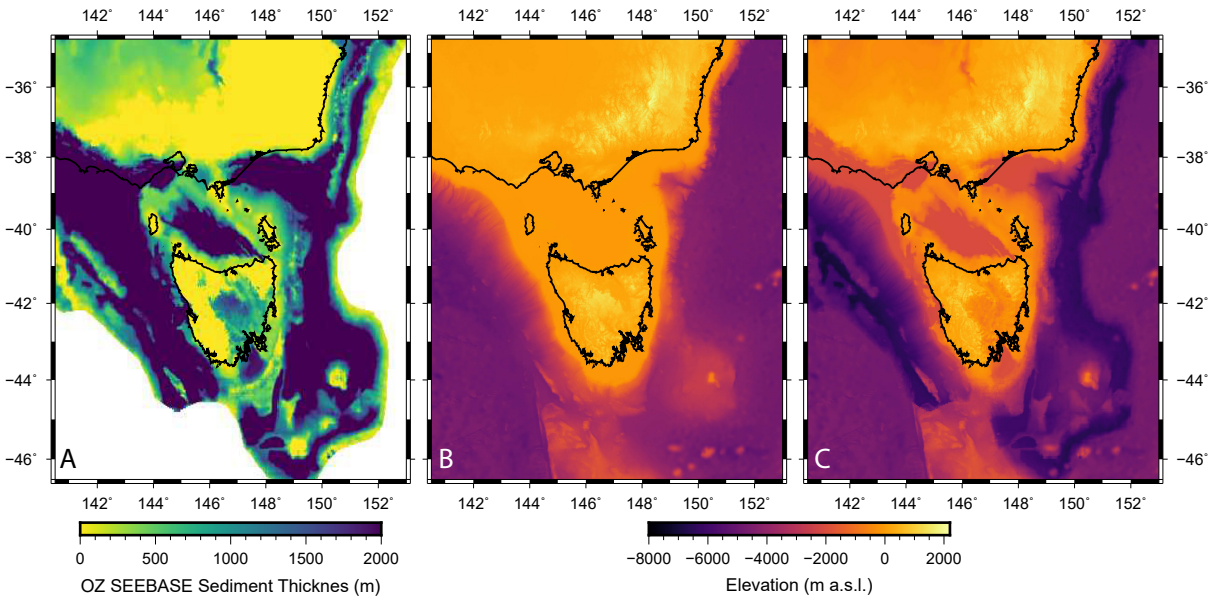

Figure 4.10: Gridded data used to generate starting models. A) depicts sediment thickness data from the OZ SEEBASE v2 data set clipped to 2 km thickness, B) depicts the AusBATH 2009 bathymetry data set, while C) presents a base of sediment grid used for model building. C) was generated by subtracting A) from B) to produce a depth to base of sediment where sediments do not exceed 2 km in thickness.

4.5.5 Model Variations

In total, 24 models using a 7 km cell size were completed, each with varying inversion parameters in an effort to investigate the influence of differing error floor values, error calculations, starting half-space resistivities, and smoothing parameters have on the inverted model result. Inversions were carried out on GDS-only data, impedance tensor-only data and combinations of both. Inversions with data parameters that yielded the best two model fits, measured as a minimum global RMS misfit, were repeated at a finer 5 km cell spacing in an effort to improve model fit.

Finer mesh sizes improved model fit greatly, with inversions converging on total RMS misfit values < 2. Improved model fit was particularly evident in northwestern Tasmania where MT sites are clustered together (<13 km separation in some places). Here, site-specific RMS misfit values often exceeded 3 in coarse 7 km inversions where inversion could not fit complex geoelectric structures between MT sites within the constraints of the coarse model space. In the fine 5 km mesh models the misfit in these sites was reduced to < 2, indicating complex structure was properly accounted for in the models presented in the results section of this chapter overleaf.

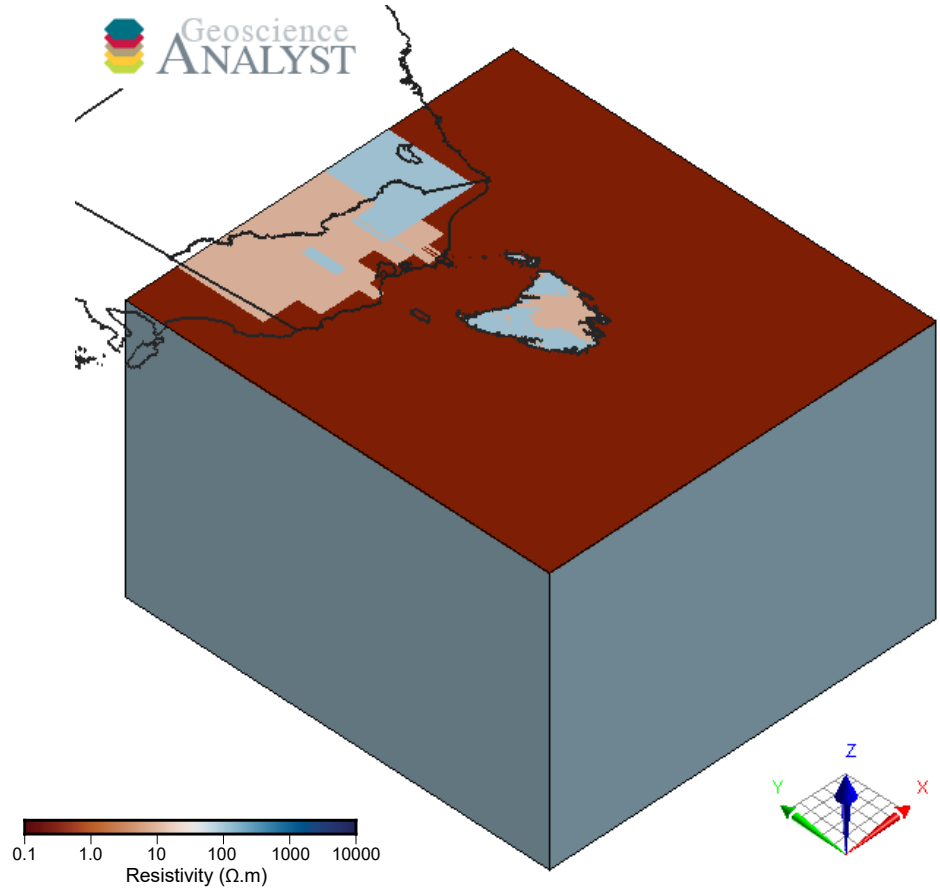

Figure 4.11: Orthographic 3D projected view of the starting model used in high resolution inverse modelling. Note the 0.3 Ω m offshore cells in the upper regions of the model space corresponding to sea water. 10 Ω m sediment and 100 Ω m non-sediment cells are visible within onshore regions in Tasmania, Flinders Island and mainland Australia.

4.5.6 Inverse Modelling Results

A total of three high resolution 5 km mesh models were inverted using data parameters that yielded the best model fits in the previous low resolution modelling (summarised in Table 4.2). These three models utilised the same inversion data file and starting model mesh while varying the degree of smoothing by assigning different covariance factors to the models. While all three converged on good data misfit values with global root mean square (RMS) error values <2, inverse model run027, hereby referred to as the preferred model, converged on the smallest global RMS value.

		Data Error Floors			Smoothing Parameters	
Inversion	**Global RMS**	$\mathbf{Z}_{xy}$ & $\mathbf{Z}_{yx}$	$\mathbf{Z}_{xx}$ & $\mathbf{Z}_{yy}$	$\mathbf{T}_x$ & $\mathbf{T}_y$	**Covariance**	**Smoothing**
`run027`	1.542	10%	20%	0.05	0.2	Less
`run030`	1.701	10%	20%	0.05	0.3	Default
`run031`	1.745	10%	20%	0.05	0.4	More

Table 4.2: Key parameters and final global RMS misfit values for final inverse models using the high resolution 5 km model mesh. Error floors for tipper data were given as absolute values while error floors for impedance tensor components were determined using the Egbert method (percent of $\sqrt{|\mathbf{Z}_{xy}\mathbf{Z}_{yx}|}$ for each period). For a complete list of inverse modelling runs the reader is referred to Appendix A.

Like previous coarse modelling efforts, the starting model for these high resolution models included 0.3 Ω m sea water and 10 Ω m conductive sediments, with remaining model space given a mid-range value of 100 Ω m typical of continental crust. Inversion was permitted to vary 10 Ω m sediment layers as well as 100 Ω m half-space, while sea water cells remained fixed.

Misfit Analysis

The preferred model fits the data well, with inversion converging on a final global RMS misfit of 1.54 over the course of 252 iterations. A relatively low starting RMS misfit of 9.62 suggests the starting model did not contain any wildly unrealistic a-priori geoelectric structure. Figure 4.12 presents plots depicting the distribution of RMS misfit values calculated on a site-by-site basis, as well as a plot of global RMS misfit decline over the course of inversion.

Small spikes in global RMS misfit throughout the inversion are the result of an error in the inversion restart procedure. Here, lambda values in an inversion parameter file were not carried over from iteration to iteration and resulted in high RMS misfit values for the first five or so iterations after restart. This procedural error had the effect of prolonging the inversion process, however it did not adversely effect the geoelectric structure of the final inverse model results.

Despite low global RMS misfit in the preferred model, it is important to investigate the spatial distribution of RMS misfit as this provides a means of evaluating the robustness of model features. Figure 4.13 presents a map of all 57 MT sites used in inversion coloured by individual total RMS computed from the preferred model. Total RMS misfit values are less

than 1.5 for 60% of sites, and only 4 sites have RMS misfit values in excess of 2. The worst fitting data point, site 142 deployed in northern Flinders Island, has a total RMS misfit of 3.5; likely the result of this site's close proximity to ocean water in the model space. Since this site is well outside the core of the model space it is not expected to unduly influence the robustness of the model results as a whole. Response plots for a typically well-fitted site is presented in Figure 4.14 (site 104), while Figure 4.15 presents a response plot for site 142, the worst-fitted MT site deployed on Flinders Island.

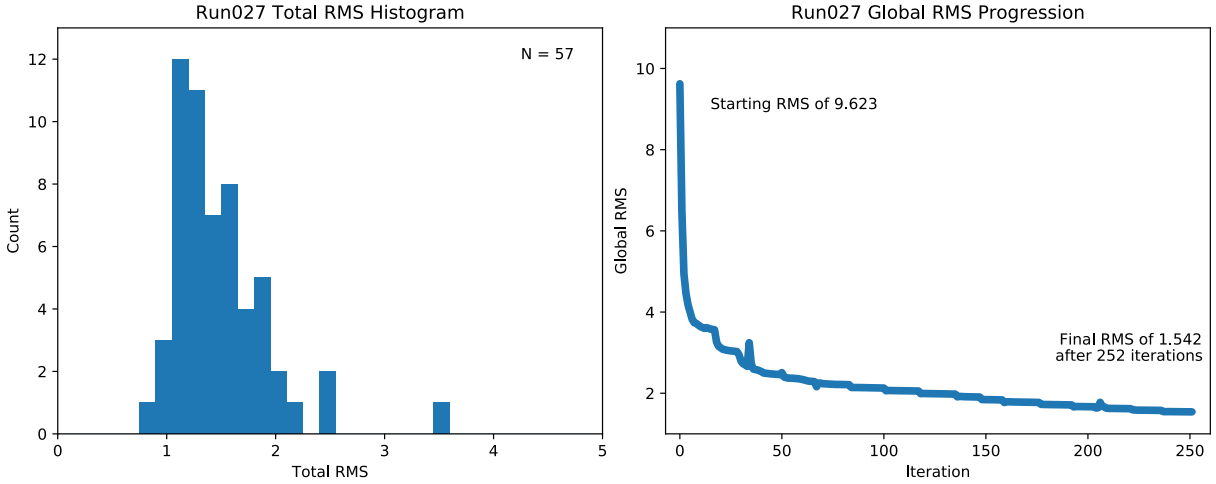

Figure 4.12: Plots depicting the distribution of total RMS misfit values computed for each MT site (left) and global RMS misfit decline per iteration during inversion (right) for inverse model run027, the preferred model. Note most MT sites cluster around a total RMS misfit value of ∼1.4, while a single outlier with RMS misfit >3.5 corresponds to the poorly fitted MT site deployed in the north of Flinders Island (site 142). Spikes and steps in global RMS misfit decline throughout inversion relate to inversion restarts.

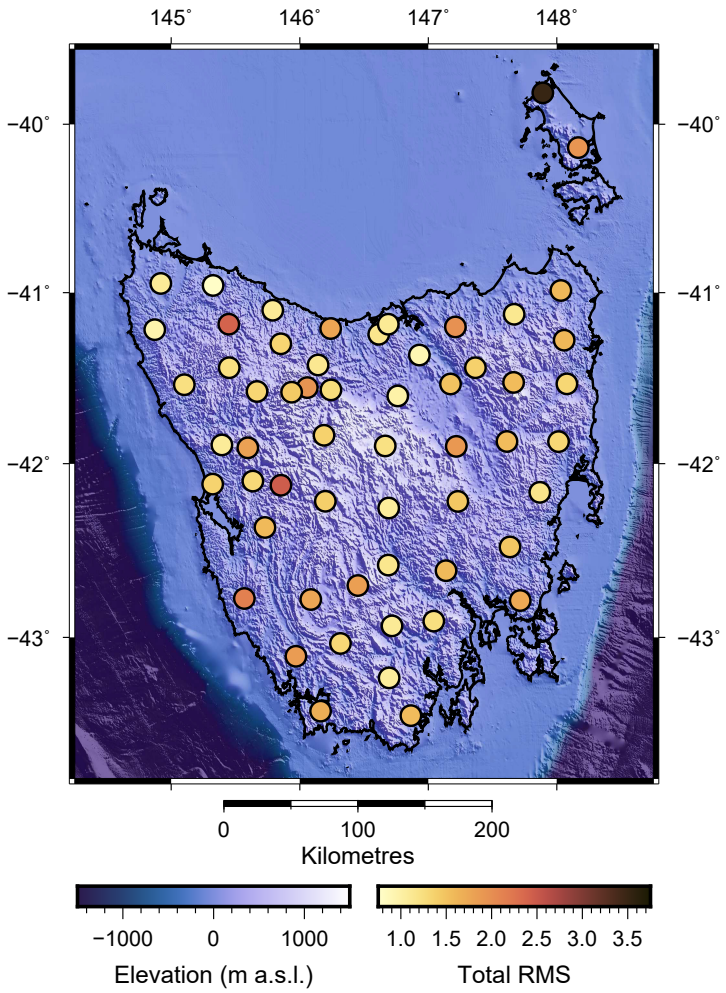

Figure 4.13: MT sites locations coloured by total site RMS misfit computed for the preferred AusLAMP 3D model superimposed on a sunshaded digital elevation model. Note the generally good model fits with exception of site 142 deployed on Flinders Island. This site was located closest to sea water in starting models, making it difficult for ModEM3DMT to fit it adequately.

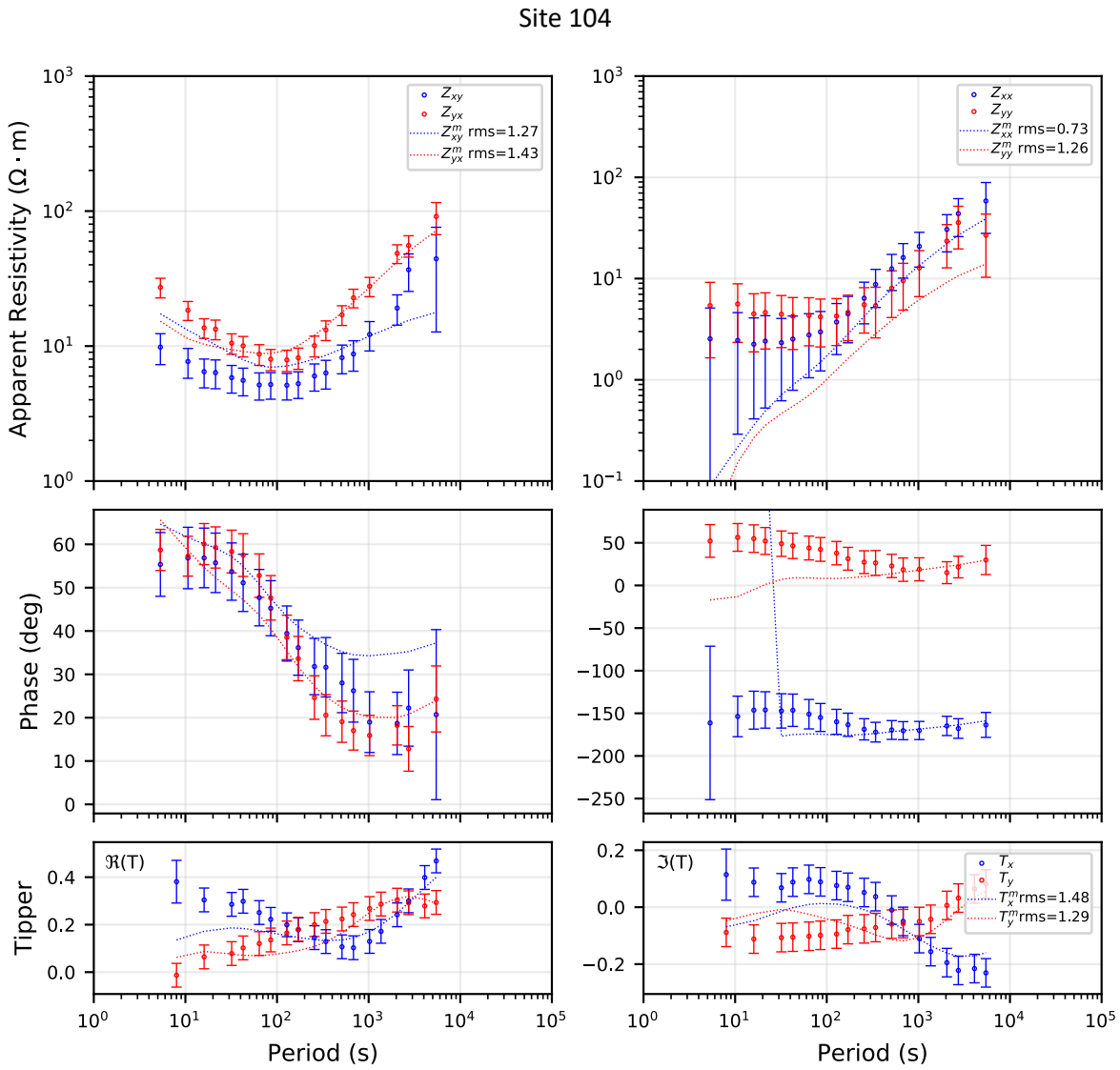

Figure 4.14: Apparent resistivity, phase and tipper curves for MT site 104 deployed in northwestern Tasmania with preferred model response curves plotted as dashed lines. Real and imaginary components of the tipper are plotted in the bottom left and right plots, respectively. This is one of the best-fitted MT sites by the preferred model, with a total RMS value of 1.24. Note the larger error bars on $\mathbf{Z}_{xx}$ & $\mathbf{Z}_{yy}$ apparent resistivity and phase estimates relative to their $\mathbf{Z}_{yx}$ & $\mathbf{Z}_{xy}$ equivalents as a result of differing error floors. This difference influences the weighting given to each component in inversion, and explains relative difference in model fit between the components. Appendix B presents similar plots for all MT stations used in inverse modelling.

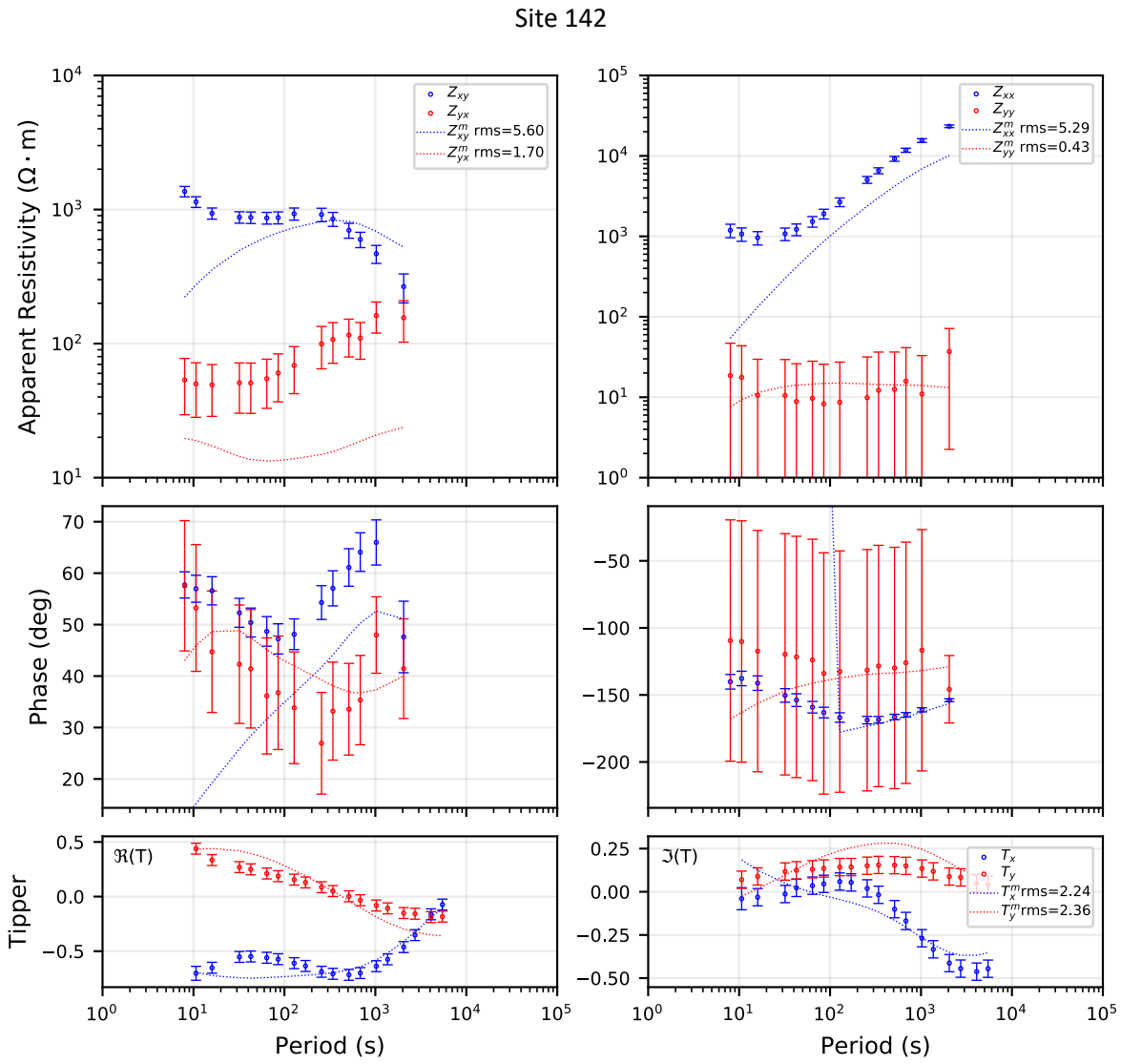

Figure 4.15: Apparent resistivity, phase and tipper curves for MT site 142 deployed on northern Flinders Island with preferred model response curves plotted as dashed lines. This is the worst-fitted MT site in inversion, with a total RMS misfit value of 3.51, likely the result of the site's close proximity to sea water cells in the model space. Locked sea water resistivities restricted the ability of the inversion to fit structure in cells within the site's immediate vicinity.

Depth Slices & Transects

The resistivity structure of the upper parts of the model space is typical of ModEM3DMT inverse models in that it is defined by incoherent, high spatial frequency variation in resistivity. This feature is the result of the inversion algorithm's approach to fitting galvanic distortion inherent in the data set. To account for galvanic distortion, and the static shifts in apparent resistivity it produces, ModEM3DMT places resistivity structure in the uppermost model space cells within close proximity of the MT sites. This propensity of ModEM3DMT is clearly demonstrated by depth slices through the top 2 km of the model space presented in Figure 4.16.

Coherent resistivity structures emerge at depths beyond ∼3 km, with very low resistivity regions appearing in northern and western Tasmania at upper crustal depths in the range 3 km to 5 km (annotated as **C1**, **C2**, **C3** and **C4** in Figure 4.17). These low resistivity structures tend to emerge around MT sites with shallow minimum signal penetration depths (illustrated in Figure 4.9) suggesting these structures are close to or within the upper bounds of depth sensitivity of nearby MT sites. The robustness of some of these features is questionable however, since a few of them appear to be related to a single MT site (**C3**), are located near MT sites with relatively high RMS misfits (total RMS misfit of 2.47 for site 342 near **C4**) and tend to be localised to very shallow parts of the model space (**C1** being an exception).

Highly resistive regions on Flinders Island, eastern Tasmania and an isolated region in central western Tasmania (annotated as **R1** in Fig. 4.17) emerge at depths exceeding 5 km. These are generally poorly constrained at such shallow upper crustal depths since sites acquired directly above the features tend to have minimum signal penetration depths >10 km. Resistive structure **R1** is considered to be quite robust however, since several MT sites in close proximity to the structure tend to have small minimum penetration depths adding a degree of constraint on this resistive structure.

Progressing deeper into the model space, now well within the sensitivity range of the data set as defined by mean signal penetration depths, several of the very low resistivity structures identified at shallower levels fade in intensity, disappear or migrate. At depths greater than 7 km, very low resistivity structures **C2**, **C3** and **C4** have all but disappeared, while **C1** has increased in resistivity by an order of magnitude, split into two zones with one remaining in the north and another migrating southward. Resistive regions in northeastern and western Tasmania intensify at these depths and, in western Tasmania, a new low resistivity zone, **C5**, emerges parallel to the very high resistivity zone **R1**. Such high resistivity contrasts on relatively small spatial scales are likely the result of the inversion fitting highly complex geoelectric structure that has given rise to out of quadrant MT responses observed in this part of Tasmania. Figure 4.19 presents a response curve plot for site 105 illustrating the model fit for one such out of quadrant site.

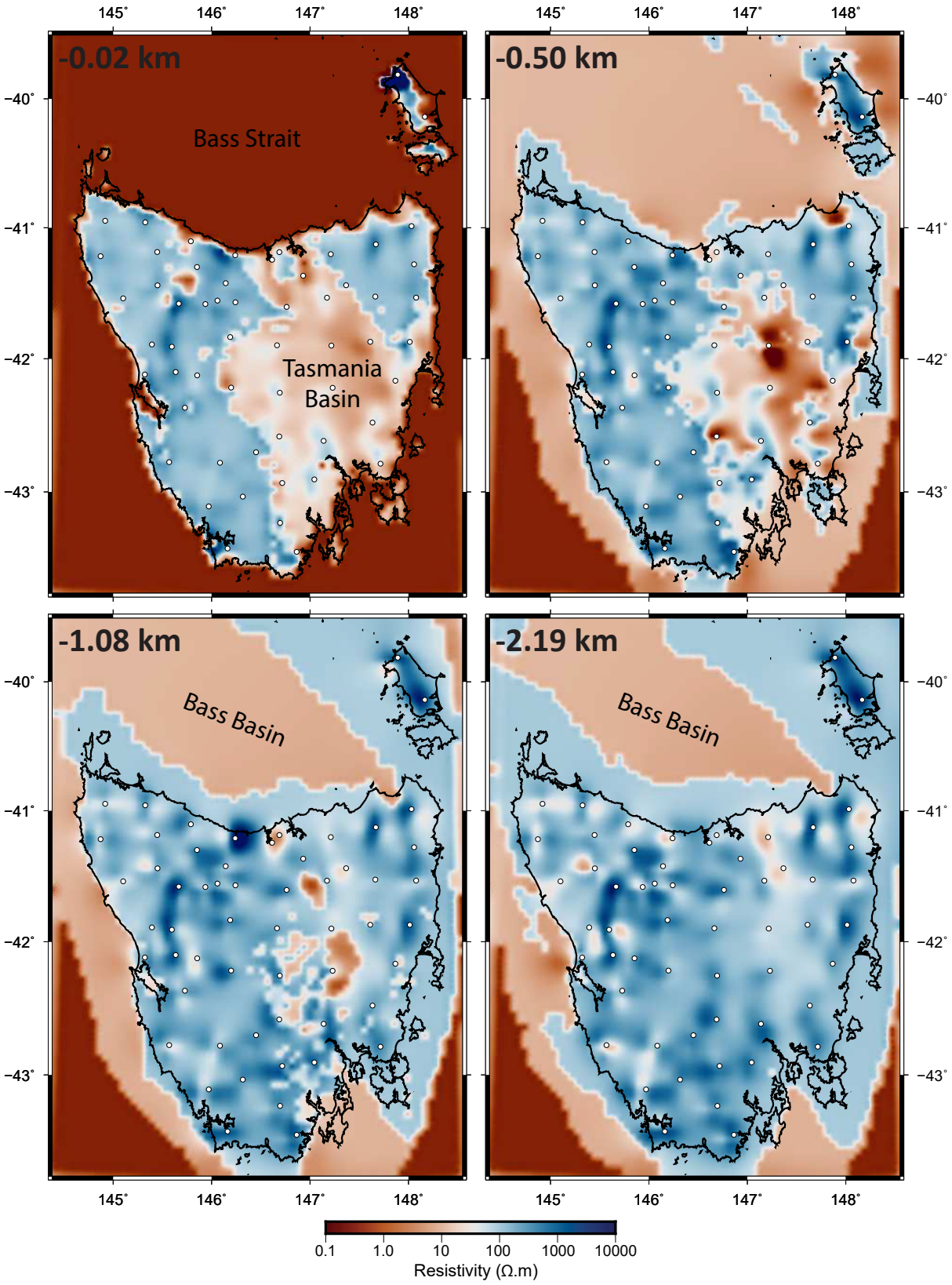

Figure 4.16: Depth slices through the upper 2 km of the preferred model (run027). Slices are taken from the vertical centre of model cells with depth presented in the top left hand corner of each slice. White dots represent MT site locations. Note the retreat of low resistivity sea water and sediment cells from the core of model space with increasing depth.

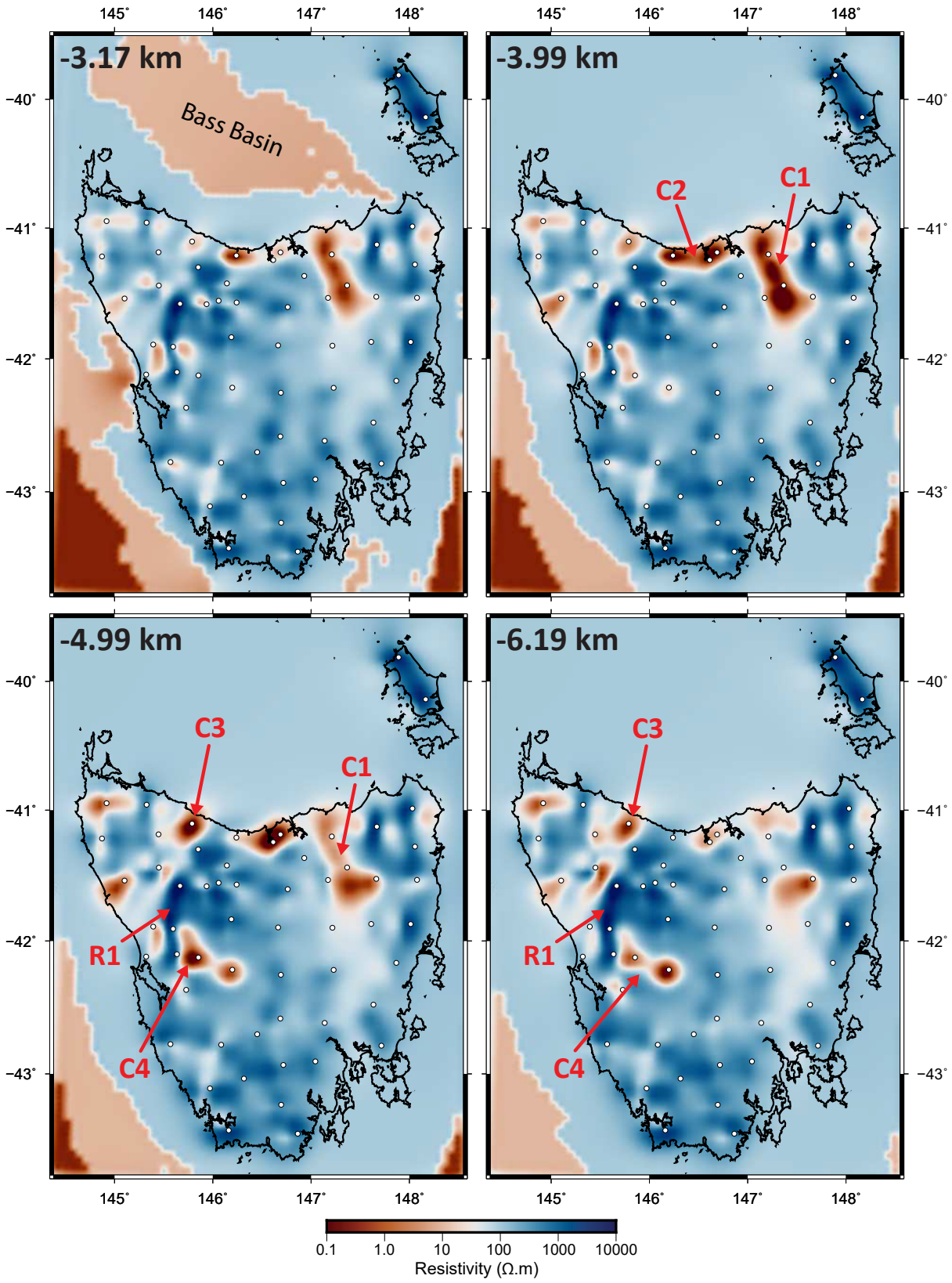

Figure 4.17: Depth slices through the preferred model (run027). Slices are taken from the vertical centre of model cells with depth presented in the top left hand corner of each slice. White dots represent MT site locations. Annotations denote resistive (**R**) and conductive (**C**) structures discussed in text.

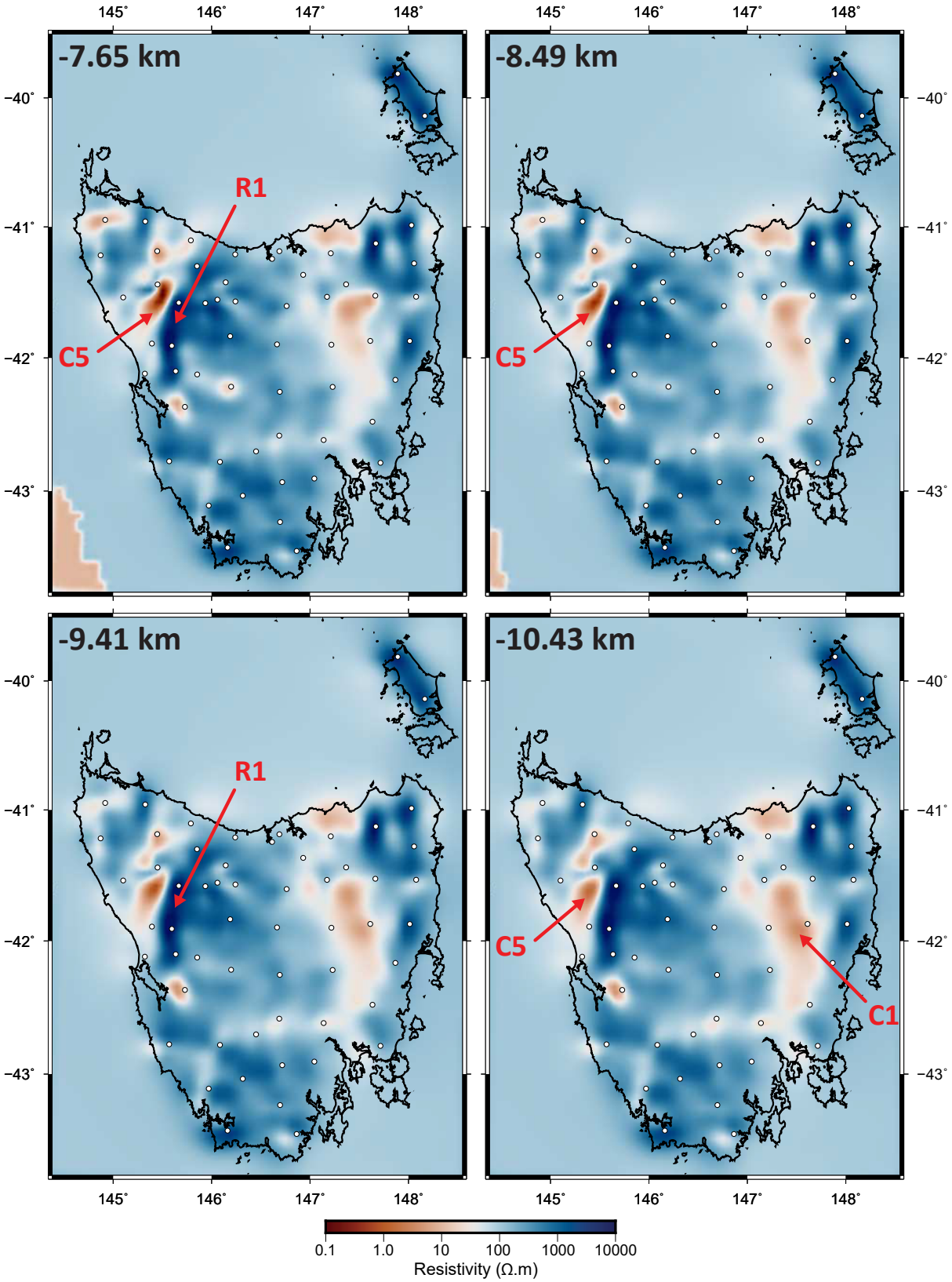

Figure 4.18: Depth slices through the preferred model (run027). Slices are taken from the vertical centre of model cells with depth presented in the top left hand corner of each slice. White dots represent MT site locations. Annotations are discussed in text.

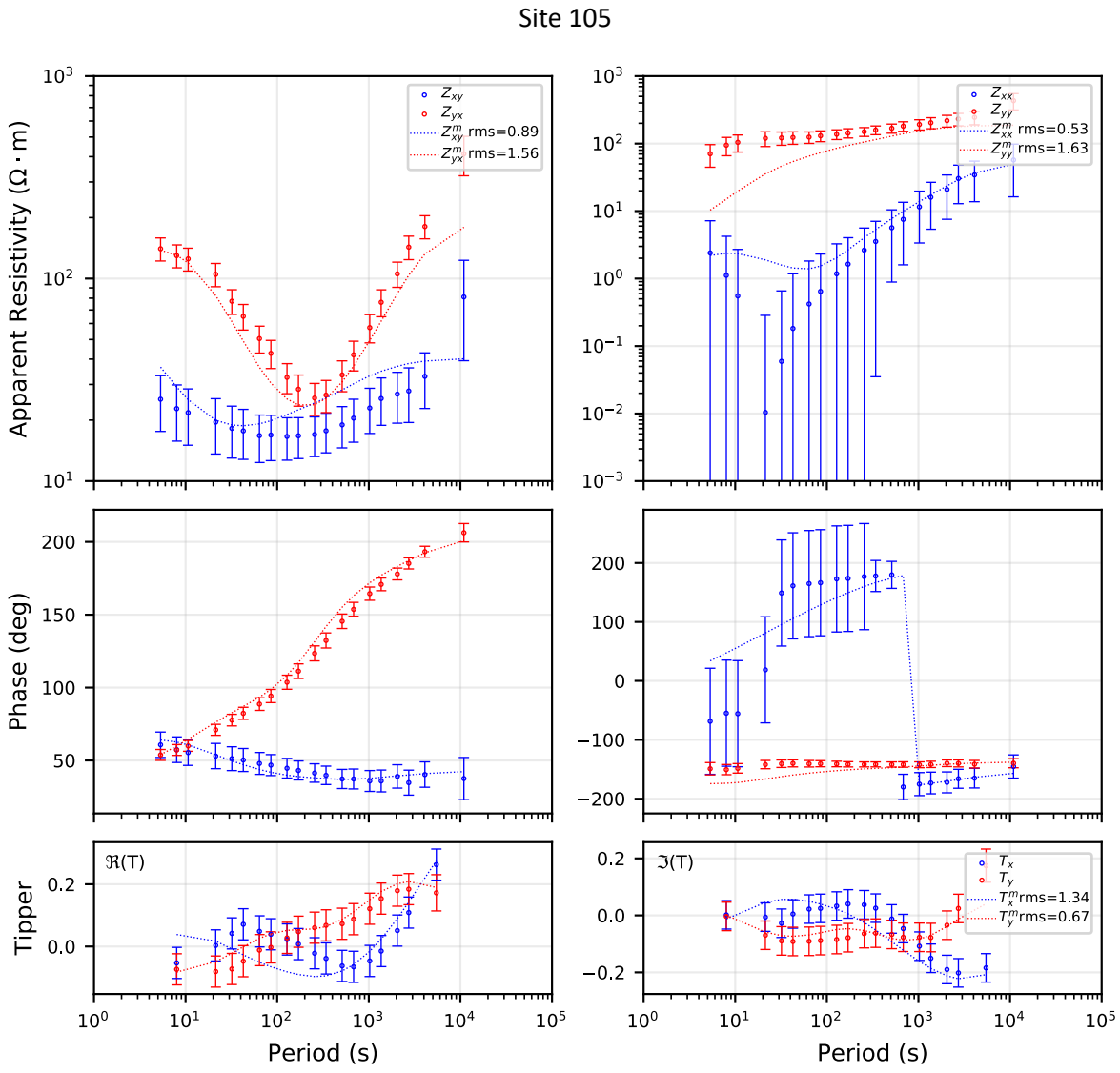

Figure 4.19: Apparent resistivity, phase and tipper curves for MT site 105 deployed in northwestern Tasmania with preferred model response curves plotted as dashed lines. This site is typical of a number of sites in the region with out of quadrant phases, suggesting highly complex 3D geoelectric structure. Total RMS misfit for this site is 1.23.

At mid-crustal depths beyond ∼10 km, remaining low resistivity zones broaden in spatial extent and coalesce into regional-scale features (Fig. 4.20). Low resistivity zone **C5** broadens northward forming a NE-SW trending corridor of low resistivity flanking the western edge of high resistivity zone **R1**. In eastern Tasmania low resistivity zone **C1** broadens into an arcuate 45 km wide corridor between the Tamar River in the north and the Coal River in the south. At depths of about 14 km, **C1** unites with smaller, less pronounced low resistivity zones west of Hobart. Deeper in the mid-crust, at about 15 km, discrete low resistivity zones emerge in the central northwest (**C6**) and the southwest (**C7**).

Mid-crustal low resistivity structures evident at 15 km become more conductive at lower crustal depths beyond 20 km while changing little in spatial extent and overall structure (Fig. 4.21). Low resistivity structures **C5**, **C6** and **C7** all reach a minimum resistivity at about 21 km depth, as do northern portions of the eastern arcuate zone (**C1**).

Lower-crustal low resistivity structures evident in Figure 4.21 broaden in spatial extent and tend toward higher resistivities with increasing depth into lithospheric mantle shown in Figure 4.22. The transition to lithospheric mantle at around 26 km to 32 km (from Rawlinson et al. [2010]) is accompanied by a decrease in overall model structure with highly resistive regions beneath eastern Tasmania, Flinders Island and western Tasmanian resistor **R1** becoming up to one order of magnitude less resistive. Low resistivity zones **C5**, **C6** and **C7** largely disappear at lithospheric mantle depths of 37 km and beyond, while **C1** cleaves into two discreet low resistivity zones in the north and south.

The broad low resistivity zones inherited from **C1** beneath northern and southern Tasmania migrates westward with increasing depth in the lithospheric mantle (Fig. 4.24), eventually forming a N-S trending keel of low resistivity at depths greater than about 60 km (Fig. 4.23). This low resistivity (∼50 Ω m) keel is flanked to the east by high resistivities in excess of 250 Ω m, and moderate resistivities in the range 100 Ω m to 200 Ω m to the west. This distinct lithospheric mantle resistivity structure fades to starting model resistivities by 100 km depth in the model space, after which inversion does not appear to have significantly modified the starting model.

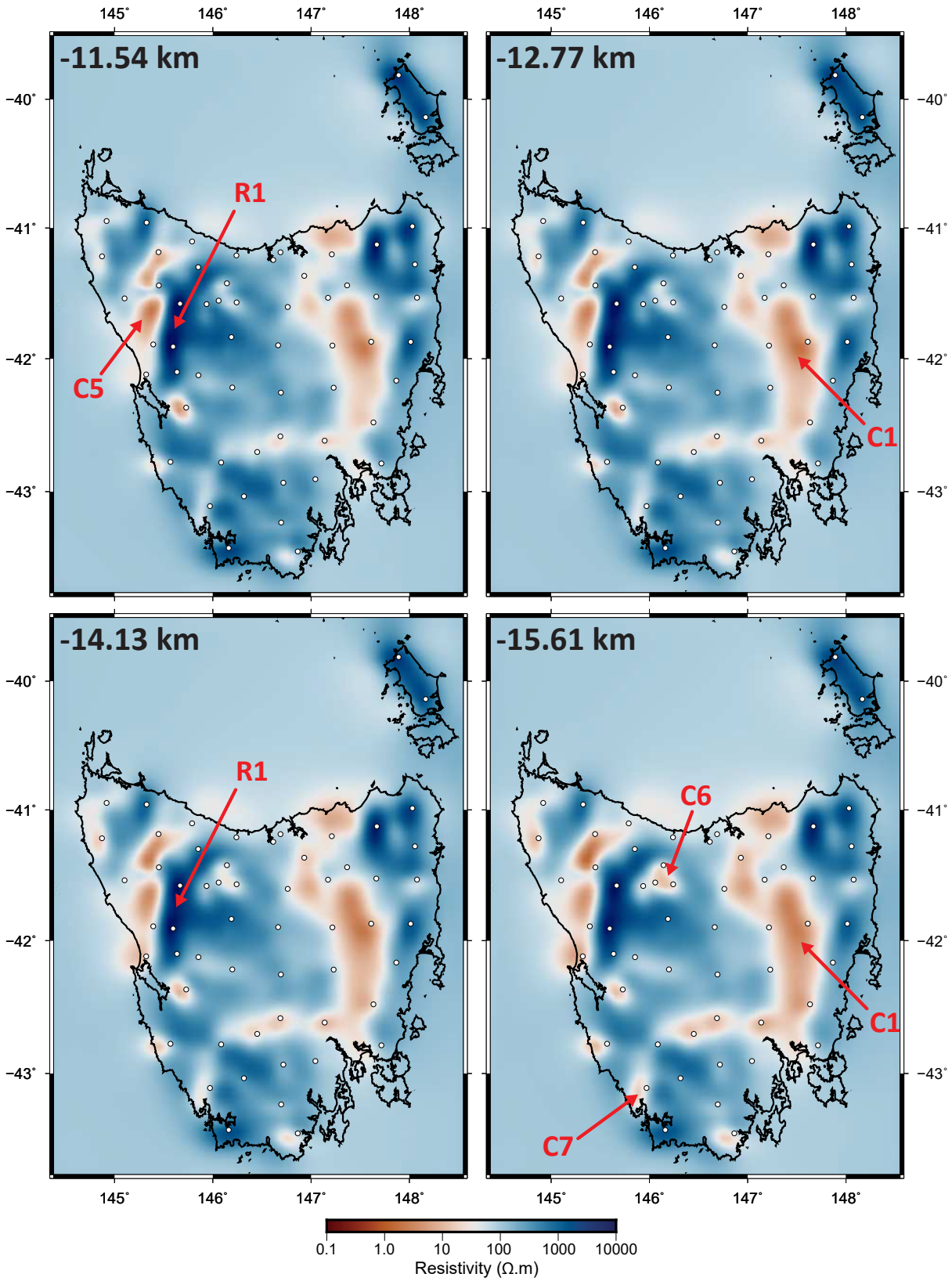

Figure 4.20: Depth slices through the preferred model (run027). Slices are taken from the vertical centre of model cells with depth presented in the top left hand corner of each slice. White dots represent MT site locations. Annotations are discussed in text.

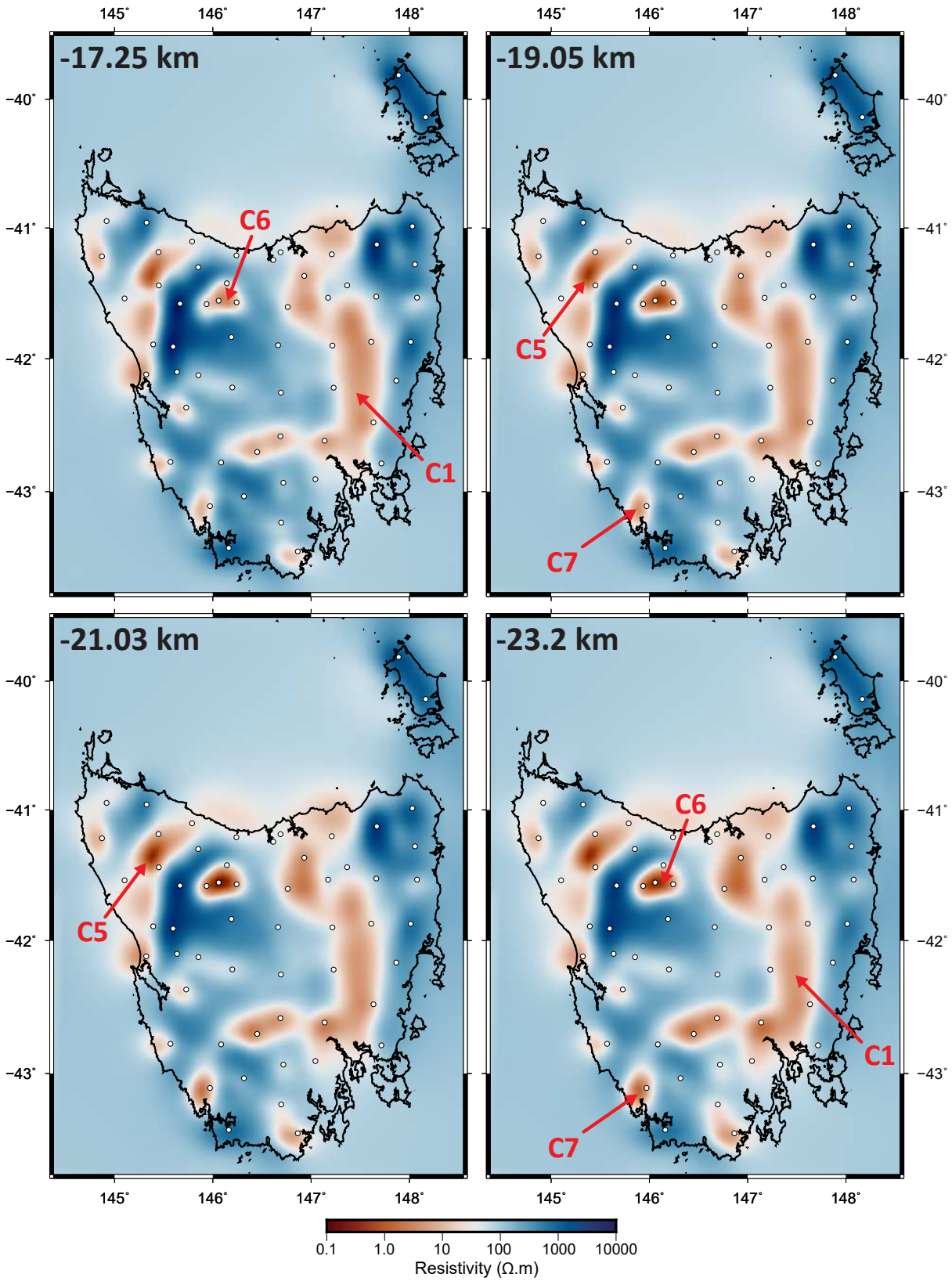

Figure 4.21: Depth slices through the preferred model (run027). Slices are taken from the vertical centre of model cells with depth presented in the top left hand corner of each slice. White dots represent MT site locations. Annotations are discussed in text.

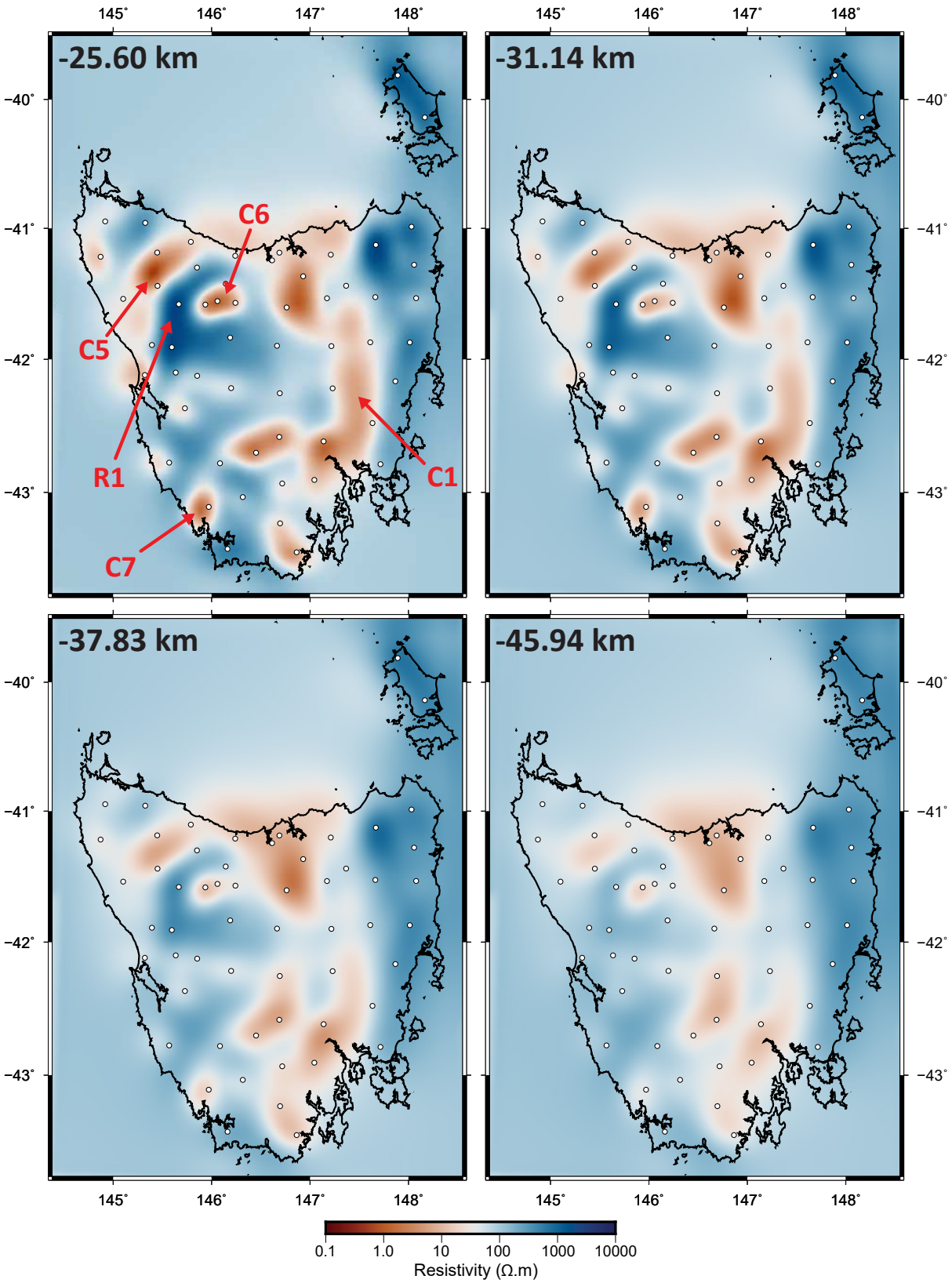

Figure 4.22: Depth slices through the preferred model (run027). Slices are taken from the vertical centre of model cells with depth presented in the top left hand corner of each slice. White dots represent MT site locations. Annotations are discussed in text.

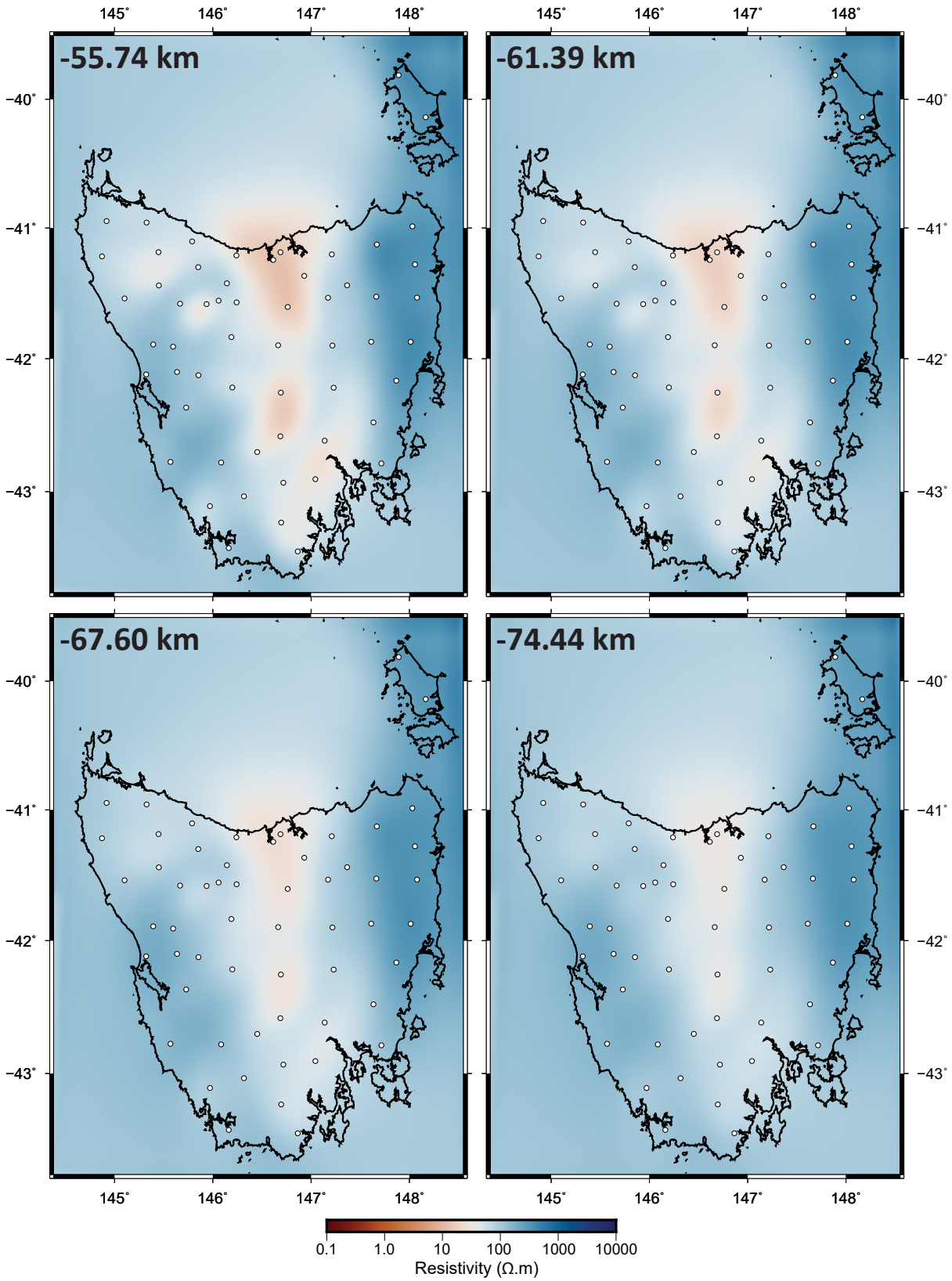

Figure 4.23: Depth slices through the preferred model (run027). Slices are taken from the vertical centre of model cells with depth presented in the top left hand corner of each slice. White dots represent MT site locations.

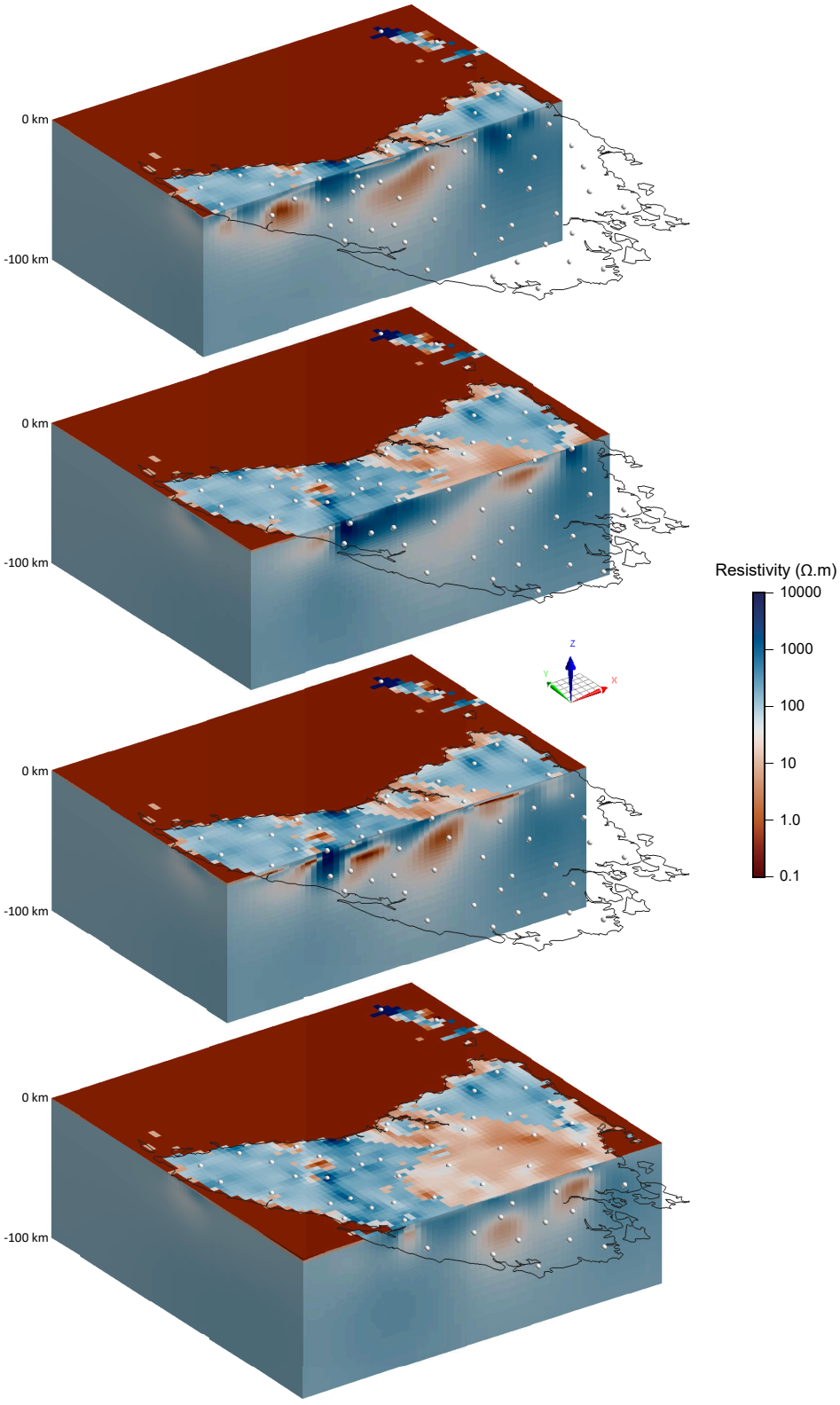

Figure 4.24: E-W transects through a orthographic projected 3D representations of the preferred model after removal of horizontal padding cells and clipping to a maximum vertical extent of 100 km. White spheres represent the locations of AusLAMP MT sites. All 3D images presented in this thesis are captured from within a Geoscience Analyst 3D data viewing project which is included as digital appendices, access instructions for which are presented in Appendix C.

4.6 Interpretation & Discussion

Interpretation of 3D inverse model results were aided by SKUA-GOCAD and Geoscience Analyst 3D geoscientific data visualisation software packages. Final model files output from ModEM3DMT were converted to GOCAD Sgrid format using Python functions provided by the MTpy library of MT codes [Kirkby et al., 2019, Krieger and Peacock, 2014], imported into 3D space and jointly interpreted alongside several other 3D data sets. Key data sets included in 3D interpretation efforts included statewide 3D geological models of Seymour et al. [2006], shear-wave velocity models of Pilia et al. [2015] and various Moho depth surfaces [Kennett et al., 2011, Rawlinson et al., 2001, 2010].

4.6.1 Upper-Crustal Depths

In the upper crust at depths ranging 0 km to 10 km resistivity is typically controlled by three key factors; 1) the presence of pore-space fluids, 2) the presence of graphite, and 3) the concentration of iron in Fe/Mg-bearing minerals [Selway, 2014]. At the upper limit of data sensitivity in the preferred model, about 5 km, the Tasmanian crust has resistivities in the range 100 Ω m to 5000 Ω m except for a few discrete zones of apparent conductivity enhancement. The most robust of these features strikes parallel with, and is offset to the east of, the Tamar River valley in Northern Tasmania (**C1** in Figs. 4.17 and 4.25). This is a manifestation of the Tamar Conductivity Anomaly (TCA) in the preferred model.

First identified by Lilley [1976], the TCA has been the subject of several electromagnetic investigations. The location and depth range of the most conductive upper-crustal portions of the TCA in the preferred model agrees with the results of previous MT and GDS studies conducted in this part of northern Tasmania [Hermanto, 1992, Parkinson et al., 1988], which is unsurprising given the close agreement in induction arrow patterns between AusLAMP and legacy data sets. In addition, the ∼20 km eastward offset of the TCA from the Tamar river is in agreement with more recent 2D resistivity models of the region derived from a geothermal exploration broadband MT transect reported in Goh and Holgate [2009]. Low resistivities (<1 Ω m) of the TCA at such shallow crustal levels are inferred as being the result of conductive fluids in highly fractured rocks of the Tamar Fracture Zone (TFZ), a crustal-scale shear zone inferred to separate the WTT and ETT. The TFZ is clearly visible in shear wave velocity models derived from tomographic modelling of passive seismic data sets as a shallow crustal low velocity corridor spatially correlated with low resistivity zone **C1** (Fig. 4.25).

The very low resistivities observed within the TCA in the upper crust appear to be restricted to northern Tasmania and represent the uppermost expression of a larger structure that extends southward with increasing depth, albiet less extreme low resistivities. This aspect of the TCA's structure is best illustrated in 3D by way of isosurface volumes such as those presented in Figure 4.26. Here, isosurface volumes encapsulate low resistivity (<6 Ω m) regions in the mid- to upper-

crust (spanning depths ranging 0 km to 20 km) and serve to highlight their 3D structure.

A potential explanation for shallow, extremely low resistivities in the northernmost reaches of then TCA may include variable degrees of fluid influx along fracture networks of the TFZ. East-west directed extension in the Latest Cretaceous and Paleogene saw the formation of a network of major fault structures across Tasmania, which in the north extended Bass Basin southwards forming the Tamar Graben and the Longford Sub-basin [Stacey and Berry, 2004]. It is likely that a greater degree of extensional tectonism in northern Tasmania may have led to a greater degree of fluid percolation into the TFZ yielding lower resistivities at the regional scale.

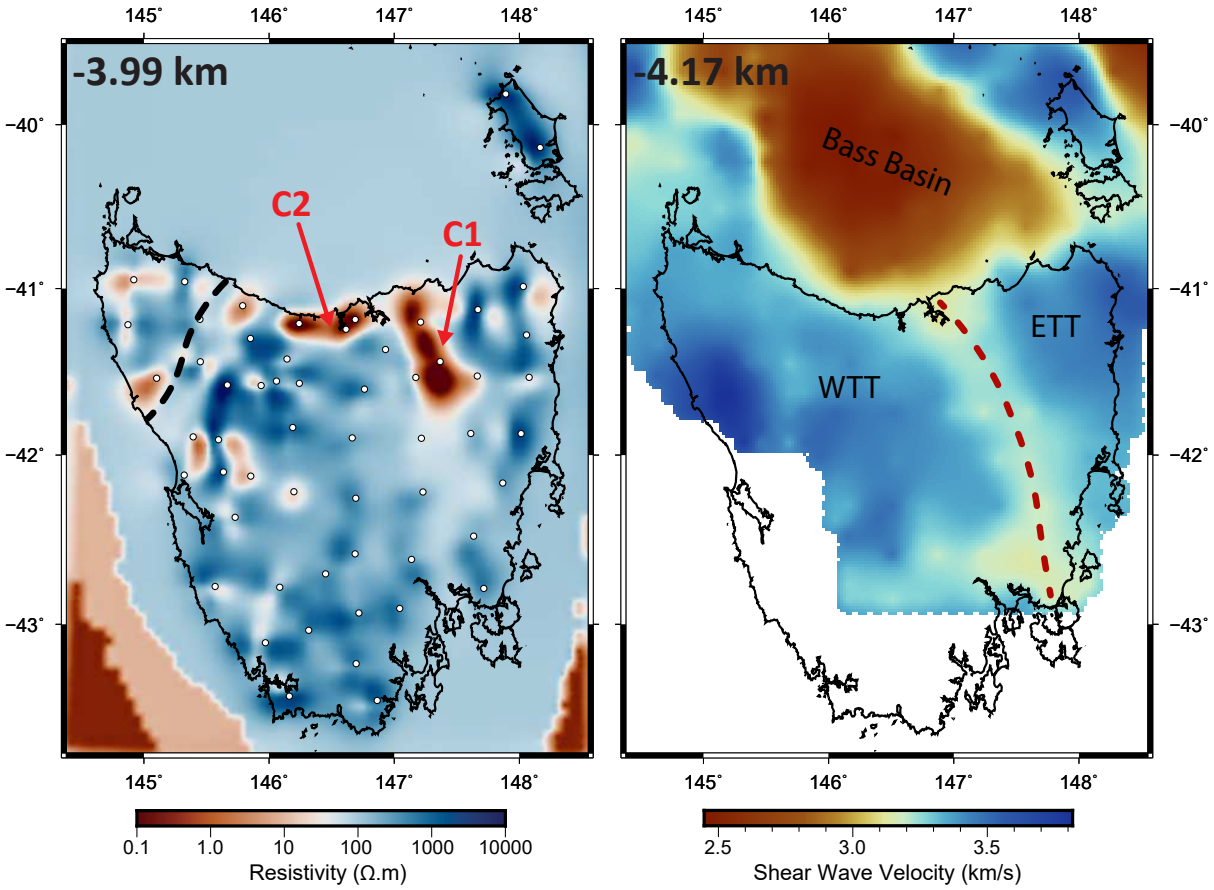

Figure 4.25: Depth slices at comparable upper crustal levels through the preferred resistivity model, left, and a shear wave velocity model of Pilia et al. [2015], right. The TFZ (dashed red line) is clearly delineated as a corridor of relatively low shear wave velocity separating the ETT and WTT. Black dashed line represents the approximate location of the Arthur Lineament, a structure coincident with low resistivity zone **C5**.

Regions of the upper crust with the highest resistivity values tend to correlate well with the subsurface distribution of Devonian and Cambrian granite bodies in the 3D geology model of Tasmania (Fig. 4.27). In western Tasmania this spatial correlation is less clear with parts of low resistivity zone **C5** apparently plotting within the Meredith batholith at depths of ∼6 km. Since

granite bodies in the 3D geology model are largely derived from potential field modelling which is most sensitive to the granite roof and relatively insensitive to granite floor, it is possible that low resistivity zones that appear to manifest within granitic bodies are actually due to some unknown conductive geologic unit beneath the granites, such as a carbonaceous metasedimentary package.

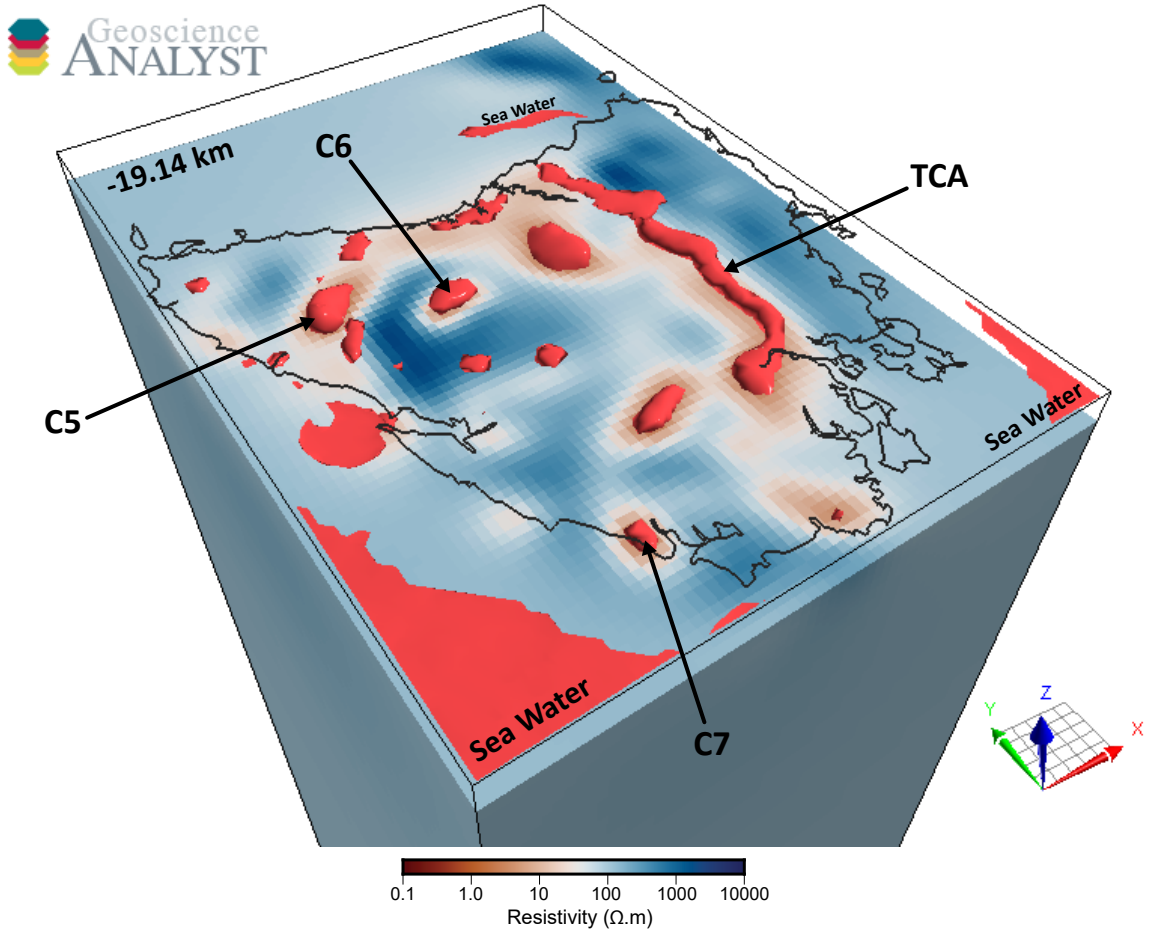

Figure 4.26: Parallel projected oblique view from the south west of the preferred model space taken from Geoscience Analyst 3D viewing software. A 3D cubic volume of the model space with horizontal padding cells removed and sliced to a top of 19.14 km depth provides context. Red volumes are isosurfaces encapsulating regions of the model space with resistivities less than 6 Ω m across a depth range of 2 km to 19 km. The TCA is clearly visible as an arcuate conductor exposed at shallow crustal levels in the north and progressively deepening to mid-crustal levels in the south.

Northern parts of low resistivity zone **C5** are spatially coincident with greenschist to amphibolite facies metamorphic rocks of the Arthur Lineament at these upper crustal depths (Fig. 4.28). Low resistivity in this part of the model space is probably attributable to graphite in metasedimentary rocks of the lineament reported in Holm [2002] and Braniff [2013]. Provided the graphite is well connected, such as through high-strain Cambrian deformation in the case of the Arthur Lineament [Holm and Berry, 2002], graphite has been shown to drastically reduce

bulk rock resistivity when present at a few ppm [Duba and Shankland, 1982]. Low resistivities imaged beneath the Meredith batholith at ~6 km could potentially be attributed low resistivity Arthur Lineament rocks dipping eastward at a shallower angle than inferred by the 3D geology model.

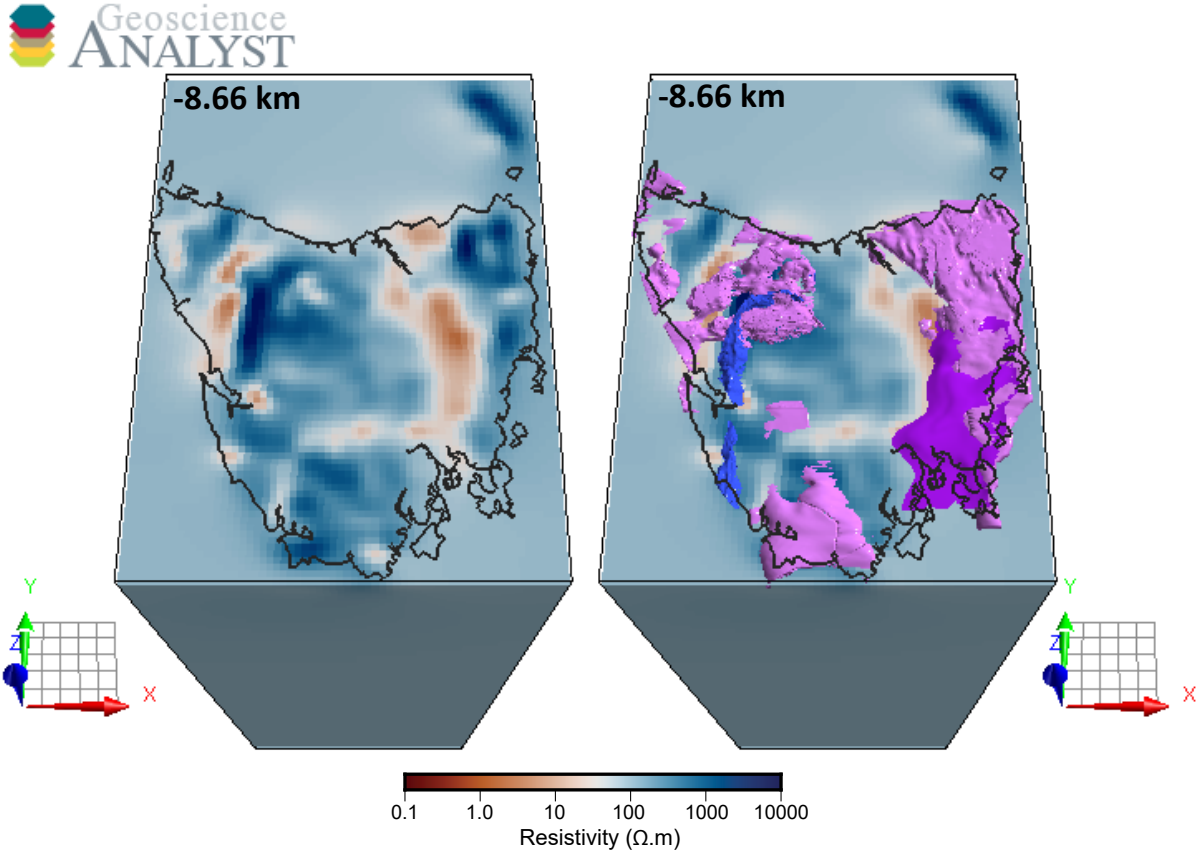

Figure 4.27: Parallel projected oblique views from the south of the preferred model space taken from Geoscience Analyst 3D viewing software. Both views present a 3D volume of the preferred model with padding cells removed and clipped to a top surface depth of 8.66 km. The view to the right presents inferred volumes for Devonian (pink) and Cambrian (light blue) granitoids derived from potential field modelling [Seymour et al., 2006]. The purple surface represents Devonian granite subsurface topography in eastern Tasmania which was updated subsequent to the publication of the 3D geology model following a significant increase in regional gravity data coverage in the region [Leaman, 2012]. Note the good correlation between granitoid intrusive packages and highly resistive regions of the model space with low resistivity regions largely restricted to the boundaries of granitoid bodies.

4.6.2 Mid-Crustal Depths

Cambrian orogenesis also emplaced several mafic-ultramafic ophiolite suites across the WTT as allocthonous relics of an overthrust forearc terrain [Berry and Crawford, 1988]. These are incorporated in the Tasmanian 3D geology model as several thin fault-bounded east dipping sheets of mafic-ultramafic rocks with dips shallowing to a horizontal base of 10 km in the model.

Given the strong magnetic and gravity signature of these lithologies, their spatial extent is well-constrained by potential field modelling lending a relatively high degree of model robustness for the uppermost parts of the 3D geology model. This robustness decreases rapidly with depth as uncertainty increases and model structures are increasingly influenced by conceptual tectonic models. Cambrian mafic-ultramafic lithologies are inferred beneath Tasmania Basin sediments in the 3D geology model, and are coincident with low resistivities of the central and southern portions of the TCA at depths of about 7 km. In the west, at the same depth, these lithologies are located at the boundary between the highly resistive arcuate resistor **R1** and conductor **C5** (Fig. 4.29). There appears to be a second order correlation between low resistivities and mafic-ultramafic rocks inferred at these depths in the 3D geology model.

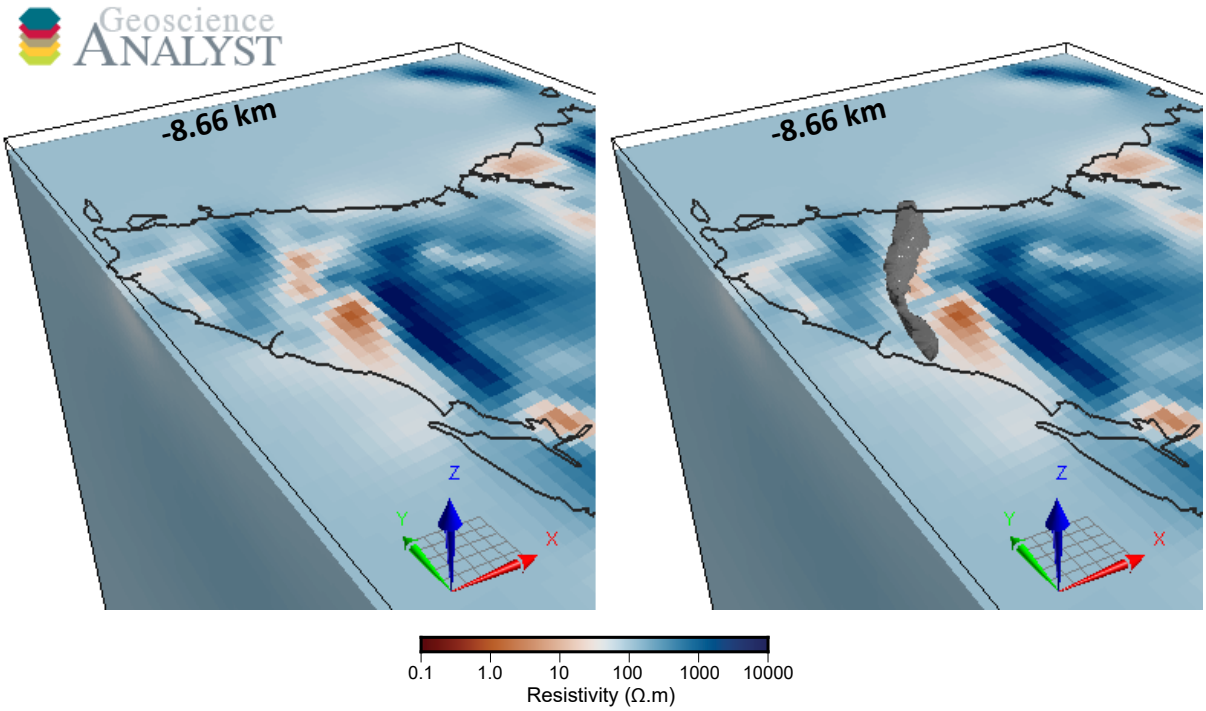

Figure 4.28: Parallel projected oblique views from the south west of the northwestern preferred model corner taken from Geoscience Analyst 3D viewing software. Both views present a 3D volume of the preferred model with padding cells removed and clipped to a top surface depth of 7.07 km. The view to the right presents inferred volumes for metamorphic rocks of the Arthur Lineament (grey) from the 3D geology model of Tasmania [Seymour et al., 2006]. Note the good correlation with a low resistivity zone **C5** which extends to a corridor parallel to the Arthur Lineament at mid-crustal depths.

Many of the Tasmanian mafic-ultramafic complexes are pervasively serpentinised. Serpentinites tend to return lower resistivities than their crystalline protoliths [Stesky and Brace, 1973]. Aside from porosity and fluid content increases, this decrease in restivity has been theorised as being the result of electrical conduction by way of interconnected magnetite crystals formed during serpentinisation. However, laboratory measurements conducted on serpentinites with varying magnetite content by Kawano et al. [2012] suggest shearing-enhanced magnetite

interconnectivity only occurs when magnetite content exceeds geologically atypical volume fractions (>25 vol%). Low resistivities observed within serpentinised mafic-ultramafic rocks are thus typically attributed to enhanced porosity and saline fluid content rather than interconnected magnetite conduction mechanisms [Chave et al., 2012]. Low apparent resistivities coincident with Cambrian mafic-ultramafic rocks inferred at depth in the 3D geology model may be more likely the result of fault-related porosity increases in surrounding rocks than low resistivities of potentially serpentinised mafic-ultramafic rocks. Figure 4.30 presents views of the preferred model sliced to upper crustal depths and overlaid with inferred crustal-scale fault structures as yellow surfaces. The distribution and relative density of these faults exhibits spatial correlations with low resistivities similar to that of mafic-ultramafic rocks.

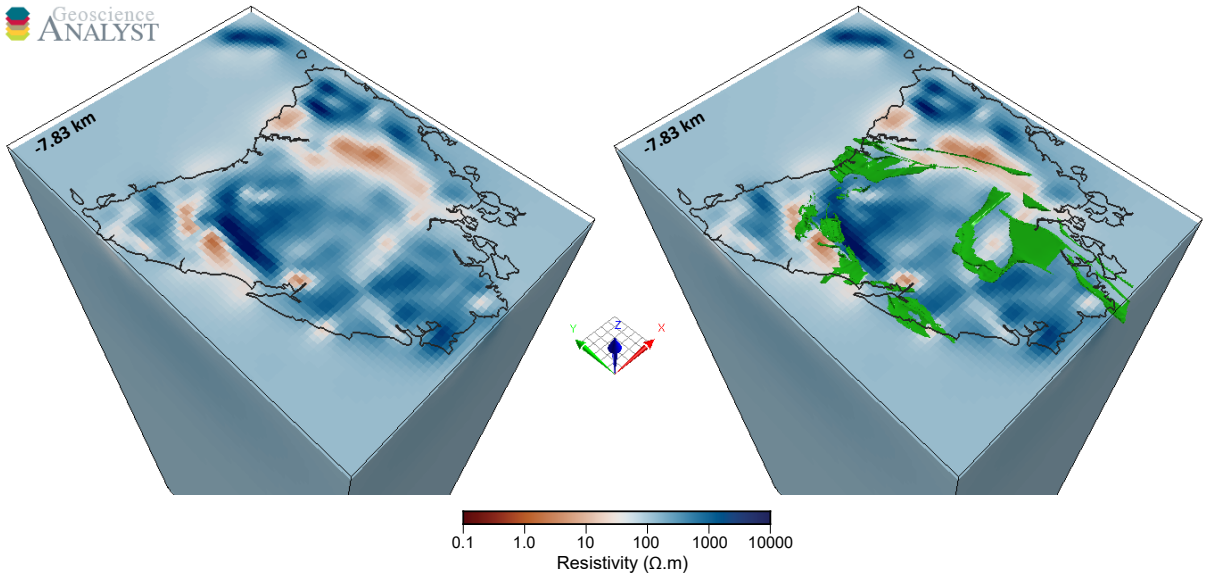

Figure 4.29: Parallel projected oblique views from the south west of the preferred model taken from Geoscience Analyst 3D viewing software. Both views present a 3D volume of the preferred model with padding cells removed and clipped to a top surface depth of 7.83 km. The view to the right presents inferred volumes for Cambrian mafic-ultramafic rocks from the 3D geology model of Tasmania [Seymour et al., 2006]. These are thin, fault-bounded structures predominantly dipping eastwards.

Moving deeper into the mid-crust, at depths exceeding 10 km, low resistivity structures beneath the Arthur Lineament and the TCA broaden into elongate low resistivity corridors while more discreet low resistivity zones emerge beneath Cambrian metamorphic complexes in the WTT. Figure 4.31 presents a mid-crustal depth slice through the model overlain with white polygons outlining Cambrian metamorphic complexes alongside 3D volumes representing the full crustal extent of Proterozoic rocks taken from the Tasmanian 3D geology model. Here, the isolated metamorphic complexes east of the Arthur Lineament are clearly located at the western margin of Tyennan metasedimentary basement rocks.

With grades ranging from amphibolite to eclogite facies implying burial to at least 20 km to 50 km depth, and geochemical signatures similar to Neoproterozoic unmetamorphosed tholei-

itic basalt and continental-derived siliciclastics, these metamorphic complexes are thought to represent partially subducted passive margin sediments metamorphosed during Cambrian arc-continent collision [Meffre et al., 2000]. The presence of high-grade metamorphic clasts within the basal sediments of the post-collisional Dundas-Fossey Trough separating the Rocky Cape and Tyennan Proterozoic terrains implies rapid exhumation of the metamorphic complexes following cessation of collision [Turner et al., 1998]. Mid-crustal low resistivity anomalies such as the ones beneath the Mersey River and Port Davey metamorphic complexes are not uncommon in MT resistivity models, and are often attributed to fluids trapped beneath the brittle-ductile transition zone in tectonically active regimes [Thiel et al., 2016b, Wannamaker et al., 2009], or graphite deposited along grain boundaries after periods of high CO_2-rich fluid flux [Heinson et al., 2006, Robertson et al., 2016, 2017].

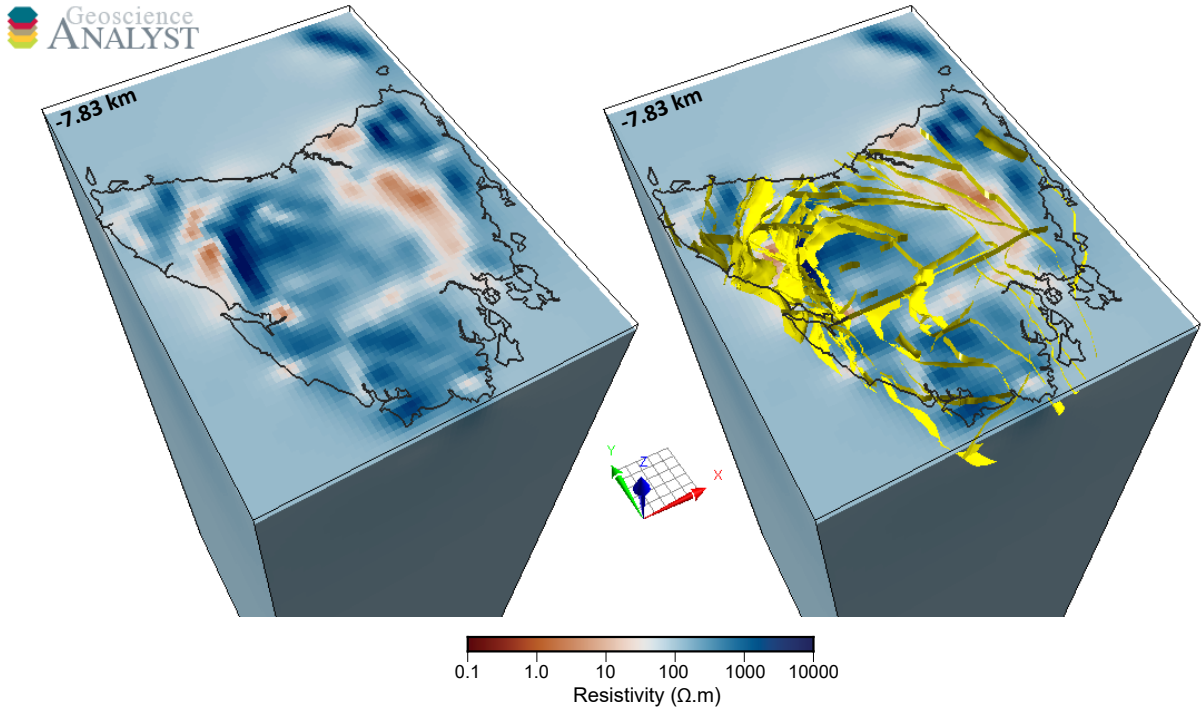

Figure 4.30: Parallel projected oblique views from the south west of the preferred model taken from Geoscience Analyst 3D viewing software. Both views present a 3D volume of the preferred model with padding cells removed and clipped to a top surface depth of 7.83 km. The view to the right presents inferred crustal-scale fault surfaces from the 3D geology model of Tasmania [Seymour et al., 2006].

Given Tasmania's current tectonically stable regime, a preferred mechanism for low resistivities beneath the Mersey River and Port Davey metamorphic complexes involves graphite exolved from CO_2-rich fluids potentially derived from metamorphic devolatilisation reactions occurring at depth beneath what is now the western edge of the Tyennan crustal block. Fluid focusing along rheologically weak zones may also explain rapid exhumation of deeply buried metamorphic rocks to shallower levels at these locations. Of course, much of this analysis is confounded by the overprinting of later tectonic events that could potentially alter the graphite-

dependent resistivity structure of these regions. In particular, deformation during the Devonian Tabberabberan orogeny was accompanied by voluminous granitoid intrusion that may have led to localised oxidative or thermal destruction of graphite which occurs at temperatures above ~900 °C [Selway, 2014].

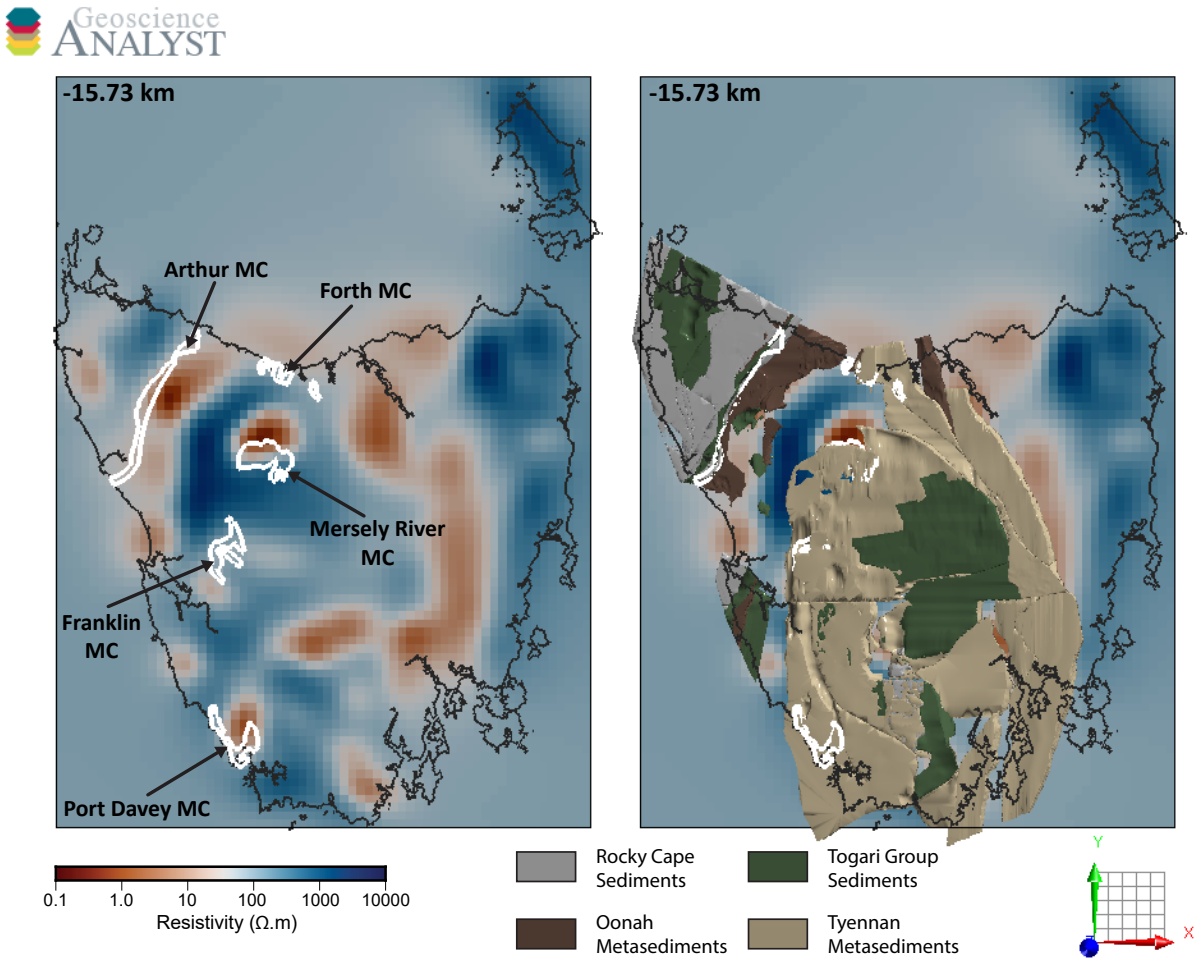

Figure 4.31: Orthographic projected vertical views of the preferred model taken from Geoscience Analyst 3D viewing software. Both views present a depth slice taken from 14.25 km depth in the model space with white polygons depicting the surface extent of Cambrian metamorphic complexes, including the elongate north-northeast trending Arthur Lineament in the west, from Meffre et al. [2000]. The view to the right presents inferred 3D volumes for the Proterozoic units representing major crustal blocks situated either side of the Dundas Fossey Trough.

At mid-crustal depths the TCA broadens and links up with another low resistivity zone in the Adamsfield region west of Hobart forming a coherent arcuate low resistivity corridor (**C1** in Fig. 4.20). The westernmost extension of the TCA at this depth is located beneath allocthonous mafic-ultramafic rocks outcropping in central southern Tasmania, though at a depth that places low resistivities within Proterozoic Tyennan basement well below the low angle thrust faults separating allocthonous units from basement inferred in the 3D geology model. As with low resistivities observed beneath metamorphic complexes in the WTT, low resistivities associated

with the TCA at these mid-crustal depths are unlikely to be the result of pore space fluid conduction given significant pore spaces do not exist at or below the mid-crustal brittle-ductile transition zone [Selway, 2014].

A likely interpretation of mid-crustal low resistivity in the TCA involves graphite deposited along Cambrian thrust fault networks associated with allocthonous ophiolite emplacement. Thrust faults likely acted as conduits for CO_2-rich fluids emanating from the devolatilisation of down-going subducted material, from which graphite probably precipitated [Luque et al., 1998]. The location of mid-crustal low resistivity beneath inferred thrust fault planes in the 3D geology model probably results from an under-estimation of thrust fault dips at these depths, with the model assuming horizontal thrust faults at its base of 10 km.

4.6.3 Lower Crust & Lithospheric Mantle

Resistivity structures that manifest at mid-crustal depths in the preferred resistivity model undergo significant change with increasing depth into the lower crust toward the crust-mantle boundary. In general, anomalous resistivities, both high and low, tend toward less extreme values by about an order of magnitude over the depth range of the lower crust ($\sim$20 km to $\sim$30 km). Low resistivities beneath Cambrian metamorphic complexes fade to background resistivity at the base of the crust, while low resistivities previously part of the TCA split into northern and southern zones and migrate westward.

At lower crustal and uppermost lithospheric mantle depths, resistivity is largely controlled by the presence of graphite and, to a lesser extent, iron content and the presence of hydrogen in nominally anhydrous minerals or NAMs. Since hydrogen behaves as an incompatible element, any melt extraction from the lower crust and uppermost mantle as a result of tectonothermal events will tend to reduce hydrogen content and, coupled with thermal destruction of any graphite present, give rise to increases in bulk resistivity. By contrast, events that lead to the enrichment of hydrogen content, such as assimilation of fluids sourced from a mantle plume or down going subducted slab, will tend to result in lower resistivities [Selway, 2014].

Melt extraction from the lower crust and uppermost mantle occurred in the Cambrian within the WTT, and later throughout Tasmania during and immediately after the Devonian Tabberabberan Orogeny. Devolatilisation associated with melt extraction explains the relationship between upper crustal granite distribution and lower crustal high resistivities evident in Figure 4.32. Higher resistivities in the ETT relative to the WTT may also imply a higher degree of partial melting, or may reflect pre-Tabberabberan low volatile content typical of oceanic lower crust inferred beneath the ETT from patterns in inherited zircon age spectra [Black et al., 2010].

Low resistivities along the TCA tend to migrate westward with increasing depth in the lower crust, and eventually coalesce into a central Tasmania north-south trending low resistivity keel within the lithospheric mantle and beneath the Tyennan block (Figs. 4.22 and 4.23). This relatively low resistivity keel lies beneath regions of Tasmania with conspicuously little Devonian

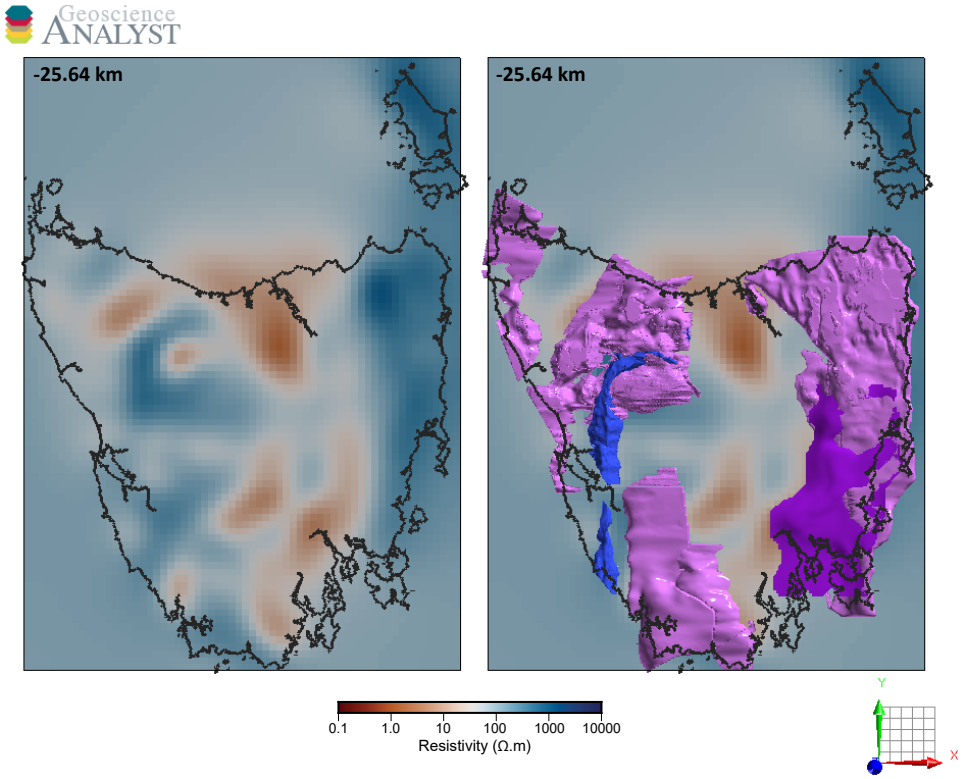

Figure 4.32: Orthographic projected vertical views of the preferred model taken from Geoscience Analyst 3D viewing software. Both views present a depth slice taken from lower crustal 25.64 km depth in the model space. The view to the right presents inferred 3D volumes for Cambrian (blue) and Devonian (pink) granites from the 3D geology model [Seymour et al., 2006]. The purple surface in the southeast represents an updated granite roof surface derived from gravity survey data acquired after the production of the 3D model [Leaman, 2012].

granitoid intrusion, suggesting melt extraction during and after the Tabberabberan orogeny was limited and thus potentially preserving pre-existing low resistivity. The west-dipping nature of the TCA, highlighted in cross sections shown in Figures 4.24 and 4.33, contrasts with the geodynamic interpretations of Hong et al. [2017] and Black et al. [2010] who inferred east-dipping TFZ as a result of east directed subduction of the WTT beneath the ETT (Fig. 2.2). Figure 4.34 presents a gridded Moho depth image derived from several seismic data sets for context.

Another explanation for low resistivities within the lithospheric mantle beneath central Tasmania relates to much more recent tectonic events. The Jurassic saw extensive intrusion of dolerite sills into sediments of the Permo-Triassic Tasmania Basin unconformably overlying pre-Carboniferous geology of the ETT and WTT, obscuring the boundary between the two. These dolerites represent the Tasmanian extension of the Karoo-Ferrar Large Igenous Province, a ∼5000 km long belt of igneous rocks emplaced along the southern margin of Gondwana across what is now Southern Africa, the Trans-Antarctic Mountains, South Australia and Tasmania.

The temporally narrow and synchronous emplacement ages of Karoo-Ferrar igneous rocks

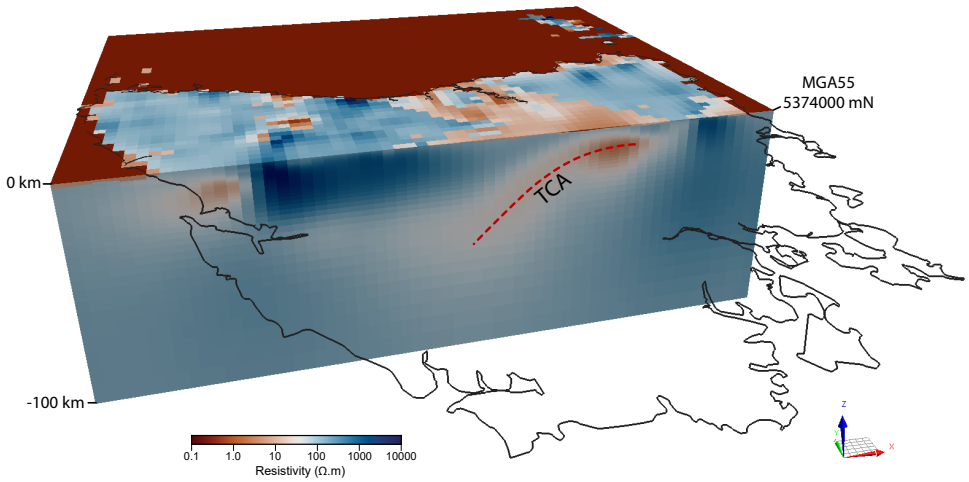

Figure 4.33: Parallel projected oblique view looking north northeast of the preferred model taken from Geoscience Analyst 3D viewing software. View presents a portion of the model space clipped between depths of 0 and 100km beneath the surface with no vertical exaggeration. Black lines represent the Tasmanian coastline plotted for spatial context. The model is sliced along an east west cross section cut along the 5374000 northing line in MGA55 coordinate and highlights the west-dipping nature of the TCA, a result that contrasts with east-dipping interpretations presented in Hong et al. [2017] and Black et al. [2010].

have led Ivanov et al. [2017] to propose a subduction-related model for the province. In this model, Karoo-Ferrar volcanism was driven by mantle metasomatism modulated by deep slab dehydration of the Phoenix plate subducted beneath southern Gondwana. In this context, it is possible that the relatively low resistivity north-south trending structure observed within Tasmania's lithospheric mantle represents relic metasomatism that drove partial melting from which the dolerites were sourced. The modern day north-south orientation of this lithospheric mantle low resistivity feature is also subparallel with reconstructions of the southern Gondwanan active margin.

The Cenozoic saw the eruption of volumetrically minor basalts across much of Tasmania, with the exception of the southwest and central west of the island. These basalts represent the southernmost extension of a ∼4400 km long belt of Cenozoic volcanism that extends across eastern Australia terminating in North Queensland. Tasmanian examples range from silica oversaturated to strongly undersaturated, and have emplacement ages in the range 8.5 Ma [Baillie, 1986] to ∼70 Ma [Zwingmann et al., 2004] with no clear temporo-spatial relationship in their distribution.

Many of the silica undersaturated Tasmanian basalts contain significant occurrences of ultramafic xenoliths, providing an indirect means of studying the lower crust and lithospheric mantle through which the basalts erupted. The majority of Tasmanian mantle xenoliths are typical anhydrous four-phase spinel lherzolites, while rare volatile-bearing websterite occurrences have been reported at isolated locations [Quilty et al., 2014]. The generally anhydrous

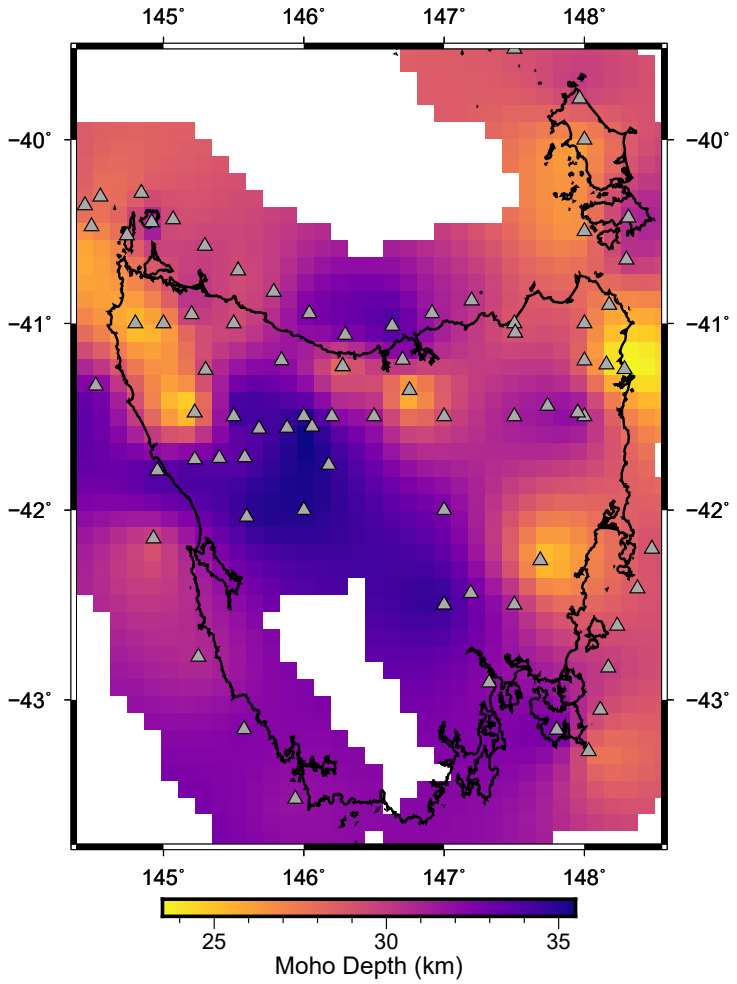

Figure 4.34: Gridded Moho depth image taken from several seismic observations (grey triangles). Data sets include marine reflection and refraction taken from the TASGO project [Rawlinson et al., 2001], stacked autocorrelogram estimates of Kennett et al. [2015] as well as tomographic modelling of passive seismic data [Rawlinson et al., 2010]. This is an updated version of the AusREM Moho surface published in Kennett et al. [2011].

and low volatile content of Tasmanian mantle xenoliths differs markedly from other southern Victorian examples, suggesting Tasmania's lithosphere has not experienced the relatively high degrees of mantle metasomatism evident in other parts of southeastern Australia [Nasir et al., 2010].

Although mineralogical compositions imply a volatile-poor lithospheric mantle, compositional variation and trace element content of xenolith minerals uncover less obvious metasomatic influences on the Tasmanian lithosphere. Mantle xenoliths within the most common chrome-diopside suite can be differentiated in terms of their fertility on the basis of olivine forsterite content. The most common of these are relatively fertile with forsterite content in the order of 89-91%, and show evidence of cryptic metasomatism in clinopyroxenes characterised by enrichment in incompatible elements [Quilty et al., 2014].

The most fertile of the Tasmanian mantle xenoliths are found in the Rocky Cape crustal element in the northwest, and are largely sampled from the basalts along the eastern margin of the element. Fertile lithospheric mantle beneath the eastern edge of the Rocky Cape element is consistent with resistivity data in the preferred model. Low resistivities associated with the Arthur Lineament at crustal depths (feature **C5** in 4.22) extend into the lithospheric mantle, with resistivities in the order of $\sim$50 Ω m at depths of 40 km. Xenoliths from a basalt plug in the Blessington area some 40 km east of Launceston yielded both fertile and infertile mantle signatures, suggesting basalt melt percolation through heterogeneous mantle in this area. This fits with the preferred resistivity model where this locality is situated above a transition zone between low resistivity WTT mantle to high resistivity ETT mantle [Quilty et al., 2014].

Isotopic studies of noble gases in Tasmanian xenoliths have yielded further insights into the fertility state of the lithospheric mantle [Czuppon et al., 2010]. Noble gas isotope compositions imply a heterogeneous lithospheric mantle beneath Tasmania with MORB-like contributions likely due to Cretaceous-Paleogene rifting, as well as radiogenic contributions indicative of subduction-related metasomatism in the Palaeozoic. Although broadly consistent with the isotopic characteristic of host basalts, these results did not show any spatial variation across the WTT and ETT, and thus do not necessarily agree with the strong resistivity contrast observed in these terrains.

4.7 Conclusion

New regional-scale long period magnetotelluric data have been acquired across Tasmania and Flinders Island in order to map the 3D geoelectric structure of the Tasmanian lithosphere. Robust processing of the raw data have yielded a 57-site data set containing estimations of the MT impedance tensor and GDS tensor, the latter of which agrees with legacy data acquired in northern Tasmania investigating the Tamar Conductivity Anomaly. Analysis of the MT phase tensor revealed strong contrasts in geoelectric structure of the ETT and WTT, with the ETT returning consistently low minimum phase angles indicative of increasing resistivities with depth and the WTT returning a more heterogeneous response.

Several 3D resistivity models were generated utilising freely available inverse modelling codes compiled on research computing infrastructure at the University of Tasmania. From a series of high resolution models that incorporated sea water and conductive sediments in the starting model as *a priori* information, a preferred model was selected on the basis of low global RMS misfit as well as acceptable fits between predicted and observed data for each site. This model represents a major outcome from this research project, as it reveals the geoelectric structure of the Tasmanian lithosphere for the first time.

Interpretation of geoelectric features in the preferred model relied heavily on the integration of existing geophysical and geologic data sets in 3D visualisation software. Upper crustal resistivity features were found to corroborate upper crustal geologic structures of the Tasmanian 3D geology model [Seymour et al., 2006], with highly resistive regions spatially correlated with unfractured crystalline Devonian and Cambrian granitoid rocks. Low resistivities in the northwest appear spatially correlated with graphite-bearing, fault bounded metasedimentary rocks for the Arthur Lineament. In northern Tasmania, very low resistivities around the Tamar graben represent the shallowest extension of the larger Tamar conductivity anomaly, a feature that extends to the south at deeper levels in the crust at the inferred boundary between the East Tasmania Terrain and West Tasmania Terrain.

Low resistivities along the boundary between the ETT and WTT are a feature throughout the crustal depth range of the preferred model, and are attributed to fracture-related porosity above the brittle ductile transition zone. Below this transition conduction is attributed to graphite deposited along fracture networks associated with thrust faulting at the terrain boundary. Although conduction mechanisms differ with depth, low resistivities along this boundary are related, and likely due to Cambrian arc-continent collision. To the west, discrete low resistivity zones emerge below this transition zone beneath Cambrian high-grade metamorphic complexes now exposed at surface. These are interpreted as rheologically weakened regions of the crust through which CO_2-rich fluids have fluxed.

With increasing depth beyond the mid-crust into lower crustal and lithospheric mantle depths, resistivity models show a gradual decrease in overall structural complexity with the

emergence of a north-south trending low resistivity keel beneath central Tasmania. Low resistivities in the lower crust and lithospheric mantle are attributed to interstitial graphite and volatile content in anhydrous minerals, and thus preserve evidence of tectonic processes that introduce or remove volatiles. High resistivities in the lower crust beneath Devonian and Cambrian granitoids likely reflect removal of volatiles, and possibly thermal destruction of graphite, during melt formation associated with Tyennan and Tabberabberan Orogenesis. By contrast, low resistivities at upper mantle depths observed beneath central Tasmania are attributed to volatile enrichment possibly associated with subduction along the southern Gondwanan margin in the Paleozoic. Evidence from mantle xenoliths sourced from Cenozoic basalts confirm metasomatism of the lithospheric mantle beneath Tasmania, but do not necessarily support a clear distinction in the degree of upper mantle metasomatism between the WTT and ETT inferred by resistivity structure.

4.8 Recommendations

Recommendations for future work relating to the regional geoelectric structure of Tasmania fall into two categories; 1) MT data and model improvements, and 2) further synthesise geoelectric data with existing data sets. For the former, recent developments in the use of HPC applied to MT time series processing could potentially improve estimation of Tasmanian MT impedance and GDS tensor, especially for longer periods. At the time of writing, this capacity is under development at the National Computing Infrastructure in Canberra and will likely be applied to Tasmanian time series MT data in the future.

Potential improvements to the inverse model include using higher resolution starting models that incorporate topography. This can be done with finite element 3D inversion codes GoFEM and HexMT of Grayver [2015] and Kordy et al. [2016], respectively. This will likely account for some static shift effects inherent in the MT data (done explicitly in HexMT), and could potentially improve the resolution of the uppermost parts of the model space. Coupled with better MT impedance and GDS tensor estimates from HPC reprocessing of time series, this could potentially extend the depth of investigation as well.

Second, the development of a systematic compilation of mantle xenolith geochemical studies in Tasmania would compliment geoelectric analyses of the Tasmanian lithospheric mantle.

Chapter 5

West Tasmania Broadband Transect and 2D Model

This chapter presents the steps taken in processing and analysing broadband magnetotelluric (MT) data acquired as part of the north and west Tasmanian broadband MT transect surveys. Transects were acquired to compliment the state-scale AusLAMP data set by bringing the geoelectric structure of major transitions between Proterozoic and Paleozoic transitions into sharper focus, albiet in 2D as opposed to 3D. Sections 5.1 and 5.2 outline the software packages and processing procedures used in raw data processing, as well as the types of noise encountered in the raw data and the procedures used to minimise their influence. Section 5.2 also makes the case for the removal of the north transect from further analysis and discussion in this body of work. Section 5.3 presents pre-inversion analyses of phase tensor and geoelectric strike of the west transect while Section 5.4 presents two dimensional (2D) inverse modelling methods and results for the same. Section 5.5 presents a discussion and interpretation of the final modelling results of the west transect with appropriate geophysical and geological context. The chapter closes with Section 5.6 with conclusions and recommendations for future transect MT studies.

5.1 Data Processing

Broadband MT data processing was carried out using the Bounded Influence Remote Reference Processing (BIRRP) code of Chave and Thomson [2004] for MT impedance tensor ($\mathbf{Z}$) estimation. Final electronic data interchange (EDI) files for each MT site containing impedance tensor estimates across a large period range resulted from the combination of outputs from two separate processing steps. All data processing steps utilised functions contained in the MTpy library of Python codes [Kirkby et al., 2019, Krieger and Peacock, 2014].

5.1.1 Instrument Outputs

AuScope MT instruments in broadband mode recorded magnetic and electric field data at a sample rate of 1000 Hz, with horizontal components of the time rate of change of the magnetic field ($\delta\mathbf{B}/\delta$t) recorded using LEMI-120 induction coils buried horizontally in the ground and aligned with magnetic north and east. Electric field data were recorded as electric potentials across two non-polarisable buried electrodes separated by a known distance.

For each site, 36 to 48 hours of electric and magnetic field data were recorded as millivolt outputs and digitised by a 24-bit PR6-24 Earth Data portable recorder unit. A typical AuScope broadband MT site records 3 GB to 4 GB of ASCII data over a deployment in this configuration. Figure 5.1 presents a schematic diagram of a typical broadband MT instrument deployment. In line with standard field procedure for AuScope instruments in broadband mode, no vertically oriented coil was deployed for measurement of the vertical magnetic field component (avoiding the need to dig a deep hole for the long coil), and thus the GDS tensor was not resolved for this study.

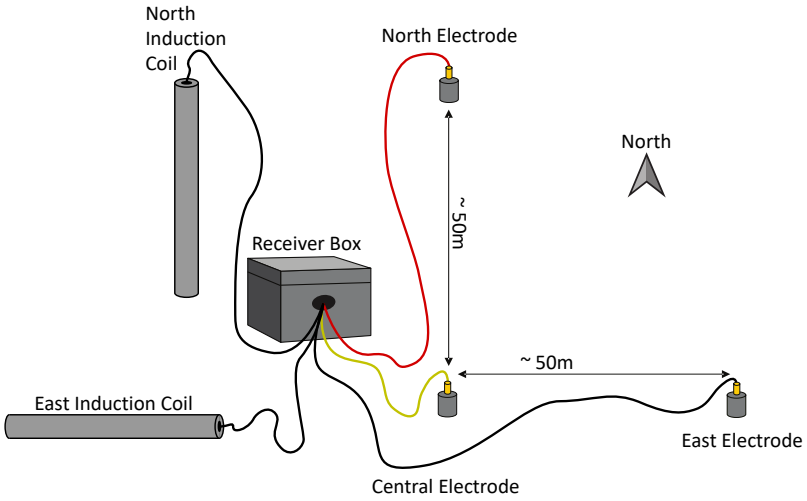

Figure 5.1: Schematic diagram of an AuSCOPE MT instrument deployed in broadband mode. Electrodes and induction coils are buried to a depth of ∼0.3 m in order to ensure vibration and temperature stability as well as good electrical contact.

5.1.2 Time Series Processing

For each broadband MT transect, time series data processing comprised two distinct steps; a high frequency step and low frequency step. Each step involved a series of pre-processing operations to output time series data in the correct format for processing in BIRRP:

1. conversion of electric field channel data to correct electric field units (μV m^{-1}),
2. conversion of magnetic field channel data to correct magnetic field units (nT),

3. rotation of electric and magnetic field data to geographic north, and,

4. generation of input files for impedance tensor computation in BIRRP.

Batch processing the time series data required two tab delimited text files containing input information for all sites in the transect; a station file, and a processing file. The station information file contained metadata compiled from MT site deployment field notes including; station ID, deployment date, coordinates, elevation, electrode separation lengths and orientations, data logger gain values and induction coil orientations. This file was constant for both high frequency and low frequency processing batches and was used to generate header information for each output EDI file from BIRRP.

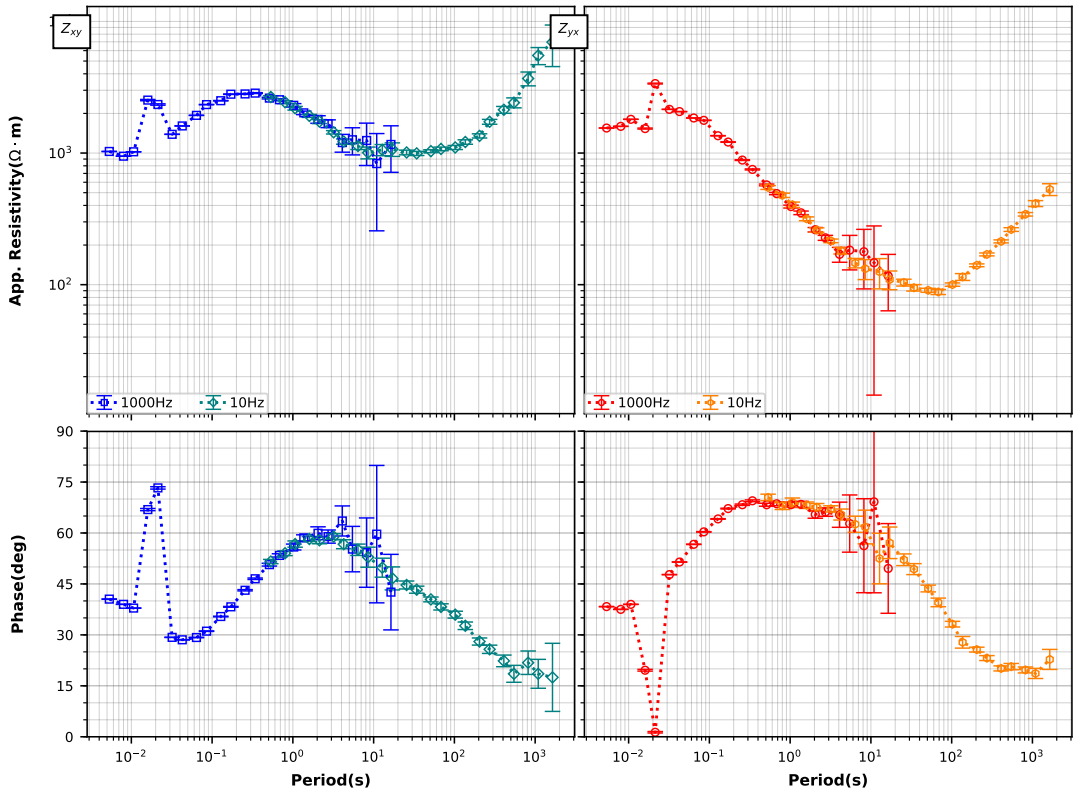

Figure 5.2: Apparent resistivity and phase curves for $\mathbf{Z}_{xy}$ and $\mathbf{Z}_{yx}$ components from low frequency and high frequency processing steps for site 301 from the west transect. Note periods from high and low frequency processing steps overlap between 0.5 s to 20 s. When combining processing steps, periods with greatest error in this range were rejected. Another feature common to Tasmanian broadband transect data is the deviation from smooth curves in apparent resistivity and phase for periods around 0.02 s, or 50 Hz, as a result of power line noise. These data were later masked prior to inversion and modelling.

The processing information file contained key parameters used by MTpy scripts to generate input files for BIRRP and differed slightly for each processing batch. Processing parameters included; station ID of the site to be processed, remote reference station ID, start and stop times denoting the time window used for processing, time series decimation factor, sampling

rate, magnetic field declination, and the electric field dipole and induction coil orientations for both. Magnetic field declination was calculated using the International Geomagnetic Reference Field 2012 (IGRF12) for each site for the date of deployment. Declination values varied between $-13.83°$ and $-13.26°$ across the transect, well within expected installation accuracy.

High Frequency Step

High frequency processing was carried out using a 3 hour window of time series data from each site and a corresponding reference site. This window was selected from the early hours of the morning (12am to 3am) where noise due to passing cars and power line load was expected to be at a minimum. Using a decimation factor of 1 (i.e. no decimation for the high frequency step) in the processing information file (1000 Hz sample rate), and after input of the correct day, start and end time for each site, batch processing was then performed for all sites in each transect using MTpy packages BIRRPTools and MTtools.

Here, MTtools was used to convert raw instrument output time series for each site and corresponding remote reference to SI unit time series for the selected window ready for processing in BIRRP. After BIRRP processing was completed, BIRRPTools was then used to edit raw BIRRP program outputs for each site in order to generate high frequency EDI file for each site with header information taken from the site information text file.

Low Frequency Step and EDI Combination

Low frequency batch processing was conducted using the same procedure as high frequency processing except with a larger time window and a decimation factor of 100, yielding a 10 Hz sample rate for BIRRP input time series. Time windows were extended to the length of the entire deployment for each site, with 20 min removed from the start and end of the time series in order to exclude spurious signals arising from instrument deployment and recovery.

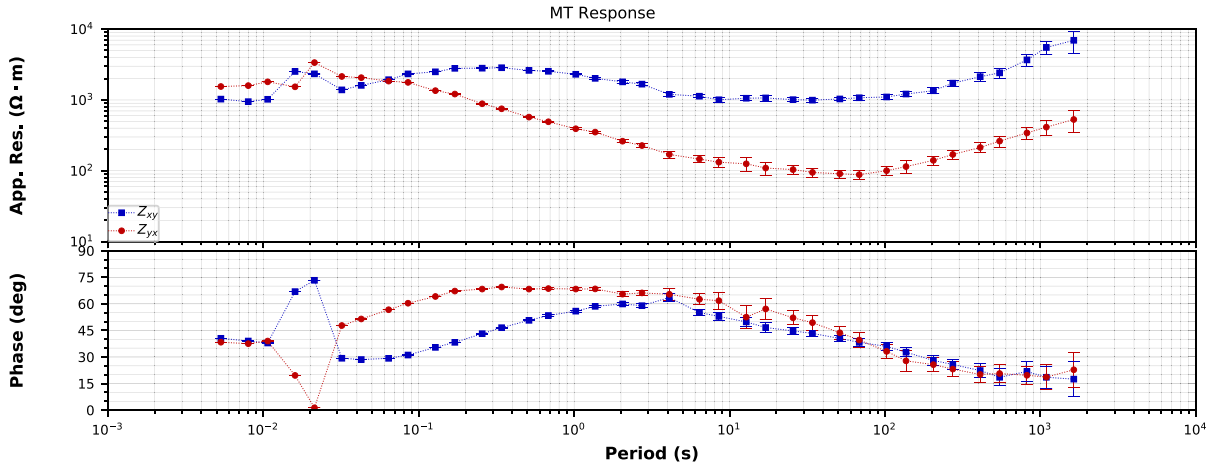

Figure 5.3: Apparent resistivity and phase curves for $\mathbf{Z}_{xy}$ and $\mathbf{Z}_{yx}$ components after combining high and low frequency processed data for site 301 shown in figure 5.2.

With both high and low frequency EDI files generated for each site, a third processing step was performed to merge the two processing output EDI files, which was done on a site by site basis. Here, MTtools was used to combine the two EDI files into a final EDI file for further interpretation and analysis. Given that there were a series overlapping periods from each processing run at around the 1 s period band, as shown in the MT response plot depicted in Figure 5.2, combination of the two EDI files involved a subjective step in which one of two potential periods were selected for final combination. Periods with relatively large apparent resistivity and phase error estimations were rejected, as were periods where apparent resistivity and phases plotted well outside the smooth curves expected of MT physics. Figure 5.3 presents a response curve resulting from the combination of the high and low frequency data shown in Figure 5.2.

5.2 Noise, Distortion & Data Masking

As north and west MT transects ran parallel to major road infrastructure and passed through small towns, several MT sites were deployed relatively close to 50 Hz AC power line infrastructure. This had an unavoidable, but significant, impact with several MT sites returning noisy impedance tensor estimates for short periods influenced by 50 Hz power line noise. Another feature of the data is the prevalence of galvanic distortion affecting electric field measurements, which gave rise to static shifts in apparent resistivity curves. A number of broadband instruments were disturbed by wildlife; particularly in the north transect within the Cradle Mountain National Park. Sites disturbed by wildlife necessitated instrument re-deployment to acquire undisturbed time series data.

5.2.1 Power Line Noise

Broadband MT site locations were selected so as to minimise the influence of power line noise, with all but one site deployed in excess of 1 km from major transmission lines. Despite this, several sites were deployed within ∼500 m of domestic power lines and recorded significant levels of 50 Hz noise as a result. Figure 5.4 illustrates this effect with plots depicting simultaneously recorded time series and frequency spectra from electric field data recorded at two west transect sites; one located within 200 m of a domestic power line and one deployed ∼20 km from the nearest electrical infrastructure.

It is clear in time series data that a significant portion of the electric field signal for the site deployed nearest to electrical infrastructure is comprised of 50 Hz signal, but useful signal was recorded at other frequency bands. Strong signal intensities are observed at higher frequency harmonics of 50 Hz, with spectral peaks for odd harmonics (150 Hz, 250 Hz, etc.) being larger than even harmonics as is typical of this type of noise [Chave et al., 2012]. Spectral leakage around the main 50 Hz peak indicate domestic power lines contribute to sub-50 Hz parts of the

signal and thus degrade the signal to noise ratio in this frequency range. This gives rise to erroneous impedance tensor estimations at periods around 0.02 s as illustrated in Figure 5.3.

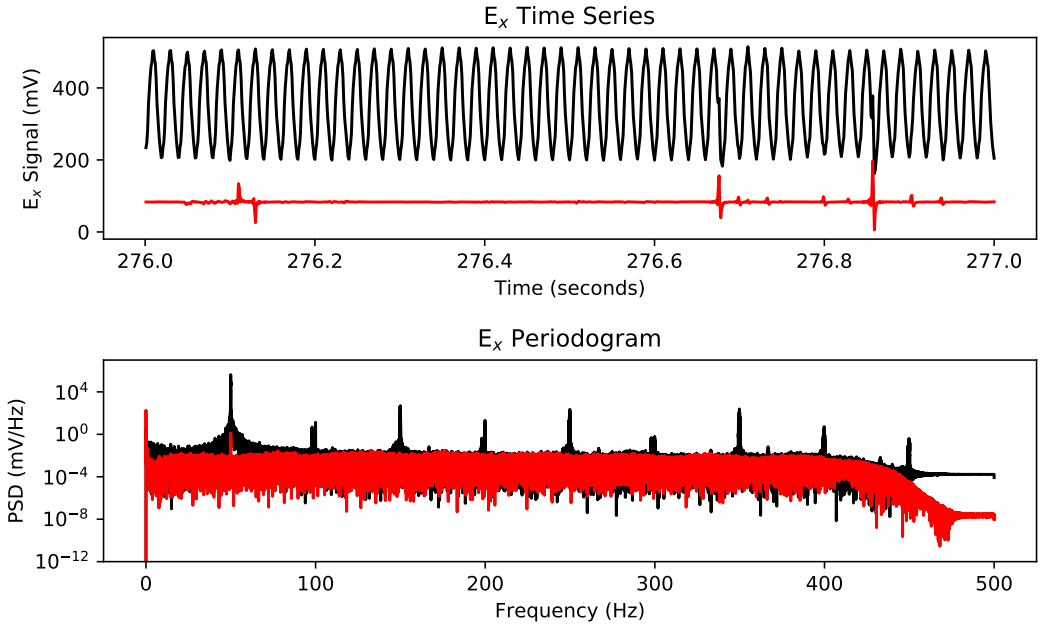

Figure 5.4: Plots depicting simultaneously recorded electric field raw (north-south) data channels from two west transect broadband MT sites; site 329 (in **black**) and site 344 (in **red**). Site 329 was deployed within 200 m of a domestic power line, while site 344 was deployed in excess of 20 km from any power infrastructure and was used for remote reference processing. The top plot presents 1 s of time series data for each site, with the the influence of 50 Hz power line noise clearly visible in site 329 data relative to site 344, in which sferic pulses are observed. The bottom plot presents a periodogram calculated for 5 min of time series from each site. Here the influence of 50 Hz power line noise on site 329 is evident as a large power spectral density peak at 50 Hz with subordinate peaks at harmonics of 50 Hz. Although unclear in time series there is a minor 50 Hz component to site 344 electric field data, despite the relative isolation from power lines.

5.2.2 Distortion

As discussed in background chapters, galvanic distortion of electric field measurements due to near-surface inhomogeneity can manifest as an unknown, frequency-independent multiplier of apparent resistivity referred to as static shift [Chave et al., 2012]. Static shifts in MT data are caused by two shallow-surface electrical phenomena; 1) distortion in the electric field measurement due to the dependency of the field on the resistivity of the material (soil) where the potential difference is being measured, and 2) current distortions due to topographic or shallow surface current channelling effects [Jones, 1988].

As with power line noise, every effort was made to control the potential causes of static shift distortions with instruments deployed on relatively flat ground as far away from potential

current channelling features as possible. However, given practical limitations surrounding land access and extremes of topography encountered along parts of the transects, a number of sites are likely to have been influenced by local electric field distortion.

5.2.3 Data Masking

Prior to dimensionality analysis and preparation for 2D inverse modelling, spurious data in the broadband transect data sets were masked. This subjective process involved the removal of periods from individual MT soundings where apparent resistivity and phase values plot outside the smooth curves required by the physics of the MT method. The near-pervasive influence of 50 Hz noise in the data, particularly for the north transect, necessitated heavy masking in the shorter periods. Figure 5.5 illustrates MT response curves for a north transect MT site before and after data masking.

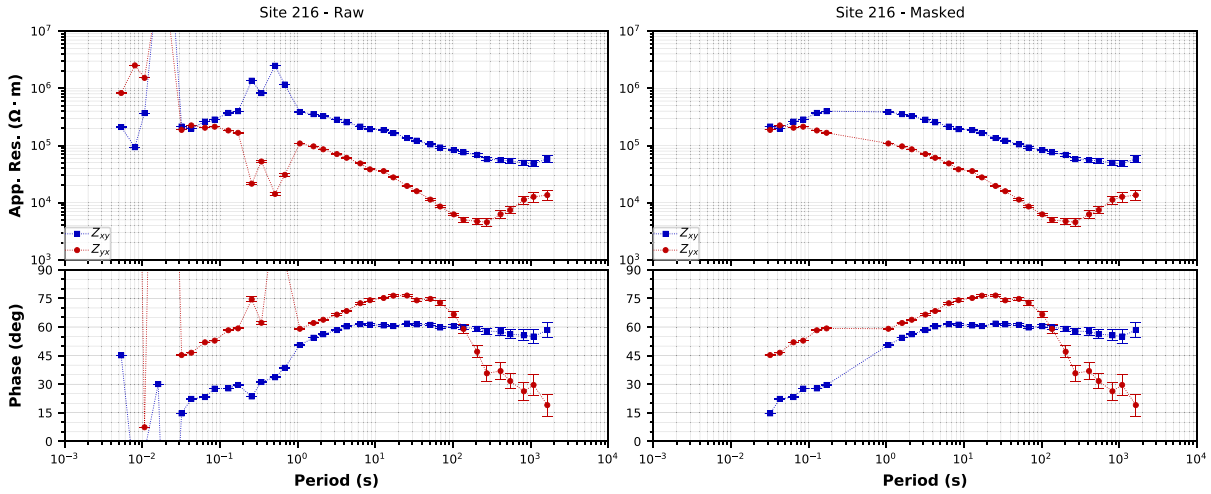

Figure 5.5: Plots depicting the MT response curves for north transect site 216 before and after masking. Note noisy periods around 0.02 s and 10 s are the product of 50 Hz power line noise and were masked out prior to inversion

North Transect Appraisal

Short periods in the north transect sites were affected by 50 Hz noise to the extent that the majority of impedance tensor estimations for periods less than 0.03 s could not be recovered. This effectively renders the data set insensitive to geoelectric structure above ∼3 km assuming typical shallow crustal resistivities of 1000 Ω m, which limits the ability of the transect data to derive subsurface geoelectric information not already known from lower resolution AusLAMP 3D inverse modelling. As a result, further analysis of this data set will not be presented in this thesis.

5.3 Dimensionality, Geoelectric Strike Analysis & Depth Sensitivity

Analysis of dimensionality and geoelectric strike direction are essential for 2D modelling. This relates to the need for MT data to be rotated so as to be parallel and normal to the regional geoelectric strike direction enabling the collapse of the impedance tensor into two components for 2D inverse modelling. These rotated transformations are typically referred to as transverse electric (TE) mode, or **E**-field polarisation, and transverse magnetic (TM) mode, or **B**-field polarisation, depending on the naming convention (see Section 2.3.7).

Given the likelihood of galvanic distortion affecting portions of the data sets, geoelectric strike and dimensionality analysis was performed using the phase tensor approach [Caldwell et al., 2004]. This uses the MT phase tensor, a second rank tensor contained within the impedance tensor ($\mathbf{Z}$) describing the phase relationships between recorded magnetic and electric fields. Calculation of the tensor does not require assumptions about the underlying conductivity structure, and since it retains regional phase information in the presence of galvanic distortion, it is a reliable means of estimating geoelectric strike necessary for data rotation.

In addition to geoelectric strike estimation, the phase tensor can also be used to determine the dimensionality of the subsurface. This can by approximated by the degree of asymmetry of the phase tensor, referred to as the skew angle β. In the ideal, synthetic 2D case all phase tensor ellipses are symmetrical and $\beta = 0$. In real-world data however, a threshold of $|\beta| < 5^\circ$ is generally considered to be a good approximation of two-dimensionality, and periods with $|\beta| > 5^\circ$ are typically excluded from inverse modelling so as to avoid introducing geologically unfeasible structure into 2D models [Caldwell et al., 2004].

Interpretation of 2D inverse models also requires an understanding of the depth sensitivity range of the input data set. This is achieved through the application of the Niblett-Bostick transformation [Jones, 1983], in which the impedance tensor is rotated so as to return minimum and maximum values for the $\mathbf{Z}_{xy}$ and $\mathbf{Z}_{yx}$ components of the tensor. Minimum and maximum impedance tensor components yield minimum and maximum apparent resistivities from which signal penetration depth is calculated using the skin depth equation. For an MT sounding, the minimum signal penetration depth is given by the minimum skin depth for the shortest period, while the longest period gives the maximum penetration depth.

5.3.1 West Transect

The west transect includes 34 broadband sites with a mean site spacing of 2.9 km across a total distance of ∼80 km (Fig. 5.6). As discussed in Chapter 3, a number of planned sites were dropped from the transect due to problems with site accessibility leaving data gaps in parts of the transect. The largest of these gaps spans ∼7 km between sites 322 and 326.

Figure 5.7 presents phase tensor pseudo sections before and after data masking for west transect MT sites projected onto the transect line shown in figure 5.6. Here, phase tensor ellipses for each period are coloured by their respective absolute skew angle values ($|\beta|$), providing a means of estimating their dimensionality. The influence of 50 Hz noise on the western two thirds of the data set is visible as highly elliptical, highly skewed, irregularly oriented phase ellipses at periods between 10^{-2} s to 10^{-1} s. Masking these noisy periods as well as periods where $|\beta| > 5°$ yielded the final data set in the bottom plot.

A high proportion of the west transect data set was masked due to large skew angles. This is particularly the case for periods greater than 10 s in the western third of the transect, and will necessarily reduce depth sensitivity of the data in this region when applied 2D inversion.

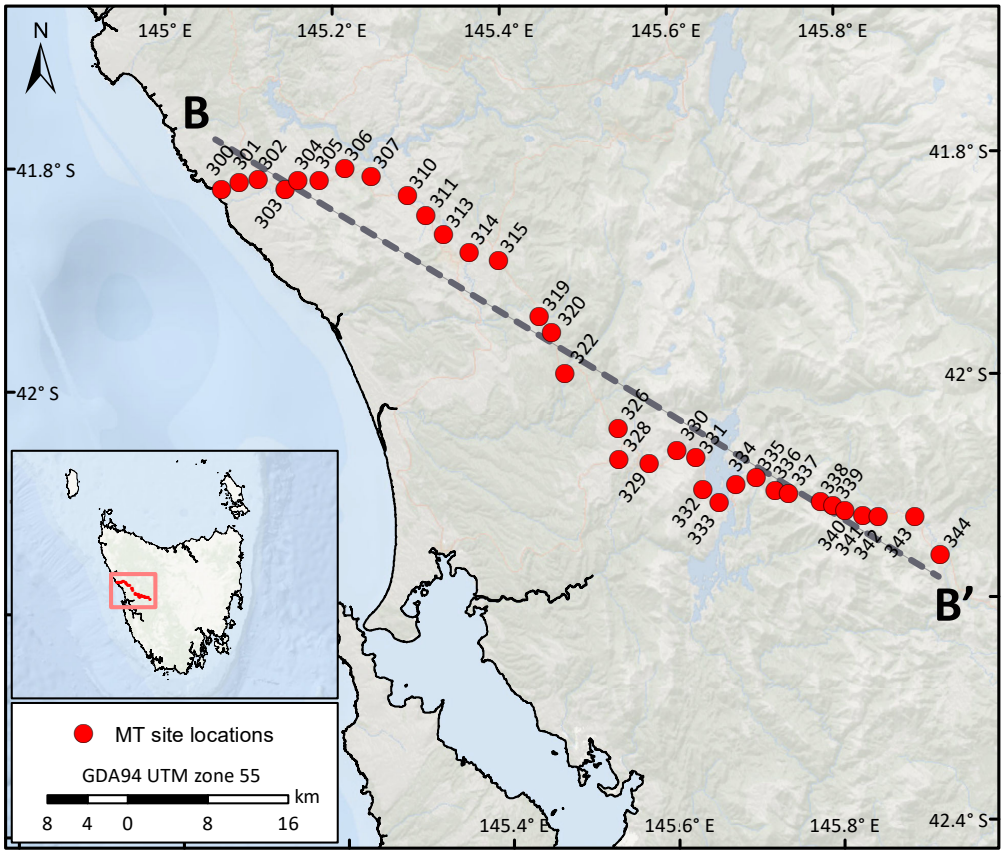

Figure 5.6: Context map depicting west transect MT sites overlain onto hillshaded topography basemap. The dashed line represents the location of 2D inverse model derived from inversion.

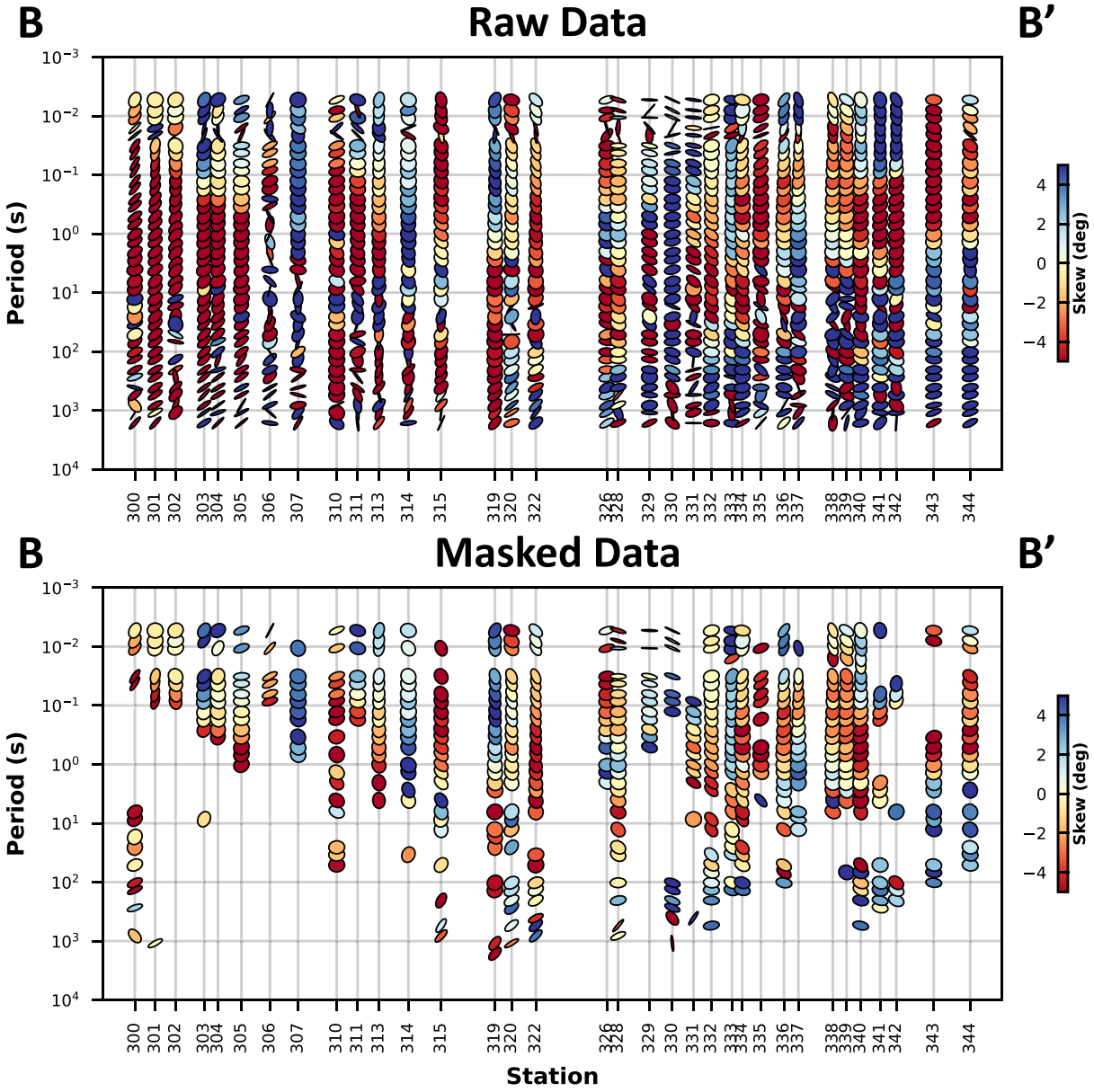

Figure 5.7: Phase tensor pseudosections depicting phase tensor ellipses for each period in the west transect broadband data set before and after data masking. Highly irregular phase tensors with large skew angles at periods in the range 0.01 s to 0.1 s in the uppermost plot reflect noisy impedance tensor estimates due to the influence of 50 Hz power line noise on the data set. This affected sites to the west of site 332 to a greater degreee as they were deployed closer to power line infrastructure. Masking of this 50 Hz noise affected periods and 3D periods on the basis of skew angles, where $|\beta| < 5°$ were excluded, yields the masked data set on the bottom plot. Note that a significant amount of data in the western end of the transect has been masked out due to increasingly 3D geoelectric structure.

Geoelectric strike analysis was conducted on the masked data set, and yielded the rose plots shown in Figure 5.8. Strike angles were computed from the phase tensor, and have an inherent 90° ambiguity giving rise to the cross-shaped rose plot patterns. Erratic strike angles computed for shorter periods (<1 s) are indicative of local-scale 3D geoelectric structures, the influence of which diminishes at longer periods. At periods greater than 1 s, a coherent regional geoelectric strike angle emerges, and a strike angle of 45.0° from N was selected for data rotation on the basis of descriptive statistics shown in Table. 5.1. The 90° ambiguity in strike angle was resolved by analysis of magnetic structures in the survey area, which tend to strike in an orientation closer to 45.0° from north than its orthogonal angle.

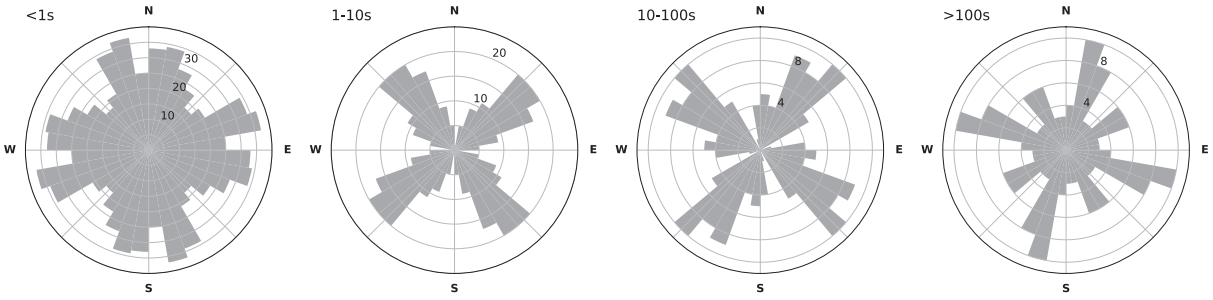

Figure 5.8: Rose diagrams depicting geoelectric strike angles derived from west transect phase tensors after data masking.

Total values	Minimum	Maximum	Median	Mean	Standard Deviation
299	0.1°	89.9°	44.9°	45.0°	23.6°

Table 5.1: Summary statistics for west transect geoelectric strike angles between 0° to 90° for periods <0.1 s. Shorter periods were not included here in order to emphasise regional, and thus longer period geoelectric strike angles that are common across the transect. The mean strike here was taken as the favoured direction on the basis of aeromagnetic imagery shown in Figure 5.9.

Figure 5.9 presents phase tensor ellipses for the masked west transect data set overlain onto total magnetic intensity images for various periods. Ellipses are coloured by minimum phase angle, and provide a qualitative measure of subsurface resistivity structure as phases <45° (coloured blue) and phases >45° (coloured red) indicate resistivity is increasing and decreasing with depth, respectively. Low minimum phase angles in the central portion of the transect, consistent with a north-south trending magnetic high, are a consistent feature across the period range of the data. This indicates resistivity is consistently increasing with depth in this region. The opposite is true to the east of this location, where resistivities appear to be decreasing with depth across the period range of the data.

The depth sensitivity of the masked data set is described in Figures 5.10 and 5.11. The majority of stations have minimum signal penetrations depths <1 km, providing good data sensitivity to upper crustal geoelectric structure. Maximum signal penetration depths vary greatly across the transect, with the western third of the transect having maximum signal

penetration depths of ∼10 km as a result of heavy masking at longer periods where the data have absolute skew angles (β) greater than 5° indicative of highly 3-dimensional geoelectric structure, hereby referred to as 'highly 3D', which cannot be resolved by 2D modelling methods. This should be kept in mind when interpreting geoelectric structure beneath this portion of the transect. Elsewhere the maximum signal penetration depth allows for interpretation of model structure to depths of about 20 km or so.

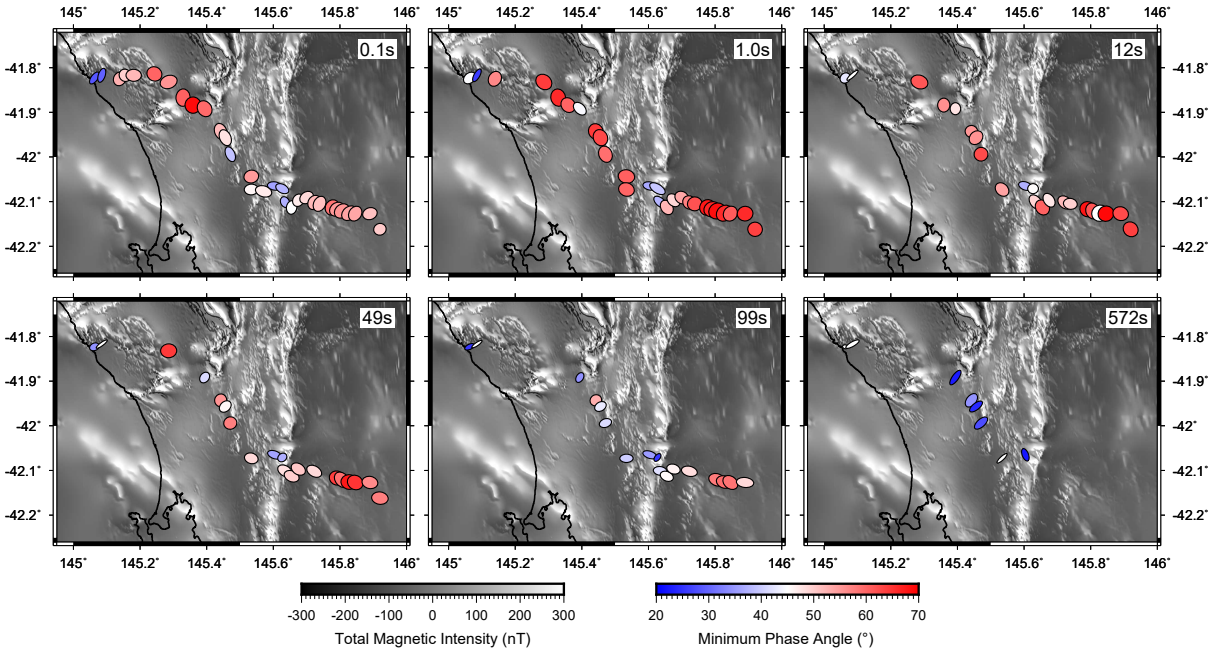

Figure 5.9: Phase ellipses for the west transect coloured by minimum phase angle plotted on total magnetic intensity data. Data masked for noise and dimensionality on the basis of skew angles prior to plotting.

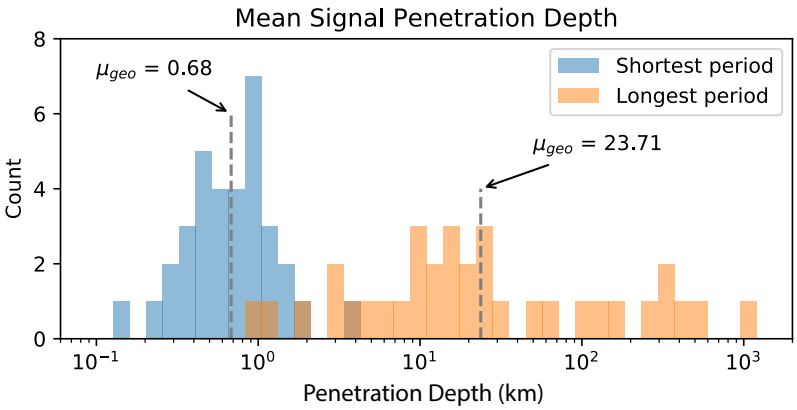

Figure 5.10: Histogram depicting the distribution of mean signal penetration depths for the shortest and longest period of each west transect MT sites after data masking for noise and 3-dimensionality. Depths were computed by way of the Niblett-Bostick transformation implemented in MTpy. For a spatial representation of signal penetration data see Figure 5.11.

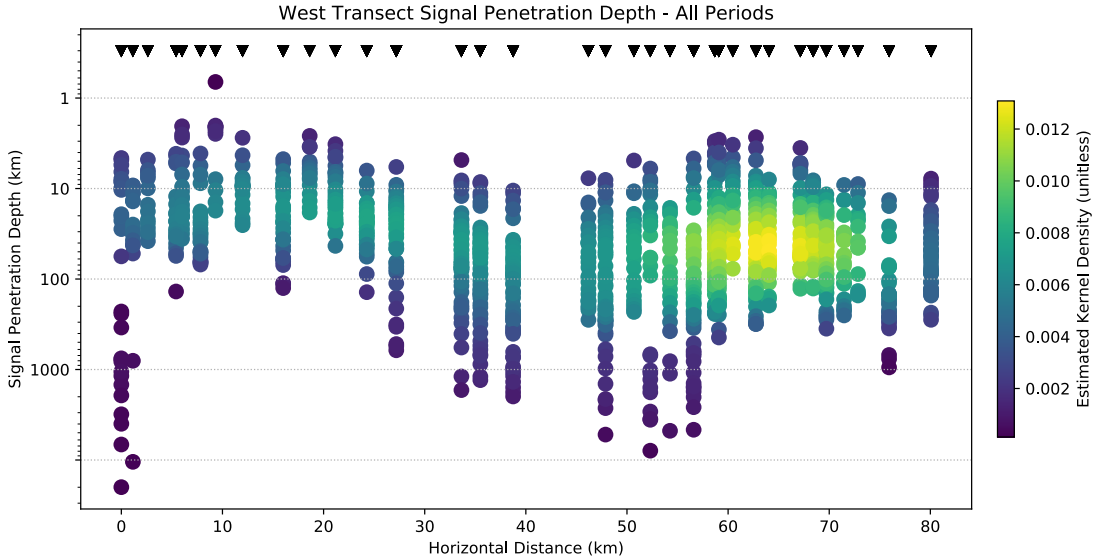

Figure 5.11: Signal penetration depth section for the west transect after masking. Each point represents an average penetration depth estimate for a given period. Sites are depicted as triangles projected to arbitrary depth. Points are coloured by a Gaussian kernel density estimate computed in log space for penetration depths, and provides a visual means of assessing data sensitivity beneath the transect. Yellow colours represent regions of the transect to which the data is highly sensitive, while blue colours represent regions with lower data sensitivity. Transect data are insensitive to regions devoid of points, such as at depths greater than ∼10 km in the western third of the transect.

5.4 West Transect 2D Inversion Results

Broadband MT transects were inverted to produce 2D resistivity models using OCCAM2D, a rectangular mesh finite element MT inversion algorithm [Constable et al., 1987, DeGroot-Hedlin and Constable, 1990]. Input files for inversion were generated using Python scripts relying on the MTpy library of codes, and all computation was completed on a desktop PC. Given the simplified 2D nature of the inverse problem, computational requirements are orders of magnitude less than that of 3D inverse modelling with a typical inversion taking 1 to 6 hours to converge. As noted above, all data were masked to minimise the impact of noisy periods as well as 3-dimensionality, and were rotated to geoelectric strike prior to inversion.

Rotated and masked west transect data were used to generate a 2D profile of best fit onto which MT sites were projected for inversion (see Fig. 5.6). Input files for inversion in OCCAM2D include a mesh file defining the configuration of the finite element model space, a model file containing *a priori* resistivity structure information and a data file containing impedance tensor information along the profile. It should be noted that conductive sea water was not included as *a priori* structure in these 2D inverse models. This differs from the statewide AusLAMP 3D models, though given the high-frequency nature of the broadband data it is unlikely that this contributes erroneous structure to the inversion results.

An initial surface cell width of 300 m was selected for the west transect finite element mesh. It was found that this led to finite element meshes that exceeded the memory limitations of the code necessitating an increase to a minimum cell width of 375 m for the inversion to proceed. Horizontal resolution of 375 m equates to approximately 1/6 the site spacing along the transect, and is fine enough to ensure the rectangular mesh does not constrain the morphology of smooth geoelectric structures fitted to the data that might give rise to high misfit. Padding cells in the horizontal plane were used to extend the model space boundaries some ∼70 km from the data set in an effort to mitigate boundary condition artefacts. This was achieved in the vertical plane by setting a maximum depth to 1084 km. Table 5.2 summarises the mesh parameters used in the final west transect model.

Cell width	**1st Layer Thickness**	***N* Layers**	**Max Depth**	***N* Padding Cells**
375 m	50 m	100	1084 km	8

Table 5.2: Mesh parameters for the west transect OCCAM2D inversion.

OCCAM2D format data files were generated from EDI files containing masked and rotated impedance tensor information. This involved the addition of error floors to apparent resistivity and phase components of the impedance tensor. Errors floors of 20% for apparent resistivity and 10% for phase were used. Larger error floors for apparent resistivity were selected so as to limit the effects of static shifts in the data by effectively weighting this component of the impedance tensor lower than the phase. All inverse modelling involved jointly inverting the

transverse magnetic and transverse electric modes. Table 5.3 below presents a summary of the data file used in 2D inversion.

N **Periods** (T)	**Min** T	**Max** T	N **Data Points**	ρ_a **Err Floor**	Φ **Err Floor**
37	0.005 s	1600 s	2954	20%	10%

Table 5.3: OCCAM2D data file parameters for the west transect inversion.

2D inversion with OCCAM2D involves a two step process involving a model misfit minimisation step followed by a model roughness minimisation step. The first step involves the selection of a low target RMS misfit (1.0) and proceeding with inversion iterations until a minimum misfit is reached. Inversion is then restarted on this minimum misfit iteration with a slightly higher (10% higher in this case) target misfit selected, allowing OCCAM2D to search for the minimum model roughness.

This two step inversion procedure was repeated for several inversion runs using the same data and mesh parameters while varying the starting resistivity in the model file. This was done to test the sensitivity to varying starting conditions. In the first inversion step, west transect inversions converged on minimum RMS misfit values of 2. Restarting inversions with a new target RMS misfit values 10% greater than the minimum for each inversion allowed inversions to minimise roughness yielding the inverse models presented in Figure 5.12. The persistence of near-identical resistivity distributions in the resultant models imply a high degree of model robustness.

Figure 5.13 presents a section of the preferred model spanning the depth range of the lithosphere. It should be noted that the highly resistive wedge in the deeper parts of the western corner of the model space is unresolved as it is beyond the depth sensitivity of the data as depicted by Figure 5.11. This effect is replicated in the shallow surface central to the data set, suggesting inversion favours high resistivities in regions of low data sensitivity. Overall model fit is good with predicted and observed responses typified by those observed in Figures 5.14 and 5.15.

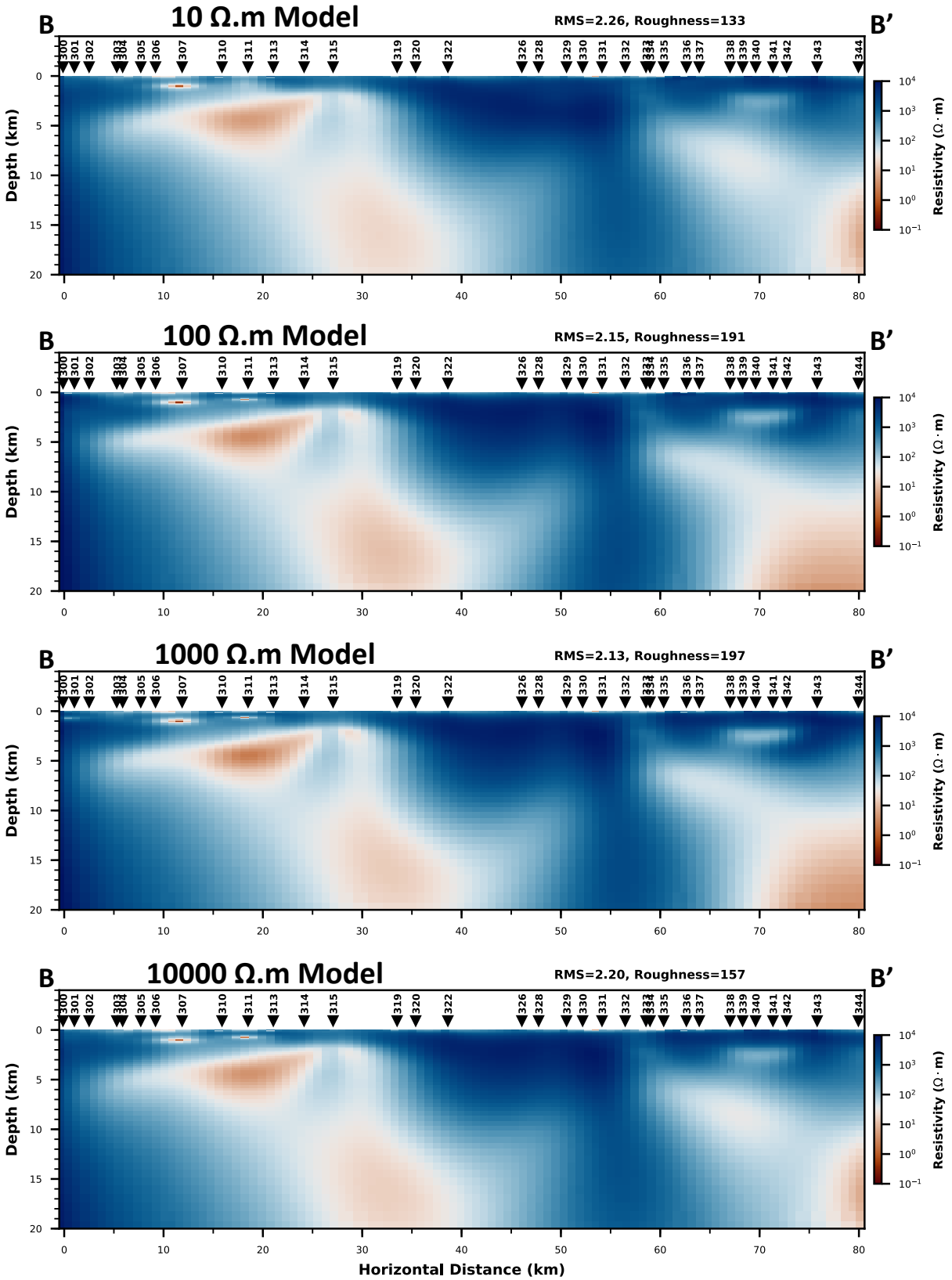

Figure 5.12: Crustal sections from west transect inverse models with different starting resistivities. Of these four models, the model with a 100 Ω m starting resistivity was selected for further interpretation and analysis.

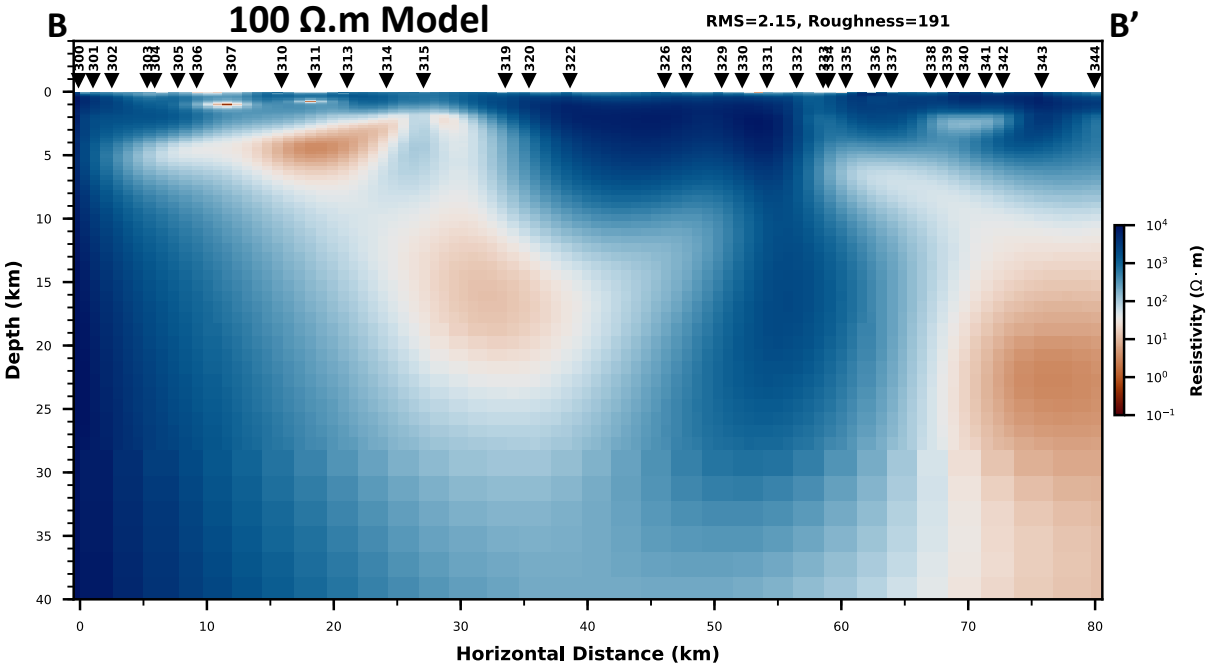

Figure 5.13: Upper lithospheric section from the preferred west transect inverse model derived from a starting resistivity of 100 Ω m.

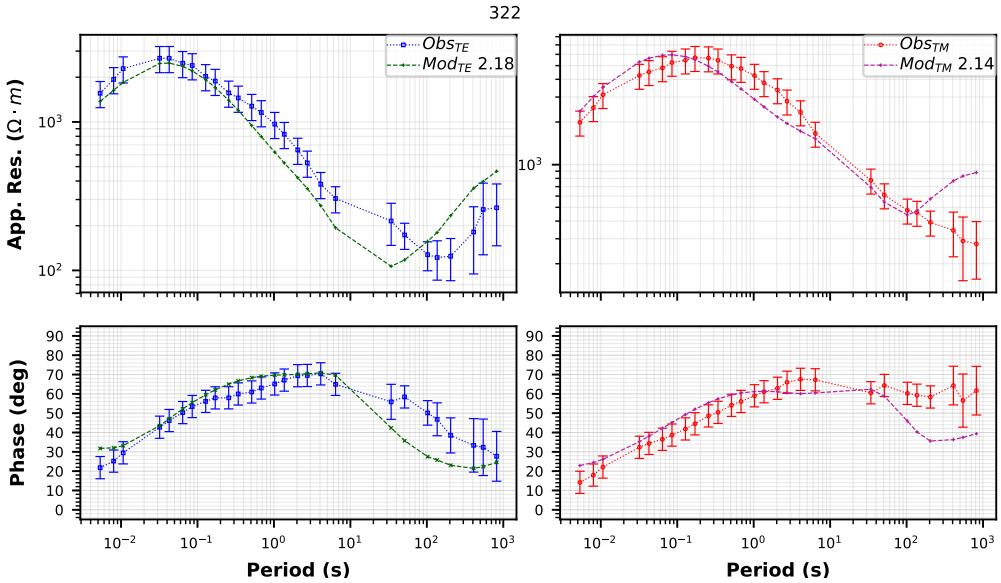

Figure 5.14: Observed data and preferred model response data for west transect site 322. This site is typical of sites in the west transect, with good model fit at shorter periods relative to longer, typically more noisy, periods.

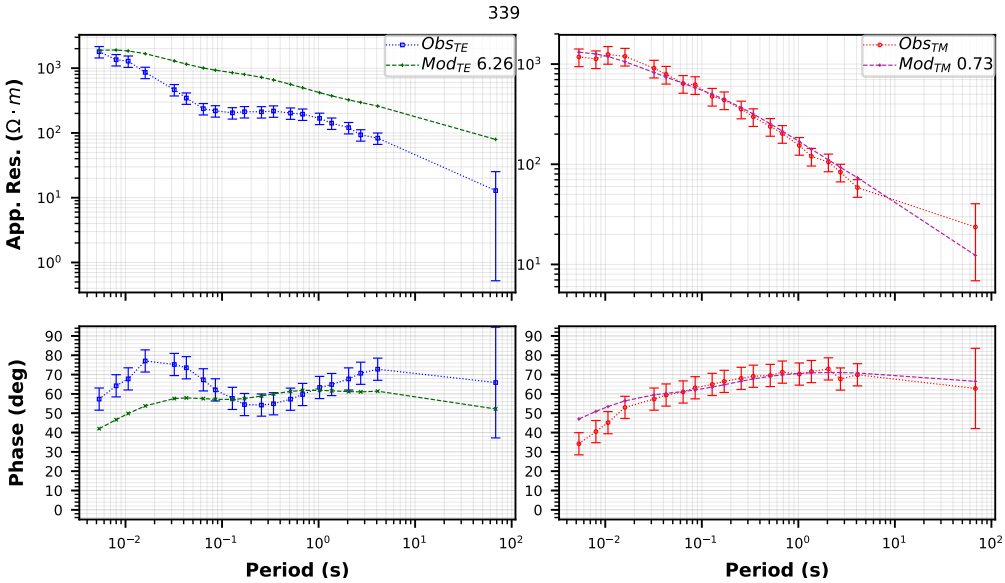

Figure 5.15: Observed data and preferred model response data for west transect site 339. This site is poorly fitted in the TE mode, with apparent resistivity model responses significantly offset from the observed response. This is likely the result of inversion being unable to fit static shifts inherent in the data. Reader is referred to Appendix D for similar plots for all western transect MT sites.

5.5 Discussion and Interpretation

Interpretation of the preferred west transect inverse model was conducted with the aid of 3D visualisation software packages SKUA-GOCAD and Mira Geoscience Analyst. The model was converted from OCCAM2D inverse model output format to an ASCII text file containing spatial information in GDA94 UTM zone 55 coordinates for import into visualisation software and interpretation together with existing geophysical and geological information. Figure 5.17 presents a view of the final west transect model projected in 3D space and gives context to subsequent 3D views presented here. Figure 5.16 presents western transect MT site locations plotted on a 1:250,000 scale geological map for further geological context.

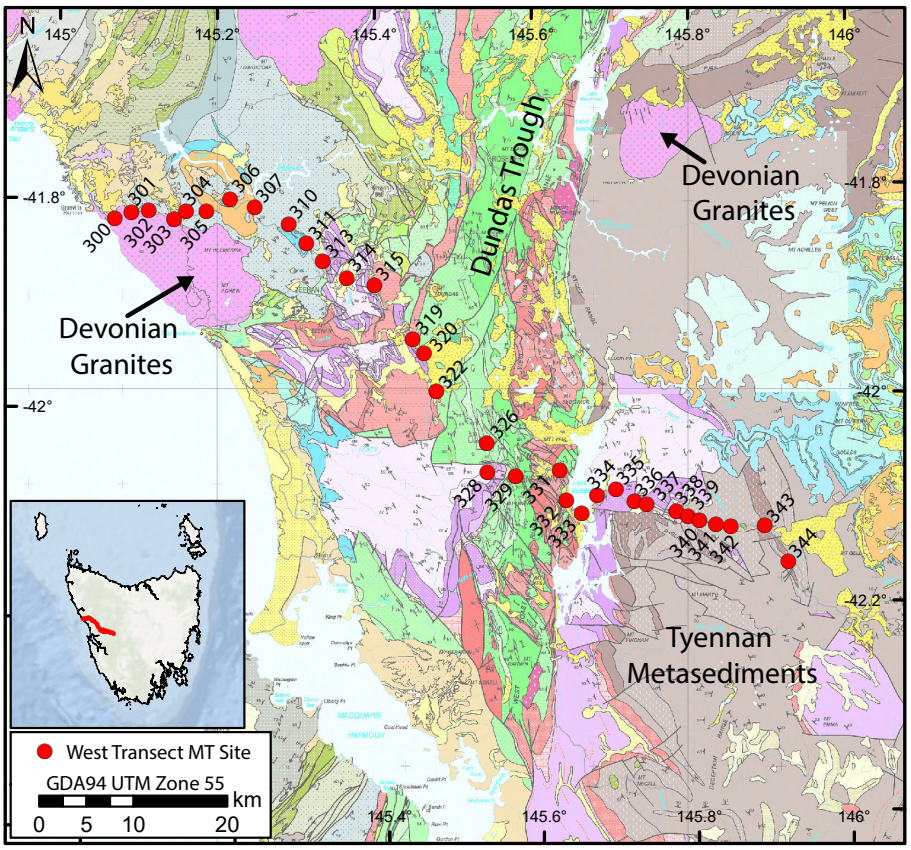

Figure 5.16: West transect MT site locations on 1:250,000 scale geology map [Mineral Resources Tasmania, 2011]. Annotations highlight site numbers and major geological domains discussed in text.

Geological interpretation of the preferred west transect inverse model was significantly aided by direct comparison of model structures with inferred geologic structure taken from Mineral Resources Tasmania's West Tasmania 3D Geological and Geophysical model [Mineral Resources Tasmania, 2019b].

The west transect preferred model reveals significant resistivity structure in the upper crust within the sensitivity range of the data. In the western third of the transect, where depth sensitivities range from ∼0.5 km to ∼8 km, the preferred inverse model images a series of small,

shallow, low resistivity zones underlain by a single, shallowly west-dipping zone with low resistivities in the order of $\sim 10\,\Omega\,\mathrm{m}$.

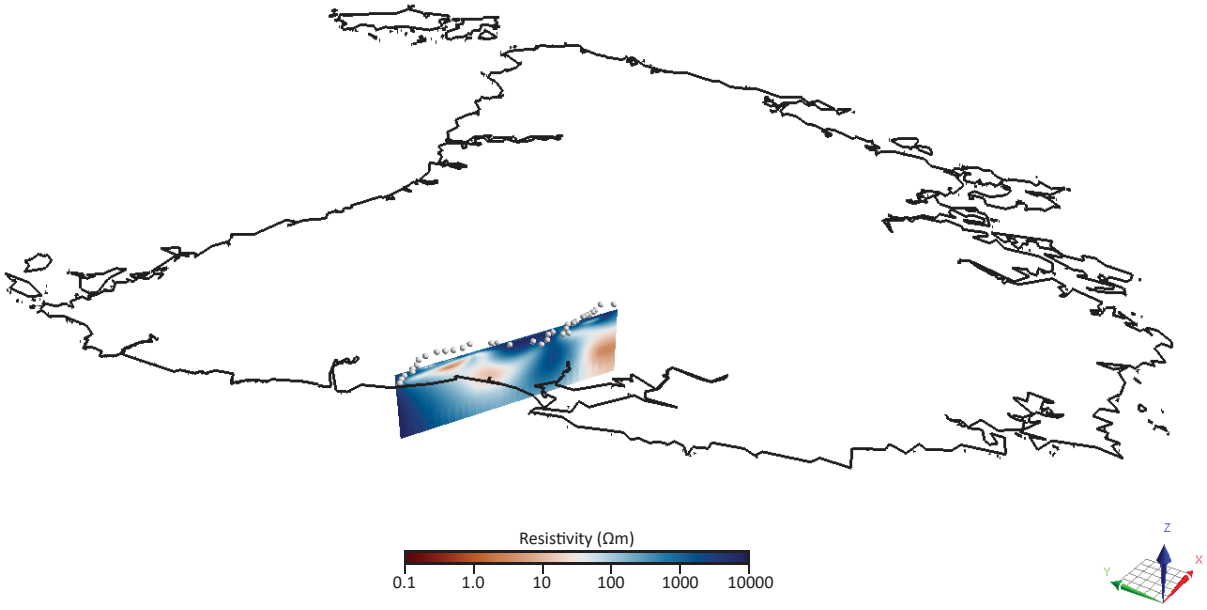

Figure 5.17: Parallel projected view from the south west of final inverse model projected in 3D space with the Tasmanian coastline for context. The model is clipped to a maximum depth of 38.23 km (the first mesh node above 40 km), and plots below gray spheres representing MT sites used in inversion.

When compared to geological model structures taken from the West Tasmania 3D Geological Model [Mineral Resources Tasmania, 2019b], the small, shallow low resistivity zones in the west of the transect appear to correlate with thin, fault-bounded slivers of pervasively serpentinised Cambrian mafic-ultramafic rocks. As serpentinisation tends to decrease resistivities by up to two orders of magnitude [Kawano et al., 2012], it is likely that this correlation is causal. The larger, deeper west-dipping low resistivity zone is imaged within Devonian granite and is roughly coincident with the Brickfield fault, which pierces the granite and is likely responsible for fault-related porosity increases giving rise to bulk resistivity reductions (see Figs. 5.19 and 5.20).

The central third of the model space is characterised by higher resistivities at shallow levels relative to the rest of the model space. This is underlain by a lower crustal low resistivity zone that is linked to the near-surface further to the east by a subtle west-dipping structure projecting to the surface at about 55 km along the profile, a region roughly coincident with significant copper mineralisation in the Lyell mineral field. The spatial correlation with both mineralisation at surface and the major west-dipping crustal faults (the Great Lyell and King River faults) likely reflects a causal relationship, and shares commonalities with similar structures observed beneath IOCG deposits in South Australia [Heinson et al., 2018, Robertson et al., 2017]. West dipping low resistivity structures likely represent relict fluid pathways through which fluids potentially associated with mineralisation percolated, an analysis which is partly supported by the apparent lack of Devonian granitoid intrusion in the area, as such a process would have

likely overprinted older Cambrian resistivity structures.

Electrical structure in the easternmost third of the model space is characterised by a broad region of low resistivity plotting below 10 km in the model space. This low resistivity zone is located beneath Mesoproterozoic and Neoproterozoic basement rocks of the Tyennan block, and is linked to the surface by moderately east-dipping low resistivity structure outcropping near the surface boundary between the Tyennan and Dundas-Fossey Trough tectonic elements. Low resistivities beneath the Tyennan block near this tectonic element boundary is likely attributable the transmission of metamorphic fluids associated with collision during the Tyennan Orogeny, a process that resulted in numerous blueschist to eclogite facies metamorphic complexes being emplaced along the western margin of the Tyennan block.

In contrast to the north transect, the preferred west transect model agrees quite well with regional scale AusLAMP inverse models from the area as shown in Figure 5.21. The broad scale transition from low resistivities, to high resistivities to moderate resistivities from west to east is replicated at lower resolution by the AusLAMP model and serves to further support the overall robustness of west transect 2D inverse models.

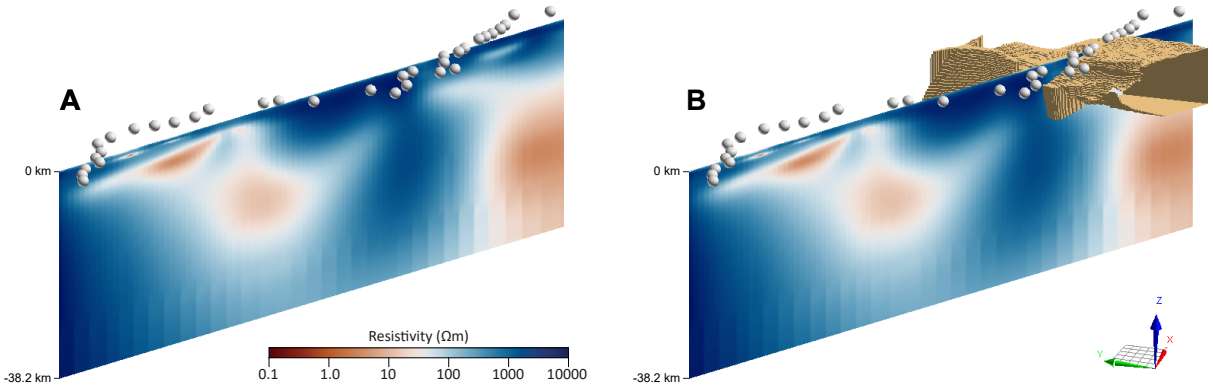

Figure 5.18: 3D view of parallel projected views of west transect region taken from GOCAD 3D viewing software. Panel A presents the final model clipped to a maximum depth of 38.23 km, while panel B presents the same model with Proterozoic Tyennan basement rocks (straw coloured volume) taken from the West Tasmania 3D geology model [Mineral Resources Tasmania, 2019b].

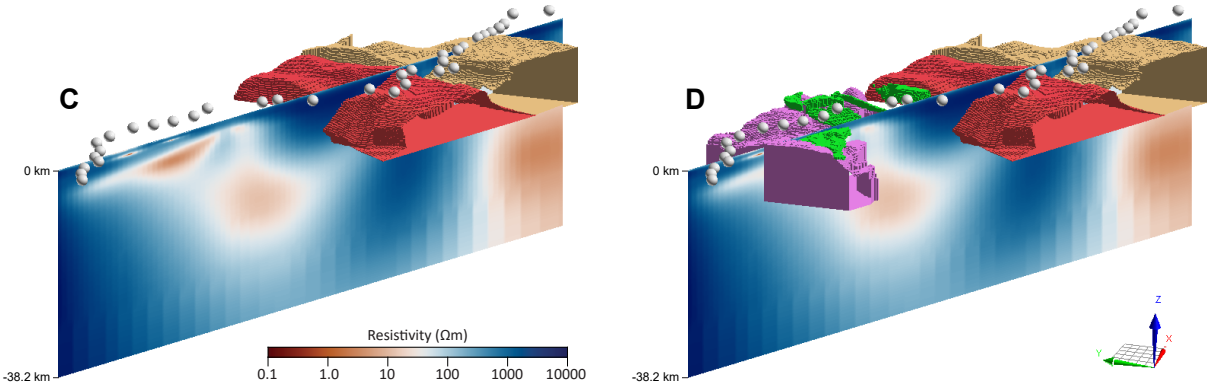

Figure 5.19: 3D views with orientation identical to that in Figure 5.18. Panel C presents the preferred model with Proterozoic Tyennan basement rocks (straw), and Cambrian granites (in red colours). Cambrian mafic-ultramafic rocks (green) and Devonian granites (pink) are added in Panel D.

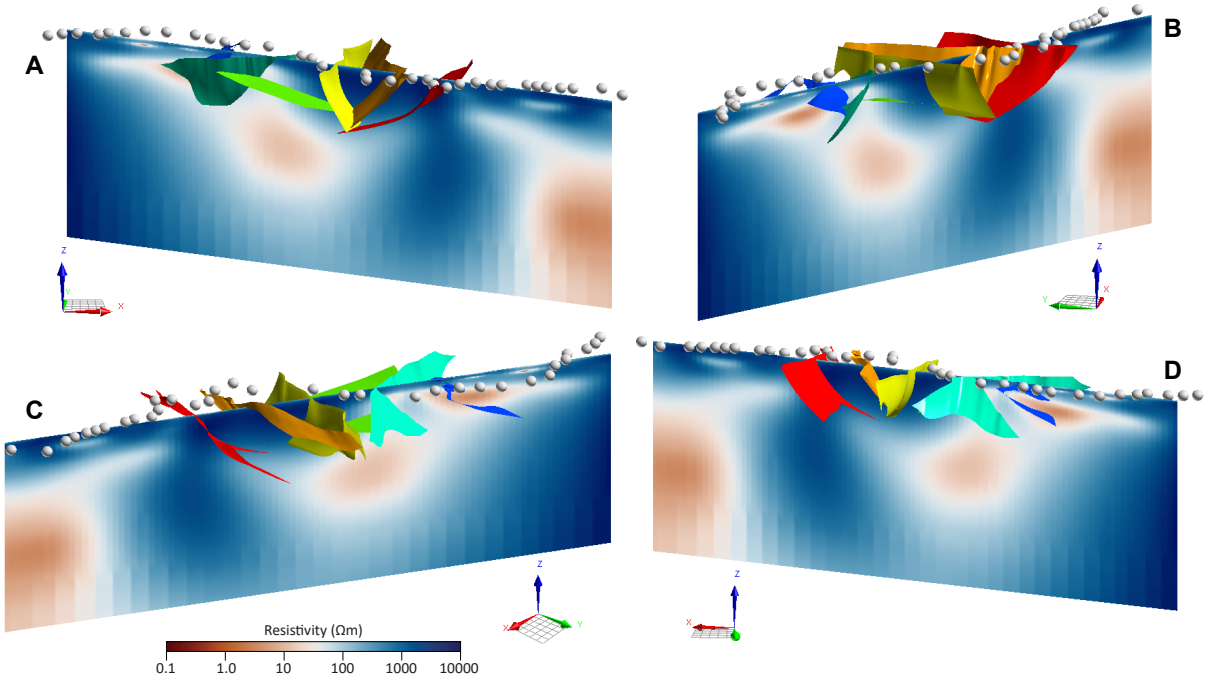

Figure 5.20: 3D views of parallel projected west transect model with major cross cutting faults from the West Tasmania 3D geology model. Panels vary in their orientations with panel A looking north, B looking east, C looking south west, and D looking south. Faults are differentiated on the basis of colour, with the King River Fault in red, Great Lyell Fault in orange, Henty Fault in yellow, Rosebery Fault (inferred) in green, Little Henty Fault in cyan and the Brickfield Fault in blue. As with the model views in Fig. 5.19, the west transect model spans a depth range of 0 km to 38.2 km.

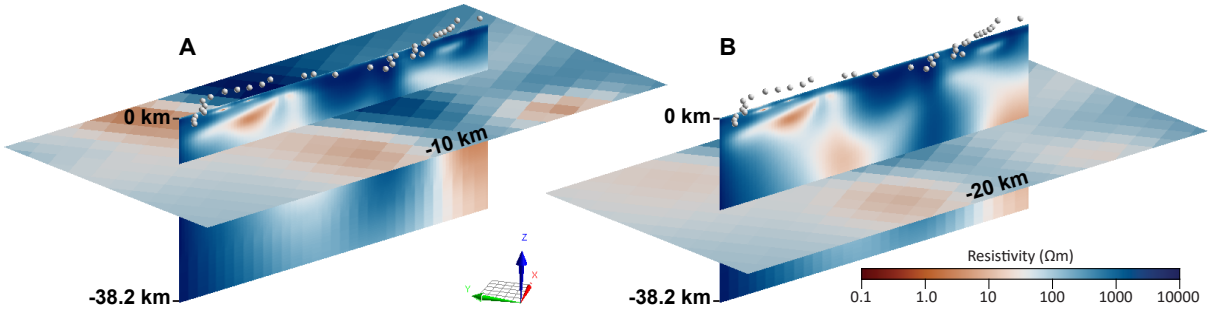

Figure 5.21: 3D views of parallel projected west transect with horizontal depth slices through the preferred AusLAMP 3D model. Panel A depicts a 10 km depth slice through the AusLAMP model while panel B presents a 20 km depth slice. Colour scales are adjusted for direct comparison between the two models.

5.6 Conclusion and Recommendations

The north transect was significantly affected by cultural noise to the extent that impedance tensors sensitive to the shallow surface could not be recovered. Characterising the geoelectric structure of the shallow surface along this transect line would prove difficult with passive survey methods given the degree to which the area is affected by power line noise. Airborne EM methods may be capable of resolving the uppermost geoelectric structure, and Controlled Source Audio-frequency Magnetotelluric (CSAMT) surveys may be able to extend the depth of investigation further still, but it is recommended that any future surveys in the region secure access to field sites at least 2 km from power lines parallel with Wilmot Road. This presents a logistic challenge in an area that is both heavily forested, and home to a significant rural population.

The west transect was less affected by cultural noise than the north transect, allowing for the recovery of most high frequency impedance tensor estimations. However, highly 3D data at longer periods, especially for the western third of the transect, limited the maximum depth sensitivity of much of the data set to ∼10 km. 2D inverse modelling yielded significant upper crustal geoelectric structure, with several low resistivity zones correlating with known geology as described by the West Tasmania 3D Geological Model [Mineral Resources Tasmania, 2019b].

Small scale, shallow surface low resistivity zones in the west of the transect appear to image fault bounded serpentinised Cambrian mafic-ultramafic rocks, while linear lower resistivity features in the western and central thirds of the model space appear to image major crustal faults. Major faults in the central and eastern thirds of the model space appear to link to deeper, lower crustal low resistivity zones suggesting a causal relationship likely related to metasomatism of lower crustal rocks and fluid focusing to shallower levels in the brittle crust.

Low resistivities in the east of the transect observed at lower crustal levels beneath Proterozoic Tyennan basement likely represents preserved metamorphic fluid pathways associated with Cambrian metamorphism along the western boundary of the Tyennan block during the Tyennan Orogeny. The preferred west transect model appears to be in agreement with the regional scale 3D resistivity model derived from the AusLAMP survey. There is reasonable potential for the inclusion of regional-scale resistivity information from the AusLAMP model as *a priori* in a 3D modelling exercise to extract further value from the data set, especially in the far western region of the transect where highly 3D data precluded inverse modelling in 2D. However, given the considerable investment in computational resources and time required to complete such an undertaking, 3D inversion of the west transect is beyond the scope of the current project.

Chapter 6

Combined Broadband and Long Period 3D Models for the Midlands of Tasmania

KUTh Energy Ltd (KUTh) conducted an extensive exploration campaign, starting in 2007, across eastern Tasmania to locate geothermal resources suitable for development as Enhanced Geothermal System (EGS) electric power generation. EGS differ from hydrothermal geothermal systems in that they involve artificial porosity enhancement of a body of radiogenically heated rock by way of subsurface fracturing in order to increase the rate at which thermal energy can be extracted through a network of fluid injection and extraction wells. KUTh's EGS exploration campaign sought to target hot Devonian granite bodies insulated by Permo-Triassic Tasmania Basin sediments, and exploited a number of geophysical methods to image beneath the Tasmania Basin cover.

Several data sets were acquired throughout the KUTh exploration campaign at varying scales of investigation. Regional-scale potential field data sets include two gravity surveys used to update gravity-derived geologic models for Tasmanian granitoids of Leaman and Richardson [2003]. Granite surface modelling results from the first survey were reported in Leaman [2007], which were superseded in Leaman [2012] following the completion of the second survey. In addition, a 200 m line spacing aeromagnetic survey was flown in 2009 to improve on previous 1.5 km line spacing aeromagnetic data sets flown by the AGSO in 1985. Joint interpretations of this new magnetic data set with gravity data and high resolution digital elevation models enabled the delineation of major fault and fracture systems reported in Godber and Reid [2009]. Other regional data sets include surface heat flow and thermal conductivity data acquired between 2007 and 2008 in a 20 km by 20 km grid pattern shallow surface drilling program, the results of which are discussed by Holgate et al. [2010].

Geothermal resource analyses conducted on the regional heat flow data set yielded an in-

ferred geothermal resource in the Lemont area, and a second geothermal prospect in the Fingal area in northeastern Tasmania. The Lemont resource, outlined in Figure 6.1, was the subject of a tenement-scale ambient seismic survey conducted between 2009 and 2010, yielding three dimensional (3D) shear wave velocity models with a relatively subtle variation in the model space [Holgate, 2011].

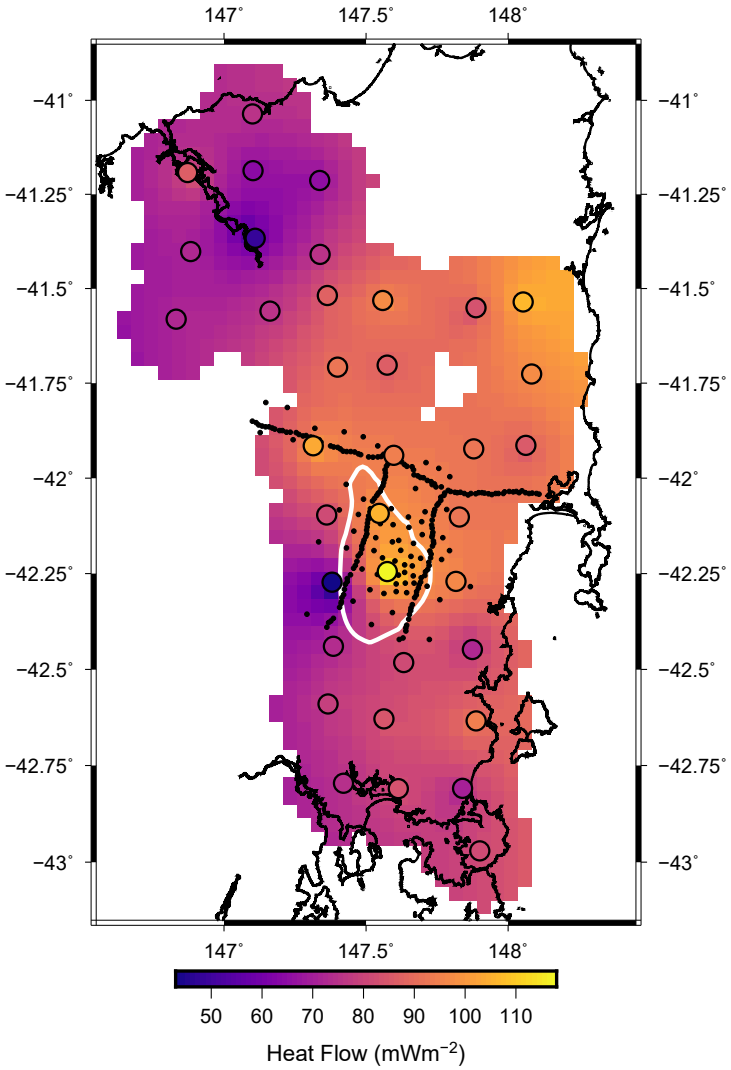

Figure 6.1: Gridded heat flow data for eastern Tasmania taken from KUTh Exploration Ltd drill holes plotted as coloured circles. The Lemont resource is outlined by a white polygon surrounding the Lemont drill hole, which had the highest measured heat flow (118 mW m^{-2}). MT sites acquired around the Lemont resource are plotted as black dots. The majority of MT sites were acquired along traverse lines with the rest located either side of traverses or infilling the region within the Lemont Resource.

Of particular relevance to the research progressed through this thesis is an extensive broad-band magnetotelluric (MT) data set acquired over the Lemont resource between 2008 and 2010 (Fig. 6.1). Early MT acquisition took the form of tightly spaced MT traverses, which were modelled in 2D by the end of 2008. Later acquisition took advantage of newly available 3D MT

inversion schemes and acquired sites in a rough grid pattern infilling gaps between traverses over the Lemont resource. Following the completion of acquisition in 2010 the consulting firm WesternGeco-Geosystem was commissioned to produce a 3D inverse model, the full report for which is presented in Battaglini et al. [2010].

The acquisition of the new long period AusLAMP MT sites in 2016, discussed in Chapter 3, in the vicinity of the Lemont resource presents an opportunity to update the 3D modelling of Lemont MT data set with the addition of longer period data for a greater depth resolution. In addition, utilising regional scale resistivity models derived from previous inversion of the AusLAMP Tasmania data set provides the option of introducing regional resistivity structure as *a priori* information in the inversion.

This chapter presents the outcomes of four alternative 3D modelling exercises incorporating both the Lemont MT and AusLAMP data sets in inversion. Sections 6.1, 6.2 and 6.3 discuss steps taken in collating and preparing data for inversion, present induction arrow plots and analyse the depth sensitivity range of the joint KUTh-AusLAMP data set. Section 6.4 describes the steps taken in 3D inverse modelling, presents the results as depth slices through various final inverse models and makes the case for a preferred model. Finally, section 6.5 presents a geologic interpretation of the preferred model and a comparison with the WesternGeco inverse modelling completed previously.

6.1 Data Assembly

Files originating from the recent and older MT field campaigns utilised in this experiment were processed to a common, EDI, format to allow inverse modelling of the combined datasets. AusLAMP data was processed from time series to EDI format using MatLAB scripts and the BIRRP code of Chave and Thomson [2004] following the procedures outlined in Chapter 4. KUTh MT data sets were downloaded directly from Mineral Resources Tasmania's web portal along with acquisition and processing reports for each of the three field campaign undertaken by the survey contractor; Moombarriga Geoscience. Figure 6.2 presents the locations of all MT sites in the vicinity of the Lemont geothermal resource.

6.1.1 Broadband Data Supplied by KUTh Energy Ltd.

The KUTh data set comprises 255 broadband MT sites acquired over three field seasons between 2008 and 2010. All sites were acquired using modern 24-bit digital data recorders (MTU-5A) and induction coils (MTC-50) manufactured by Phoenix Geophysics, and time series to EDI data processing was conducted using the Phoenix SSMT software package. This differs from the BIRRP code utilised in AusLAMP data processing in that it relies on the robust processing jackknife approach of Jones and Jödicke [1984] to compute the impedance tensor from electric and magnetic field data. In a separate step conducted prior to impedance tensor estimation, the

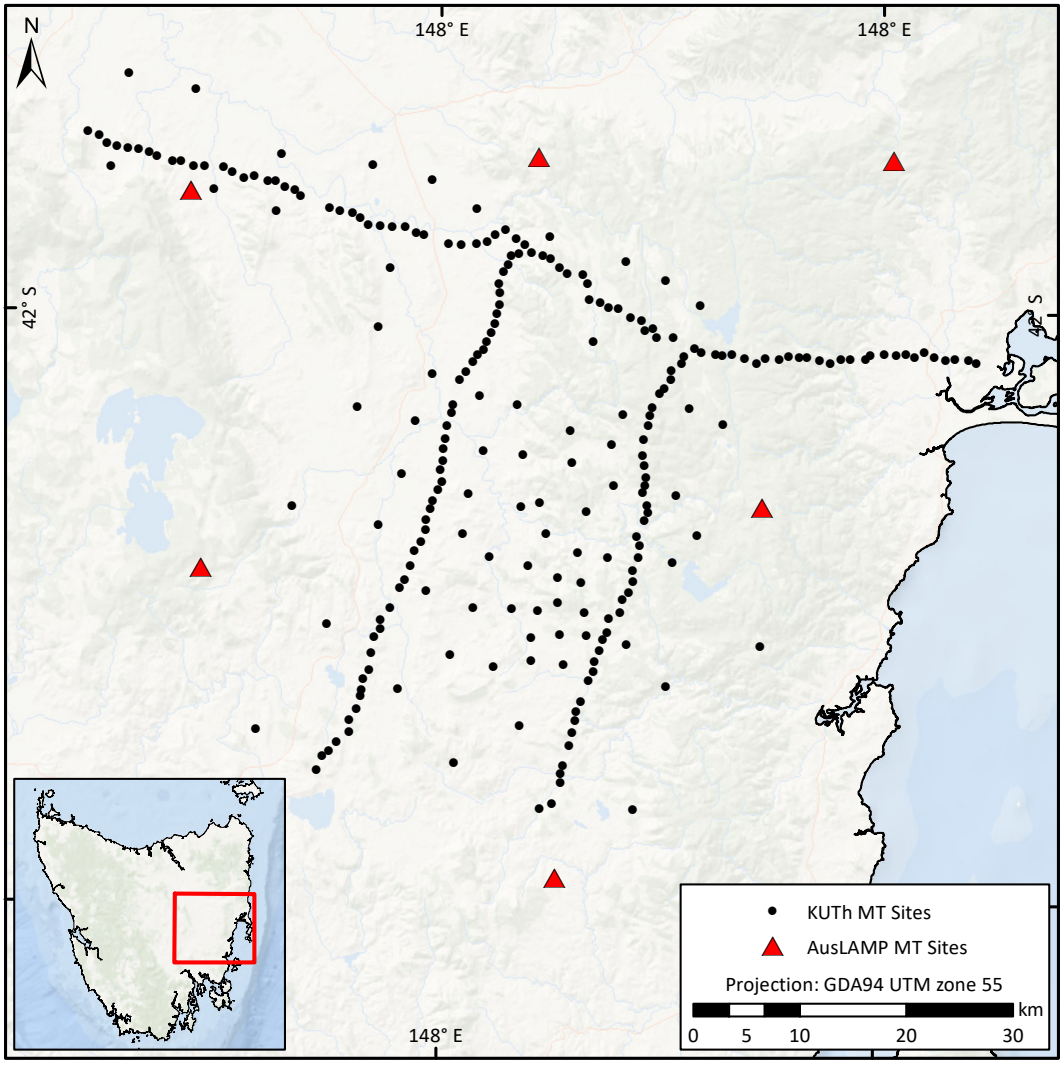

Figure 6.2: The distribution of all 255 KUTh MT sites and nearby AusLAMP long period MT sites.

magnetic field time series is processed alongside magnetic field data from a remote reference site using the processing technique of Gamble et al. [1979]. Final processed MT data were delivered to KUTh in spectral format EDI files containing 80 periods ranging from 0.003 s to 3000 s.

6.1.2 Period Count Considerations

Given that the CPU requirements of the ModEM3DMT inversion code are dependent on the number of periods (T) in the data set, where $CPUs\ required = 2T + 1$, it was important to consider the architecture of the compute power available when constructing the data set for inversion. The Kunanyi HPC cluster utilised in the inversion exercises that follow has 28 cores available per node, thus a period count of 27 was selected for the inversion data set. This enabled the inversion to run on a relatively modest two nodes, limiting the amount of time computing jobs had to wait in the scheduling queue for nodes to become available.

In order to reconcile the 80 period KUTh data set with the 24 period AusLAMP data set for joint inversion, both had to be interpolated onto a new set of 27 periods spanning the period range of the two data sets. This was performed using Python scripts relying on the MTpy library of codes [Krieger and Peacock, 2014], where a set of 27 periods equally spaced in log-space were generated between the shortest period of the KUTh data set (0.003 s) and the longest period of the AusLAMP data set (16,400 s).

6.1.3 Combined Data QA/QC

Following combination and interpolation of the AusLAMP and KUTh data sets into a single common-period data set, a rigorous assessment of data quality was conducted. This involved removal of spatially duplicated and excessively noisy MT sites as well as site-by-site masking of spurious periods. This masking process involved the manual removal of periods where apparent resistivity, phase and tipper values plot outside of the smooth curves assumed to represent the deterministic physics underlying the MT inversion. A final step in preparing the data for inverse modelling involved the removal of tipper data for periods in excess of 8000 s, where the quasi-static assumption begins to break down. Since all AusLAMP sites had noisy impedance tensor data at the longest period (16,400 s) that was masked out, the final data set consisted of 26 periods ranging 0.003 s to 9000 s.

Eleven KUTh MT sites were excluded altogether due to excessively noisy data or co-location with other sites (see Table 6.1). Data quality was generally good with respect to impedance tensor information however tipper data, where present, required heavy masking as it seems to have been affected by a greater degree of noise. In summary, the data quality assessment process yielded a data set encompassing 6 AusLAMP and 244 KUTh sites, 99 of which contained tipper information.

Excluded for excess noise	**Excluded for co-location**
EWA023, EWA024, EWOB05, NSA017, NSA036, NSA047, NSA048, NSB048, SITE03, STL027.	EWA013.

Table 6.1: KUTh MT sites excluded from 3D inverse modelling.

6.2 Induction Arrows

Induction arrows present a means of qualitatively assessing tipper information in MT data. These are typically plotted as arrows representing the vector quantity that is the real component of the tipper data for a given period. When plotted on a map these arrows point toward zones of greater conductance and, due to the skin depth effect, arrows plotted for longer periods reflect deeper geoelectric structure in the Earth.

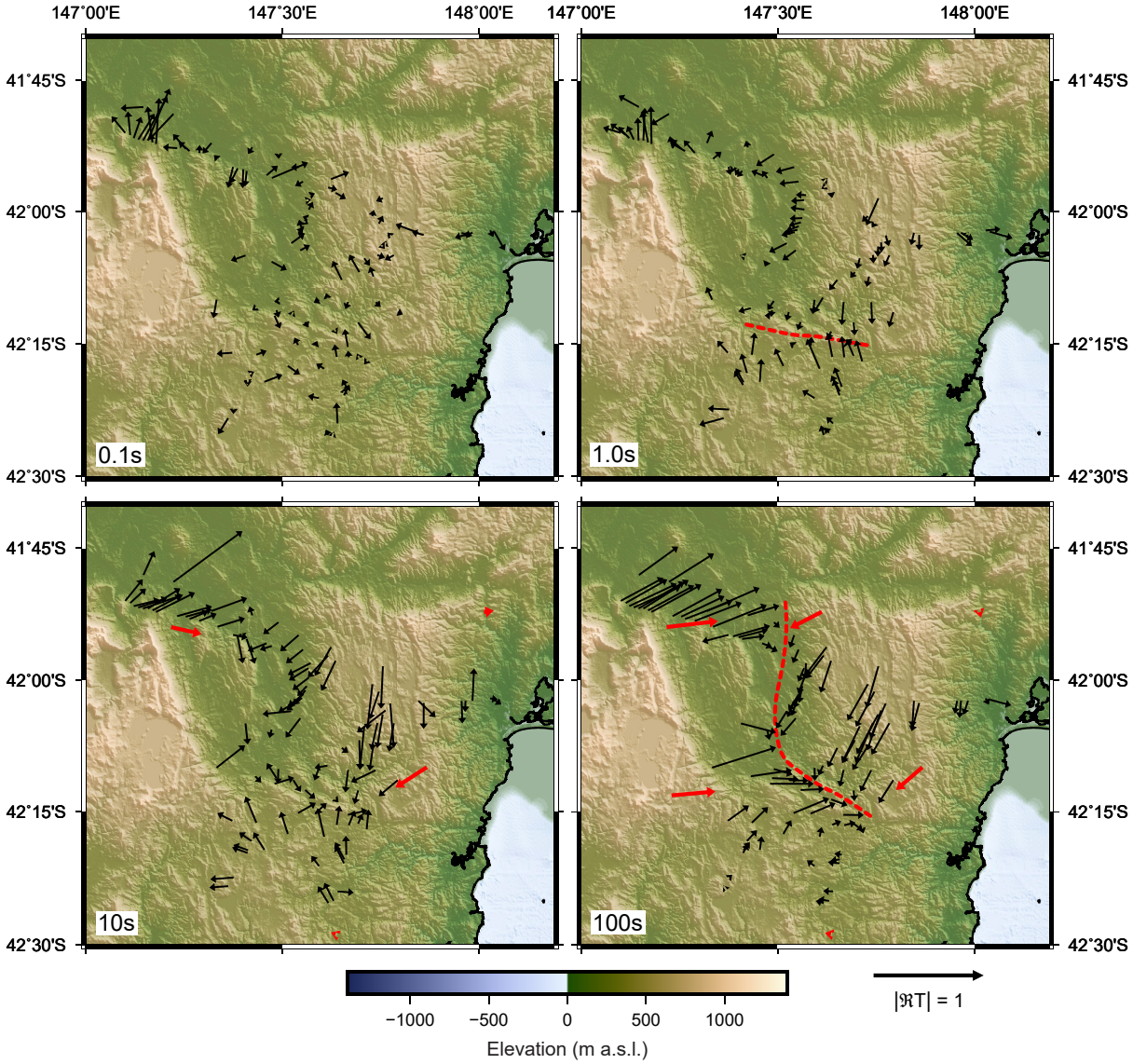

Figure 6.3: Real component induction arrows for MT sites used in the 3D inversions. Black arrows correspond to broadband KUTh MT sites, while red arrows correspond to AusLAMP sites. Arrows are plotted on a 30 m resolution digital surface model gridded from NASA's 1 second SRTM data set [Geoscience Australia, 2011] merged with ∼250 m resolution bathymetry information from the AusBATH2009 data set [Australian Institute of Marine Sciences, 2009]. Dashed red lines depict low resistivity corridors evident at different periods.

Tipper plots for the KUTh MT sites that had sufficiently low-noise tipper information are presented in Figure 6.3. At shorter periods (<1 s) the arrows tend to have small magnitudes and incoherent direction. This reflects the highly variable geoelectric structure of the shallow surface with resistivity heavily influenced by local scale features such as current channelling river valleys. At periods greater than 1 s coherent structures begin to emerge with a east-west trending feature evident at 1 s. At 100 s this feature extends northwestwards before turning northwards and appears to elicit a response from the majority of sites in the data set, including

longer period AusLAMP sites. This low resistivity corridor is reminiscent of induction arrow patterns observed in AusLAMP data presented in Chapter 4 and likely represents the southern extension of the Tamar Conductivity Anomaly in the survey area.

6.3 Depth Sensitivity

Estimation of the depth sensitivity of the data set is important in understanding the depth ranges for which the data can be used to infer geoelectric structure. A common method, the Niblett-Bostick transformation [Jones, 1983], rotates the impedance tensor to obtain minimum and maximum $\mathbf{Z}_{xy}$ and $\mathbf{Z}_{yx}$ for which lower and upper bounds of apparent resistivity can be calculated. Computing the skin depth of the signal using these apparent resistivity values thus yields an estimate of depth sensitivity of the signal. Figure 6.4 presents histograms of these estimates computed for the inversion data set.

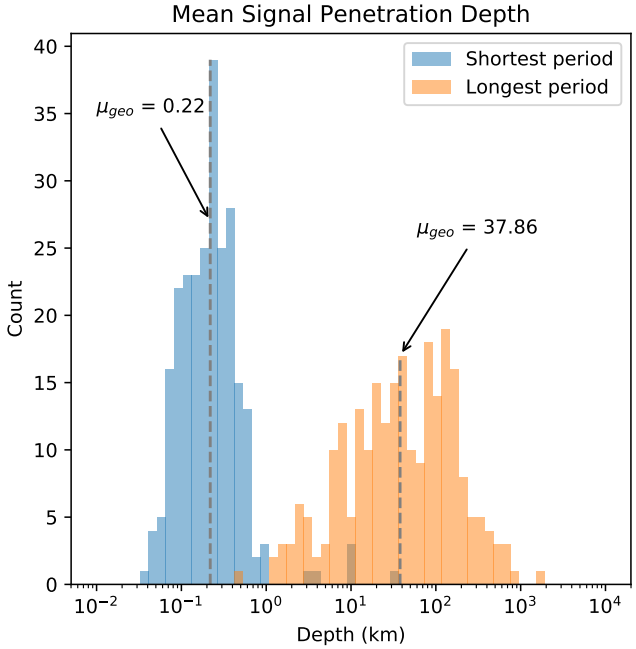

Figure 6.4: Histograms presenting mean depth of penetration for the shortest and longest period of each site in the inversion data set. Depth of penetration was calculated by averaging the minimum and maximum depths of penetration for each period computed by the Niblett-Bostick transformation.

The values of the geometric mean for the average minimum and average maximum penetration depths indicate that the data set is most sensitive to depths ranging from about 200 m to 40 km. The spatial distribution of signal penetration depths is presented in Figure 6.5, where a first order pattern in the distribution of penetration depths is apparent. Shallower minimum signal penetration depths are found for sites in the central west and northwest of the data set, and are broadly coincident with the low-lying, relatively flat topography of the central midlands.

Shallow minimum signal penetration depths are also found for the easternmost sites located around the Swan River Valley, the north trending topographic low evident in the easternmost end of the data set in Figure 6.5. It is likely that low resistivity sediments in these areas are impacting skin depth calculations at short periods, thus reducing the estimated signal penetration values. Maximum signal penetration values tend to increase from west to east, likely reflecting a terrain-scale transition to higher resistivity from west to east.

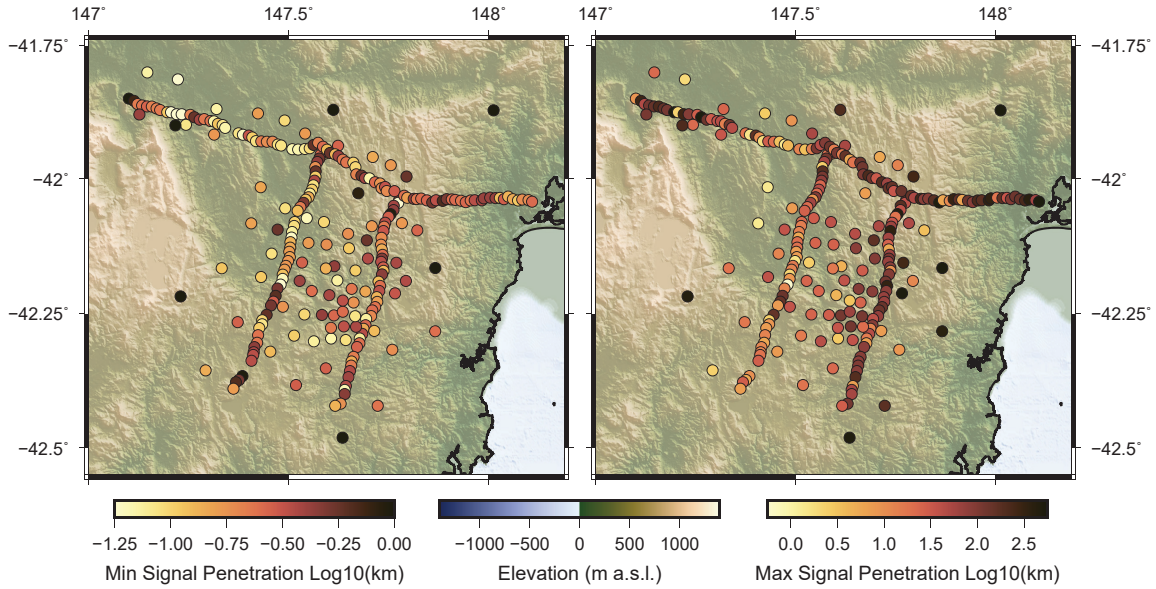

Figure 6.5: MT site locations coloured by signal penetration depths calculated using the Niblett-Bostick transformation for the minimum period, left, and maximum period, right. MT sites are overlain onto NASA's 30m resolution SRTM digital surface model [Geoscience Australia, 2011] with AusBATH2009 bathymetry [Australian Institute of Marine Sciences, 2009].

6.4 3D Modelling

Inverse modelling of the KUTh and AusLAMP data sets were significantly delayed due to limited access to HPC facilities at the University of Tasmania following the inundation of the 'kunanyi' HPC cluster in a May 2018 flooding event. Temporary access to compute power on the OzSTAR HPC cluster at Swinburne University was granted some 4 weeks afterwards, allowing for the commencement of modelling efforts in June 2018.

Initial attempts at inverse modelling using ModEM3DMT on the OzSTAR cluster were hindered by issues surrounding the inclusion of topography in the model space. Inverse models would iterate normally on OzSTAR but would not yield appreciable decreases in global RMS misfit from iteration to iteration. Considerable effort was expended troubleshooting this, including inversion attempts with a subsampled data set and a data set where MT sites were re-located to the centre of mesh cells so as to avoid cell boundary effects.

With the re-commissioning of the kunanyi cluster following the floods in July 2018, access

to the OzSTAR cluster was revoked. At this point the decision to exclude topography from inverse models, for the purpose of the research described in this thesis, was made. Preliminary trials were carried out to find an optimal horizontal mesh resolution for inverse modelling on kunanyi as described in section 6.4.2.

6.4.1 Data Preparation

Preparing the 250-site data set for 3D inversion required the creation of a ModEM3DMT-format data file. This was performed using Python scripts relying on ModEM utility packages within the MTpy library of codes [Krieger and Peacock, 2014]. As with data preparation in Chapter 4, error floors were added to the data so as to avoid over-fitting shallow surface features at the expense of deeper structure. Two inversion data files were generated with differing error floors: 1) a relatively small error floor data file with 10% errors in the impedance tensor and 0.3 error in the tipper and 2) a larger error floor file with 15% impedance error and 0.4 error in tipper data (Tab. 6.2). Error floors for the impedance tensor were calculated as a percentage of $\sqrt{|\mathbf{Z}_{xy}\mathbf{Z}_{yz}|}$ for each period.

Data File Name	Z Error Floor	T Error Floor	Min Period	Max Period
`kuthdat_egbert_z10_t30.dat`	10%	0.3	0.00312 s	9036 s
`kuthdat_egbert_z15_t40.dat`	15%	0.4	0.00312 s	9036 s

Table 6.2: Data files and parameters for 3D inversion.

6.4.2 Practicalities and HPC Considerations

Given the relatively fine resolution of the data set, with MT sites separated by 1 km along traverse lines, it was necessary to find the optimum spatial resolution with which to construct a model mesh. Ideally, model mesh cells would be 1/5 to 1/3 the data spacing, but at this resolution the number of cells in a model mesh for this data set would push compute time scales beyond practical limits.

Previous WesternGeco inverse models used a model mesh of 800 m in horizontal directions. A series of meshes were therefore built in MTpy using this starting resolution and increasing to mesh sizes of 700 m and 600 m. Input data files were generated for the model meshes and each were submitted to kunanyi for inverse modelling. Of these, calculations relating to the higher 600 m resolution model resulted in MPI memory bandwith errors related to the total number of cells, while the calculations using the lower resolution models proceeded satisfactorily.

These memory bandwidth constraints dictated the 700 m mesh cell size for subsequent inverse modelling. Given the finer mesh relative to previous industry inverse modelling, and a 47 % increase in total cells, it was anticipated that subsequent inversion would yield better fitting models that have the capacity to resolve geoelectric structures beneath the broadly

spaced MT sites acquired as infill to the 1 km spaced transect, while limited mesh cells between some tightly spaced transect sites would yield imperfect model fits. Table 6.3 summarises the differences between the new 700 m model mesh and the previous WesternGeco model.

Model	nX cells	nY cells	nZ cells	Total cells
New 700m mesh model	147	160	84	1,975,680
WesternGeco model	121	99	112	1,341,648

Table 6.3: Model dimensions of new 700 m mesh model and previous WesternGeco model.

6.4.3 Starting Model Construction

Two different starting models were generated from a common 700m horizontal cell size mesh. One used a standard 100 Ω m halfspace while another used resistivity data taken from a final 5 km resolution regional AusLAMP inverse model (run027). Inclusion of run027 resistivity information in the second starting model was performed in SKUA-GOCAD 3D software. Sea water cells in the southeast of the model space, and within padding cells, was added to both models using an MTpy script and the AusBATH2009 bathymetry data set decimated to a horizontal resolution of ∼1 km.

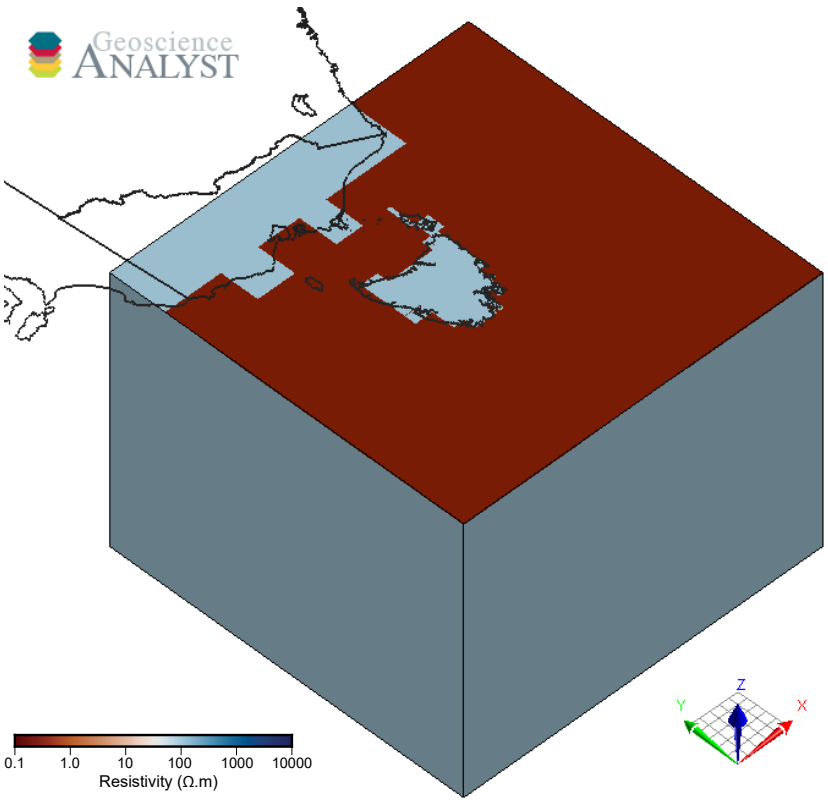

Figure 6.6: Orthographic 3D projection of the 100 Ω m starting model with no vertical exaggeration viewed obliquely from the south west. Note 0.3 Ω m resistivity values in uppermost cells corresponding to conductive sea water. Black lines correspond to coastlines and Australian state boundaries.

The mesh employed by both models was generated using MTpy and consisted of ∼1.97 million cells with 14 padding cells in both X and Y directions. Extensive padding was incorporated to ensure model boundaries were ∼ 2 skin depths distant from the data set; or about 1000 km as computed for the longest period in the data set (9000 s) in a 100 Ω m half space. Vertical cell thicknesses increase exponentially from an uppermost cell thickness of 30 m to a lowermost cell thickness of 242.2 km over a total vertical extent of 1003.9 km. See Figure 6.6 for a 3D rendition of the 100 Ω m starting model.

6.4.4 Results

Inverse modelling was completed after approximately 3 months of computation time yielding four inverse models with remarkably similar geoelectric structure, despite varying starting models and data parameters. Given the 300 h time limit afforded to compute jobs on the kunanyi cluster, each inversion required manual restarting every twelve days. An error in the inversion restart procedure prolonged the inverse modelling processes. Specifically, failure to carry over updated values (defining λ, the initial damping factor for inversion) in an inversion parameter file resulted in high RMS misfit values for the first five or so iterations after restart. This is evident in inversion progress plots as spikes in RMS misfit values throughout the inversion process (Fig. 6.7). Nevertheless, the inverse models reconverged to previous fit quickly, giving confidence in the ability of the data to constrain the model, and finally converged on well-fitting models with acceptable overall RMS misfit <3.

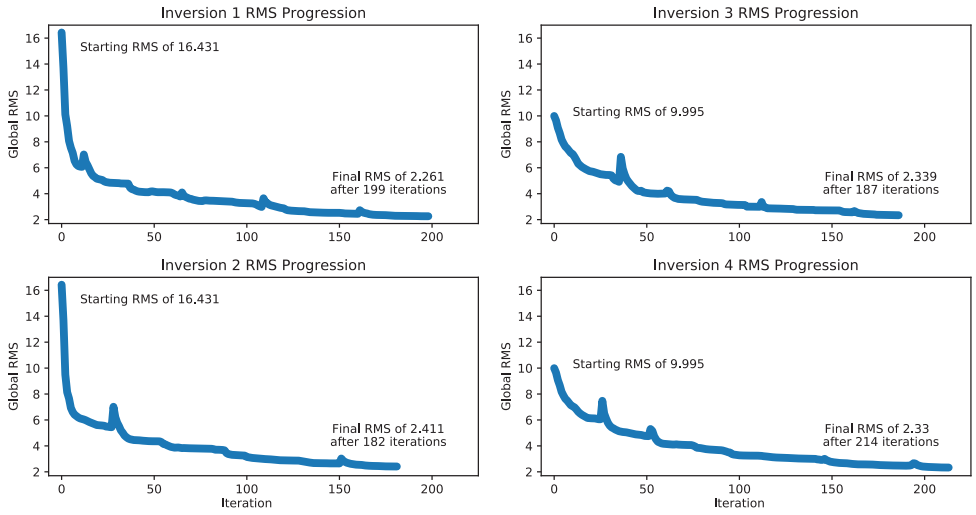

Figure 6.7: Global RMS misfit for successive iterations of each KUTh inverse model.

An inspection of site-by-site RMS misfit values yields information about where the models are best fitted to the data. Such RMS misfit alues suggest the models are best fitted in the central and northwestern regions of the data set for all models, where data points are more evenly distributed in space (see Fig. 6.8). Conversely, higher RMS misfit values are observed in regions where data are spatially concentrated along profile lines, especially for the easternmost

and southwestern data points. This behaviour likely reflects the inability of the inversion to place enough resistivity structure between data points given the 700 m mesh resolution and ∼1 km data spacing along profile lines. Better model and data fit in these regions would require a higher resolution mesh, which would necessitate significantly more computational power to invert.

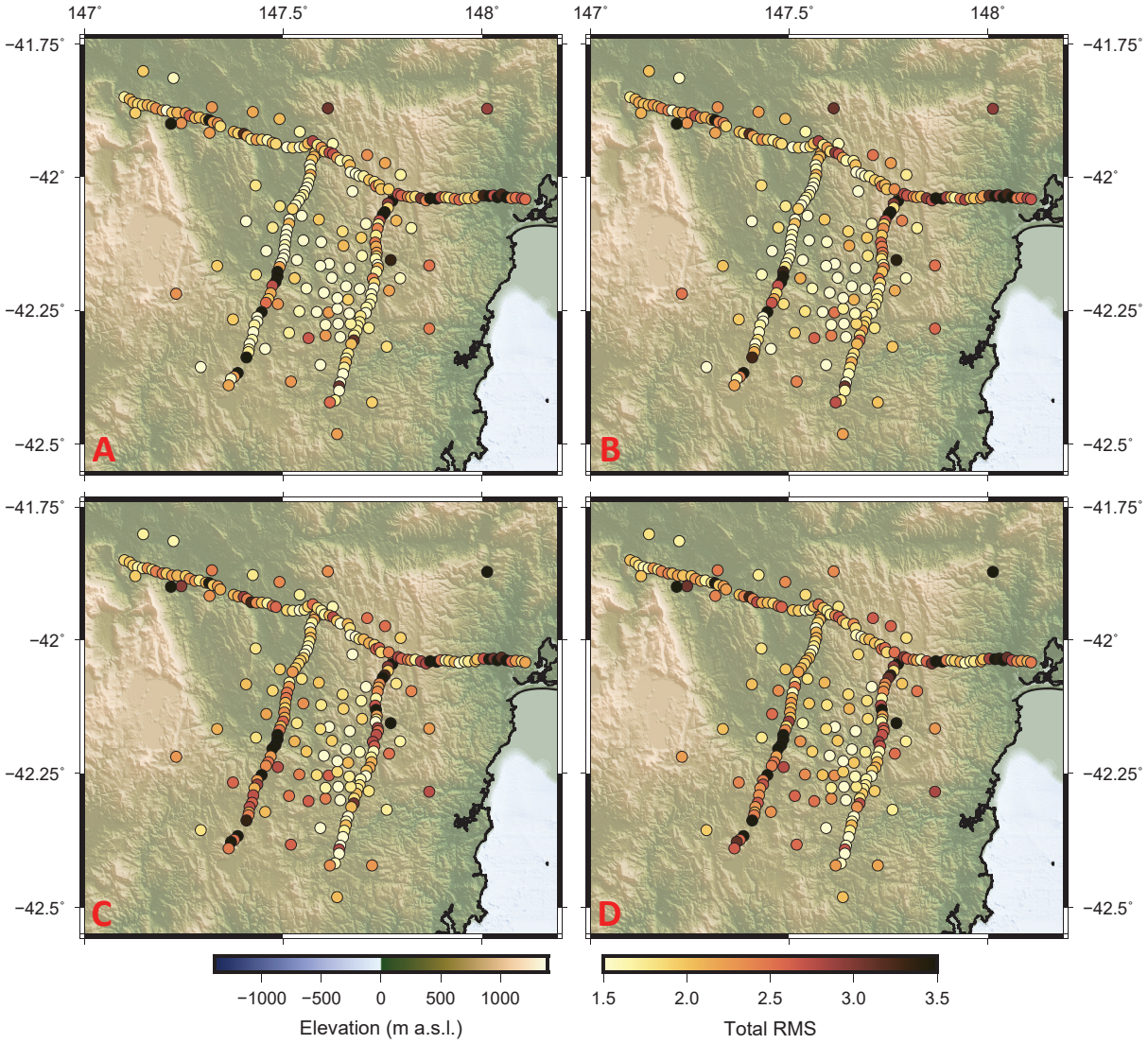

Figure 6.8: Site-by-site total RMS misfit plots for inverse models overlain onto 30 m resolution SRTM digital surface model and AusBATH2009 bathymetry data. Panels A, B, C and D correspond to inversions 1, 2, 3 and 4, respectively. Total RMS misfit is taken as the average RMS misfit across all impedance tensor (Z) and tipper (T) components for each MT site used in the inversion. Dark coloured dots represent MT sites poorly fitted in inversion.

100 Ωm Starting Models

Inversions 1 and 2 utilised a homogeneous halfspace resistivity, with the exception of sea water, of 100 Ω m in the starting model. These were inverted using ModEM3DMT's default smoothing parameters, and began inversion with a relatively high global starting RMS misfit of 16.4. Despite this, RMS misfit values rapidly decreased to ∼6 after the first 10 iterations or so, at which point the rate of RMS misfit decline with iteration is comparable to that of inversions 3 and 4 (Fig. 6.7).

In terms of geoelectric structure, inversions 1 and 2 are very similar such that the influence of different error floors in the impedance tensor (Z) and tipper (T) data (Table. 6.2) on inverse model outcomes appears to be near-negligible. For both, the top ∼1 km of the model space is dominated by a mottled resistivity structure typical of ModEM3DMT inverse models. This artefact is caused by the inversion algorithm placing resistivity structure within close proximity to MT sites to account for frequency-independent galvanic distortion due to near-surface resistivity features. At a depth of 500 m, just within the window of data sensitivity, coherent low resistivity zones emerge beneath the easternmost sites on the east-west traverse (feature **C1** in Figure 6.9).

At depths greater than about 1 km the mottled resistivity patterns evident at shallower levels in the model space begin to disappear and larger scale geoelectric structures emerge. Discrete low resistivity zones, labelled **C2**, **C3** and **C4** in Figure 6.9, are first visible at these depths and appear to surround a broadly resistive zone containing the highly resistive structure **R1** in the central north of the data set. The low resistivity zone **C1** identified at shallower levels in the model space begins to migrate eastward beyond the extent of the data as depth increases. AusLAMP sites have yet to contribute much structure at these shallow levels as this is well outside the depth sensitivity range of their minimum periods. Figure 6.9 demonstrate the near-identical geoelectric structure of inverse models 1 and 2. Further side-by-side comparison is unnecessary, and subsequent plots present depth slices through inverse model 1.

Low resistivity structures evident at 1 km to 2 km depth in the model space begin to intensify beyond 2 km. At 2.46 km, low resistivity zones **C1** through to **C5** broaden in extent and reach very low resistivities in the order of 0.1 Ω m (Fig. 6.10). These structures continue to broaden with increasing depth such that **C2**, **C4** and **C5** effectively link together at ∼3.71 km depth to form a roughly arcuate corridor of low resistivity between them. The emergence of this low resistivity corridor is concomitant with a general decrease in resistivity in the western end of the data set, and the complete disappearance of the highly resistive region **R1**.

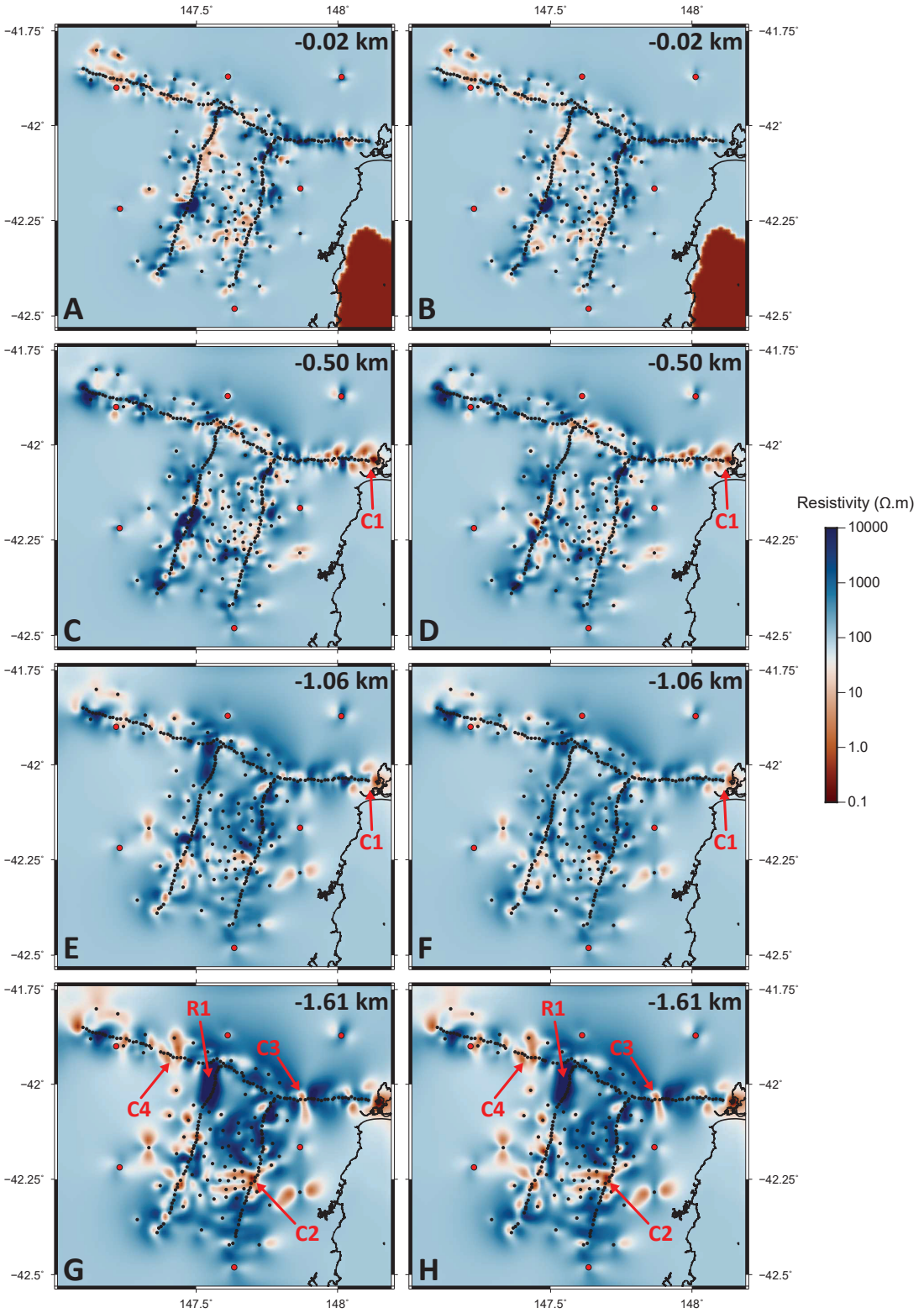

Figure 6.9: Depth slices through inverse models 1 and 2 with AusLAMP MT site locations given by red dots, and KUTh MT sites given by black dots. Panels A), C), E) and G) present slices through inverse model 1, while panels B), D), F) and H) present slices through inverse model 2. Value in top right corner of each pane presents the depth in the model space of the slice. Annotated structures are discussed in text.

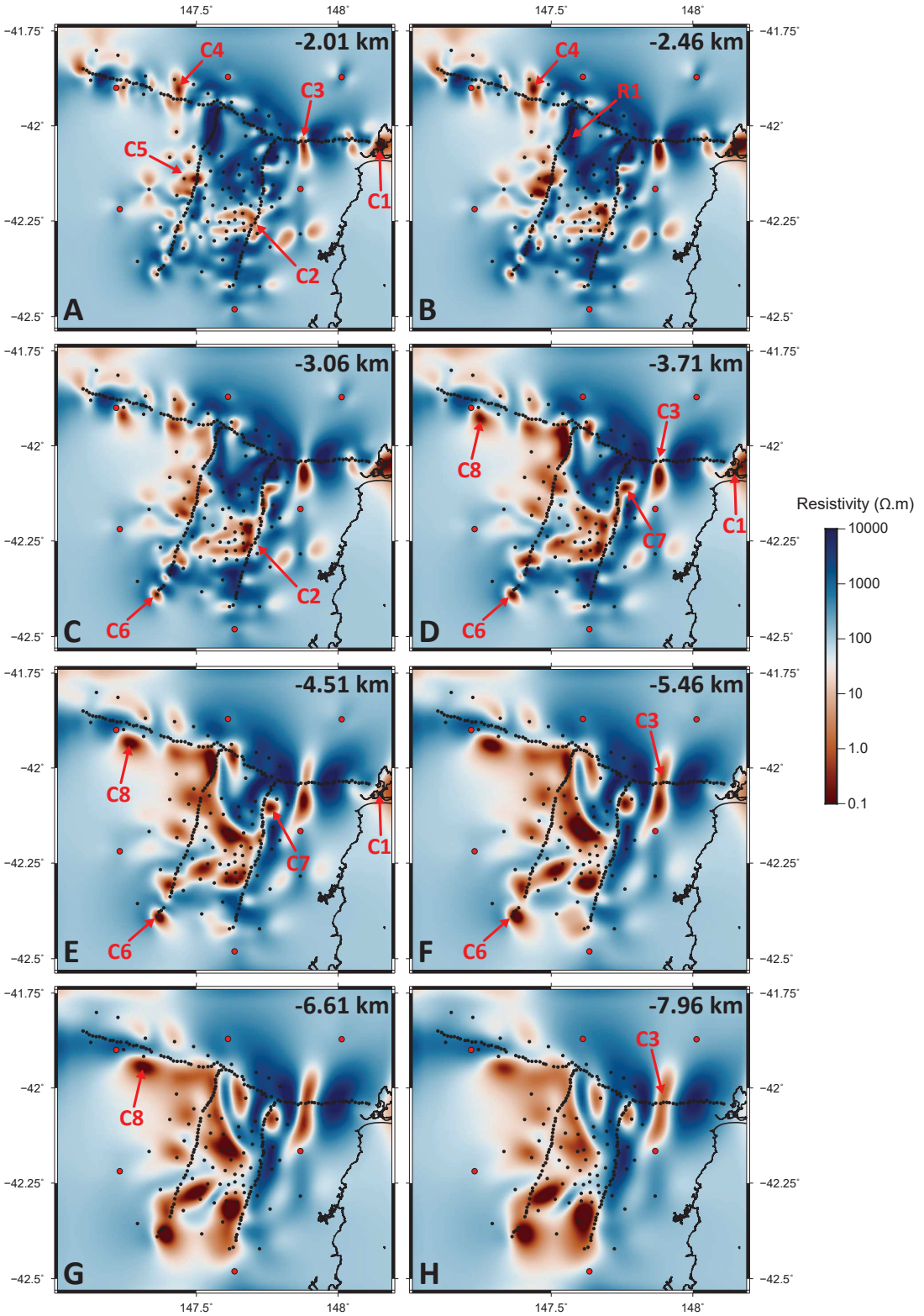

Figure 6.10: Depth slices through inverse model 1. The value in the top right corner of each pane gives the depth in the model space of the slice. Annotated structures are discussed in text.

At depths greater than 3.06 km low resistivity zones **C6**, **C7** and **C8** begin to manifest. Here, **C6** is centred on a single MT site in the far southwestern end of the data set but migrates northward with increasing depth, eventually broadening out and linking with low resistivity zones to the northeast connected to the central arcuate zone at ∼6.61 km depth (panel G in Fig. 6.10). **C8** is located just off the northwest-southeast MT traverse and is therefore poorly constrained by the data. With increasing depth **C8** broadens and fades into what appears to be a regional trend for low resistivities in the west of model space.

The low resistivity zone **C7**, linked to the central arcuate low resistivity zone at ∼3.7 km, becomes isolated at depths beyond 4.51 km (panel E in Fig. 6.10). Since it is confined to a region between a single off-traverse MT site and a portion of the easternmost north-south MT traverse where MT sites return relatively high RMS misfit values (see Fig. 6.8), this is not expected to be a very robust feature of the model. The relatively poor model fit observed for transect site NSB005 typifies the high RMS misfit sites adjacent to **C7** (Fig. 6.11). A similar explanation is likely for **C3** on the eastern end of the east-west MT traverse. The lack of nearby off-traverse sites and the high RMS misfit values for traverse sites in the immediate vicinity of **C3** make it a poorly constrained model feature.

By contrast, low resistivity zones **C2**, **C4** and **C5** arise in regions of the model space where MT sites return low RMS misfit values. As Figure 6.8 shows, these central parts of the data set are well fitted by all inverse models, and response curves similar to that presented in Figure 6.12 are typical for MT sites surrounding these structures.

At depths greater than ∼10 km, in the mid-crust, the minimum resistivity of low resistivity structures identified at shallower levels in the model space tends to increase. By 16.76 km, structures **C3**, **C6**, **C7** and **C8** have largely disappeared yielding a bi-polar resistivity structure with high resistivities in the eastern half of the data set, and lower resistivities in the western half. This regional trend continues to depths of about 25 km, within the lower crust, where higher resistivity regions in the western end of the data split and migrate north and south toward model padding cells (Fig. 6.13). At the limit of data sensitivity, a depth of ∼38 km, the model space is near-uniform in terms of resistivity structure with a very slight regional trend favouring higher resistivities in the east and lower resistivities in the west.

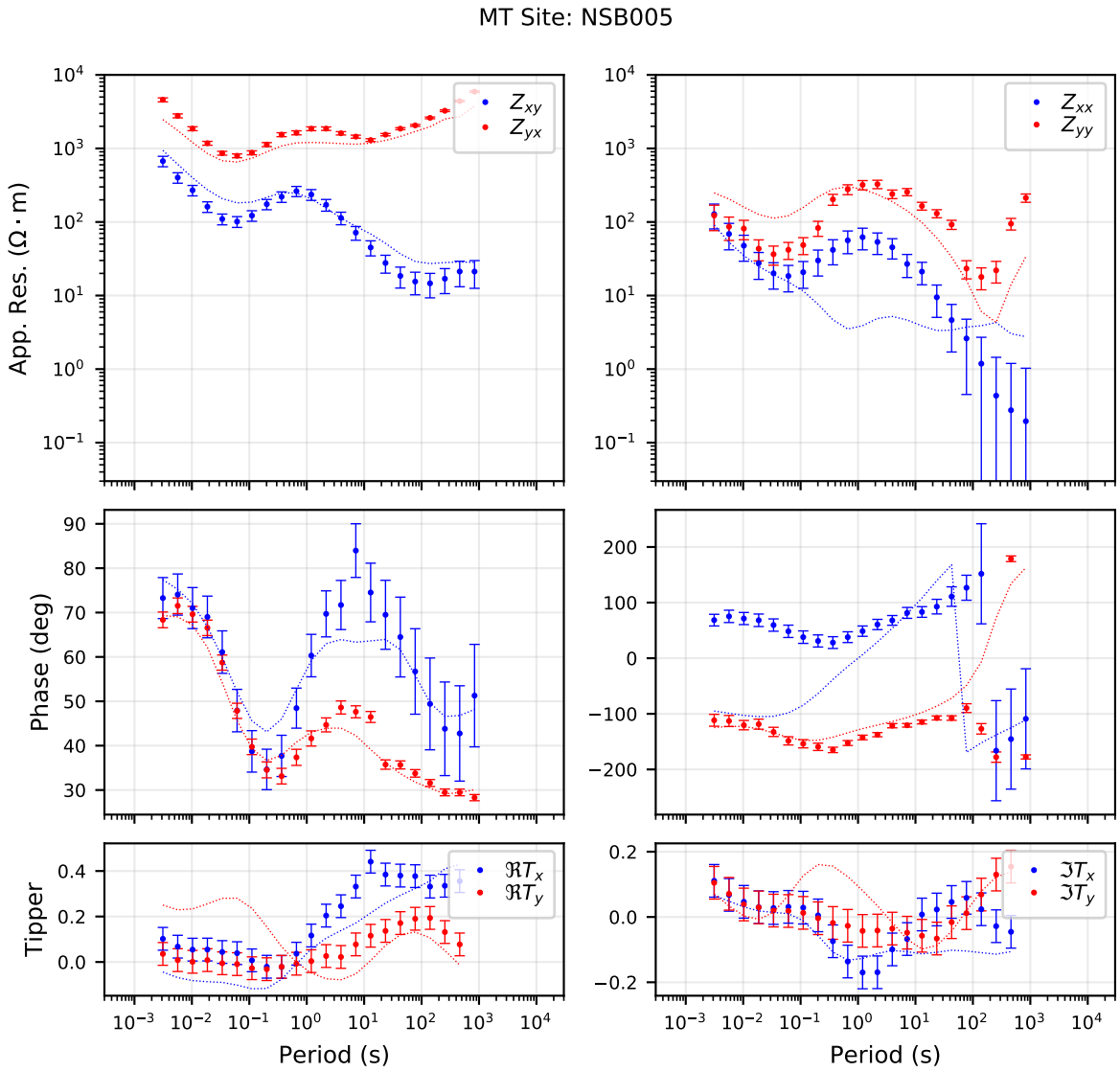

Figure 6.11: Apparent resistivity, phase and tipper curves for MT site NSB005 with inversion 1 model response curves plotted as dashed lines. This site returned a total RMS misfit of 3.71, with impedance tensor components $\mathbf{Z}_{xx}$ and $\mathbf{Z}_{yx}$ having especially high RMS misfit values of 4.38 and 5.55, respectively. Tipper RMS misfit values are less extreme despite poor model fit at various periods with 1.98 and 2.58 for components $\mathbf{T}_x$ and $\mathbf{T}_y$, respectively.

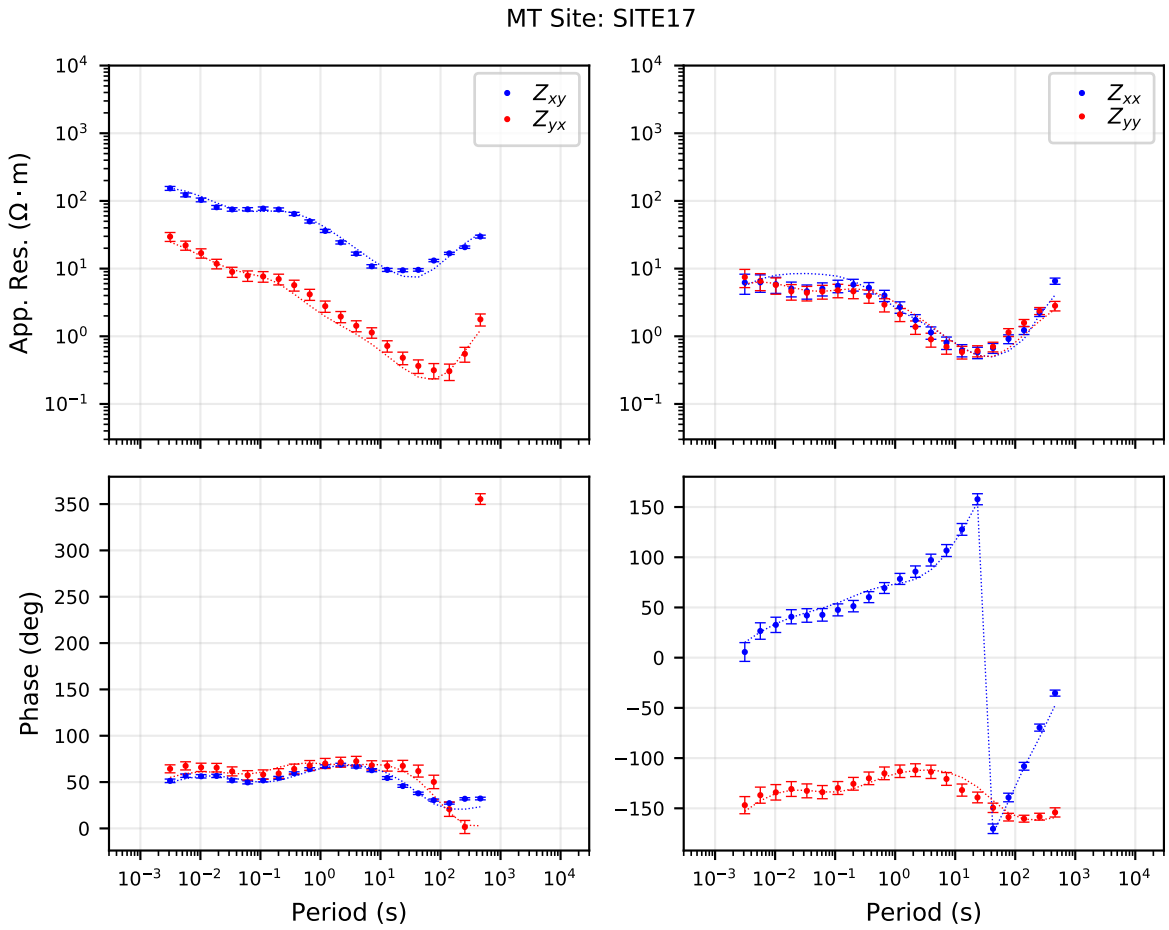

Figure 6.12: Apparent resistivity and phase curves for MT site SITE17 with inversion 1 model response curves plotted as dashed lines. This site is one of 146 sites where tipper data was either not recorded or of low quality (and hence not included in the inversion). Model response curves fit data points for all components very well, with this site returning a total RMS misfit of 1.94.

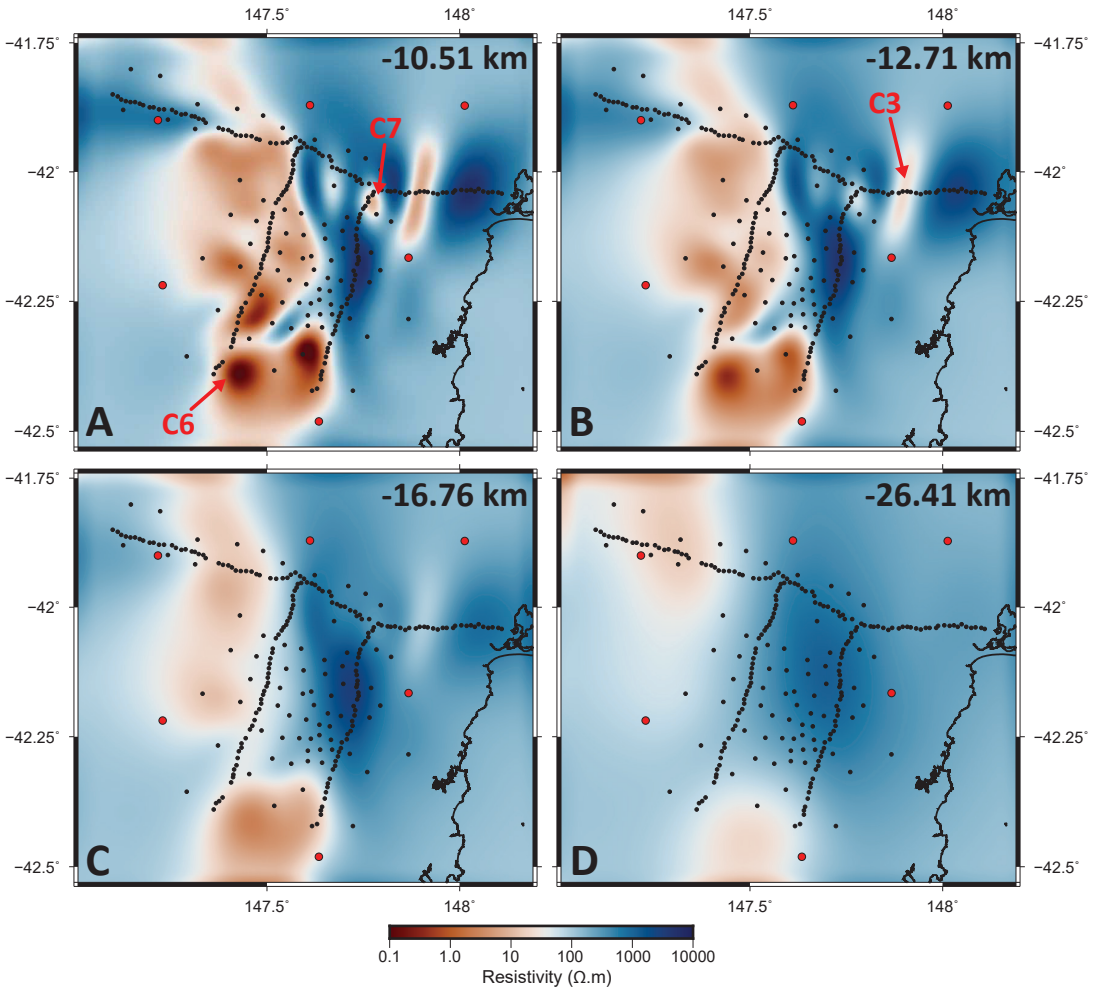

Figure 6.13: Depth slices through inverse model 1. The value in the top right corner of each pane gives the depth in the model space of the slice. Annotated structures are discussed in text.

AusLAMP Starting Models

Inversions 3 and 4 used resistivity information from a regional AusLAMP-derived resistivity model as a starting model (see Chapter 4). Relatively low starting RMS misfit values of ∼9 for this prior model in comparison to the homogeneous halfspace models suggest that the KUTh broadband data is in broad agreement with the regional structure derived from AusLAMP inversion (Fig. 6.7). Despite significant differences in starting models, and noting differences between final inverse models, the final global RMS misfit values of all four models are comparably small.

Comparable final global RMS misfit values for inversions with the different starting models is not reflected in site-by-site RMS misfit maps presented in Figure 6.8. Inversions 3 and 4 show near-identical distributions of RMS misfit, but in comparison to inversions 1 and 2 larger RMS misfit values are found for southwestern transect sites and smaller values for eastern transect sites. RMS misfit values for sites in the centre of the data set around the Lemont resource are very low, a model feature shared by all inverse models.

Depth slices through the uppermost cells of inverse models 3 and 4 are presented in Figure 6.14. Features inherited from the regional, 5 km resolution AusLAMP starting model are immediately obvious as coarse block structures of varying resistivity. This block structure presents a means of qualitatively assessing the regions of the model space to which data are most sensitive. Regions mostly unsmoothed by the inversion algorithm are outside the sensitivity range of the data, while smoothed regions are within the sensitivity range of the data set.

At these shallow depths in the model space, where data is sensitive, inversion has generated the typical mottled resistivity structure observed in inverse models 1 and 2. Again, here the inversion algorithm is accounting for local geoelectric structure giving rise to galvanic distortion in the data.

The majority of cells in the uppermost levels of inverse models 3 and 4 have relatively low resistivities in the order of 10 Ω m. This is a feature inherited from the starting model used in regional AusLAMP inversion discussed in Chapter 4. Here, a 10 Ω m sediment layer taken from the OZSEEBASE data set was included as geological *a priori* information. Low resistivity regions in the west of the model spaces evident at 0.5 km depth (panels C and D in Fig. 6.14) and 1.06 km depth (panels E and F in Fig. 6.14) therefore correspond to *a priori* model features and do not necessarily represent subsurface geoelectric structure at these locations. As with 100 Ω m starting model inversions, inverse models 3 and 4 are essentially identical in terms of geoelectric structure and subsequent depth slice images will present slices through inverse model 3.

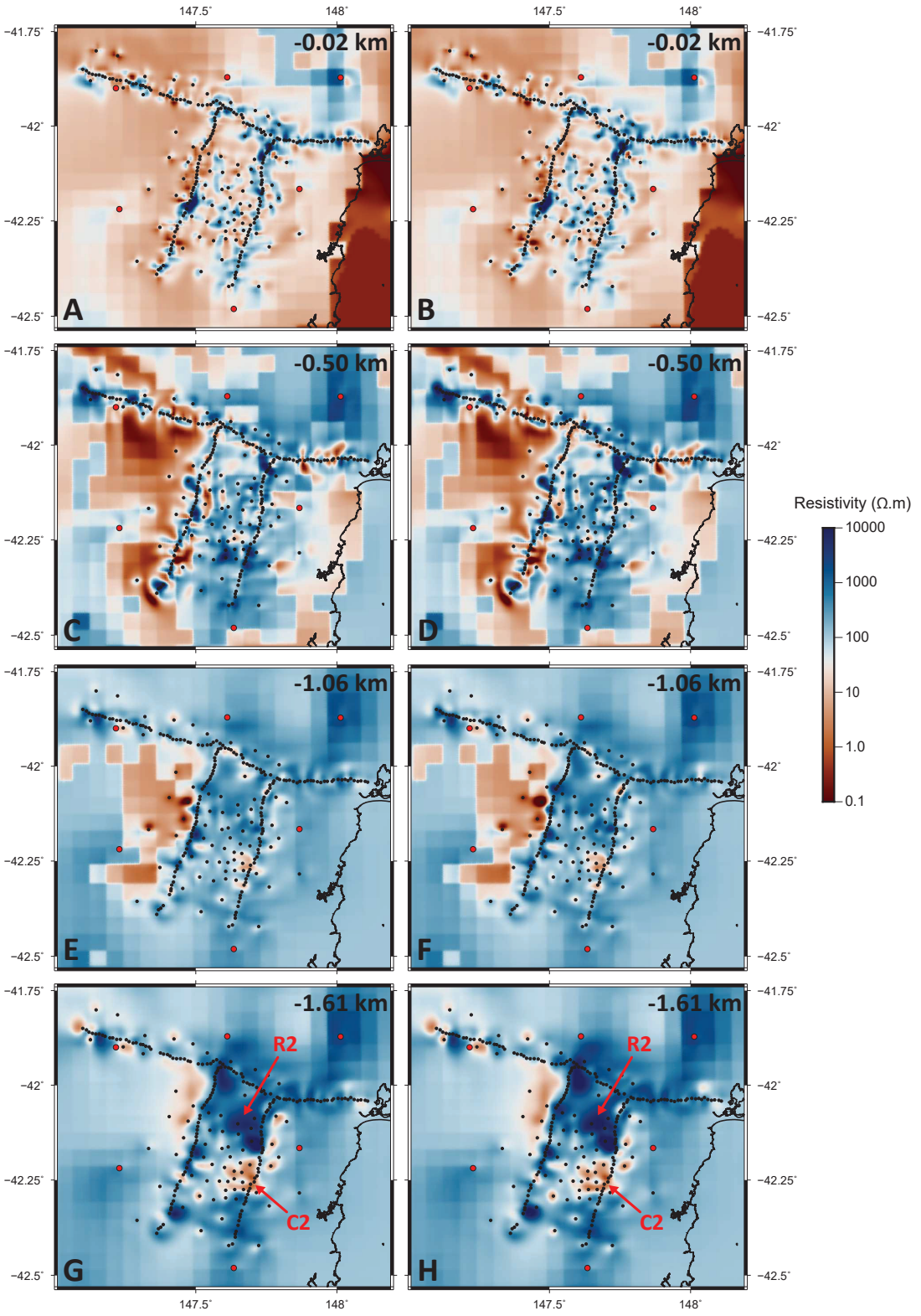

Figure 6.14: Depth slices through inverse models 3 and 4 with AusLAMP MT site locations given by red dots, and KUTh MT sites given by black dots. The coastline is depicted by the solid black line in the southwest of each panel. Panels A), C), E) and G) present slices through inverse model 3, while panels B), D), F) and H) present slices through inverse model 4. The value in the top right corner of each pane gives the depth in the model space of the slice.

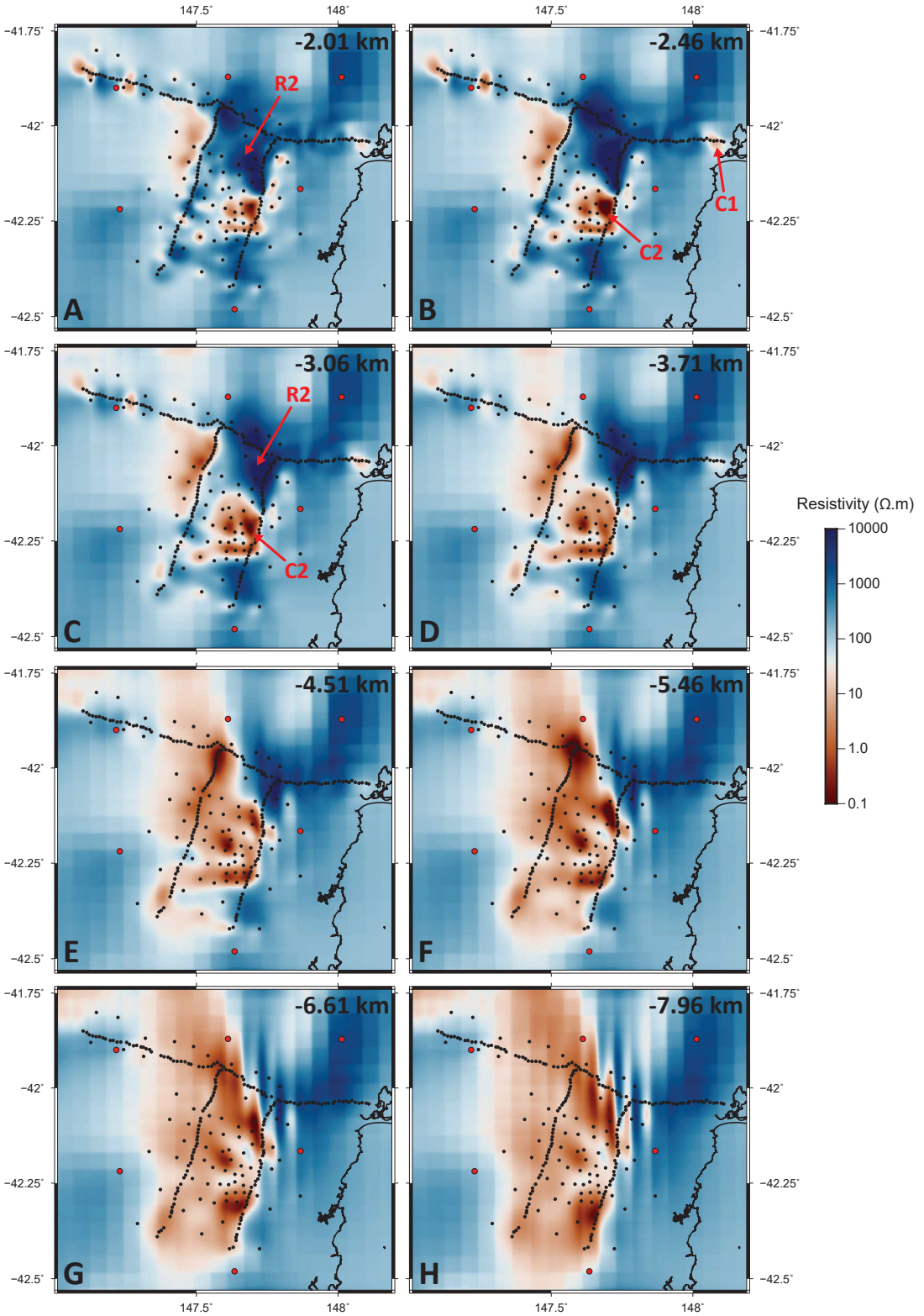

Figure 6.15: Depth slices through inverse model 3. The value in the top right corner of each pane gives the depth in the model space of the slice. Annotated structures are discussed in text.

Coherent geoelectric structures begin to emerge within the sensitivity range of the data set at depths beyond 1.2 km, below ∼10 Ω m sediment cells inherited from the AusLAMP starting model (panels G and F in Fig. 6.14). These structures; a central northern resistive region (**R2**) and a central southern low resistivity zone (**C2**) persist with increasing depth (Fig. 6.15). Low resistivity feature **C2** intensified and broadens with increasing depth, eventually linking to a northern low resistivity zones to form a large zone of low resistivity in the central west of the data set. Resistive zone **R2** also intensifies with increasing depth, and migrates northwestwards as **C2** broadens.

The central low resistivity zone broadens at depths beyond ∼5 km into a north-south trending low resistivity corridor spanning the entire model space. Here the high resistivity zone **R2** continues to retreat to the northwest, broadening into a high resistivity zone linking the northwesternmost AusLAMP MT site with western KUTh transect MT sites. At this depth in the model space, the regional-scale resistivity blocks in the AusLAMP derived starting model appears to induce an artefact in the model space. This takes the form of north-south trending 'streaks' most evident at depths ranging 7.96 km to 16.76 km (Fig. 6.15 and Fig. 6.16).

It is unclear exactly why ModEM3DMT generates these artefacts at these depths, though it should be noted that MT sites in this region of the model space returned high RMS misfit values for both the 100 Ω m and AusLAMP derived starting models (Fig. 6.8). In both cases the inversion procedure was less successful with regard to the fit of this region of the data set, possibly due to tight site spacing. Figure 6.17 presents inversion 3 apparent resistivity, phase and tipper model responses for site NSB005 located near the traverse junction, where north-south resistivity streak artefacting is most intense, and is typical of the model fits in the region.

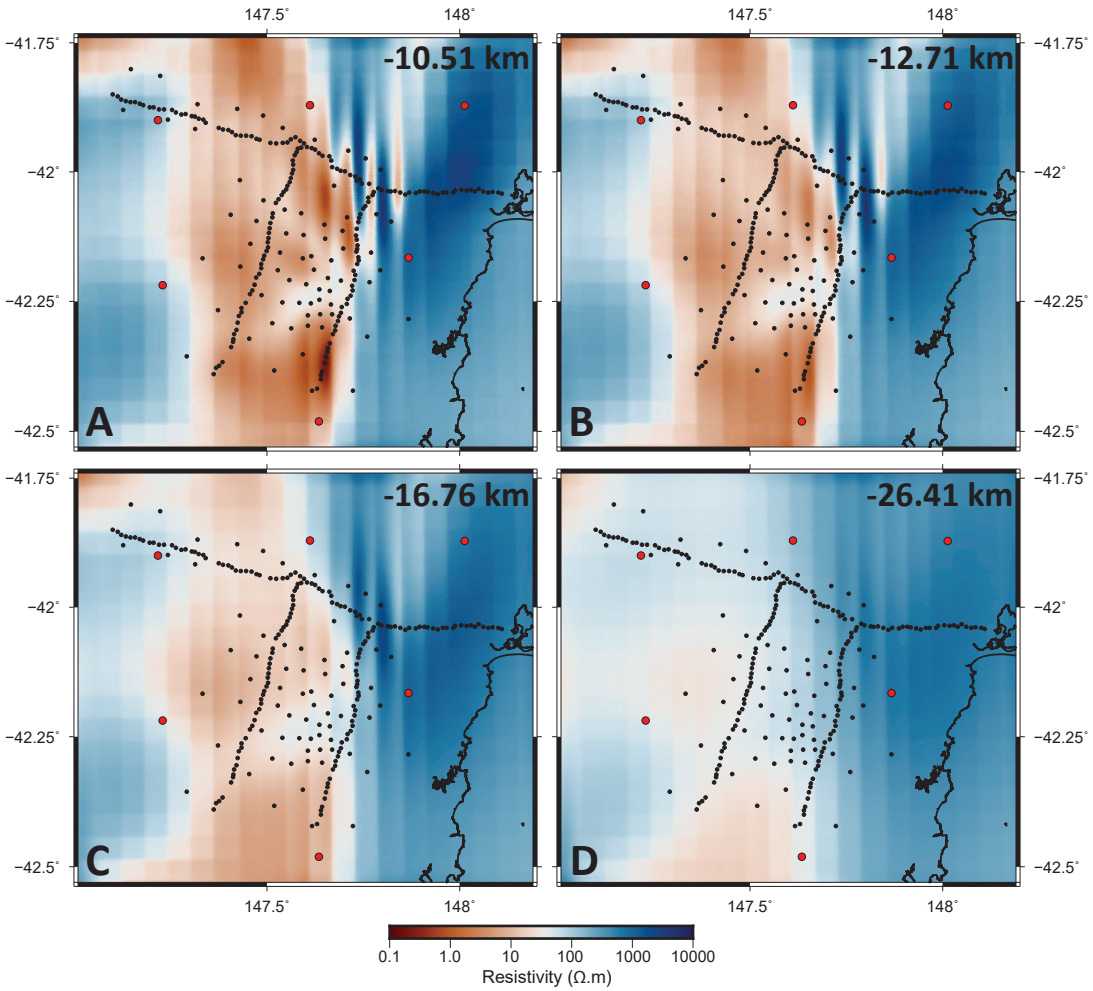

Figure 6.16: Depth slices through inverse model 3. The value in the top right corner of each pane gives the depth in the model space of the slice. Annotated structures are discussed in text.

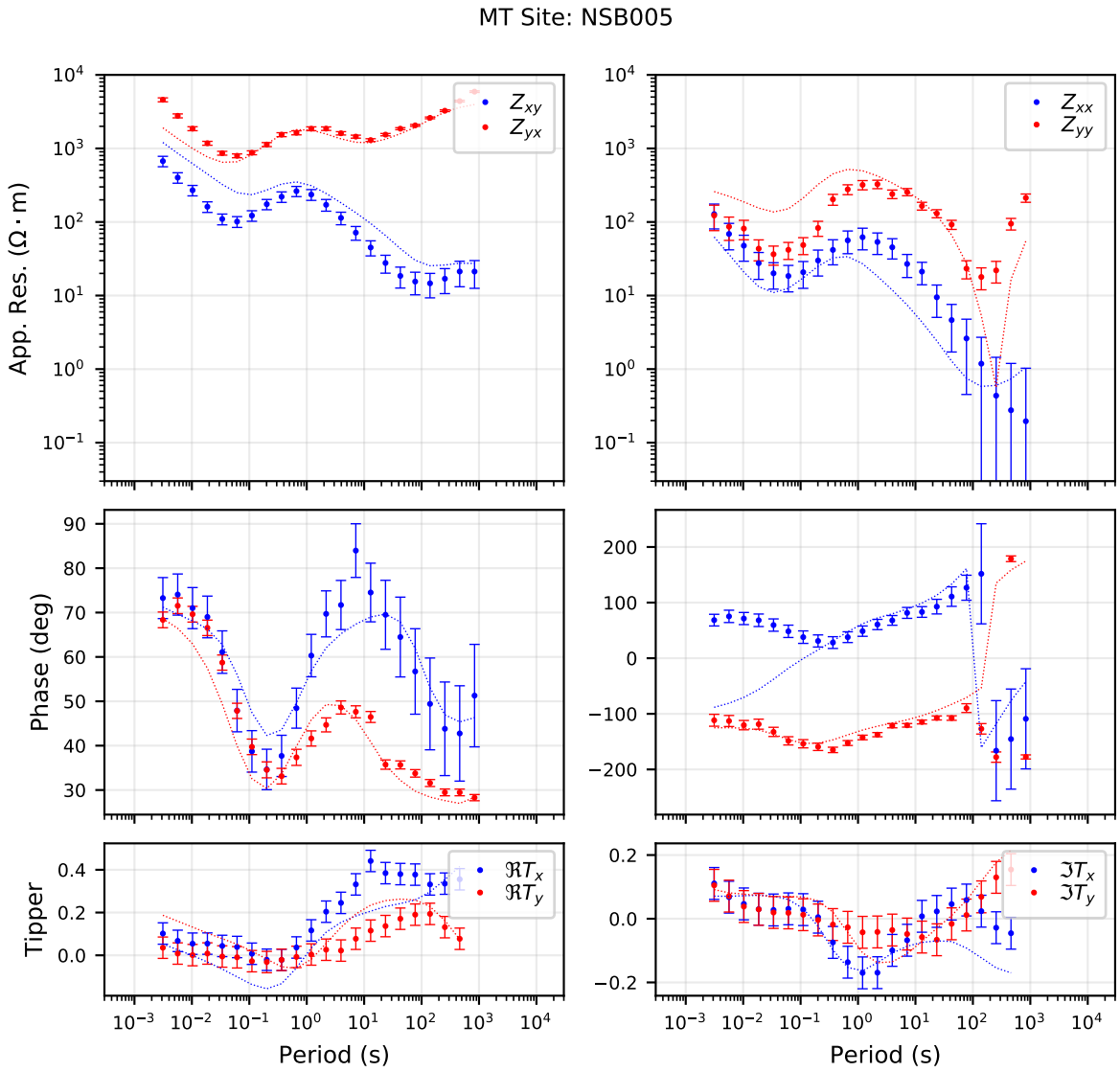

Figure 6.17: Apparent resistivity, phase and tipper curves for MT site NSB005 with inversion 3 model response curves plotted as dashed lines. This site returned a total RMS misfit of 3.25, with impedance tensor components $\mathbf{Z}_{yy}$ and $\mathbf{Z}_{yx}$ having especially high RMS misfit values of 4.00 and 4.62, respectively. Tipper RMS misfit values are less extreme despite poor model fit at various periods with RMS misfit values 1.91 and 1.44 for components $\mathbf{T}_x$ and $\mathbf{T}_y$, respectively.

Comparison of Combined, and AusLAMP Regional, Model Structures

Comparing depth slices through the combined inversion 3 and regional-scale AusLAMP derived resistivity model provides a means of assessing the improvement in geoelectric structure resolution this joint inversion exercise has achieved within the study area. Figure 6.18 clearly demonstrates resolution improvements, and shows the benefit of using coarse regional models as a starting model with respect to visualising the sensitivity range of the data.

Beneath the low resistivity uppermost cells inherited from the AusLAMP starting model sediment layers, the low resistivity and high resistivity structures that emerge deviate significantly from the starting model (panels C and D in Fig. 6.18). Deviations can largely be summarised by increased resistivity in the north and east, and a trend toward reductions in resistivity in the central regions of the model broadly coincident with the Lemont geothermal resource across a depth range encompassing the top 10 km of the model space. Beyond 10 km depth the low resistivity north-south trending structure inherited from regional modelling is slightly modified by increases in resistivity which become less and less significant with depth such that by ∼30 km depth the two models are near-identical (Fig. 6.19).

A curious feature of inverse model 3 that requires explanation is the limited degree of smoothing in the southeast of the model space within cells designated as sea water in the starting model (panels A and B in Fig. 6.18). Here inversion has slightly increased the resistivity of some of the sea water cells in inverse model 3 from 0.3 Ω m to ∼1 Ω m. This is a product of differing resolution in both model meshes and bathymetric data sets used in the generation of the starting models for the regional AusLAMP inverse models and KUTh inverse models 3 and 4.

The AusBATH 2009 bathymetry data set was used to apply bathymetric information to all 3D inverse models. This surface model lists very shallow water depths of 0 m to 4 m for the northern reaches of Great Oyster Bay in the southeast of the KUTh model space (see digital elevation model presented in Fig. 6.3 and Fig. 6.8). A down sampled (by a factor of 12) version of the data set was used to apply sea water resistivities of 0.3 Ω m to offshore cells in the 5 km resolution mesh used in AusLAMP regional inverse models, and given the coarse grid cell sizes and the decimation factor of dataset, the nearest-neighbour interpolation performed in 3DGrid software applied sea water resistivities parallel to the coastline.

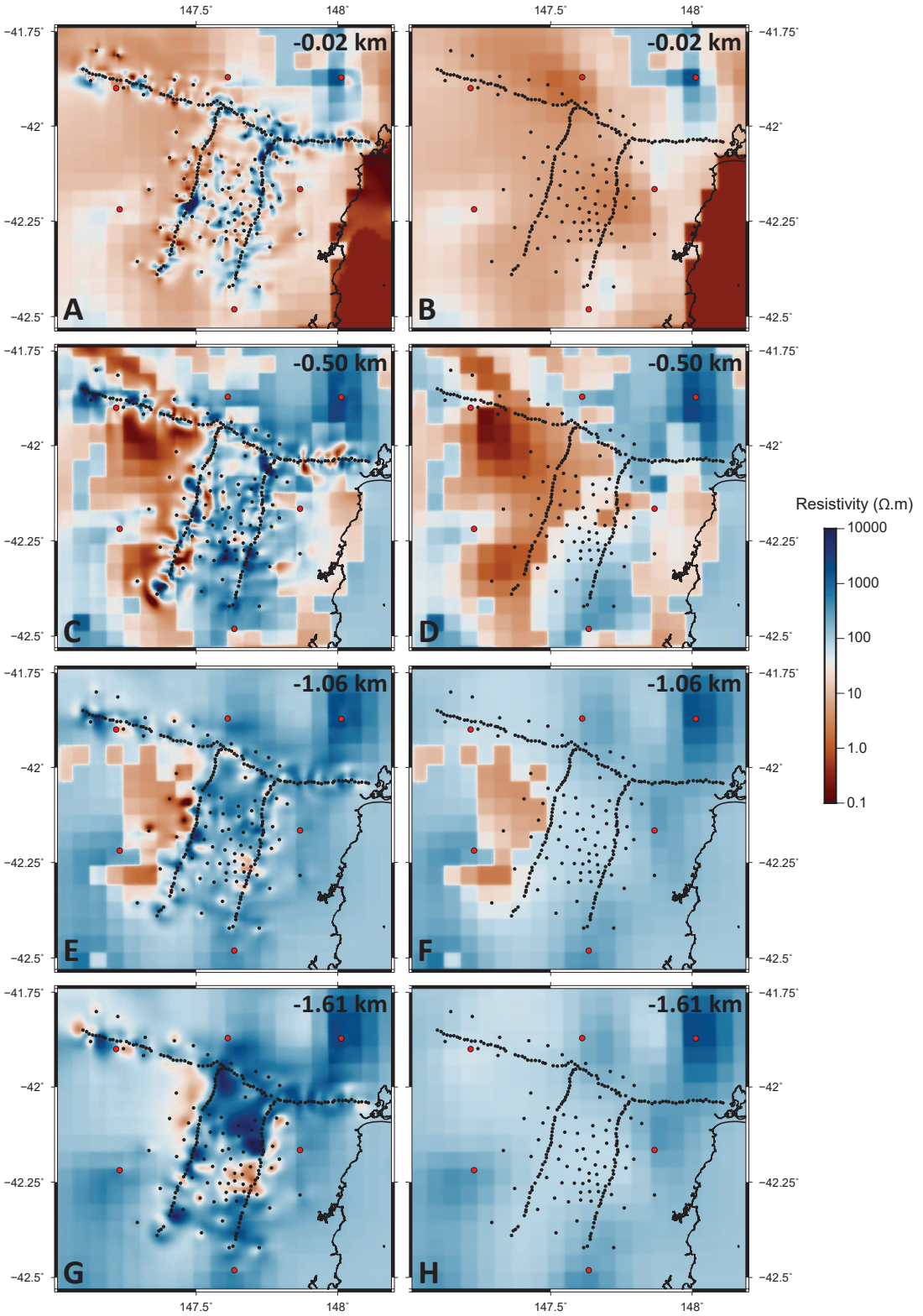

Figure 6.18: Depth slices through inverse models 3 and regional AusLAMP model 27 used as the starting model for inversion 3. Panels A), C), E) and G) depict slices through inverse model 3, while panels B), D), F) and G) present slices through the AusLAMP model. The value in the top right corner of each pane gives the depth in the model space of the slice.

A similar procedure was applied to all 700 m resolution grid meshes used in KUTh inverse modelling. This time, a version of the AusBATH data set decimated by a factor of 4, to a resolution of ∼1 km was used and the assignment of sea water resistivities to the model space performed using MTpy scripts. The finer resolution of both the mesh and bathymetry data set ensured sea water cells were added only where water depths exceed 20 m in the bathymetry model, effectively shifting the model coastline southwards. This is clearly illustrated by the location of sea water cells for the uppermost depth slice in inverse models 1 and 2 shown in Figure 6.9. Inversion smoothing of cells other than these explains smoothing of inherited sea water cells in inverse models 3 and 4.

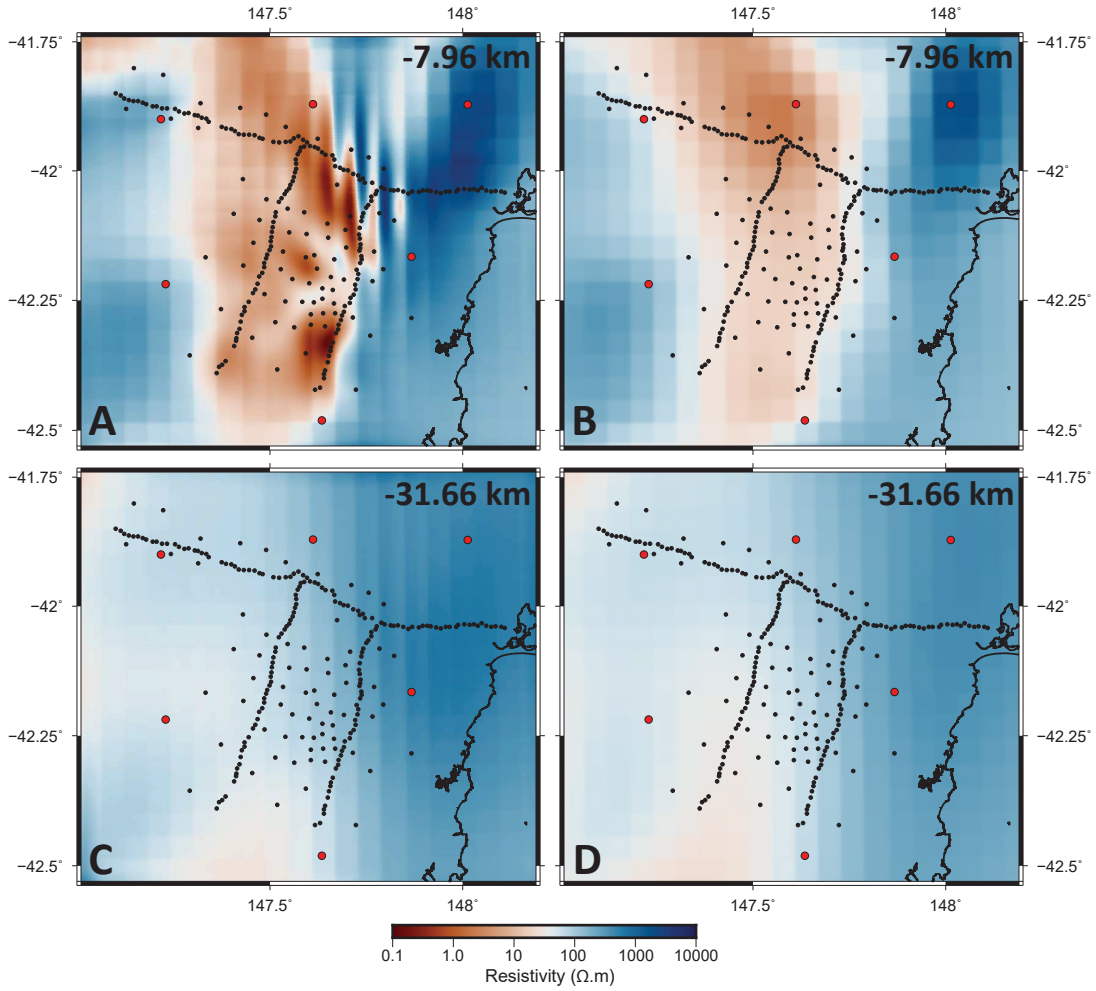

Figure 6.19: Depth slices through inverse models 3 and regional AusLAMP model 27 used as the starting model for inversion 3. Panels A) and C) present slices through inverse model 3, while panels B) and D) present slices through the AusLAMP model. The value in the top right corner of each pane gives the depth in the model space of the slice.

100 Ωm and AusLAMP Starting Models Compared

KUTh inverse models derived from the standard 100 Ω m starting model and the regional AusLAMP model share several key features, but differ in significant ways. The central low resistivity structures (**C2** in Fig. 6.10 and Fig. 6.15) are spatially comparable in the top ∼3 km of the models. Given that this central low resistivity structure is located within a region of the data space with consistently low RMS misfit values for all inversions, this structure is perhaps the most robust feature to be identified in inverse modelling. Another common feature is the regional trend favouring lower resistivities in the west of the model spaces relative to the east, and is consistent with regional resistivity modelling results.

Points of difference in the model spaces include the greater number of discrete low resistivity zones evident in the 100 Ω m models relative to the AusLAMP-derived models. Low resistivity structures that emerge off-transect and in the west of the inverse models 1 and 2 model spaces are diminished, if not wholly absent, in models 3 and 4. This is likely a result of overall lower resistivities in AusLAMP-derived starting model space, particularly at shallow surface levels encompassing the 10 Ω m sediment layer included in regional inversion starting models. A thicker sediment layer in the west of the starting model space effectively lowers the overall resistance of the region, thereby suppressing the formation of discrete low resistivity zones in subsequent inversion.

The disappearance of several discrete low resistivity zones observed in inverse models 1 and 2 once *a priori* moderately conductive overburden information is included brings the robustness of these features into question. This is especially the case when low resistivity zones are located off-transect and are adjacent to MT sites with poor model fits, such as; **C1**, **C3**, **C5**, **C6**, **C7**, **C8** shown in Figure 6.20.

The greater degree of structure evident in homogeneous halfspace models 1 and 2 are considered unlikely to be geologically feasible. Inverse models 3 and 4, which began inversion with a significantly lower starting RMS misfit and did not return the same degree of subsurface structure are the preferred models for geologic interpretation, despite the noted artefacts at mid-crustal depths in the model space. Plots depicting the model response curves on a site by site basis for the preferred model (model 3) are presented in Appendix E.

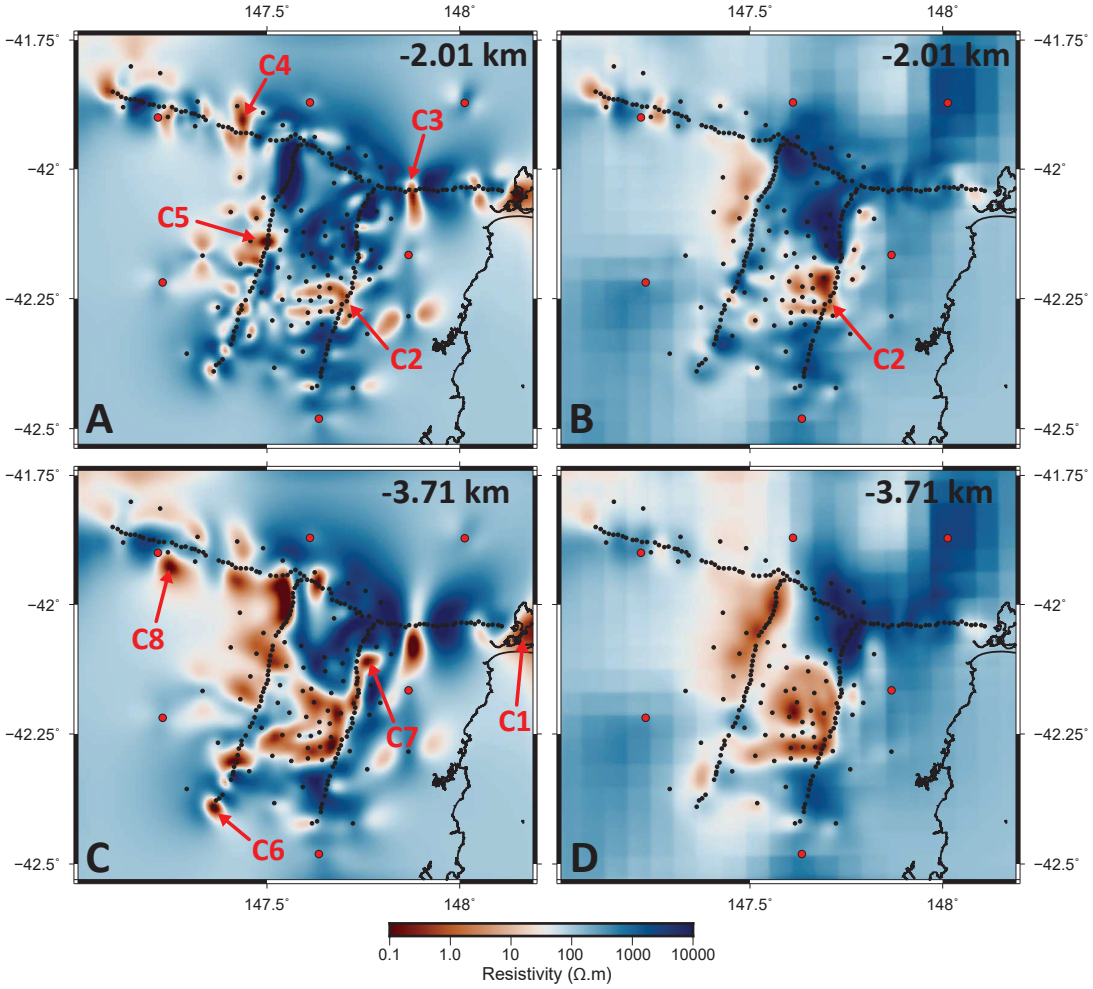

Figure 6.20: Depth slices through inverse models 1 and 3. Panels A) and C) present slices through inverse model 1, while panels B) and D) present slices through inverse model 3. The value in the top right corner of each pane gives the depth in the model space of the slice. Annotations discussed in text.

6.5 Discussion and Interpretation

Geological interpretation of inverse models was facilitated by the use of 3D viewing software packages Skua-GOCAD and Geoscience Analyst. All available geological and geophysical information was imported into the software to enable true 3D comparisons between data sets, yielding insights difficult to obtain from conventional 2D slices and cross sections. Key data sets used in interpretations include a granite topography model [Leaman, 2012] derived from gravity data [Mineral Resources Tasmania, 2019a], and fault structures interpreted from aeromagnetic surveys [Godber and Reid, 2009].

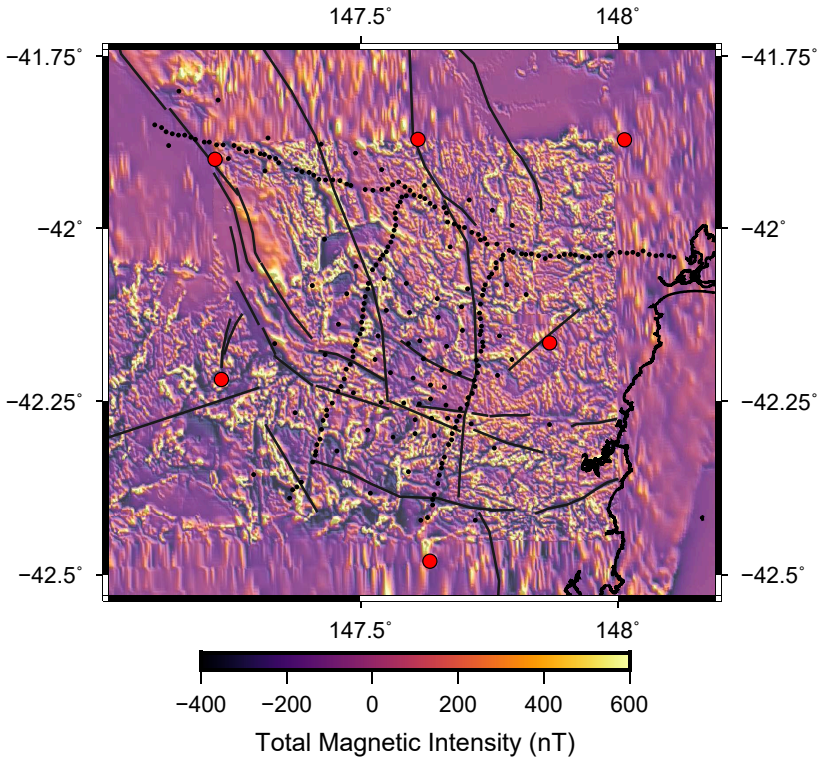

Figure 6.21: Image showing hillshaded aeromagnetic data around the Lemont resource. MT sites used in inversion are given by red dots for AusLAMP MT sites and black dots for KUTh MT sites. Dark grey lines are deep crustal lineaments derived from aeromagnetic and digital elevation model data sets reported in Godber and Reid [2009].

The aeromagnetic picture of the Lemont survey area is dominated by an arcuate feature extending to the south and east from the northwestern corner of the MT data set (Fig. 6.21). This structure, evident in both digital elevation models and residual Bouguer anomaly images, is interpreted to be a major fault structure penetrating to depth in basement. The fact that it is evident in digital elevation models implies that the structure has been reactivated as recently as the Late Paleocene when east-west directed extension affected much of Tasmania and resulted in the formation of the Longford sub-basin to the immediate north of the survey area [Stacey and Berry, 2004]. Lineaments traced from these magnetic features are presented in Figure 6.22

alongside KUTh and AusLAMP MT site induction arrows overlain onto a isostatic residual Bouguer anomaly gravity grid. At periods of ∼100 s it is clear that the central northwest-southeast trending lineament is highly spatially correlated with a conductive corridor evident in induction arrow patterns and highlighted in Figure 6.3. This spatial relationship implies low resistivity regions may be related to fracture-related permeability enhancement.

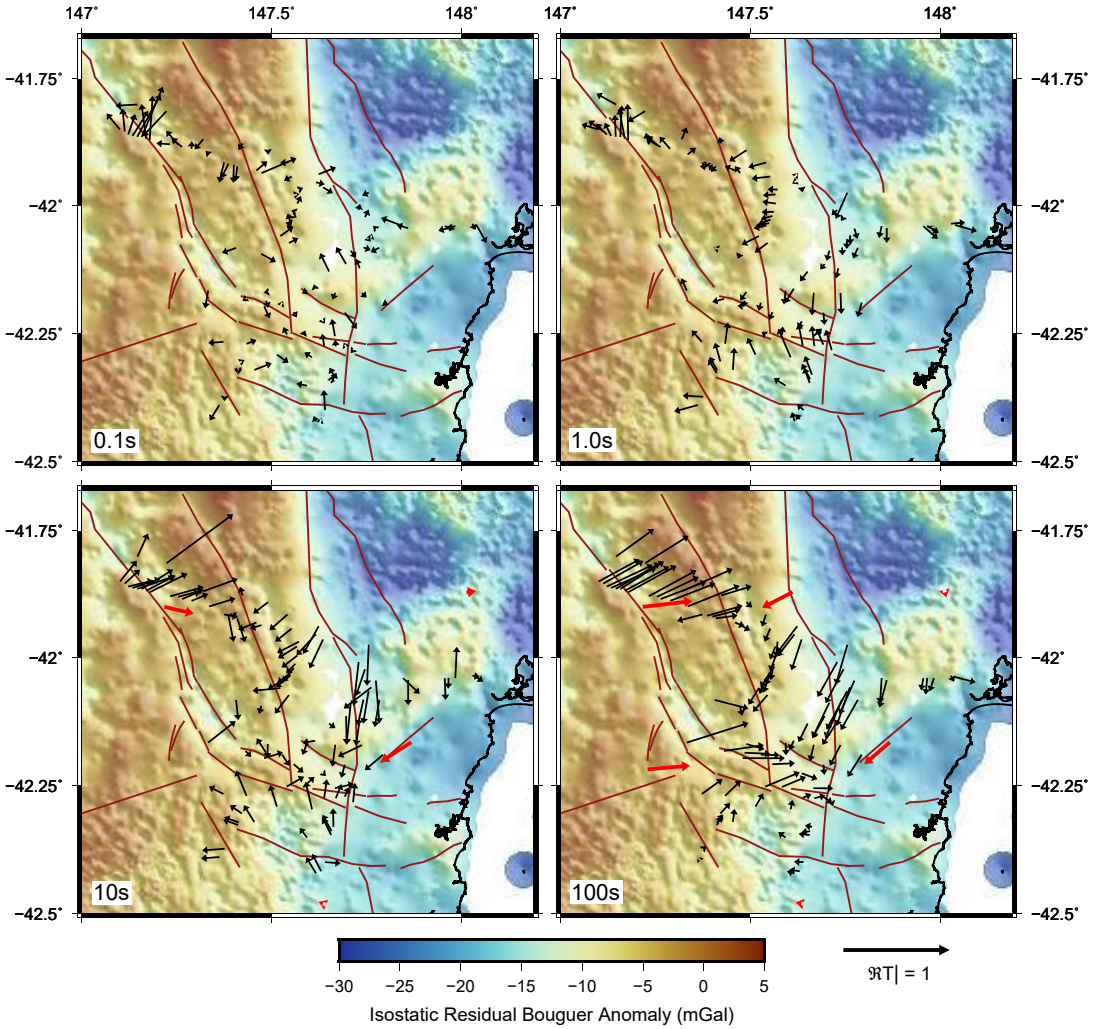

Figure 6.22: Real component induction arrows for KUTh (black) and AusLAMP (red) MT sites used in 3D inversion. Arrows are plotted on isostatic residual Bouguer anomaly gravity data highlighting lateral density variation in the upper crust. The broad eastward trend of higher to lower residual Bouguer anomaly values reflects a shallowing of the comparatively low density Devonian granite surface underlying Eastern Tasmania.

Numerical fault stress modelling commissioned by KUTh in 2010 investigated the stress state of a simplified fault network derived from aeromagnetic lineaments presented in Figure 6.22. Modelling relied on typical bulk moduli values for common lithologies and used an east-west directed thrust fault stress regime inferred from a single earthquake nearby the survey area. Despite largely hypothetical structure at depth, modelling indicated shallow to moderate

dipping faults are likely to be critically stressed in the Lemont area and thus have greater potential for fracture enhanced permeability. This is especially true for faults proximal to granite contacts in the stress model [Holgate, 2011].

Bringing these findings together, Figure 6.23 presents aeromagnetic lineaments superimposed on upper crustal depth slices through the preferred resistivity model and a gridded granite topography image derived from granite topography contour maps of Leaman [2012]. Here, in panels A, B and C, the central low resistivity zone annotated as **C2** previously appears to manifest just to the north of the junction between two major lineaments; an arcuate northwest-southeast trending lineament and a north-south trending lineament. This location also marks the point at which the northwest-southeast trending lineament crosses a step change in residual Bouguer anomaly gravity interpreted as a shelf in granite surface topography by Leaman [2012] (panel D in Fig. 6.23).

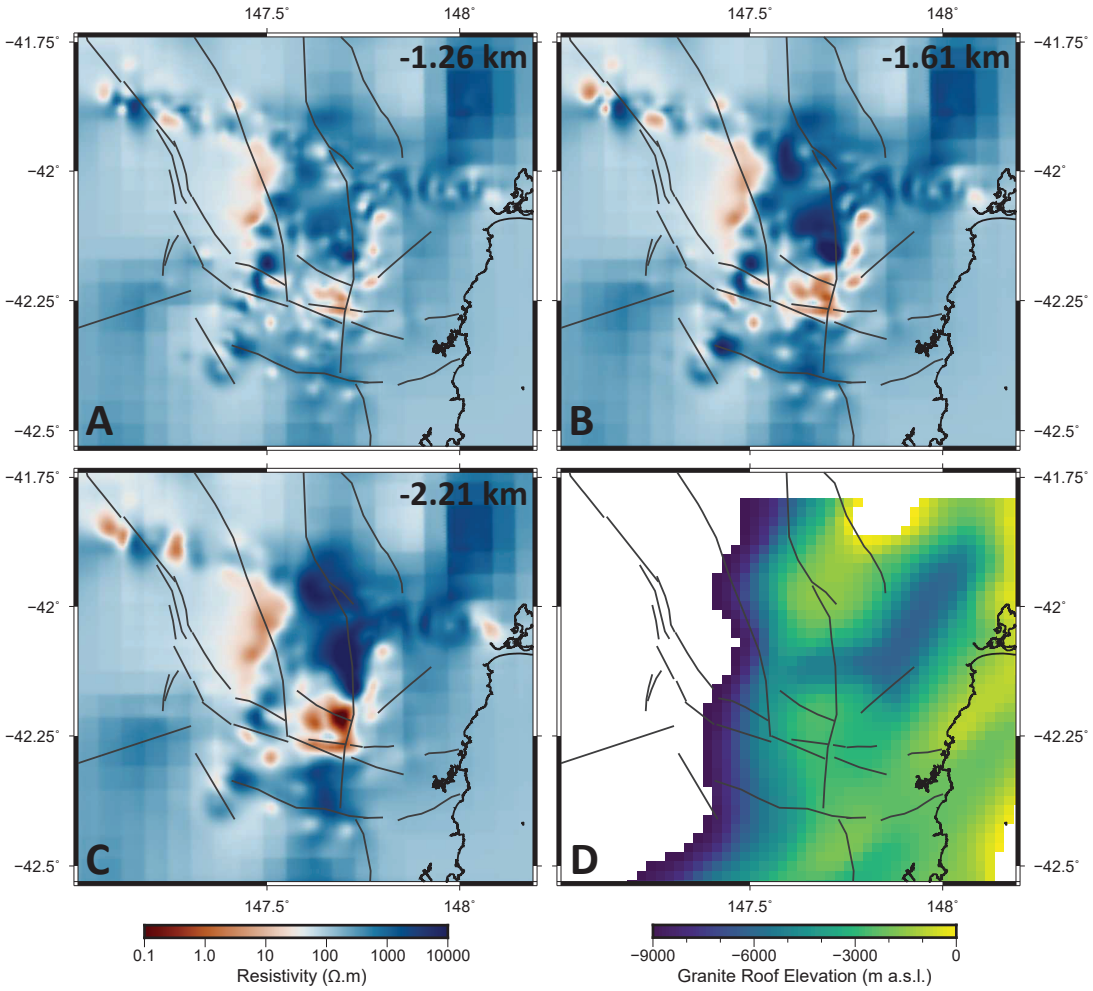

Figure 6.23: Aeromagnetic lineaments overlain onto depth slices through inverse model 3 (panels A, B and C) and gridded granite topography data of Leaman [2012] (panel D). Depth of resistivity model slices is given in the top right hand corner of each panel.

The close spatial relationship between low resistivity zones, aeromagnetic lineaments and

granite topography is best illustrated in 3D. Figures 6.24 and 6.25 present screenshots from Geoscience Analyst depicting the preferred model volume with granite topography plotted as a semi-transparent purple surface. Here the central low resistivity zone (**C2**) is clearly visible just below a narrow ridge in granite topography. Plotting low resistivity zones as isosurfaces provides another means of highlighting the relationship between resistivity, granite surfaces and inferred fault structures.

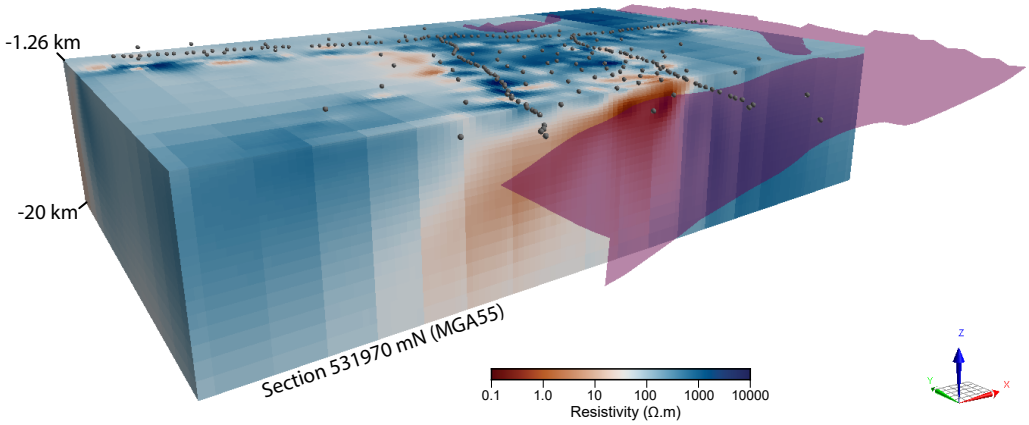

Figure 6.24: Oblique view from the southwest of parallel projected inverse model 3 model space sliced to a uppermost depth of 1.26 km and cross sectioned along the central low resistivity zone. The model space has been clipped to a vertical extent of 20km and stripped of lateral padding cells. The semitransparent purple surface represents the top of subsurface granites derived from Leaman [2012], while grey spheres represent the spatial location of the MT sites used in inversion. For more 3D visualisation of the preferred model the reader is referred to Appendix C.

In Figures 6.27, 6.28, 6.29 and 6.30; the 3D structure of low resistivity zones is depicted by pink isosurface volumes encapsulating regions of the preferred model space with resistivities less than 1 Ω m. In Figures 6.29 and 6.30, aeromagnetic lineaments have been projected to a depth of 7 km as semi-transparent red 3D surfaces using dip and dip direction information taken from Holgate [2011]. Despite high uncertainties in dip and dip directions, which compound with increasing depth, these inferred fault planes show remarkable correlation with low resistivity 1 Ω m structures in the preferred model. This relationship is most probably causal, and is likely diagnostic of fluid filled fracture networks surrounding these inferred fault structures.

Another observation of note is the tendency for the low resistivity zones to mostly reside beneath the modelled granite surface at upper- to mid-crustal depths spanning 5 km to 10 km. In cases where low resistivity regions breach the granite surface, this occurs along narrow conduits proximal to the inferred granite-fault interface. This may reflect a temperature control on minimum resistivities, as fault-fracture fluids within radiogenically heated granites are likely to be significantly hotter than fluids located distal to the granites. Nesbitt [1993] investigated resistivities of typical crustal fluids and found that resistivities tend to decrease steadily from near surfaces temperature to minimum resistivities at around 250 °C to 300 °C, after which

resistivities are largely constant with temperature. This temperature dependency is constant across varying fluid salinities, and shows up to an order of magnitude decrease in resistivity across the temperature ranges observed.

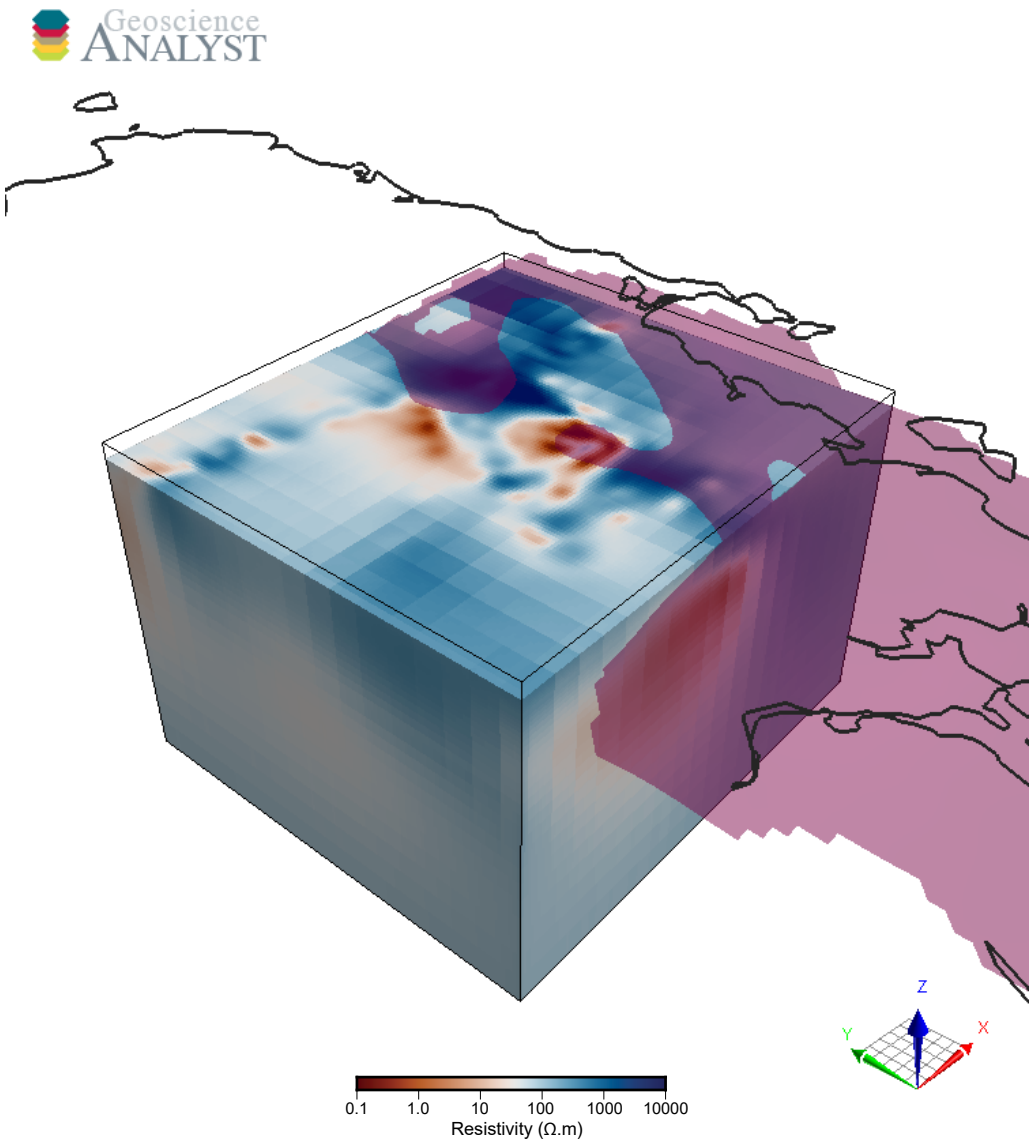

Figure 6.25: Oblique view from the southwest of parallel projected inverse model 3 model space sliced to a uppermost depth of 3.06 km. The model space has been clipped to a vertical extent of 60km and stripped of lateral padding cells. Black lines trace the east coast of Tasmania while the partly transparent purple feature represents the top of subsurface granites derived from Leaman [2012].

Heat flow modelling conducted by KUTh in 2009 using idealised geologic structure for the Lemont area informed by seismic reflection surveys to the west suggested peak temperatures of up to 200 °C at a depth of 5 km [Goh and Holgate, 2009]. The Lemont geothermal resource polygon presented in Figure 6.1 at the beginning of this chapter was derived from this geothermal modelling exercise and represents the 150 °C isotherm at 4 km depth in the model. At

these temperatures any fluids trapped in fracture networks are approaching their minimum temperature-dependent resistivity, and are likely to be ∼½ an order of magnitude less resistive than they would be at surface. For fluids with salinity comparable to sea water (3.6 wt%), temperatures of 150 °C translates to resistivities in the order of 0.05 Ω m. Fluids with higher salinities in the order of ∼15 wt% tend give resistivities of ∼0.02 Ω m at these temperatures [Nesbitt, 1993].

With plausible ranges for the electrical resistivity of pore space fluid, it is possible to derive porosity estimates from bulk rock resistivity data inferred by the preferred model using Archie's Law [Archie, 1942]. Understanding the likely range of porosity values within the model space allows for an assessment of the probable conduction mechanisms at play, and also has implications for the density structure of the subsurface. For example, a granite with a density of 2.75 g cm^{-3} fractured to a porosity of 10% and saturated with saline fluids of density 1.05 g cm^{-3} gives rise to a decrease in bulk density of ∼6.2%. Since the granite topography surface of Leaman [2012] is derived from gravity data and assumes no porosity, it is possible that regions with significant porosity enhancement and associated density reduction may have erroneously shallow granite roof topography estimates. For a comprehensive treatment of the relationship between electrical resistivity, porosity and bulk density in the context of MT resistivity models, the reader is referred to Maier [2011].

Figure 6.26 presents porosity estimates derived using Archie's Law for bulk resistivities between 0.1 Ω m and 10 Ω m with fluid resistivities in the range 0.01 Ω m to 0.1 Ω m. It should be noted that this approach to estimating porosity is highly idealised as it does not take into account conductive phases other than pore space fluids, or the nature of the connection between pores. Glover [2010] developed a generalised formulation of Archie's Law to take into account other conductive phases, but an application of this would require a great number of assumptions about the mineralogy of the mid- to upper-crust beneath the Lemont resource and is beyond the scope of this thesis.

Continuing with Archie's Law, and assuming fluid resistivities of 0.02 Ω m for moderately saline (15 wt%) water at temperatures of ∼150 °C, the region of the model space encapsulated by the 1 Ω m isosurfaces in Figures 6.27 6.28, 6.29 and 6.30 would return porosities ranging between ∼15% and ∼40%. Given the ∼2 km depths at which minimum 0.1 Ω m resistivities manifest within the isosurfaces, lithostatic pressures make a such porosity values for these regions geologically implausible, and complimentary conduction mechanisms are required to account for these very low resistivities.

Candidates for conduction mechanisms contributing to very low resistivities within the central low resistivity zone include clay minerals, graphite and possibly granite-related sulfide mineralisation along major fault networks. Smectite clay minerals forming in low temperature, high porosity and shallow parts of hydrothermal geothermal systems have been observed to contribute to anomalously low resistivities [Heise et al., 2008], and may play a role in the Lemont

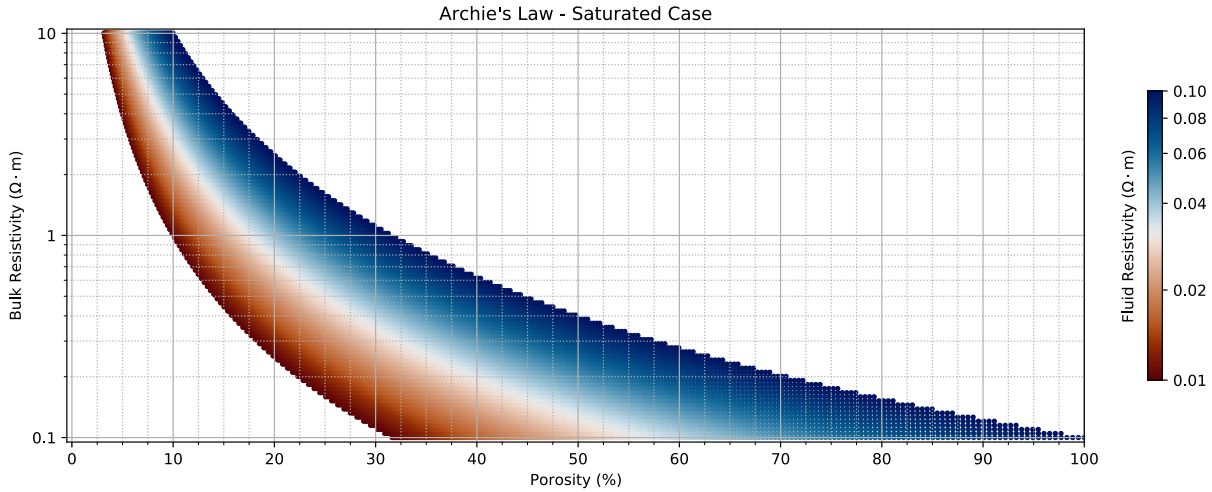

Figure 6.26: Plot populated by 20,000 porosity estimates computed using Archie's Law for bulk resistivity values found in conductive regions of the preferred model and typical high temperature saline fluid resistivity values. Computation assumed 100% fluid saturation, a cementation exponent of 2 and a tortuosity factor of 1.

system. Given the depths at which minimum resistivities manifest in the model space, and the apparent fracture-related structure of the minimum resistivity regions it is likely that other mechanisms are at play in addition to clay minerals.

Graphite may be sourced from basement lithologies below Permo-Triassic Tasmania Basin sediments, with a single drill hole (RG146) intersecting 'folded carbonaceous hornfels' some ∼30 km northwest of the central low resistivity zone outside the sensitivity range of the KUTh MT data set [Forsyth, 1989]. Graphitisation of these lithologies within the contact aureole of granites with subsequent mechanical concentration of graphite into fault networks may explain minimum resistivities proximal to the granite roof at locations transected by faults [Cao and Neubauer, 2019, Crespo et al., 2005].

A second, possibly complimentary, mechanism invokes the deposition of highly conductive sulfide minerals from granite-derived fluids at the time of granite emplacement along planes of weakness that today present as major, recently activated fault systems. This analysis is reminiscent of the Renison Bell tin deposit in western Tasmania, where calcareous sedimentary units and cross-cutting fault systems are extensively (pyrrhotite-pyrite) mineralised by fluids emanating from the Devonian Renison Granite [Bajwah et al., 1995, Kitto, 1992]. These sulfide-rich zones are highly conductive [Bishop et al., 1987], dense and magnetically susceptible, making them ideal geophysical targets [Roberts and Mudge, 1997]. Pyrrhotite mineralisation of the type and magnitude seen at Renison Bell is unlikely at Lemont however, as this would necessarily give rise to strong magnetic anomalism which is not present in aeromagnetic data sets (Fig. 6.21). The most likely explanation for very low resistivities within the central low resistivity zone involves some degree of fracture related pore space electrolytic conduction enhanced by contact metamorphism derived graphite, or low magnetic susceptibility pyrite mineralisation

along fault networks, or both.

A general interpretation of the nature of heat flow within the Lemont survey area is that it is facilitated by crustal scale faults active as recently as the Paleocene that pierce hot granites at depth. Convective heat transport along fault-related fracture networks, imaged by the preferred resistivity model as low resistivity zones emerging from the granite surface, may explain anomalous surface heat flow measurements in the Lemont area. This is supported by the observation that two of the three highest heat flow measurements recorded by KUTh are located in close proximity to the central north-south trending fault zone, with the maximum heat flow measurement ($118\,\mathrm{mW\,m^{-2}}$) taken proximal to the junction of this lineament and the northwest-southeast trending lineament (see coloured spheres in Figs. 6.27 to 6.30). This is consistent with the 'Naturally Fractured Hot Rock' geothermal play conceptual model of Holgate [2011].

A highly resistive region in the upper $\sim$3 km of the preferred model is found to the north of the central low resistivity zone (Fig. 6.15). Resistivities in excess of $1000\,\Omega\,\mathrm{m}$ represent a one to two order of magnitude increase in resistivity in this part of the model space relative to the AusLAMP starting model (Fig. 6.18). Curiously, this resistive structure (previously referred to as **R2**) is cross-cut by the same north-south trending aeromagnetic lineament as the anomalously conductive region to the south, and appears to include granite as well as Mathinna bed host rocks (Fig. 6.23). Such high resistivities, which are consistent with the upper bounds of typical resistivities observed for old sediments and within the resistivity range of crystalline rocks [Haak and Hutton, 1986], effectively rule out the possibility of significant fracture networks associated with faulting along the cross-cutting aeromagnetic lineament.

At depths beyond 3 km in the preferred model, the high resistivities associated with upper crustal resistor **R2** migrate to the the east and northeast. Higher resistivities in the east of the preferred model relative to the AusLAMP starting model is a consistent feature throughout the depth sensitivity range of the KUTh data set (Figs. 6.18 to 6.19). This is most pronounced in the upper crust, above 10 km, and reflects the sensitivity of the KUTh data to high resistivities of unfractured Siluro-Devonian Mathinna sediments and crystalline Devonian granites underlying eastern Tasmania.

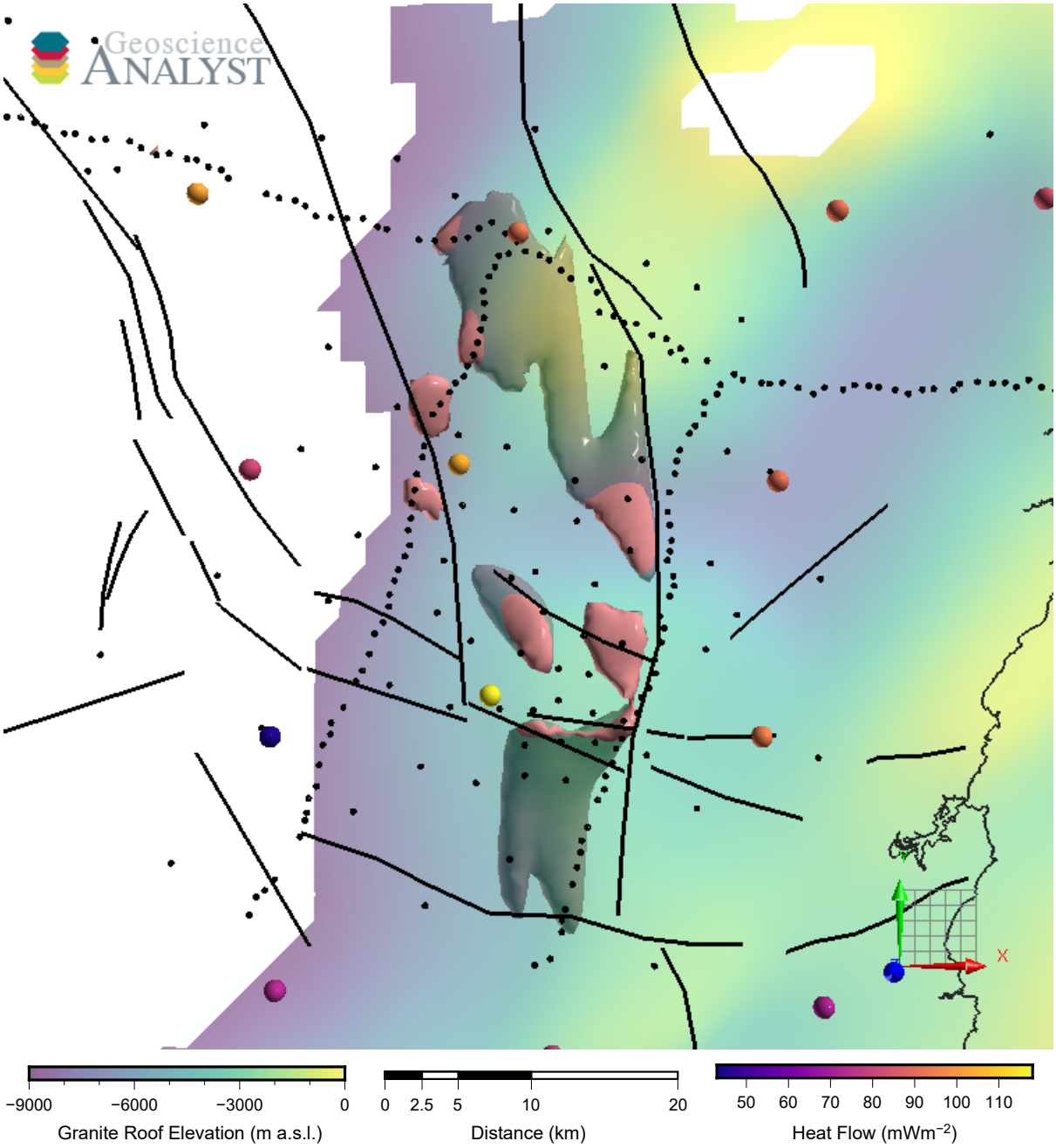

Figure 6.27: Birds eye view of the KUTh MT data set in an orthographic projection. Black dots represent the location of MT sites used in inverse modelling, thick black lines are aeromagnetic lineaments while the thin black line represents the east Tasmanian coastline. Large spheres are the locations of heat flow drill hole measurements coloured by heat flow. Granite topography is presented as a semi-transparent 3D surface coloured by depth. Pink shapes represent $1\,\Omega\,\mathrm{m}$ isosurface volumes derived from resistivity model 3 and clearly outline the most conductive regions of the model space.

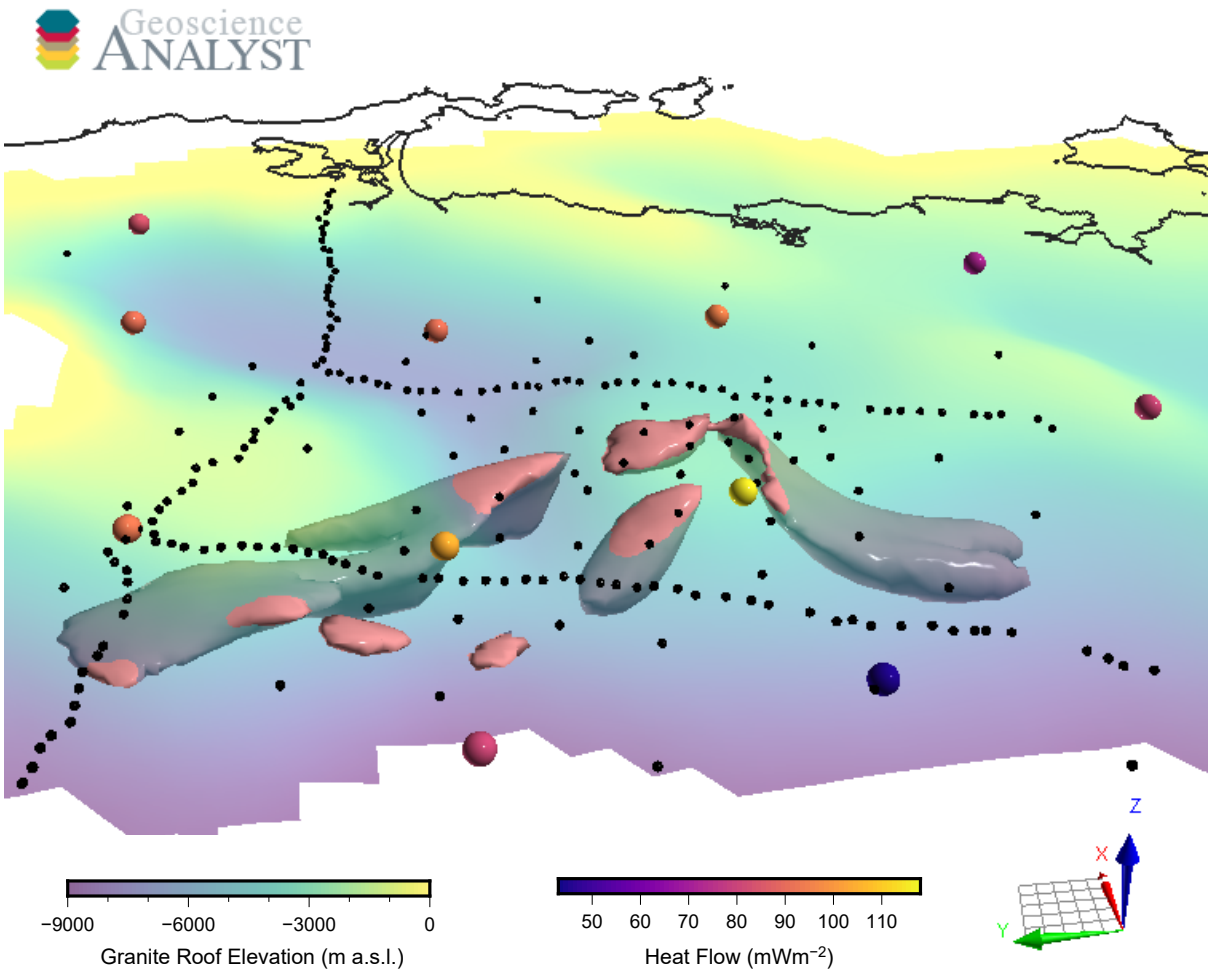

Figure 6.28: Oblique view from the west of parallel projected model space. Black dots represent the location of MT sites used in inverse modelling and the thin black line represents the east Tasmanian coastline. Large spheres represent the location of heat flow drill hole measurements coloured by heat flow. Granite topography is presented as a semi-transparent 3D surface coloured by depth. Pink shapes represent 1 Ω m isosurface volumes derived from resistivity model 3 and clearly outline the most conductive regions of the model space. Scale bar is absent due to parallel projection however the horizontal separation between the two north-south trending MT transects is ∼20 km, as shown in Figure 6.27.

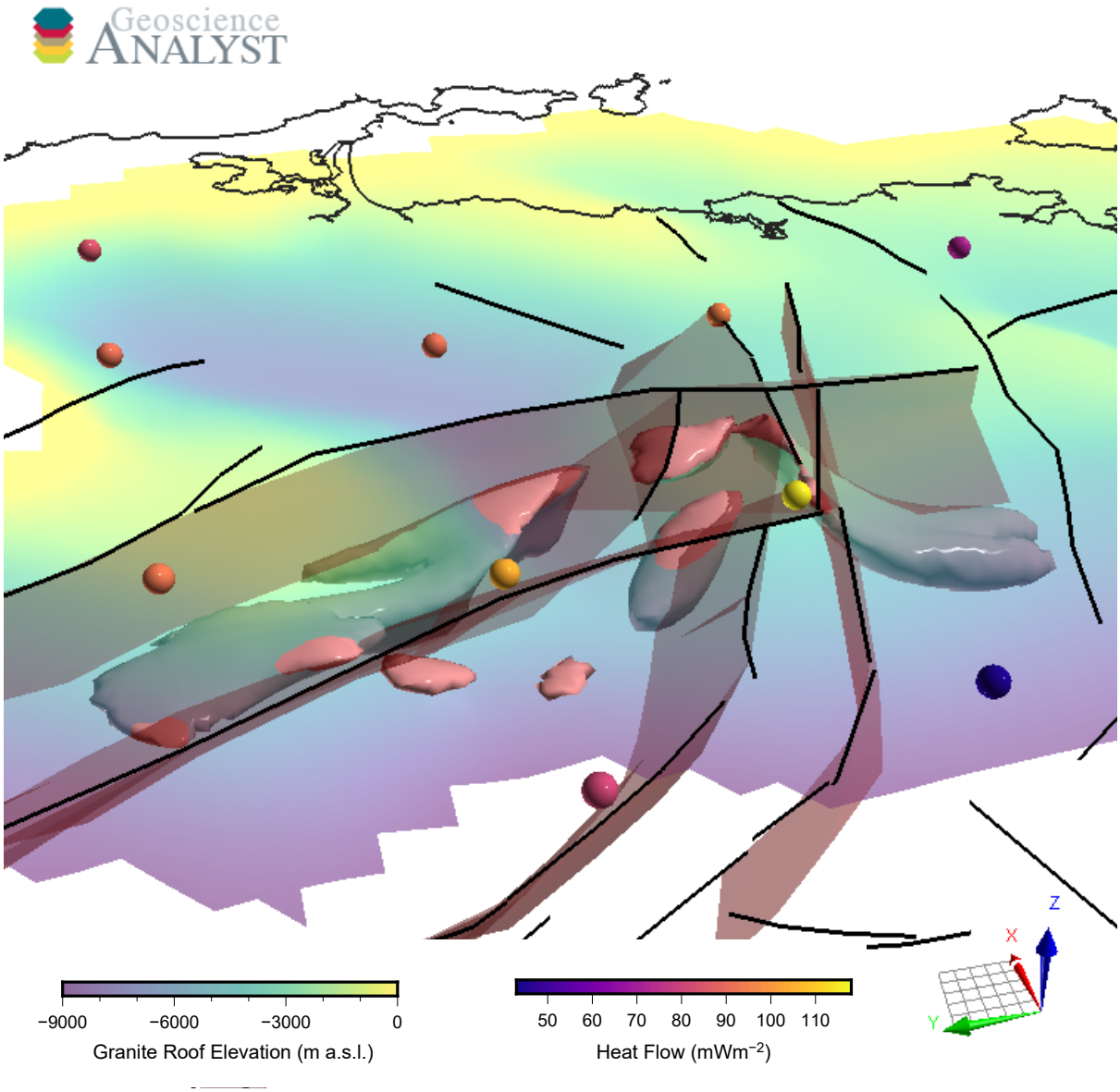

Figure 6.29: Oblique view from the west of parallel projected model space similar to that shown in Figure 6.28. Thick black lines are aeromagnetic lineaments and the thin black lines are the east Tasmanian coastline. Large spheres represent the location of heat flow drill hole measurements coloured by heat flow. Fault planes derived from simplified aeromagnetic lineaments are shown as semi-transparent red 3D surfaces. Rounded pink shapes are resistivity isosurfaces encapsulating regions of the preferred resistivity model where resistivities are $<1\,\Omega\,\mathrm{m}$. Refer to Figure 6.28 for an explanation of scale.

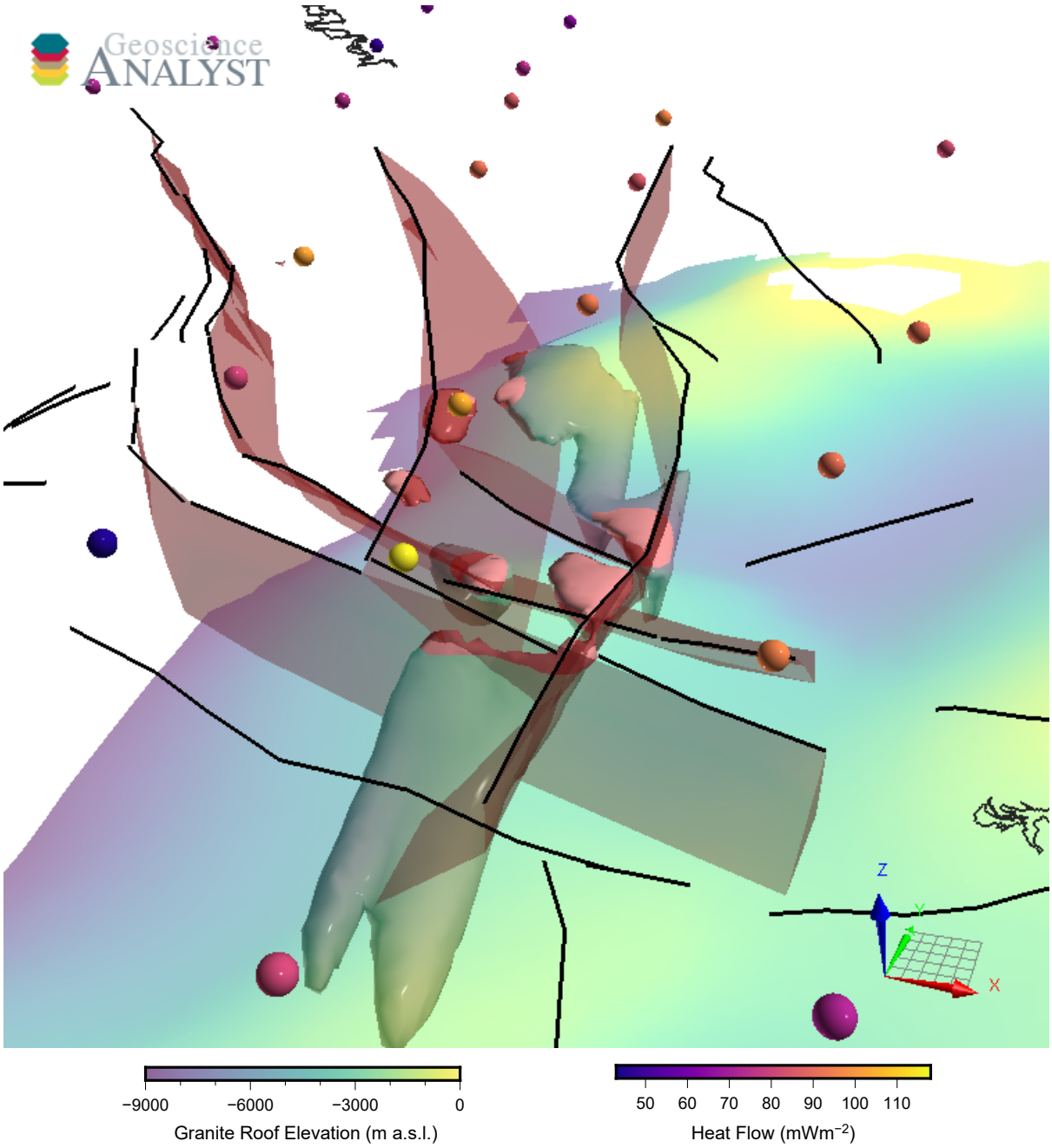

Figure 6.30: Oblique view from the southeast of parallel projected scene shown in Figure 6.29.

6.5.1 Comparison with WesternGeco-Geosystem 2010 3D Model

The 2010 WesternGeco-Geosystem model, hereby referred to as the WesternGeco model, utilised an in-house inversion algorithm which, like ModEM3DMT, relies on a 3D application of the 2D non-linear conjugate gradient (NLCG) method described by Rodi and Mackie [2001]. Despite the similarity in approach, the two inversion schemes arrive at quite different geoelectric structure over the Lemont area. These differences in inverse model structure appear to arise from differences in the respective algorithm's approaches to accounting for galvanic distortion in the KUTh data set.

Mesh Parameters		**Data Parameters**	
Horizontal Resolution	800m X 800m	$\mathbf{Z}_{xy}$ & $\mathbf{Z}_{yx}$ error floor	3%
Starting Resistivity	20 Ω m	$\mathbf{Z}_{xx}$ & $\mathbf{Z}_{yy}$ error floor	20%
Top Cell Thickness	30 m	$\mathbf{T}_x$ & $\mathbf{T}_y$ error floor	0.2
Mesh Rotation	16° from N	Static Shift Variance	10%
Total Cells	1,341,648	Number of Frequencies	21
Number of Padding Cells	10 in x and y	Frequency Range	0.003 Hz to 300 Hz

Table 6.4: WesternGeco inversion mesh and data parameters.

As discussed in the results section, ModEM3DMT accounts for galvanic distortion inherent in the data by placing geoelectric structure in the uppermost cells of the model space in close proximity to the MT sites. By contrast, the WesternGeco inversion scheme models galvanic distortion directly by explicitly fitting apparent resistivity static shifts in the data.

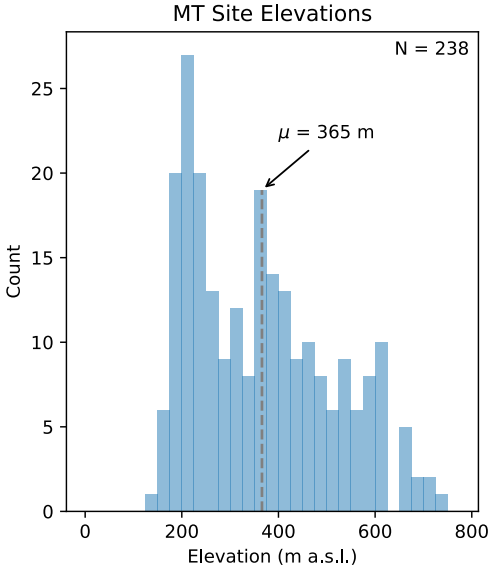

Figure 6.31: Histogram of MT site elevations used in the WesternGeco 3D inverse model.

The extent to which static shifts are fitted by inversion is controlled by placing constraints on the total variance of predicted shifts, and tends to result in smoother models [Soyer et al., 2008]. Table 6.4 summarises key features of the WesternGeco model reported in Battaglini et al. [2010]. The tendency toward smoother models when explicitly inverting for static shifts is immediately apparent when comparing the geoelectric structure of the WesternGeco and ModEM3DMT preferred model. The WesternGeco model has significantly less structure across all depth ranges, with less extreme resistivity minima and maxima relative to ModEM3DMT models. In order to illustrate this, in the form of depth slices, it is first necessary to consider an appropriate datum of comparison.

Ideally, depth slices in resistivity models should be taken relative to the location of the data. For the preferred ModEM3DMT model, which does not incorporate topography, this datum is represented by the flat top of the model space onto which data are projected prior to inversion. For the WesternGeco model this datum was taken as the arithmetic mean elevation of MT sites used in inversion, the distribution of which is presented as a histogram in Figure 6.31. All subsequent side-by-side depth slice plots present depth slices from mesh nodes at comparable depth in ModEM3DMT and WesternGeco models using this mean site elevation as a datum.

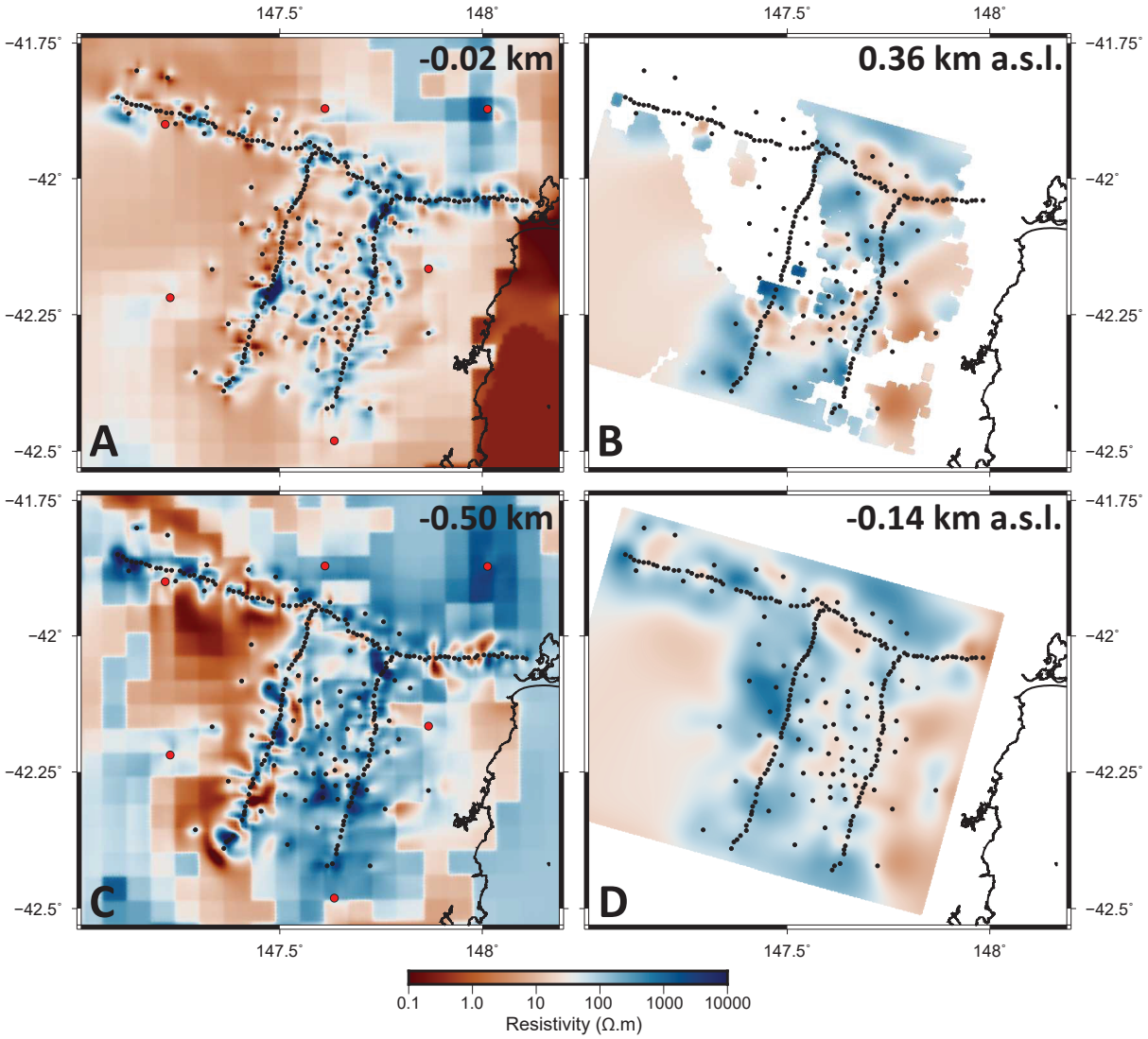

Figure 6.32: Depth slices through Lemont resistivity models. Panels A and C present depth slices through the preferred model while panels B and D present slices through the WesternGeco model. Panels are arranged such that preferred model slices on the left are the depth in model space equivalent of WesternGeco slices on the right. WesternGeco model slices are shown without padding cells.

Figures 6.32 to 6.37 present depth slices through the preferred model (panels A and C) and the WesternGeco model (panels B and D). The influence of explicit galvanic distortion modelling on the inverse model structure is most obvious when comparing shallow depth slices

from the two models in Figure 6.32. Here the preferred model is dominated by high spatial frequency resistivity structure. At this depth resistivity structure in the WesternGeco model is, by contrast, far smoother with roughly three orders of magnitude less total variance in resistivity values.

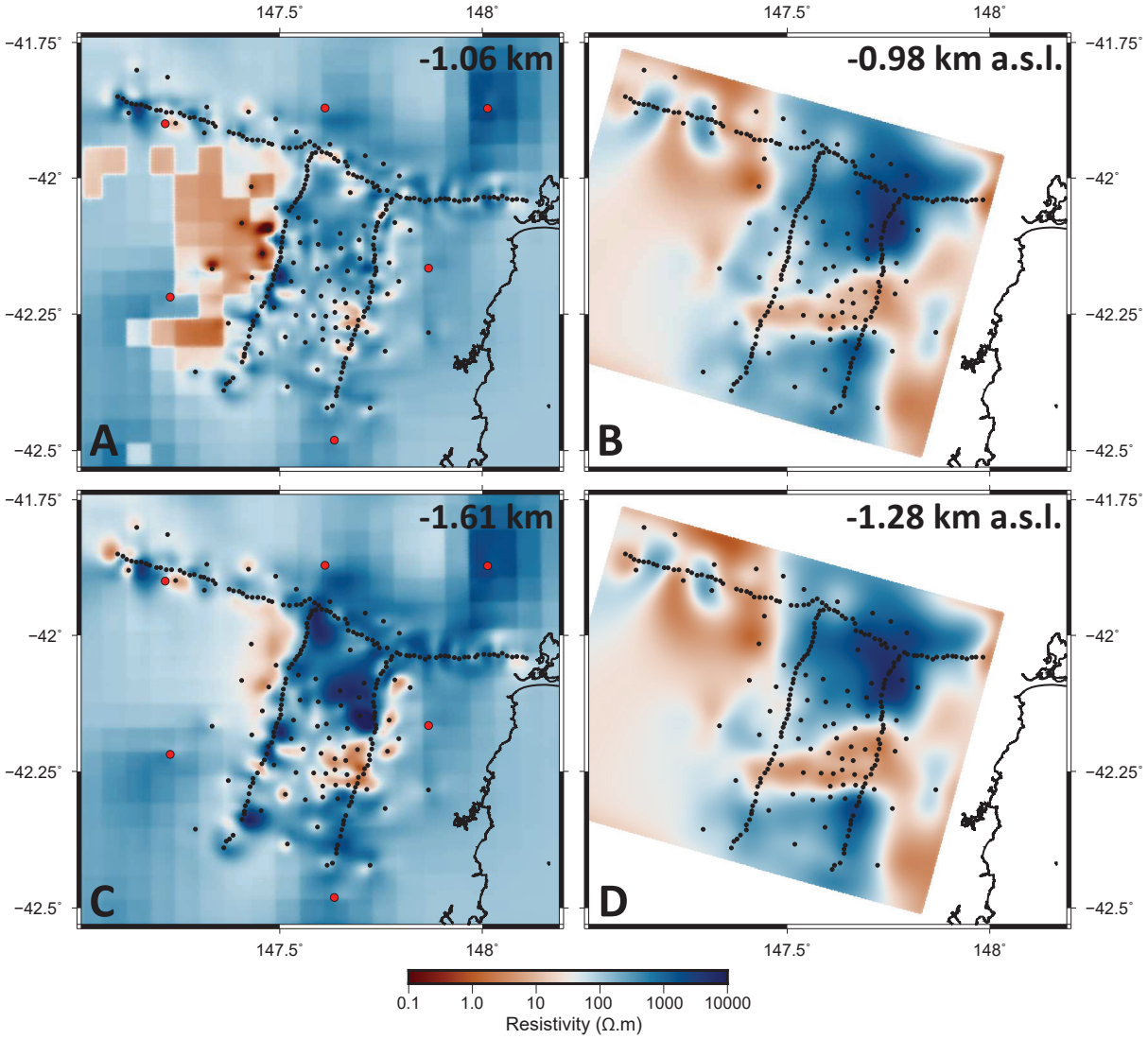

Figure 6.33: Depth slices through Lemont resistivity models. Panels A and C present depth slices through the preferred model while panels B and D present slices through the WesternGeco model. Panels are arranged such that preferred model slices on the left are the depth in model space equivalent of WesternGeco slices on the right. WesternGeco model slices are shown without padding cells.

At deeper levels in the model spaces, below the preferred model's low resistivity layers inherited from the AusLAMP OzSEEBASE sediment layer, the WesternGeco model has much higher total resistivity variance than shallower levels. There is good first order agreement between the models, with both models returning high resistivity in central northeast of the data set as well as low resistivity in the central portion of the data set discussed previously as the central low resistivity zone (**C2**). Another illustration of the first order similarity in model

structure is presented in Figure 6.38 as a north-south transect through the centre of the model spaces.

Despite major similarities, the WesternGeco model is considerably smoother in its overall structure and appears to more readily extrapolate resistivity values outside of the sensitivity range of the data and between MT sites separated by significant horizontal distances. The low resistivities situated off-transect in the northwestern corner of the WesternGeco model in shallow surface Figures 6.33 and 6.34 illustrates this well.

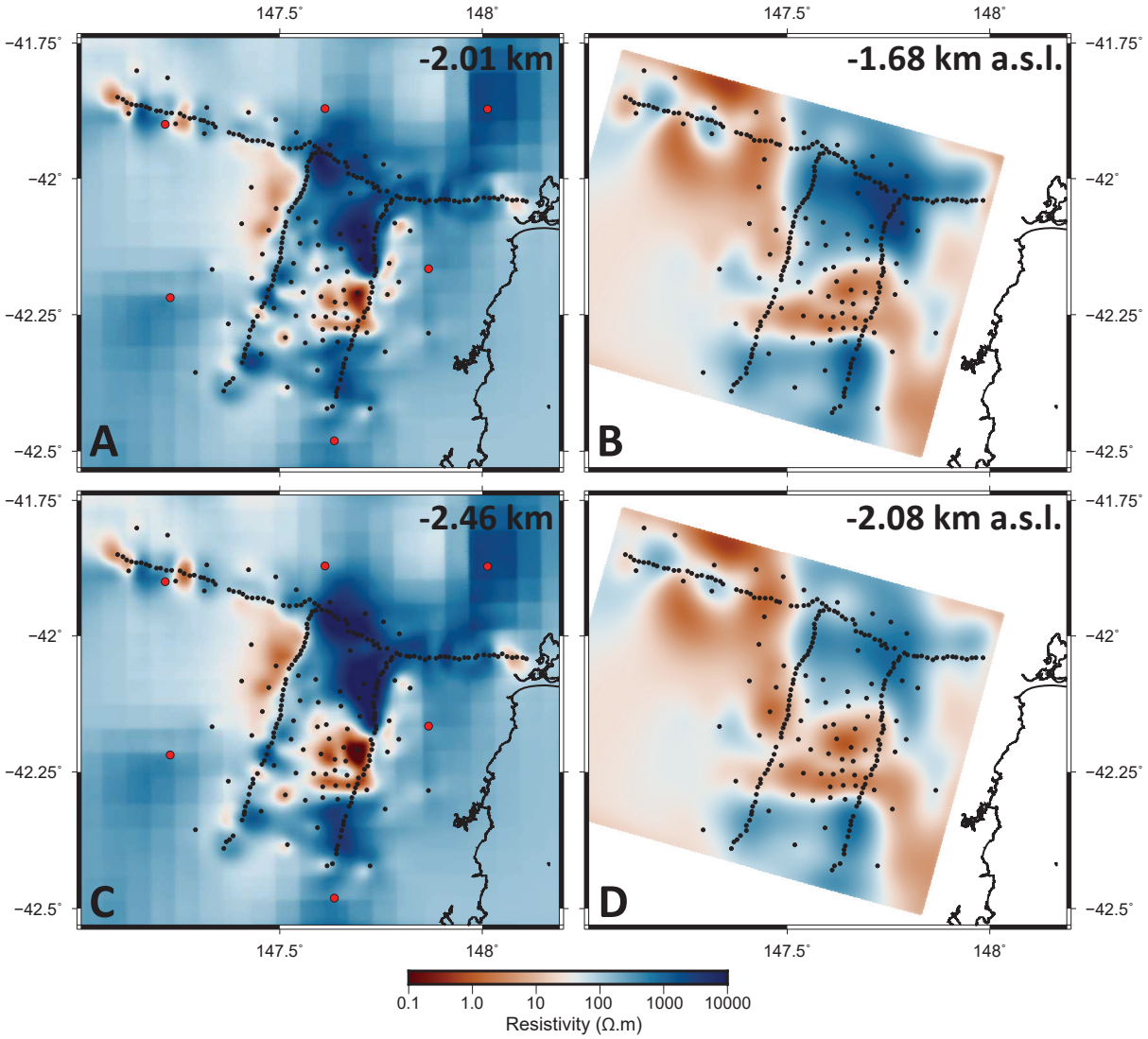

Figure 6.34: Depth slices through Lemont resistivity models. Panels A and C present depth slices through the preferred model while panels B and D present slices through the WesternGeco model. Panels are arranged such that preferred model slices on the left are the depth in model space equivalent of WesternGeco slices on the right. WesternGeco model slices are shown without padding cells.

Another feature of the WesternGeco model is a tendency of low resistivity zones to be flattened in the vertical direction relative to the preferred model. This isn't easily visualised in 2D, but is clearly illustrated in 3D screenshots depicting isosurface volumes shown in Figure

6.39. This structural distinction at the extreme end of low resistivity in the two models is of particular interest as these structures represent potential targets for geothermal exploration activities.

Another distinction between the models is the comparatively limited extent to which low resistivity structures in the WesternGeco model correlate spatially with inferred fault planes. This, coupled with geologically questionable vertical concentration of low resistivity structures, and a far greater degree of smoothing throughout, make the preferred ModEM3DMT model a more feasible model of subsurface geoelectric structure.

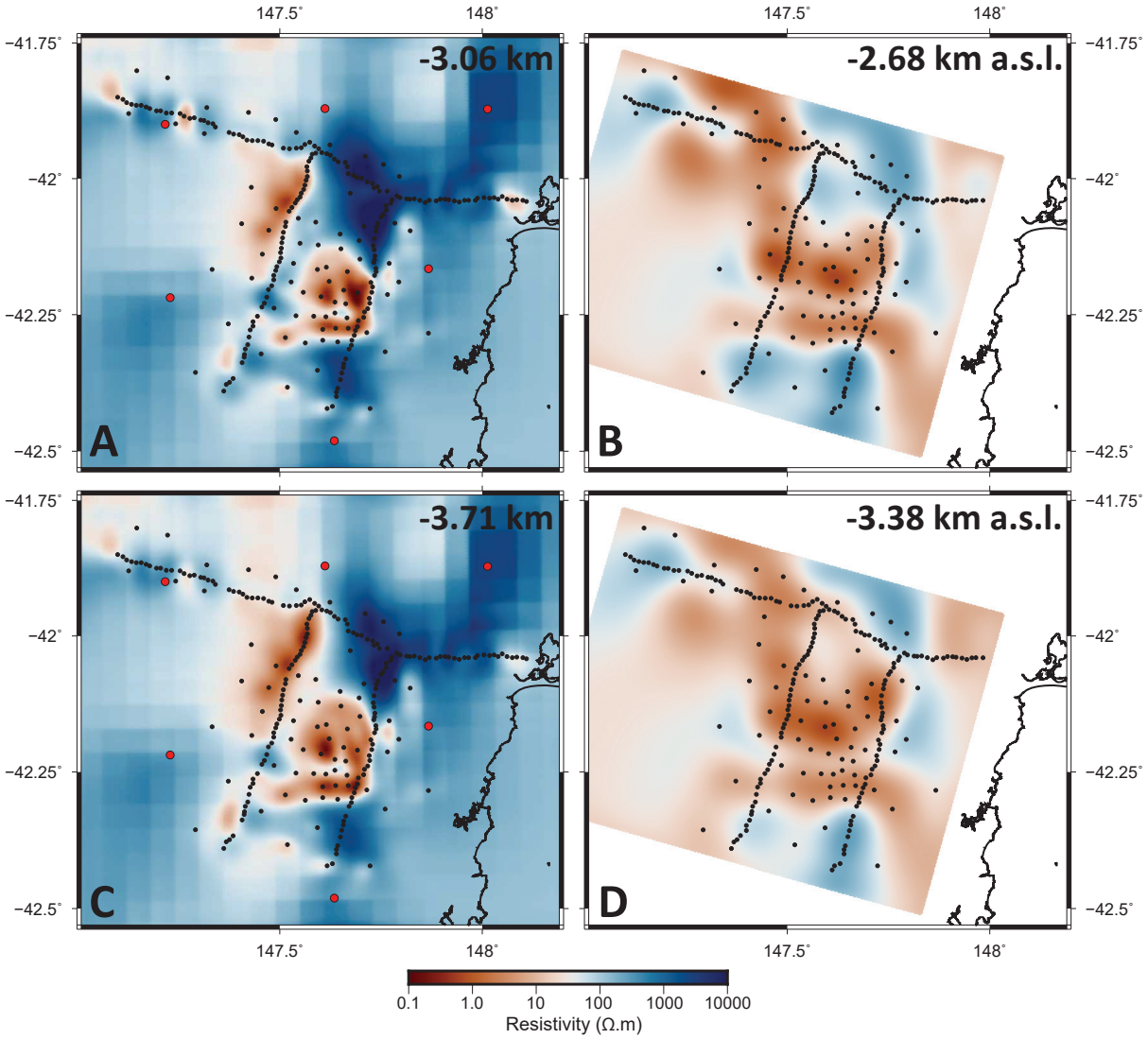

Figure 6.35: Depth slices through Lemont resistivity models. Panels A and C present depth slices through the preferred model while panels B and D present slices through the WesternGeco model. Panels are arranged such that preferred model slices on the left are the depth in model space equivalent of WesternGeco slices on the right. WesternGeco model slices are shown without padding cells.

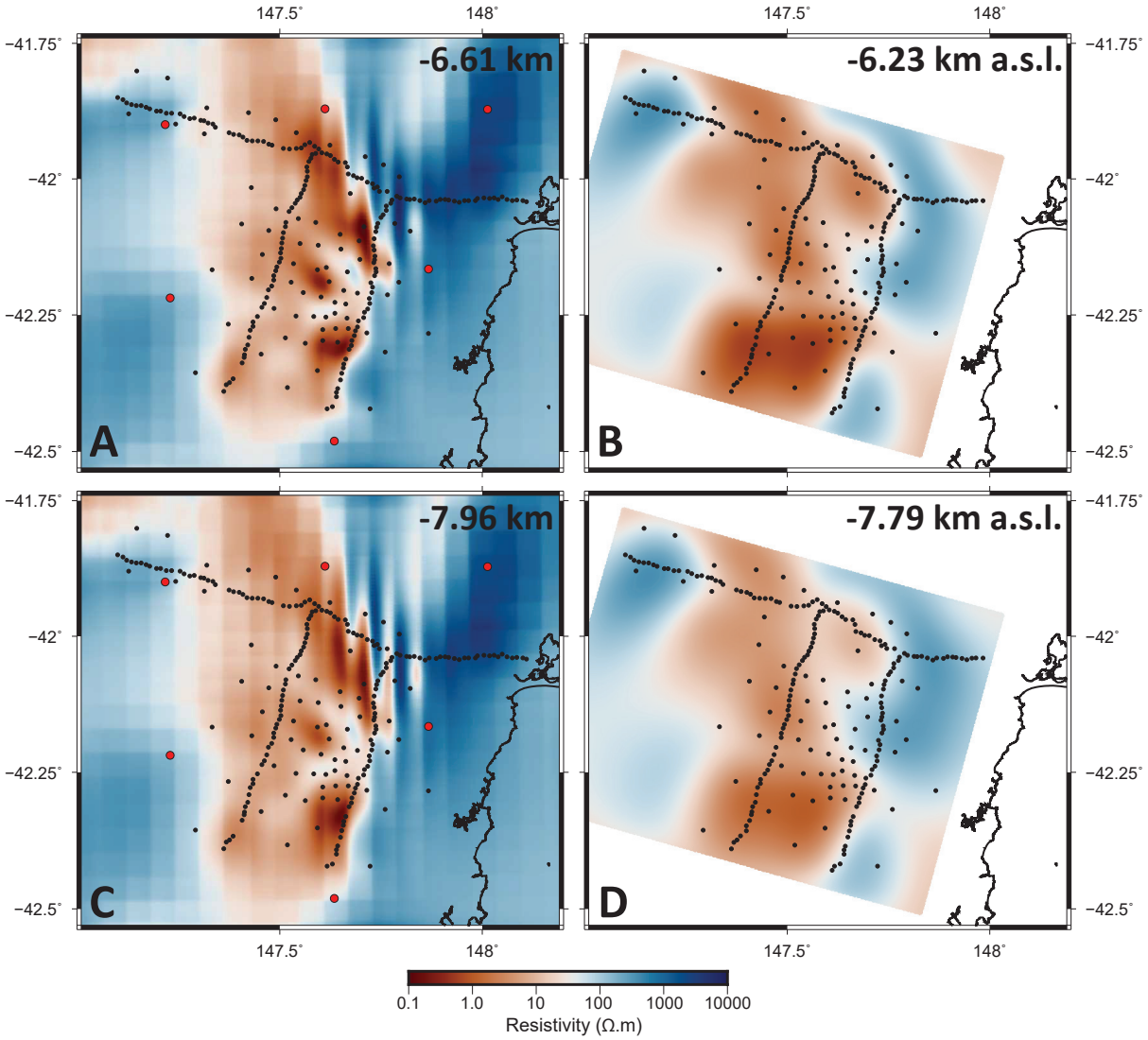

Figure 6.36: Depth slices through Lemont resistivity models. Panels A and C present depth slices through the preferred model while panels B and D present slices through the WesternGeco model. Panels are arranged such that preferred model slices on the left are the depth in model space equivalent of WesternGeco slices on the right. WesternGeco model slices are shown without padding cells.

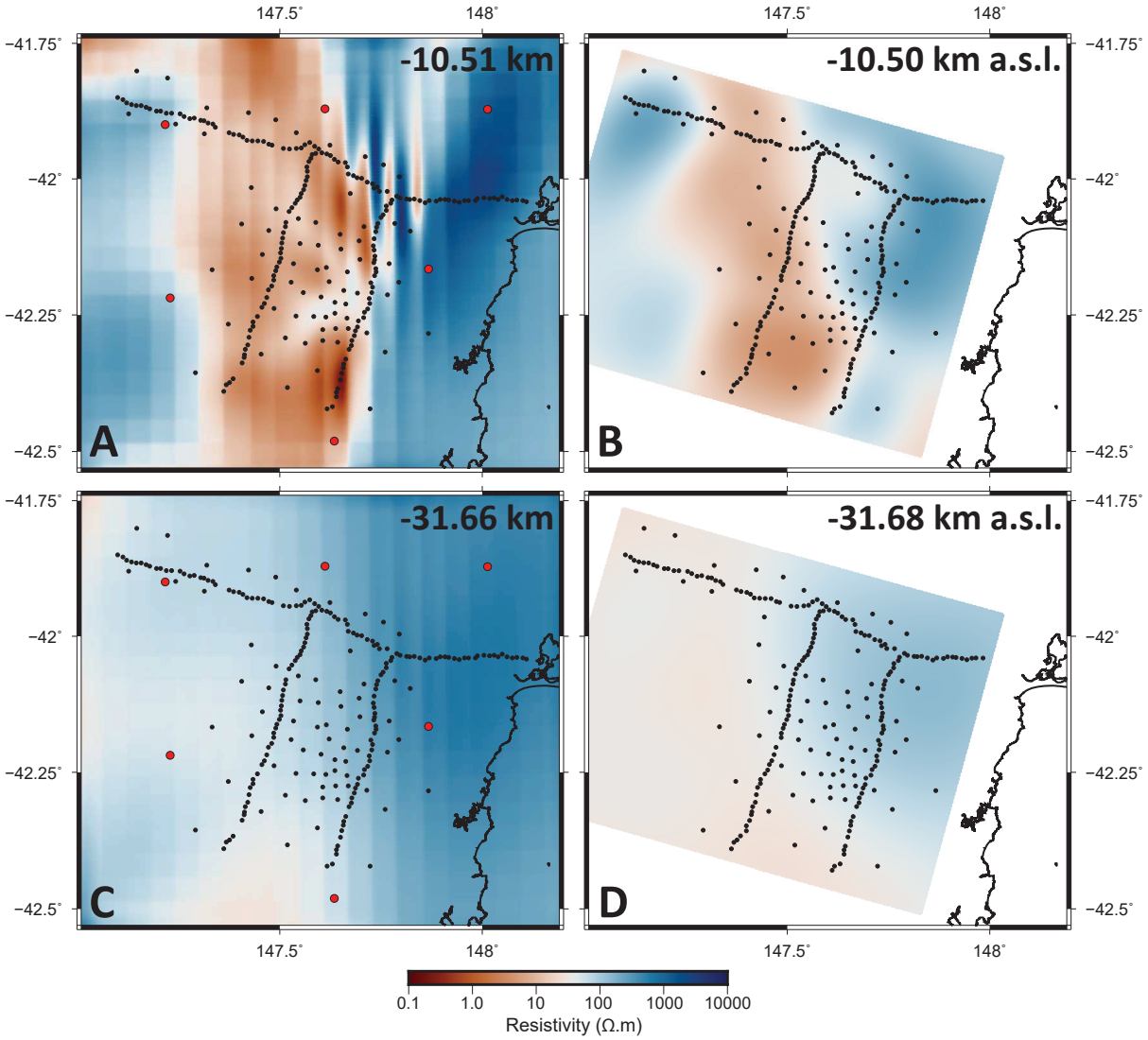

Figure 6.37: Depth slices through Lemont resistivity models. Panels A and C present depth slices through the preferred model while panels B and D present slices through the WesternGeco model. Panels are arranged such that preferred model slices on the left are the depth in model space equivalent of WesternGeco slices on the right. WesternGeco model slices are shown without padding cells.

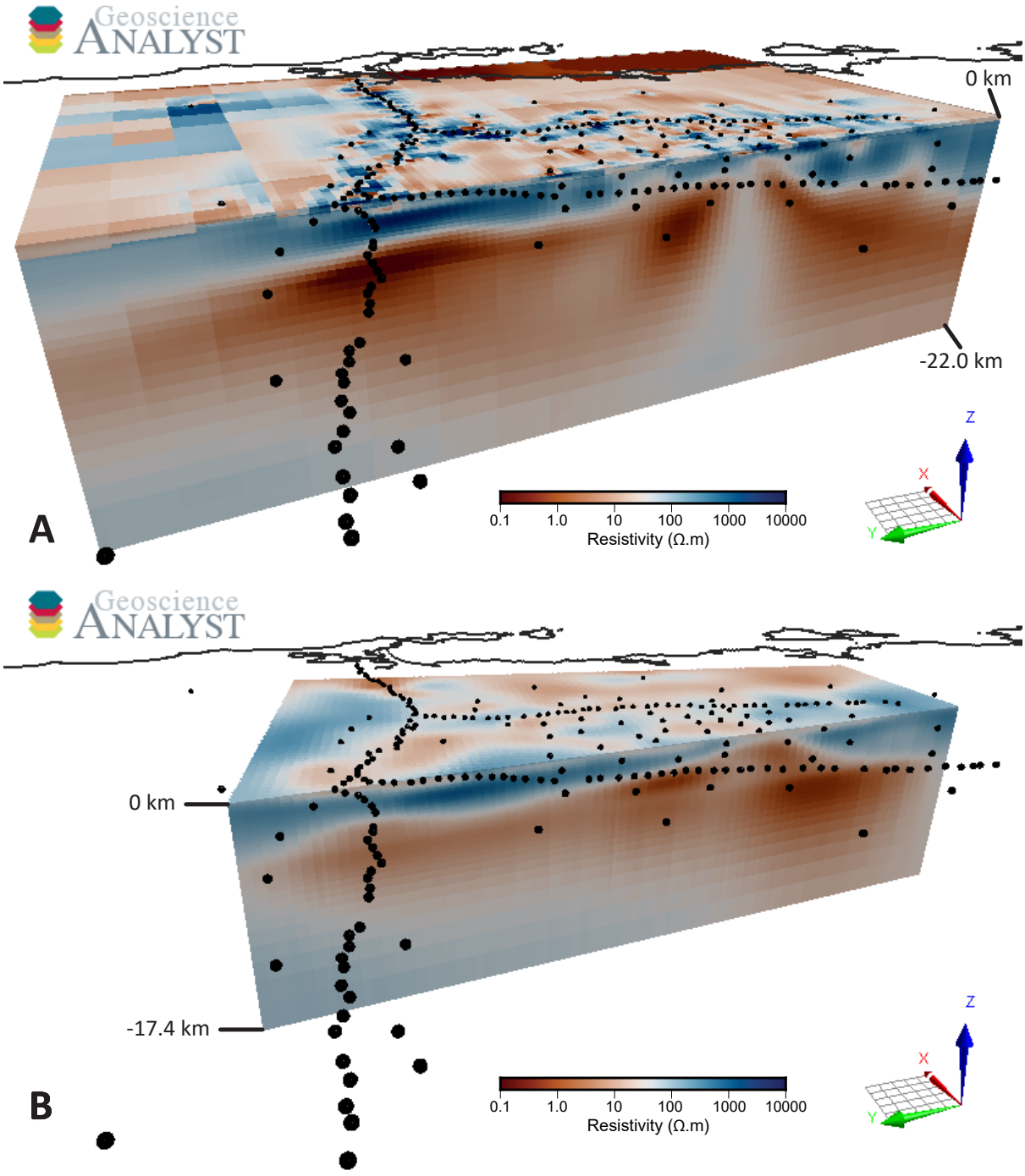

Figure 6.38: Oblique view from the northwest of parallel projected portions of the preferred model (panel A), and the WesternGeco model (panel B). Model volumes have been sliced in the north-south plane along the GDA94 UTM zone 55 548200 mE easting coordinate. Black dots represent KUTh and AusLAMP MT sites used in inversion of the preferred model. Black lines represent the east Tasmanian coastline.

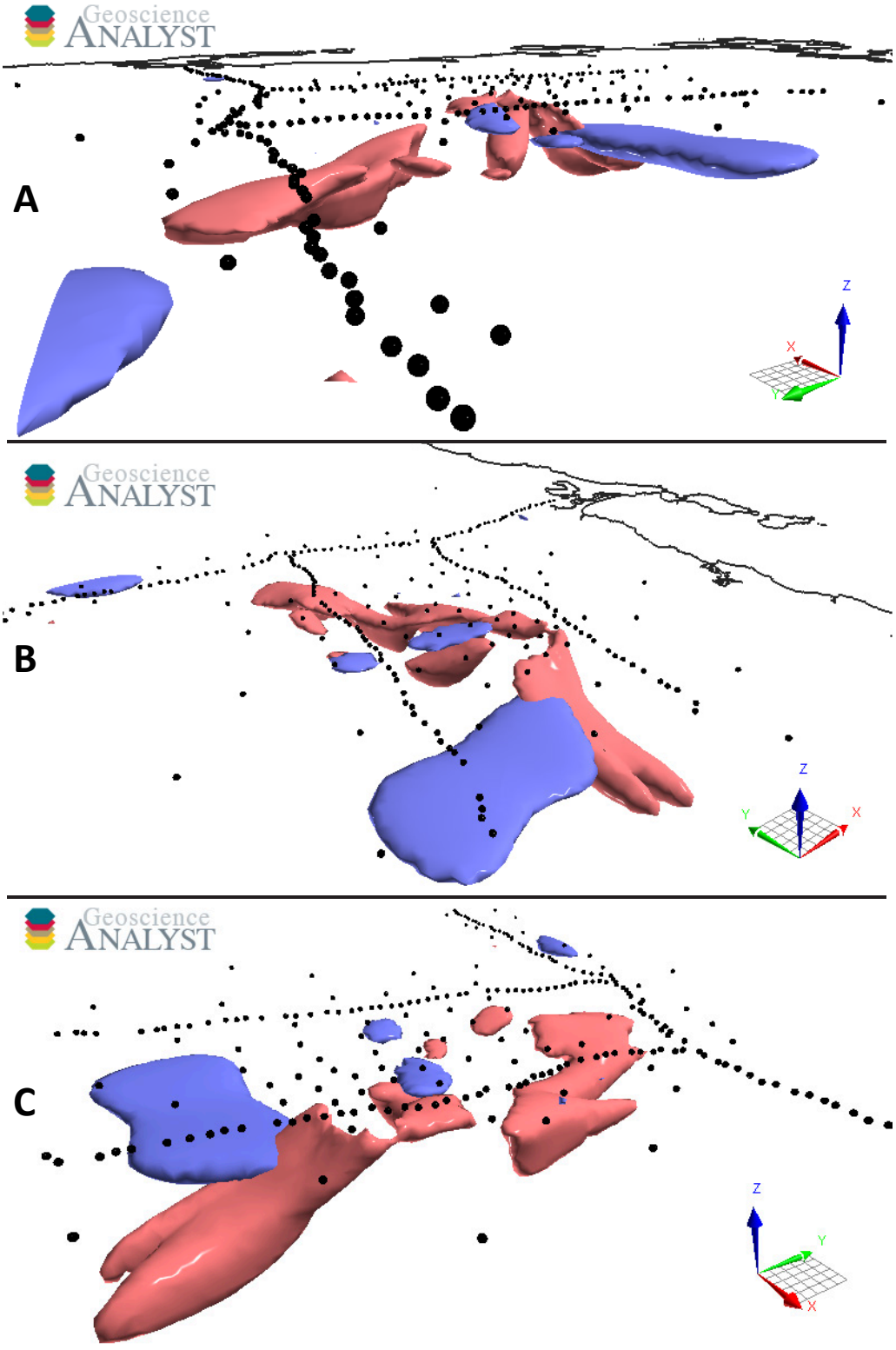

Figure 6.39: Parallel projected oblique views of 1 Ω m isosurfaces from the preferred model (pink) and the WesternGeco model (blue). Views A, B and C are separated by horizontal thick black lines and are taken from the northwest, southwest and southeast respectively. Black dots represent MT sites used in preferred model inversion while thin black lines represent the Tasmanian coastline.

6.6 Conclusion

This investigation has set out to incorporate new, regional-scale resistivity structure into an inverse modelling process combining legacy KUTh broadband MT data with newly acquired AusLAMP long period MT data. New models of the geoelectric structure surrounding the Lemont geothermal resource have been generated using the 3D inverse modelling code ModEM3DMT. Of the four models produced, interpretation of a preferred model was conducted utilising 3D visualisation software tools alongside all available geologic and geophysical data.

Interpretation of the preferred model gives high credibility to the existing conceptual model for the Lemont geothermal resource. Low resistivity structures in the new preferred model were found to be highly spatially correlated with recently active upper crustal fault networks, a result that was less clear in previous modelling. Very low minimum resistivities appear to manifest at the intersection of Devonian granite roof topography with inferred fault planes, and are attributed to fracture-induced porosity enhanced by some degree of clay, graphite or sulfide mineralisation along fault systems, or a mixture of three.

In comparison to previous inverse modelling conducted by WesternGeco, the new preferred model is of higher spatial resolution, contains more overall structure and is a better fit to the geological conceptual model of the Lemont resource. Differences in model structure between the WesternGeco model and the new preferred model are largely due to different algorithmic approaches to dealing with galvanic distortion inherent in the data. The approach taken by WesternGeco gives rise to a highly smoothed resistivity model that obscures resistivity structure potentially critical to geothermal targeting.

Geothermal energy is a high capacity factor, low-carbon source of energy that has seen little investment in Australia since the closure of the South Australian Paralana project in 2014. It is hoped that by bringing the geoelectric structure of the Lemont geothermal resource in sharper focus, the work documented in this thesis may contribute to the further development of the resource as an Enhanced Geothermal System.

6.6.1 Recommendations

Further investigation of the geoelectric structure in the Lemont area would benefit from the following activities, the first being of highest priority;

1. a second inverse modelling effort incorporating topography in the starting model as well as regional resistivity structure, and;

2. more MT sites infilling portions of the data set so as to improve model robustness around the central low resistivity zone, especially to the east of the eastern north-south traverse (see Fig. 6.40).

Given the high frequency nature of KUTh MT data set, with minimum signal penetration depths of ∼200 m, the inclusion of topography in future inversion would likely account for some static shift-like artefacts in inverse models, particularly in the shallow surface. The likely result of this is a better-fitting model with less geologically unfeasible high spatial resolution structure in the uppermost cells. Future inverse modelling efforts should also incorporate higher density meshes if computationally feasible, as this will likely improve model fit along tightly spaced transect lines.

Any future infill surveys should aim to improve model robustness around the central low resistivity zone. Constraining the eastern extent of the zone beyond the easternmost north-south transect is especially important. Suggested locations for infill surveys are presented in Figure 6.40.

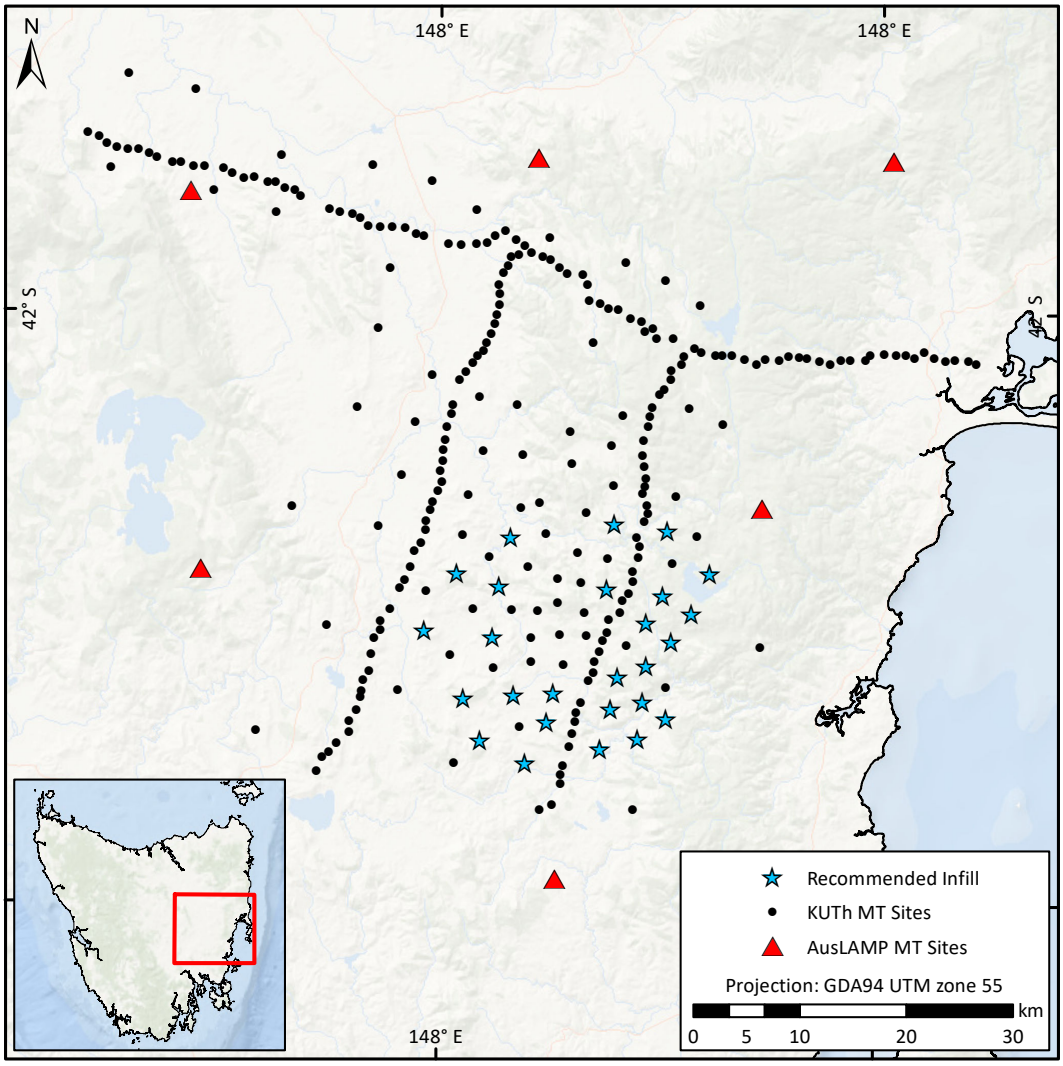

Figure 6.40: Recommended locations for infill surveys. Infill sites are designed to improve data coverage over the central low resistivity zone.

Chapter 7

Synthesis and Future Directions

This chapter synthesises key results and recommendations from preceding chapters and presents an overview of the state of geoelectric research in Tasmania. Results are divided into two sections by way of their relevance to understanding Tasmania's tectonic evolution, and implications for resource exploration.

7.1 Tectonic Evolution

The current understanding of Tasmania's enigmatic tectonic history has been informed by geological information observed or sampled at the Earth's surface coupled with geophysical data sets sensitive to magnetic, density and seismic properties of the rocks forming the crust and mantle beneath. The work documented in this thesis adds several new geophysical data sets exploiting the electrical resistivity of the Tasmanian lithosphere at state to regional scale (Fig. 7.1). Given that the electrical resistivity response has a different mechanism (or mechanisms) than the other noted geophysical data sets, it provides a new set of evidence for consideration in the analysis of tectonic structure and evolution.

State-scale resistivity structure for the mid-crust to lithospheric mantle has been inferred, at 5 km horizontal resolution from 3D inversion of the AusLAMP MT data set. This model images the full extent of known anomalous conductive structures in the Tamar region, building on the work of Lilley [1976], Parkinson et al. [1988] and Hermanto [1992] by describing the Tamar Conductivity Anomaly in greater detail as a crustal-scale conductor extending from northern to southern Tasmania along the boundary between the ETT and WTT, and extending westward with increasing depth. Elevated conductivities may be attributed to fluids and/or graphite along fracture networks between the two terrains, an analysis consistent with state-scale shear-wave velocity models derived from inversion of passive seismic data sets [Pilia et al., 2015]. The west-dipping nature of the Tamar Conductivity Anomaly contrasts with geodynamic models of east-directed subduction leading to Devonian collision between the ETT and WTT of Hong et al. [2017].

The 3D AusLAMP model and west transect 2D model also imaged low resistivity mid-crustal structures along the margins of Proterozoic terrains in western Tasmania likely linked to Cambrian metamorphism. A consistent feature across all models is the tendency to image high to very high resistivities in regions pervasively intruded by Cambrian and especially Devonian granites, throughout the depth range of the lithosphere. This is especially the case in the ETT, where state-scale AusLAMP inverse models enable us to infer relatively high resistivities from the uppermost reaches of data sensitivity to lithospheric mantle depths.

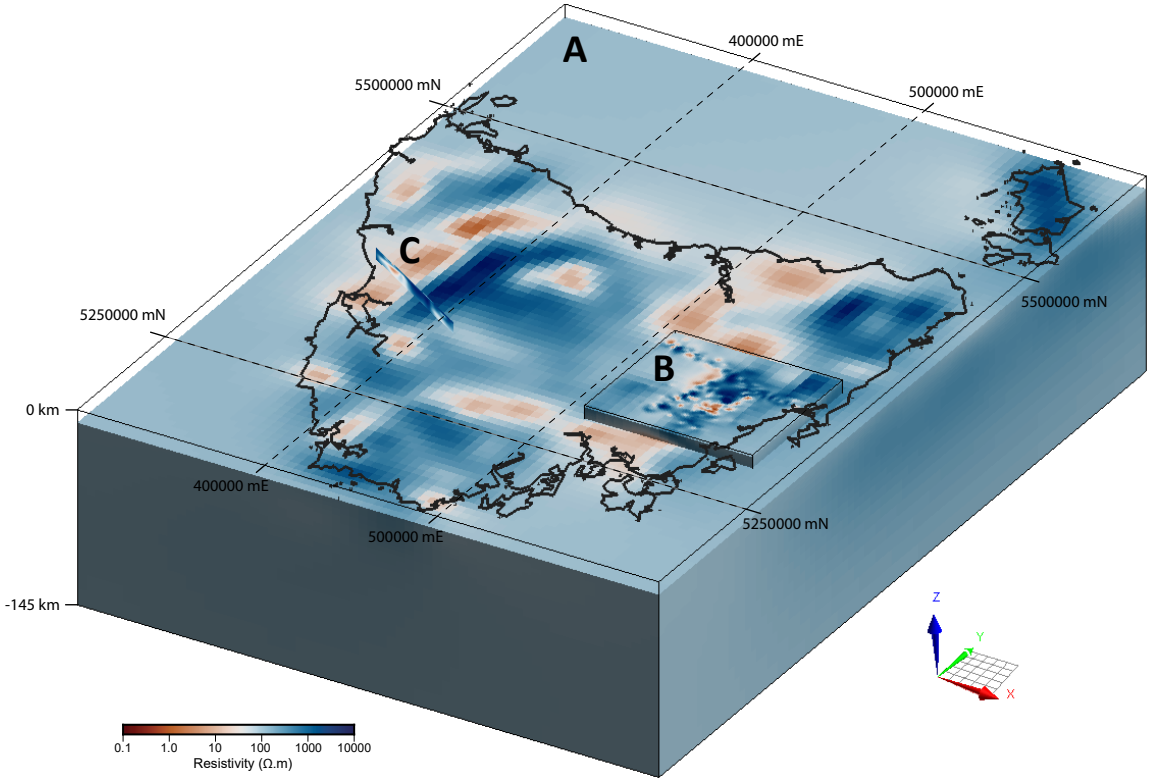

Figure 7.1: Orthographic projected oblique view from the southeast showing 2D and 3D resistivity models generated through the research described in this thesis. Horizontal coordinates are in the GDA94 UTM zone 55 coordinate system. The state-scale AusLAMP model A) is discussed in Chapter 4, the regional-scale broadband-AusLAMP joint inverse model B) is discussed in Chapter 6, while the broadband 2D traverse model C) is discussed in Chapter 5.

At lower crustal and lithospheric mantle depths electrical resistivity is largely controlled by the volatile content of nominally anhydrous minerals, and can thus be used as a proxy for the 'fertility' state or degree of metasomatism at these depths. Devolatilisation of the lower crust and lithospheric mantle in Tasmania is evident in the 3D resistivity model as a correlation between high resistivity regions at these depths and regions with abundant upper crustal Devonian and Cambrian granitoids. Low resistivities elsewhere in the lower crust and lithospheric mantle may be the result of relict metasomatism that drove the Karoo-Ferrar Large Igneous Province responsible for Tasmania's ubiquitous Jurassic dolerites. The resistivity structure of the lithospheric mantle largely agrees with sparse mantle xenolith geochemical

studies, and represents a major contribution to the understanding of the Tasmanian lithospheric mantle. Further analysis of mantle geochemistry and its relationship to mantle resistivity is highly recommended and could be carried out following a systematic compilation of existing mantle xenolith geochemical studies for Tasmania.

In general, geologic interpretation of the electrical structure of the Tasmanian lithosphere is consistent with the impact of overprinting tectonothermal events. Profound changes to the lithosphere during the Cambrian, Devonian and Jurassic appear to have left an enduring mark on the resistivity structure of the Tasmanian lithosphere. Future work on the tectonic significance of the geoelectric structure of Tasmania should seek to compare these results with those from comparable resistivity investigations in Victoria. A full comparison is beyond the scope of this thesis, but with the generation of state scale resistivity models from AusLAMP in both states it is now possible. Such a study could inform current discussion regarding the nature of basement to the Melbourne Zone in southern Victoria and its relationship to Tasmanian tectonic terrains.

7.2 Exploration Implications

The spatial scales and frequency bands at which MT data were acquired for this research project preclude the direct detection of deposit scale targets. However, regional and terrain-scale structures evident in inverse models could inform pre-competitive exploration studies for mineral resources and the setting of possible geothermal energy systems.

7.2.1 Minerals

Geoelectric models discussed herein have implications for mineral exploration that can be divided into two categories on the basis of depth. The first relates to direct imaging of low resistivity crustal structures that represent relict fluid pathways potentially associated with mineralising events, such as that identified beneath iron-oxide copper-gold deposits in South Australia Heinson et al. [2018, 2006]. These were imaged in both the AusLAMP state-scale resistivity models beneath known mineralisation at Savage River, and in the west transect 2D models beneath the Queenstown mineral field (Fig. 7.2). The new knowledge generated through the work described in this thesis supports ongoing exploration activities in the vicinity of these known mineral deposits. Similar low resistivity structures along the eastern boundary of the WTT, obscured by Tasmania basin cover sequences, may be prospective on this basis. Again, this provides support for future exploration activities.

A second key implication for mineral exploration relates to new information derived from the state-scale resistivity model regarding the fertility state of the lithospheric mantle. High resistivities at mantle depths typically image dry, depleted mantle that is unlikely act as a source region for mineralising fluids at large scales. This has implications for a whole of lithosphere approach to mineral exploration [Griffin et al., 2013], where the geochemical state of lithospheric

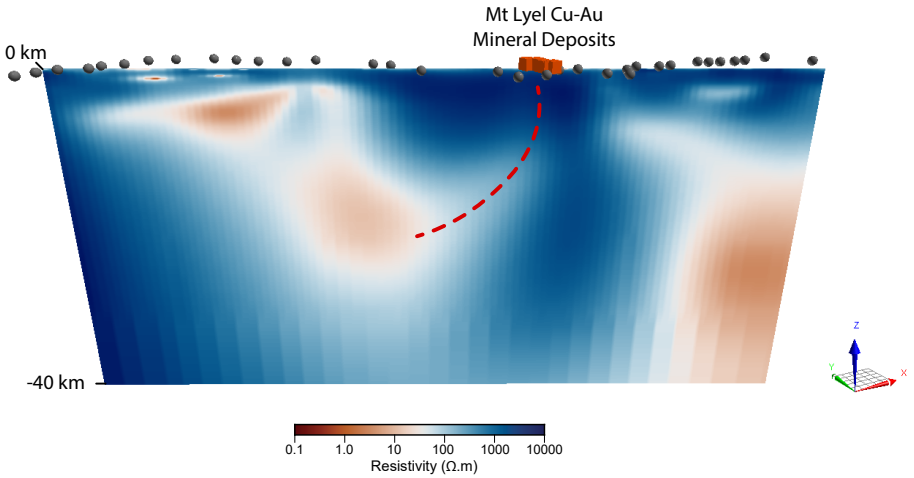

Figure 7.2: Annotated inclined parallel projected view of the west transect preferred model looking north east. Note the low resistivity arcuate feature linking Mt Lyell mineral deposits with a lower-crustal to lithospheric mantle conductor. Gray spheres represent the spatial location of broadband MT sites used in inversion.

mantle is a consideration. Resistivity data indicate the Tasmanian lithospheric mantle is depleted beneath regions extensively intruded by granites in the Cambrian and Devonian, and is considerably more fertile in central and western Tasmania. This is reflected in the relative paucity of base metal deposits in eastern Tasmania (Fig. 7.3).

7.2.2 Geothermal

The combined broadband and long period MT inverse modelling presented herein has served to refine the understanding of the geoelectric structure of a portion of Tasmanian Midlands surrounding the Lemont geothermal resource. The implications of this body of work are both practical and methodological, with new higher resolution models containing geologically feasible resistivity structures representing an immediate practical outcome that provides better defined drill targets for the development of an Enhanced Geothermal System on the Lemont resource (Fig. 7.4).

Methodological implications stem from the combined modelling approach and include a clear demonstration of a potential use case for coarse AusLAMP-derived state scale geoelectric models in higher resolution, targeted modelling. The inclusion of AusLAMP geoelectric structure as *a priori* information in the combined modelling workflow at Lemont greatly improved geological feasibility of the final preferred model, and it is likely that similar applications elsewhere in Australia may benefit from the same.

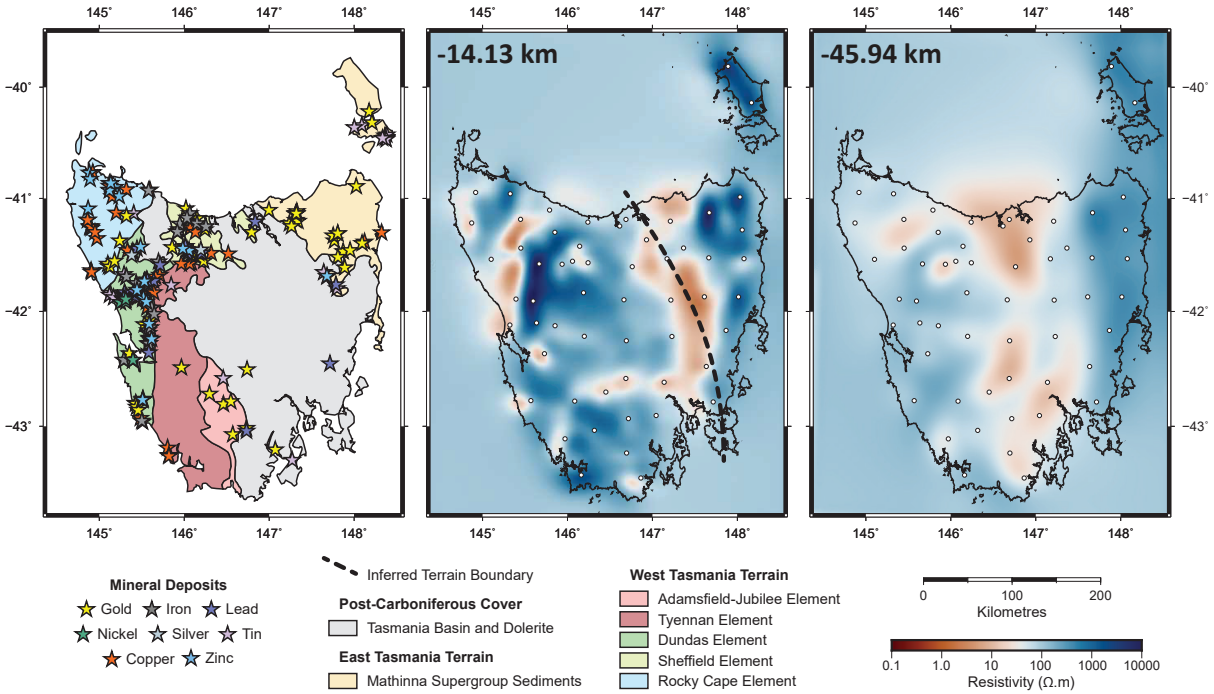

Figure 7.3: Maps depicting Tasmanian precious and base metal deposits plotted onto tectonic elements map (left, modified from Seymour and Calver [1995]). The central and right-most plots present depth slices through the preferred state-scale model at mid-crustal and lithospheric mantle depths, respectively.

7.2.3 3D Combined Interpretation

Interpretation of all inverse models derived from MT data sets in this thesis was greatly enhanced by the importation of models into a single 3D visualisation environment (Geoscience Analyst and Skua-GOCAD). Visualisation in 3D space proved to be a highly valuable part of the overall workflow, as it provides a rigorous means of interpreting geoelectric structures in terms of their spatial relationships to known geology and other petrophysical properties.

Figure 7.4 presents an example of the power of 3D integrated interpretations. Here low resistivities in the model are represented by pink isosurfaces coincident with 3D fault planes intersecting a 3D surface representing Devonian granite roof topography. The benefit of the 3D visualisation environment is further leveraged by viewing new results in an integrated context using interactive functionality. The Geoscience Analyst '`master.geoh5`' project file used throughout this research project has been provided in a digital appendix as a resource for combined geology and geophysics going forward.

7.3 Recommendations Summary

Key recommendations derived from the work completed herein can be split into three broad categories including scientific understanding, data processing and modelling, and further data acquisition. In order to extract further scientific understanding from the geoelectric informa-

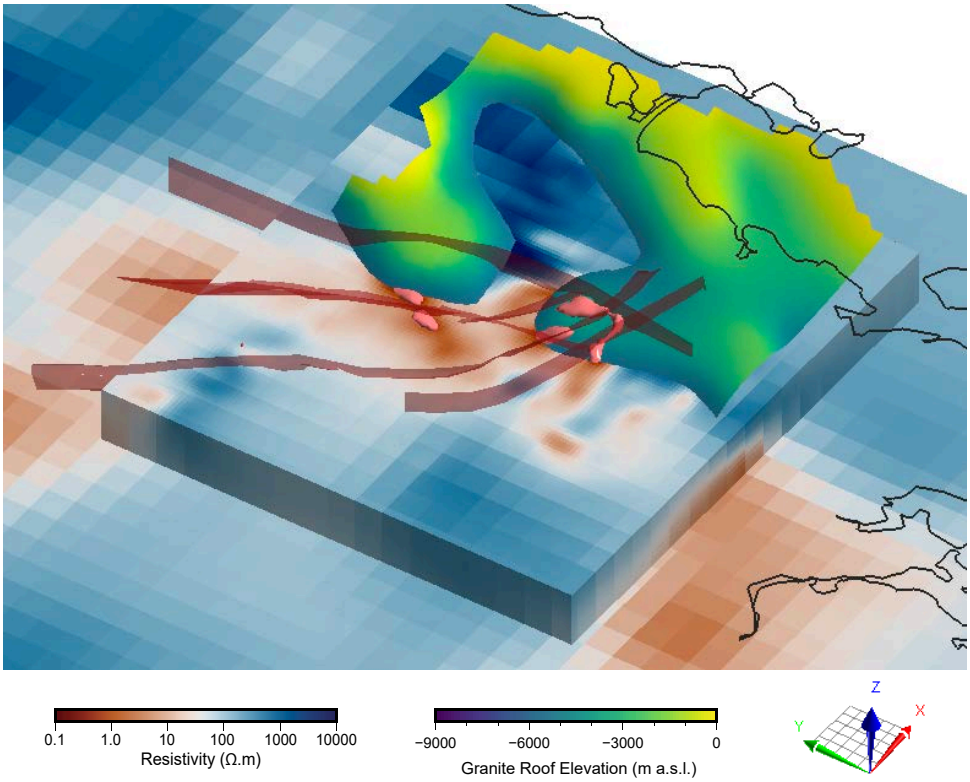

Figure 7.4: Orthographic projected oblique view from the southwest of the KUTh 3D model on top of the state-scale AusLAMP model. Figure includes granite roof elevation derived from Leaman [2012], regional faults (semi-transparent red structures) derived from Goh and Holgate [2009], coastlines as black lines and isosurfaces encapsulating regions of the model space with resistivities less than 1 Ω m. Note the first order correlation between low resistivity zones highlighted by the isosurface and crustal faults piercing Devonian granites. See Figure 7.1 for model volume location.

tion derived in this body of work, it is recommended that geoelectric models be interpreted alongside a foreshadowed comprehensive compilation of mantle xenolith geochemistry. Analysis of geoelectric structure with such a database would improve interpretations of the geochemical state and tectonic history of the lithospheric mantle beneath Tasmania.

With respect to data processing, it is recommended that raw time series MT data sets acquired in Tasmania be reprocessed using new HPC implementations of the BIRRP MT processing code currently (July, 2020) under development by Geoscience Australia. These new implementations leverage HPC to process MT time series without the need to perform conventional data reduction steps such as down sampling or windowing. Early results show improved impedance tensor estimates, especially at longer periods (Robertson, K. 2020, pers. comm.). Reprocessing of all Tasmanian MT data using this approach could improve the depth of investigation of all MT data sets, especially for cases where recorded days in the long period deployments were cut short by the limited daylight hours.

General recommendations related to inverse modelling include the need to incorporate topography in starting models (functionality that was not available at the outset of this research).

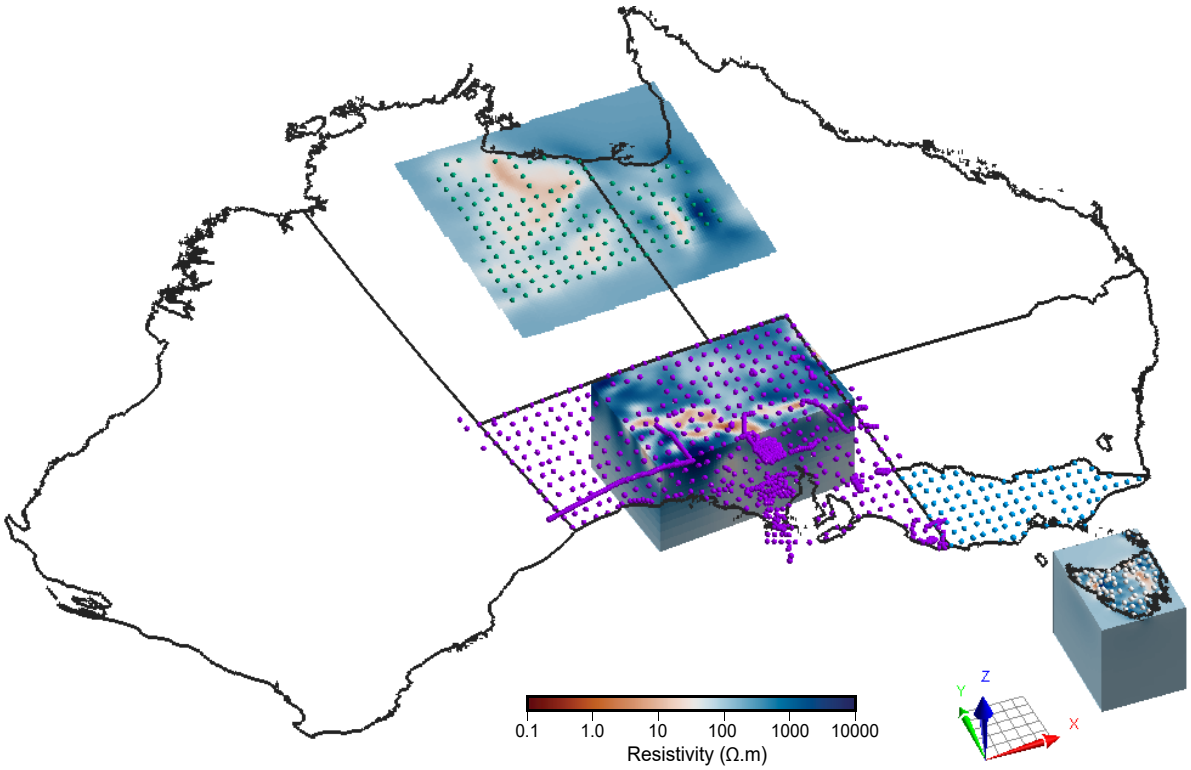

Figure 7.5: AusLAMP data sets for which 3D models have been generated at time of writing. All South Australian MT sites have been inverted to generate 3D inverse models, while models from Victoria and northern Australia are at preliminary modelling stages.

This is unlikely to impact the results of the state-scale long period MT modelling, but will probably improve model fits for smaller, regional-scale broadband MT modelling, especially in shallow surface influenced by topography-induced electric field distortion. Resistivity structure beneath the west transect MT data set could benefit from the 3D combined inversion workflow implemented in Chapter 6. Three dimensional inversion of transect data sets would negate the need to mask 3D periods, and thus incorporate more information in the models.

At the state-scale, AusLAMP data coverage for Tasmania is complete with an average data spacing of ∼35 km. The data have been supplied to Geoscience Australia, and a national archive associated with HPC infrastructure and will contribute to the growing, overall national AusLAMP resource for the nation of Australia. Given the long period nature of the data, and the comparably high spatial resolution of the Tasmanian data set (see Fig. 7.5), further AusLAMP infill surveys are difficult to justify at this stage. Similar recommendations apply to the two transect data sets, where data spacing was largely governed by site accessibility just as much as pre-planned site locations. Infill surveys along these transects would represent a major logistical challenge with little return in terms of the likely benefit from added data.

In contrast to state-scale and transect data sets, further data acquisition around the Lemont geothermal resource is recommended. Acquisition in this area should focus on the central low resistivity zone, with the aim of improving confidence in the location of minimum resistivity

drill targets. Infill surveys should be followed with further, higher resolution inverse modelling incorporating regional resistivity structure as *a priori* information.

Chapter 8

Conclusions

This thesis has presented the results of an investigation into the geoelectric structure of the Tasmanian lithosphere using the MT geophysical method. The aims of the overarching research project were largely achieved through the acquisition of new data sets focused at the statewide scale in 3D, and at the regional scale transects in 2D. Analysis and interpretation was carried out in the form of three separate studies, also incorporating an existing data set from the Tasmanian Midlands.

AusLAMP Long Period Data Set

The statewide data set, comprising a total of 57 long period MT sites was acquired across Tasmania as part of the nationwide AusLAMP survey. These were deployed at a spacing of ∼35 km, resulting in a considerably higher resolution data set in Tasmania relative to the rest of the country where spacing is a nominal 50 km. Once processed, qualitative geoelectric structure analyses were produced by way of the phase tensor and induction arrow approaches. In agreement with previous studies, a low resistivity region extending southward from the Tamar River was clearly identified. Strong contrasts between the high resistivity ETT and more heterogenous WTT were revealed.

Quantitative analysis of the data set was achieved through 3D inverse modelling using the ModEM3DMT algorithm of Kelbert et al. [2014]. This computationally expensive modelling approach used high performance computing infrastructure made available by the the Tasmanian Partnership for Advanced Computing (TPAC), and yielded a state-scale 3D resistivity model with a horizontal resolution of 5 km, a first for Tasmania. Interpretation of a preferred 3D resistivity model was conducted within a 3D viewing environment enabled by software packages SKUA-GOCAD and Geoscience Analyst. Importation of all available geologic and geophysical data sets co-located with the preferred resistivity model into the 3D viewing environment proved to be a powerful tool in interpreting geoelectric structures, and provided a degree of robustness unavailable in 2D interpretations.

Thus, the first comprehensive statewide geoelectrical survey of Tasmania was successfully completed and provided to Mineral Resources Tasmania for ongoing usage. Anomalously low resistivities were revealed along major terrain boundaries in the mid- to upper-crust likely resulting from conductive phases and pore fluids in shear zones. Highly resistive zones in the upper-crust correlate with the distribution of voluminous Devonian and Cambrian granitoid intrusive rocks.

Broadband Transect Data Sets

Two broadband MT transects were acquired across tectonic element boundaries representing transition zones between Precambrian and Phanerozoic rocks in northern and western Tasmania. The west transect was deployed in Western Tasmania along the Heemskirk Road and the Lyell and Zeehan Highways crossing the Tyennan and Dundas Trough tectonic elements. With 34 broadband MT sites in total, the west transect spanned a distance of 80 km at a site spacing of ∼3 km and was the largest of the two transects. The north transect also crossed the Tyennan-Dundas Trough tectonic element boundary spanning a 50 km distance between Dove Lake and Forth along the Wilmot Road and Cradle Mountain Road. A total of 28 broadband sites were deployed along the north transect at a site spacing of ∼2 km.

The influence of 50 Hz power line noise was visible in both transect data sets during processing. This adversely affected the short period bands in both data sets and necessitated masking of noisy impedance tensor estimates for shorter period bands. 50 Hz power line noise was especially evident in the north transect, and resulted in heavy masking for periods <0.1 s rendering the data insensitive to upper crustal geoelectric structure. As a consequence, 2D inverse modelling of the north transect was not undertaken in this study.

Imaging of geoelectric structure beneath the west transect was achieved by way of 2D inverse modelling using the OCCAM2D inversion algorithm of Constable et al. [1987] and DeGroot-Hedlin and Constable [1990]. Inversion required a robust analysis of the dimensionality and geoelectric strike direction using the phase tensor approach, and ultimately resulted in a new 2D resistivity model describing the electrical structure of the mid to upper crust along the transect. Importation of this 2D model into the same 3D environment used to interpret the state-scale preferred resistivity model allowed for robust 3D interpretations of model structures.

Along the west transect, 2D inverse modelling broadly agrees with regional 3D modelling derived from AusLAMP MT data. Upper crustal rocks within the Precambrian basement are considerably less resistive than younger Dundas-Fossey rocks and preserve internal heterogeneity potentially imaging relict metamorphic fluid pathways. The highly resistive Dundas-Fossey Trough contains small scale low resistivity structure coincident with crustal scale faults observed at surface. Low resistivities in the western part of the west transect are interpreted to image serpentinised Cambrian ultramafic rocks. The west transect survey results have been provided to Mineral Resources Tasmania for ongoing usage in assisting pre-competitive mineral exploration.

Tasmanian Midlands Combined Broadband and Long Period Modelling

Legacy broadband MT data acquired by KUTh Energy Ltd in the Tasmanian Midlands was assessed for combined inversion with a subset of the AusLAMP long period data set. This process involved sampling both the long period and broadband data to a common period range, and masking for noisy periods. After masking the combined data set included 244 broadband sites and six long period sites. All AusLAMP sites and 93 of the broadband sites contained tipper information allowing for qualitative analysis of induction arrow relationships and their relation to fault systems inferred from potential field surveys.

3D geophysical inversion of the combined broadband and long period data set was completed using the ModEM3DMT algorithm on the same computing infrastructure used to invert the statewide models. This yielded a series of models computed with different starting conditions. A preferred model was selected which used the 5 km statewide preferred model as a starting point for 3D geological interpretation in the same 3D environment as the 2D transect models and the state-scale model.

Geological interpretation of the preferred model gives high credibility to the Lemont geothermal prospect conceptual model, and represents an improvement in terms of both resolution and geological feasibility over existing 3D inverse models for the KUTh data set. In addition, the shallower depths at which low resistivity geothermal targets manifest in the new preferred model suggest improved economic feasibility of drill hole testing, a major insight resulting from this component of the research.

Bibliography

Archie, G. E. (1942). The electrical resistivity log as an aid in determining some reservoir characteristics. *Transactions of the AIME*, 146(01):54–62.

Asten, M. W., Vicary, M., Rutter, H., and Cull, J. P. (2005). An all-frequency resistivity-depth and static-correction technique for CSAMT data, with applications to mineralised targets under glacial cover (Western Tasmania) and basalt cover (Victorian goldfields). *Exploration Geophysics*, 36(3):287–293.

Australian Institute of Marine Sciences (2009). Australian bathymetry and topography grid depth contours.

Baillie, P. W. (1986). A radiometric age for the Moriarty Basalt, north-western Tasmania. *Tasmania Department of Mines Unpublished Report*, 38.

Bajwah, Z. U., White, A. J. R., Kwak, T. A. P., and Price, R. C. (1995). The Renison Granite, northwestern Tasmania; a petrological, geochemical and fluid inclusion study of hydrothermal alteration. *Economic Geology*, 90(6):1663–1675.

Battaglini, A., Wolfgang, S., and Stephen, H. (2010). Magnetotelluric (MT) Data - 3D Inversion Modelling, Eastern Tasmania, Australia. Technical report, WesternGeco EM, Milan, Italy.

Beka, T. I. (2016). *Geoelectrical structures beneath Spitsbergen-Svalbard derived from magnetotelluric imaging*. PhD thesis, Arctic University of Norway.

Berry, R. F. and Bull, S. W. (2012). The pre-Carboniferous geology of Tasmania. *Episodes*, 35(1):195–204.

Berry, R. F. and Crawford, A. J. (1988). The tectonic significance of Cambrian allochthonous mafic-ultramafic complexes in Tasmania. *Australian Journal of Earth Sciences*, 35(4):523–533.

Berry, R. F., Steele, D. A., and Meffre, S. (2008). Proterozoic metamorphism in Tasmania: implications for tectonic reconstructions. *Precambrian Research*, 166(1):387–396.

Bibby, H. M., Caldwell, T. G., and Brown, C. (2005). Determinable and non-determinable parameters of galvanic distortion in magnetotellurics. *Geophysical Journal International*, 163(3):915–930.

Bishop, J. R., Lewis, R. J. G., and Macnae, J. C. (1987). Down-hole electromagnetic surveys at Renison Bell, Tasmania. *Exploration Geophysics*, 18(3):265–277.

Black, L. P. (1997). *Dating Tasmania's oldest geological events*. Australian Geological Survey Organisation.

Black, L. P., Everard, J. L., McClenaghan, M. P., Korsch, R. J., Calver, C. R., Fioretti, A. M., Brown, A. V., and Foudoulis, C. (2010). Controls on Devonian–Carboniferous magmatism in Tasmania, based on inherited zircon age patterns, Sr, Nd and Pb isotopes, and major and trace element geochemistry. *Australian Journal of Earth Sciences*, 57(7):933–968.

Black, L. P., McClenaghan, M. P., Korsch, R. J., Everard, J. L., and Foudoulis, C. (2005). Significance of Devonian–Carboniferous igneous activity in Tasmania as derived from U–Pb SHRIMP dating of zircon. *Australian Journal of Earth Sciences*, 52(6):807–829.

Blewett, R. S., Henson, P. A., Roy, I. G., Champion, D. C., and Cassidy, K. F. (2010). Scale-integrated architecture of a world-class gold mineral system: The Archaean eastern Yilgarn Craton, Western Australia. *Precambrian Research*, 183(2):230–250.

Booker, J. R. (2014). The magnetotelluric phase tensor: a critical review. *Surveys in Geophysics*, 35(1):7–40.

Braniff, V. L. R. (2013). *Integration of Geotechnical and Structural Data from Savage River Mine, Tasmania*. PhD thesis, University of Tasmania.

Buyung, N. (1980). *A geomagnetic induction study in the north east of Tasmania*. PhD thesis, University of Tasmania.

Cagniard, L. (1953). Basic theory of the magneto-telluric method of geophysical prospecting. *Geophysics*, 18(3):605–635.

Caldwell, T. G., Bibby, H. M., and Brown, C. (2004). The magnetotelluric phase tensor. *Geophysical Journal International*, 158(2):457–469.

Calver, C. R., Baillie, P. W., Banks, M. R., and Seymour, D. B. (2014a). Ordovician-Lower Devonian successions. In Corbett, K. D., Quilty, P. G., and Calver, C. R., editors, *Geological Evolution of Tasmania*, pages 241–271. Geological Society of Australia (Tasmania Division), 1st edition.

Calver, C. R., Everard, J. L., Berry, R. F., Bottrill, R. S., and Seymour, D. B. (2014b). Proterozoic Tasmania. In Corbett, K. D., Quilty, P. G., and Calver, C. R., editors, *Geological evolution of Tasmania*, pages 34–94. Geological Society of Australia (Tasmania Division), 1st edition.

Cao, S. and Neubauer, F. (2019). Graphitic material in fault zones: Implications for fault strength and carbon cycle. *Earth-Science Reviews*.

Cayley, R. A. (2011). Exotic crustal block accretion to the eastern Gondwanaland margin in the Late Cambrian–Tasmania, the Selwyn Block, and implications for the Cambrian–Silurian evolution of the Ross, Delamerian, and Lachlan orogens. *Gondwana Research*, 19(3):628–649.

Chave, A. D., Evans, R. L., Ferguson, I. J., Jones, A. G., Mackie, R. L., Rodi, W. L., Viljanen, A., Weidelt, P., and Weiss, C. (2012). *The magnetotelluric method: Theory and practice*. Cambridge University Press, 1st edition.

Chave, A. D. and Thomson, D. J. (2004). Bounded influence magnetotelluric response function estimation. *Geophysical Journal International*, 157(3):988–1006.

Constable, S., Parker, R., and Constable, C. (1987). Occam's inversion: A practical algorithm for generating smooth models from electromagnetic sounding data. *GEOPHYSICS*, 52(3):289–300.

Corbett, K. D., Berry, R. F., Everard, J. L., Calver, C. R., Crawford, A. J., Vicary, M. J., Bottrill, R. S., and McNeill, A. W. (2014). Cambrian Tasmania. In Corbett, K. D., Quilty, P. G., and Calver, C. R., editors, *Geological Evolution of Tasmania*, pages 95–240. Geological Society of Australia (Tasmania Division), 1st edition.

Crawford, A. J. and Berry, R. F. (1992). Tectonic implications of Late Proterozoic-Early Palaeozoic igneous rock associations in western Tasmania. *Tectonophysics*, 214(1-4):37–56.

Crawford, A. J., Corbett, K. D., and Everard, J. L. (1992). Geochemistry of the Cambrian volcanic-hosted massive sulfide-rich Mount Read Volcanics, Tasmania, and some tectonic implications. *Economic Geology*, 87(3):597–619.

Crespo, E., Luque, J., Barrenechea, J. F., and Rodas, M. (2005). Mechanical graphite transport in fault zones and the formation of graphite veins. *Mineralogical Magazine*, 69(4):463–470.

Cull, J. P. (1985). Magnetotelluric soundings over a Precambrian contact in Australia. *Geophysical Journal of the Royal Astronomical Society*, 80:661–675.

Czuppon, G., Matsumoto, T., Matsuda, J., Everard, J. L., and Sutherland, L. (2010). Noble gases in anhydrous mantle xenoliths from Tasmania in comparison with other localities

from eastern Australia: Implications for the tectonic evolution. *Earth and Planetary Science Letters*, 299(3–4):317–327.

DeGroot-Hedlin, C. and Constable, S. (1990). Occam's inversion to generate smooth, two-dimensional models from magnetotelluric data. *GEOPHYSICS*, 55(12):1613–1624.

Dennis, Z. R., Thiel, S., and Cull, J. P. (2012). Lower crust and upper mantle electrical anisotropy in southeastern Australia. *Exploration Geophysics*, 43(4):228–241.

Dentith, M., Johnson, S. P., Evans, S., Aitken, A., Joly, A., Thiel, S., and Tyler, I. M. (2014). A magnetotelluric traverse across the eastern part of the Capricorn Orogen. *Geological Survey of Western Australia, Report*, 135.

Drummond, B. J., Barton, T. J., Korsch, R. J., Rawlinson, N., Yeates, A. N., Collins, C. D. N., and Brown, A. V. (2000). Evidence for crustal extension and inversion in eastern Tasmania, Australia, during the Neoproterozoic and Early Palaeozoic. *Tectonophysics*, 329(1):1–21.

Duba, A. G., Huengest, E., Nover, G., Will, G., and Jödicke, H. (1988). Impedance of black shale from Münsterland 1 borehole: an anomalously good conductor? *Geophysical Journal International*, 94(3):413–419.

Duba, A. G. and Shankland, T. J. (1982). Free carbon & electrical conductivity in the Earth's mantle. *Geophysical Research Letters*, 9(11):1271–1274.

Duffett, M. (2016). Revising gravity terrain corrections in Tasmania. *ASEG Extended Abstracts*, 2016(1):1–8.

Dwipa, S. (1992). *Electrical Structures of the Crust in Southeastern Tasmania.* PhD thesis, University of Tasmania.

Egbert, G. and Kelbert, A. (2012). Computational recipes for electromagnetic inverse problems. *Geophysical Journal International*, 189(1):251–267.

Everard, J. L., Seymour, D. B., Reed, A. R., McClenaghan, M. P., Green, D. C., Calver, C. R., and Brown, A. V. (2007). Regional geology of the southern Smithton Synclinorium. *Explanatory Notes for Roger, Sumac and Dempster*, 1(25):0.

Everard, J. L., Zhang, M., Lo, C.-H., O'Reilly, S. Y., and Forsyth, S. (2004). Overview of Tasmanian Tertiary basalts. In *Geol. Soc. Aust. Abstr*, volume 73, page 74.

Everett, J. E. and Hyndman, R. D. (1967a). A digital portable magnetotelluric observatory. *Journal of Scientific Instruments*, 44(11):943–946.

Everett, J. E. and Hyndman, R. D. (1967b). Magneto-telluric investigations in south-western Australia. *Physics of the Earth and Planetary Interiors*, 1(1):49–54.

Fishwick, S. and Rawlinson, N. (2012). 3-D structure of the Australian lithosphere from evolving seismic datasets. *Australian Journal of Earth Sciences*, 59(6):809–826.

Forsyth, S. M. (1989). Geological Survey Explanatory Report, Geological Atlas 1:50 000 series, sheet 61 (8313N) Interlaken. Technical report, Mineral Resources Tasmania.

FrOGTech (2006). OZ SEEBASE Study. *Public Domain Report to Shell Development Australia by FrOG Tech Pty Ltd.*

Fullagar, P. K., Pears, G. A., and Milkereit, B. (2007). Towards geologically realistic inversion. In Melkereit, B., editor, *Proceeding of Exploration 07: Fifth Decennial International Conference on Mineral Exploration*, volume 7, pages 444–460.

Gamble, T., Goubau, W., and Clarke, J. (1979). Magnetotellurics with a remote magnetic reference. *GEOPHYSICS*, 44(1):53–68.

Geoscience Australia (2011). SRTM-derived 1 Second Digital Elevation Models Version 1.0.

Geoscience Australia (2021). AusLAMP explanatory webpage, accessed 3 April 2021, [https://www.ga.gov.au/about/projects/resources/auslamp].

Glover, P. W. J. (2010). A generalized Archie's law for n phases. *Geophysics*, 75(6):E247–E265.

Godber, K. and Reid, J. (2009). Qualitative Interpretation of Central Midlands Aeromagnetics and Gravity. Technical report, Geoforce Geophysical Solutions.

Goh, H. K. H. and Holgate, F. L. (2009). Annual Report SEL 26/2005 and SEL 45/2007. Technical report, KUTh Energy Limited.

Gough, D. I. (1986). Seismic reflectors, conductivity, water and stress in the continental crust. *Nature*, 323(6084):143–144.

Gough, D. I., Lilley, F. E. M., and McElhinny, M. W. (1972). A polarization-sensitive magnetic variation anomaly in South Australia. *Nature*, 239(93):88–91.

Gray, J. D. and Cull, J. P. (1990). Magnetotelluric soundings and resistivity profiles in the Willyama Complex. *Australian Journal of Earth Sciences*, 37(2):127–134.

Grayver, A. V. (2015). Parallel three-dimensional magnetotelluric inversion using adaptive finite-element method. Part I: theory and synthetic study. *Geophysical Journal International*, 202(1):584–603.

Griffin, W. L., Begg, G. C., and O'reilly, S. Y. (2013). Continental-root control on the genesis of magmatic ore deposits. *Nature Geoscience*, 6(11):905.

Haak, V. and Hutton, R. (1986). Electrical resistivity in continental lower crust. *Geological Society, London, Special Publications*, 24(1):35–49.

Halpin, J. A., Jensen, T., McGoldrick, P., Meffre, S., Berry, R. F., Everard, J. L., Calver, C. R., Thompson, J., Goemann, K., and Whittaker, J. M. (2014). Authigenic monazite and detrital zircon dating from the Proterozoic Rocky Cape Group, Tasmania: Links to the Belt-Purcell Supergroup, North America. *Precambrian Research*, 250:50–67.

Heinson, G., Didana, Y., Soeffky, P., Thiel, S., and Wise, T. (2018). The crustal geophysical signature of a world-class magmatic mineral system. *Scientific reports*, 8(1):1–6.

Heinson, G., Direen, N. G., and Gill, R. M. (2006). Magnetotelluric evidence for a deep-crustal mineralizing system beneath the Olympic Dam iron oxide copper-gold deposit, southern Australia. *Geology*, 34(7):573–576.

Heinson, G. and White, A. (2005). Electrical resistivity of the Northern Australian lithosphere: Crustal anisotropy or mantle heterogeneity? *Earth and Planetary Science Letters*, 232(1–2):157–170.

Heise, W., Caldwell, T. G., Bibby, H. M., and Bannister, S. C. (2008). Three-dimensional modelling of magnetotelluric data from the Rotokawa geothermal field, Taupo Volcanic Zone, New Zealand. *Geophysical Journal International*, 173(2):740–750.

Hermanto, M. R. (1992). *Magnetotelluric investigations of the Tamar lineament*. PhD thesis, University of Tasmania.

Hill, P. J. and Yeates, A. N. (1995). *Circum-Tasmania and South Tasman Rise: Cruise Proposal for Deep Crustal Seismic Data Acquisition, 1995*. Australian Geological Survey Organisation.

Holgate, F. L. (2011). Annual Report SEL 26/2005 and SEL 45/2007. Technical report, KUTh Energy Limited.

Holgate, F. L., Goh, H. K. H., Wheller, G., and Lewis, R. G. J. (2010). The Central Tasmanian Geothermal Anomaly: A Prospective New EGS Province in Australia. *World Geothermal Congress*, pages 25–29.

Holm, O. H. (2002). *Structural and metamorphic evolution of the Arthur Lineament, northwestern Tasmania, Australia*. PhD thesis, University of Tasmania.

Holm, O. H. and Berry, R. F. (2002). Structural history of the Arthur Lineament, northwest Tasmania: an analysis of critical outcrops. *Australian Journal of Earth Sciences*, 49(2):167–185.

Hong, W., Cooke, D. R., Huston, D. L., Maas, R., Meffre, S., Thompson, J., Zhang, L., and Fox, N. (2017). Geochronological, geochemical and Pb isotopic compositions of Tasmanian granites (southeast Australia): Controls on petrogenesis, geodynamic evolution and tin mineralisation. *Gondwana Research*, 46:124–140.

Hyndman, R. D., Vanyan, L. L., Marquis, G., and Law, L. K. (1993). The origin of electrically conductive lower continental crust: saline water or graphite? *Physics of the Earth and Planetary Interiors*, 81(1-4):325–345.

Ivanov, A. V., Meffre, S., Thompson, J., Corfu, F., Kamenetsky, V. S., Kamenetsky, M. B., and Demonterova, E. l. (2017). Timing and genesis of the Karoo-Ferrar large igneous province: New high precision U-Pb data for Tasmania confirm short duration of the major magmatic pulse. *Chemical Geology*, 455:32–43.

Jiracek, G. R. (1990). Near-surface and topographic distortions in electromagnetic induction. *Surveys in Geophysics*, 11(2-3):163–203.

Jones, A. G. (1983). On the equivalence of the "Niblett" and "Bostick" transformations in the magnetotelluric method. *J. Geophys*, 53(1):72–73.

Jones, A. G. (1988). Static shift of magnetotelluric data and its removal in a sedimentary basin environment. *Geophysics*, 53(7):967–978.

Jones, A. G., Fullea, J., Evans, R. L., and Muller, M. R. (2012). Water in cratonic lithosphere: Calibrating laboratory-determined models of electrical conductivity of mantle minerals using geophysical and petrological observations. *Geochemistry, Geophysics, Geosystems*, 13(6).

Jones, A. G. and Jödicke, H. (1984). Magnetotelluric transfer function estimation improvement by a coherence-based rejection technique. In *SEG Technical Program Expanded Abstracts 1984*, pages 51–55. Society of Exploration Geophysicists.

Jupp, D. L. B., Kerr, D., Lemaire, H., Milton, B., Moore, R., Nelson, R., and Vozoff, K. (1979). Joint magnetotelluric — DC resistiviy survey eastern Officer basin. *Exploration Geophysics*, 10(3):209–212.

Jupp, D. L. B. and Vozoff, K. (1975). Stable iterative methods for the inversion of geophysical data. *Geophysical Journal International*, 42(3):957–976.

Karato, S. (1990). The role of hydrogen in the electrical conductivity of the upper mantle. *Nature*, 347:272.

Kawano, S., Yoshino, T., and Katayama, I. (2012). Electrical conductivity of magnetite-bearing serpentinite during shear deformation. *Geophysical Research Letters*, 39(20).

Kelbert, A., Meqbel, N., Egbert, G., and Tandon, K. (2014). ModEM: a modular system for inversion of electromagnetic geophysical data. *Computers & Geosciences*, 66:40–53.

Kennett, B. L. N., Salmon, M., Saygin, E., and Group, A. W. (2011). AusMoho: the variation of Moho depth in Australia. *Geophysical Journal International*, 187(2):946–958.

Kennett, B. L. N., Saygin, E., and Salmon, M. (2015). Stacking autocorrelograms to map Moho depth with high spatial resolution in southeastern Australia. *Geophysical Research Letters*, 42(18):7490–7497.

Key, K. (2016). MARE2DEM: a 2-D inversion code for controlled-source electromagnetic and magnetotelluric data. *Geophysical Journal International*, 207(1):571–588.

King, S. D. and Anderson, D. L. (1998). Edge-driven convection. *Earth and Planetary Science Letters*, 160(3-4):289–296.

Kirkby, A., Zhang, F., Peacock, J. R., Hassan, R., and Duan, J. (2019). The MTPy software package for magnetotelluric data analysis and visualisation. *Journal of Open Source Software*, 4(37):1358.

Kitto, P. A. (1992). The geological and structural controls on mineralisation at the Renison tin mine. Technical report, Mineral Resources Tasmania, Hobart, TAS.

Kordy, M., Wannamaker, P., Maris, V., Cherkaev, E., and Hill, G. (2016). 3-dimensional magnetotelluric inversion including topography using deformed hexahedral edge finite elements and direct solvers parallelized on symmetric multiprocessor computers–Part II: direct data-space inverse solution. *Geophysical Journal International*, 204(1):94–110.

Krieger, L. and Peacock, J. R. (2014). MTpy: A Python toolbox for magnetotellurics. *Computers & Geosciences*, 72:167–175.

Larsen, J. C. (1981). A new technique for layered earth magnetotelluric inversion. *Geophysics*, 46(9):1247–1257.

Leaman, D. E. (2007). Subsurface Form of Granites - Eastern Tasmania. Technical report, Leaman Geophysics, Hobart, TAS.

Leaman, D. E. (2012). An interpretation of the granitoid rocks of eastern Tasmania. *Mineral Resources Tasmania, Geophysics Contractor Report*, 1:43.

Leaman, D. E. and Richardson, R. G. (2003). A geophysical model of the major Tasmanian granitoids. *Tasmanian Geological Survey Record*, 11:2003.

Leaman, D. E. and Richardson, R. G. (2014). Crustal Architecture and Geophysics. In Corbett, K. D., Quilty, P., and Calver, C. R., editors, *Geological Evolution of Tasmania*, pages 13–31. Geological Society of Australia (Tasmania Division).

Lewis, R. J. G. (1965). Conductivity of the crust in Tasmania.

Li, Y. and Oldenburg, D. W. (1998). 3-D inversion of gravity data. *Geophysics*, 63(1):109–119.

Lilley, F. E. M. (1976). A Magnetometer Array Study Across Southern Victoria and Bass Strait Area, Australia. *Geophysical Journal of the Royal Astronomical Society*, 46(1):165–184.

Luque, F. J., Pasteris, J. D., Wopenka, B., Rodas, M., and Barrenechea, J. F. (1998). Natural fluid-deposited graphite: mineralogical characteristics and mechanisms of formation. *American Journal of Science*, 298(June):471–498.

Madden, T. and Nelson, P. (1964). A defense of Cagniard's magnetotelluric method. *Magnetotelluric methods*, pages 89–102.

Maier, R. E. (2011). A petrophysical joint inversion of magnetotelluric and gravity data for enhanced subsurface imaging of sedimentary environments.

Meffre, S., Berry, R. F., and Hall, M. (2000). Cambrian metamorphic complexes in Tasmania: tectonic implications. *Australian Journal of Earth Sciences*, 47(6):971–985.

Meqbel, N. (2016). 3DGrid Model And Data Visualizer.

Meqbel, N., Egbert, G., Wannamaker, P. E., Kelbert, A., and Schultz, A. (2014). Deep electrical resistivity structure of the northwestern US derived from 3-D inversion of USArray magnetotelluric data. *Earth and Planetary Science Letters*, 402:290–304.

Mineral Resources Tasmania (2011). *Tasmania 1:250,000 Scale Geological Map*. PhD thesis.

Mineral Resources Tasmania (2019a). Tasmanian Gravity Database.

Mineral Resources Tasmania (2019b). West Tasmania 3D Geological & Geophysical Model.

Mulder, J. A., Everard, J. L., Cumming, G., Meffre, S., Bottrill, R. S., Merdith, A. S., Halpin, J. A., McNeill, A. W., and Cawood, P. A. (2019). Neoproterozoic opening of the Pacific Ocean recorded by multi-stage rifting in Tasmania, Australia. *Earth-Science Reviews*, page 103041.

Mulder, J. A., Halpin, J. A., and Daczko, N. R. (2015). Mesoproterozoic Tasmania: witness to the east Antarctica–Laurentia connection within Nuna. *Geology*, 43(9):759–762.

Nasir, S. J., Everard, J. L., McClenaghan, M. P., Bombardieri, D., and Worthing, M. A. (2010). The petrology of high pressure xenoliths and associated Cenozoic basalts from Northeastern Tasmania. *Lithos*, 118(1-2):35–49.

Nesbitt, B. E. (1993). Electrical resistivities of crustal fluids. *Journal of Geophysical Research: Solid Earth*, 98(B3):4301–4310.

Newman, G. A. and Alumbaugh, D. L. (2000). Three-dimensional magnetotelluric inversion using non-linear conjugate gradients. *Geophysical Journal International*, 140(2):410–424.

Palacky, G. J. (1988). Resistivity Characteristics of Geologic Targets. In Nabighian, M. N., editor, *Electromagnetic Methods in Applied Geophysics*, chapter 3, pages 52–129. Society of Exploration Geophysicists, Tulsa, Oklahoma, 1st edition.

Parkinson, W. D. (1959). Directions of rapid geomagnetic fluctuations. *Geophysical Journal International*, 2(1):1–14.

Parkinson, W. D. (1962). The influence of continents and oceans on geomagnetic variations. *Geophysical Journal International*, 6(4):441–449.

Parkinson, W. D. (1964). Conductivity anomalies in Australia and the ocean effect. *Journal of geomagnetism and geoelectricity*, 15(4):222–226.

Parkinson, W. D., Hermanto, M. R., Sayers, J., Bindoff, N. L., Dosso, H. W., and Nienaber, W. (1988). The Tamar conductivity anomaly. *Physics of the Earth and Planetary Interiors*, 52(1):8–22.

Parkinson, W. D. and Jones, F. W. (1979). The geomagnetic coast effect. *Reviews of Geophysics*, 17(8):1999–2015.

Pilia, S., Arroucau, P., Rawlinson, N., Reading, A. M., and Cayley, R. A. (2016). Inherited crustal deformation along the East Gondwana margin revealed by seismic anisotropy tomography. *Geophysical Research Letters*.

Pilia, S., Rawlinson, N., Cayley, R. A., Bodin, T., Musgrave, R. J., Reading, A. M., Direen, N. G., and Young, M. K. (2015). Evidence of micro-continent entrainment during crustal accretion. *Scientific reports*, 5.

Quilty, P. G., Hill, P. J., Exon, N. F., Baillie, P. W., Everard, J. L., Forsyth, S. M., Calver, C. R., Bottrill, R. S., Taheri, J., Bayer, E. E., Doyle, R. B., O'Reilly, S. Y., Zhang, M., Macphail, M., Hill, R. S., Partridge, A. D., Jordan, G. J., and Lewis, S. (2014). Cretaceous-Neogene Evolution of Tasmania. In Corbett, K. D., Quilty, P. G., and Calver, C. R., editors, *Geological Evolution of Tasmania*, pages 409–510. Geological Society of Australia (Tasmania Division), 1st edition.

Rawlinson, N., Houseman, G. A., Collins, C. D. N., and Drummond, B. J. (2001). New evidence of Tasmania's tectonic history from a novel seismic experiment. *Geophysical research letters*, 28(17):3337–3340.

Rawlinson, N., Reading, A. M., and Kennett, B. L. N. (2006). Lithospheric structure of Tasmania from a novel form of teleseismic tomography. *Journal of Geophysical Research: Solid Earth*, 111(B2).

Rawlinson, N., Tkalčić, H., and Reading, A. M. (2010). Structure of the Tasmanian lithosphere from 3D seismic tomography. *Australian Journal of Earth Sciences*, 57(January 2015):381–394.

Reed, A. R. (2001). Pre-Tabberabberan deformation in eastern Tasmania: A southern extension of the Benambran Orogeny. *Australian Journal of Earth Sciences*, 48(6):785–796.

Rikitake, T. (1951). Changes in earth current and their relation to the electrical state of the earth's crust. *Bull. Earthq. Res. Inst, Univ. Tokyo*, 29:271–276.

Roberts, S. S. J. and Mudge, S. T. (1997). Magnetic and Gravity Modelling of the Renison Tin Mine, Tasmania. *Exploration Geophysics*, 28(1-2):292–295.

Robertson, K., Heinson, G., and Thiel, S. (2016). Lithospheric reworking at the Proterozoic–Phanerozoic transition of Australia imaged using AusLAMP Magnetotelluric data. *Earth and Planetary Science Letters*, 452:27–35.

Robertson, K., Heinson, G., and Thiel, S. (2017). Mapping lithospheric alteration using AusLAMP MT data in the Ikara-Flinders Ranges and Curnamona Province. *MESA Journal*, 83:4–7.

Robertson, K., Taylor, D., Thiel, S., and Heinson, G. (2015). Magnetotelluric evidence for serpentinisation in a Cambrian subduction zone beneath the Delamerian Orogen, southeast Australia. *Gondwana Research*, 28(2):601–611.

Rodi, W. L. and Mackie, R. L. (2001). Nonlinear conjugate gradients algorithm for 2-D magnetotelluric inversion. *Geophysics*, 66(1):174–187.

Rodi, W. L. and Mackie, R. L. (2012). The Inverse Problem. In Chave, A. D. and Jones, A. G., editors, *The Magnetotelluric Method: Theory and Practice*, chapter 8, pages 347–420. Cambridge University Press, 1 edition.

Selway, K. (2014). On the Causes of Electrical Conductivity Anomalies in Tectonically Stable Lithosphere. *Surveys in Geophysics*, 35(1):219–257.

Selway, K., Hand, M., Heinson, G., and Payne, J. L. (2009a). Magnetotelluric constraints on subduction polarity: Reversing reconstruction models for Proterozoic Australia. *Geology*, 37(9):799–802.

Selway, K., Hand, M., Payne, J. L., Heinson, G., and Reid, A. (2011). Magnetotelluric constraints on the tectonic setting of Grenville-aged orogenesis in central Australia. *Journal of the Geological Society*, 168(1):251–264.

Selway, K., Sheppard, S., Thorne, A. M., Johnson, S. P., and Groenewald, P. B. (2009b). Identifying the lithospheric structure of a Precambrian orogen using magnetotellurics: The Capricorn Orogen, Western Australia. *Precambrian Research*, 168(3–4):185–196.

Seymour, D. B. and Calver, C. R. (1995). Explanatory notes for the time-space diagram and stratotectonic elements map of Tasmania. *Tasmanian Geological Survey Record*, 1.

Seymour, D. B., Green, G. R., and Calver, C. R. (2006). *The geology and mineral deposits of Tasmania: a summary*, volume 72. Dept. of Infrastructure, Energy and Resources.

Seymour, D. B., McClenaghan, M. P., Green, G. R., Everard, J. L., Berry, R. F., Callaghan, T., Davidson, G. J., and Hills, P. B. (2014). Mid-Palaeozoic orogensis, magmatism and mineralisation. In Corbett, K. D., Quilty, P. G., and Calver, C. R., editors, *Geological Evolution of Tasmania*, pages 273–362. Geological Society of Australia (Tasmania Division), 1 edition.

Shaw, R. D., Wellman, P., Gunn, P., Whitaker, A. J., Tarlowski, C., and Morse, M. P. (1996). *Australian Crustal Elements based on the distribution of geophysical domains*. Geoscience Australia, Canberra, 2.4 edition.

Siripunvaraporn, W. (2012). Three-Dimensional Magnetotelluric Inversion: An Introductory Guide for Developers and Users. *Surveys in Geophysics*, 33(1):5–27.

Siripunvaraporn, W., Egbert, G., Lenbury, Y., and Uyeshima, M. (2005). Three-dimensional magnetotelluric inversion: data-space method. *Physics of the Earth and planetary interiors*, 150(1):3–14.

Smith, J. T. and Booker, J. R. (1988). Magnetotelluric inversion for minimum structure. *Geophysics*, 53(12):1565–1576.

Smith, J. T. and Booker, J. R. (1991). Rapid inversion of two- and three-dimensional magnetotelluric data. *Journal of Geophysical Research: Solid Earth*, 96(B3):3905–3922.

Soyer, W., Hallinan, S., Mackie, R. L., and Cumming, W. (2008). Statics in magnetotellurics-shift or model? In *70th EAGE Conference and Exhibition incorporating SPE EUROPEC 2008*.

Stacey, A. R. and Berry, R. F. (2004). The structural history of Tasmania: a review for petroleum explorers. In *PESA Eastern Australian Basin Symposium II*, pages 151–162, Adelaide, SA. Petroleum Exploration Society of Australia (PESA).

Stesky, R. M. and Brace, W. F. (1973). Electrical conductivity of serpentinized rocks to 6 kilobars. *Journal of Geophysical Research*, 78(32):7614–7621.

Tammemagi, H. Y. and Lilley, F. E. M. (1971). Magnetotelluric studies across the Tasman geosyncline, Australia. *Geophysical Journal International*, 22(5):505–516.

Tammemagi, H. Y. and Lilley, F. E. M. (1973). A magnetotelluric traverse in southern Australia. *Geophysical Journal International*, 31(4):433–445.

Thiel, S. (2008). LMTraw2ts: A MATLAB script to generate input files from raw time series data recorded by AuScope long period MT instruments.

Thiel, S. and Heinson, G. (2009). Modelling the effects of ocean and sediments on electromagnetic fields, example from the Gawler Craton, South Australia. *ASEG Extended Abstracts*, 2009(1):1–6.

Thiel, S. and Heinson, G. (2010). Crustal imaging of a mobile belt using magnetotellurics: an example of the Fowler Domain in South Australia. *Journal of Geophysical Research: Solid Earth*, 115(B6).

Thiel, S., Heinson, G., Reid, A., and Robertson, K. (2016a). Insights into lithospheric architecture, fertilisation and fluid pathways from AusLAMP MT. *ASEG Extended Abstracts*, 2016(1):1–6.

Thiel, S., Heinson, G., and White, A. (2005). Tectonic evolution of the southern Gawler Craton, South Australia, from electromagnetic sounding. *Australian Journal of Earth Sciences*, 52(6):887–896.

Thiel, S., Soeffky, P., Krieger, L., Regenauer-Lieb, K., Peacock, J. R., and Heinson, G. (2016b). Conductivity response to intraplate deformation: Evidence for metamorphic devolatilization and crustal-scale fluid focusing. *Geophysical Research Letters*, 43(21):11–236.

Tikhonov, A. N. (1950). On determination of electric characteristics of deep layers of the earth's crust. In *Doklady*, volume 73, pages 295–297. Citeseer.

Turner, N. J., Black, L. P., and Kamperman, M. (1998). Dating of Neoproterozoic and Cambrian orogenies in Tasmania. *Australian Journal of Earth Sciences*, 45(5):789–806.

Uchida, T. (1993). Smooth 2-D inversion for magnetotelluric data based on statistical criterion ABIC. *Journal of geomagnetism and geoelectricity*, 45(9):841–858.

Unsworth, M. (2010). Magnetotelluric Studies of Active Continent–Continent Collisions. *Surveys in Geophysics*, 31(2):137–161.

Veevers, J. J. (2000). Mid-Cretaceous and mid-Eocene events in the Indo-Australian and Antarctic Plates. In Veevers, J. J., editor, *Billion-year earth history of Australia and neighbours in Gondwanaland*, pages 102–109. GEMOC Press.

Wang, L. and Chamalaun, F. (1995). A magnetotelluric traverse across the Adelaide Geosyncline. *Exploration Geophysics*, 26(4):539–546.

Wang, L., Hitchman, A. P., Ogawa, Y., Siripunvaraporn, W., Ichiki, M., and Fuji-ta, K. (2014). A 3-D conductivity model of the Australian continent using observatory and magnetometer array data. *Geophysical Journal International*, 198(2):1143–1158.

Wang, L., Lilley, F. E. M., and Chamalaun, F. (1997). Large-scale electrical conductivity structure of Australia from magnetometer arrays. *Exploration Geophysics*, 28(1/2):150–155.

Wannamaker, P. E., Caldwell, T. G., Jiracek, G. R., Maris, V., Hill, G. J., Ogawa, Y., Bibby, H. M., Bennie, S. L., and Heise, W. (2009). Fluid and deformation regime of an advancing subduction system at Marlborough, New Zealand. *Nature*, 460(7256):733–736.

Wiese, H. (1962). Geomagnetische Tiefentellurik Teil II: die Streichrichtung der Untergrundstrukturen des elektrischen Widerstandes, erschlossen aus geomagnetischen Variationen. *Geofisica pura e applicata*, 52(1):83–103.

Williams, E. (1989). Summary and synthesis. In Burrett, C. F. and Martin, E. L., editors, *Geology and Mineral Resources of Tasmania*, pages 468–499. Special Publication Geological Society of Australia.

Yang, X., Keppler, H., McCammon, C., and Ni, H. (2012). Electrical conductivity of orthopyroxene and plagioclase in the lower crust. *Contributions to Mineralogy and Petrology*, 163(1):33–48.

Yoshino, T. and Noritake, F. (2011). Unstable graphite films on grain boundaries in crustal rocks. *Earth and Planetary Science Letters*, 306(3-4):186–192.

Zwingmann, H., Sutherland, L., Graham, I., Forsyth, S. M., Everard, J. L., and Wartho, J. A. (2004). No Title. *Geological Society of Australia Abstracts*, 73:141.

Appendices

Appendix A

AusLAMP 3D Inverse Model Iteration Summary

Key parameters and final global RMS misfit for inverse models using the low resolution 7 km model mesh. Error floors for tipper data were given as absolute values while error floors for impedance tensor components were determined using the Egbert method (percent of $\sqrt{|\mathbf{Z}_{xy}\mathbf{Z}_{yx}|}$ for each period). Inversions in which either tipper or impedance tensor information was not included have impedance tensor or tipper error floors given as 'OFF'.

		Data Error Floors			**Smoothing Parameters**
Inversion	**Global RMS**	$\mathbf{Z}_{xy}$ & $\mathbf{Z}_{yx}$	$\mathbf{Z}_{xx}$ & $\mathbf{Z}_{yy}$	$\mathbf{T}_x$ & $\mathbf{T}_y$	**Covariance**
run001	3.27	10%	5%	0.10	0.2
run002	3.86	10%	5%	0.10	0.2
run003	3.03	10%	5%	0.10	0.2
run004	1.91	20%	10%	0.10	0.2
run005	2.01	20%	10%	OFF	0.2
run006	4.08	10%	5%	OFF	0.2
run007	1.82	10%	20%	0.10	0.2
run008	1.83	10%	20%	OFF	0.2
run009	2.26	5%	10%	0.10	0.2
run010	2.48	5%	10%	OFF	0.2
run011	1.02	OFF	OFF	0.05	0.2
run012	1.04	OFF	OFF	0.02	0.2
run013	1.47	OFF	OFF	0.01	0.2
run014	2.45	5%	10%	0.05	0.2
run015	6.70	2%	5%	0.05	0.2
run016	3.12	5%	10%	0.10	0.2

		Data Error Floors			Smoothing Parameters
Inversion	**Global RMS**	$\mathbf{Z}_{xy}$ & $\mathbf{Z}_{yx}$	$\mathbf{Z}_{xx}$ & $\mathbf{Z}_{yy}$	$\mathbf{T}_x$ & $\mathbf{T}_y$	**Covariance**
run017	3.00	5%	10%	0.10	0.2
run018	3.37	5%	10%	0.10	0.2
run019	2.59	5%	10%	0.02	0.2
run020	2.03	5%	10%	0.05	0.2
run021	1.91	10%	20%	0.05	0.2
run022	1.85	10%	20%	0.05	0.2
run023	2.18	10%	20%	0.05	0.2
run024	2.33	10%	20%	0.05	0.2

Appendix B

AusLAMP Long Period 3D Statewide 3D Inverse Model Response Curves

Observed (points with error bars) and modelled (dashed lines) responses from the preferred 3D inverse model of the AusLAMP long period statewide data set.

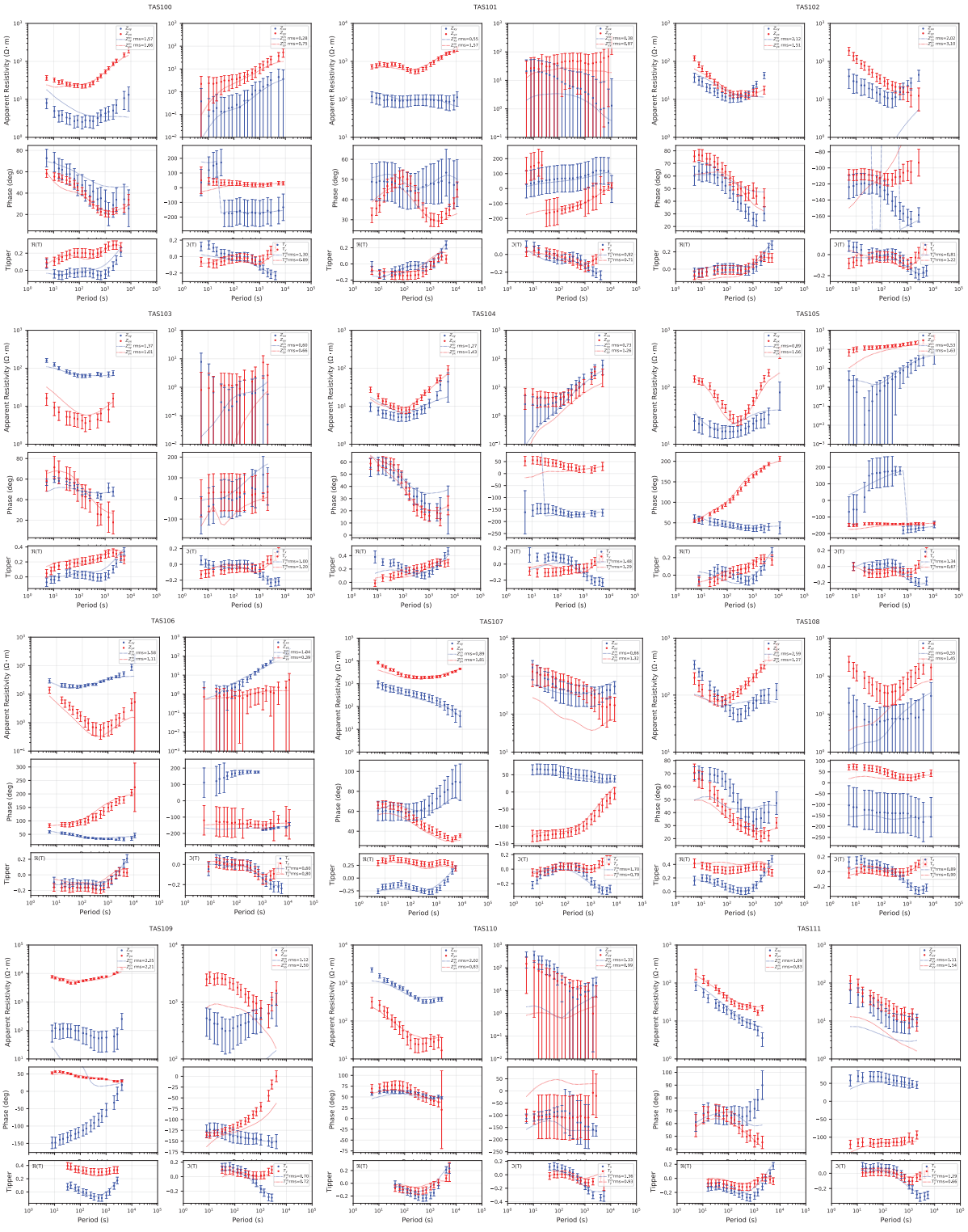
TAS100
TAS101
TAS102
TAS103
TAS104
TAS105
TAS106
TAS107
TAS108
TAS109
TAS110
TAS111
Apparent Resistivity (Ω·m)
Phase (deg)
Tipper
Period (s)

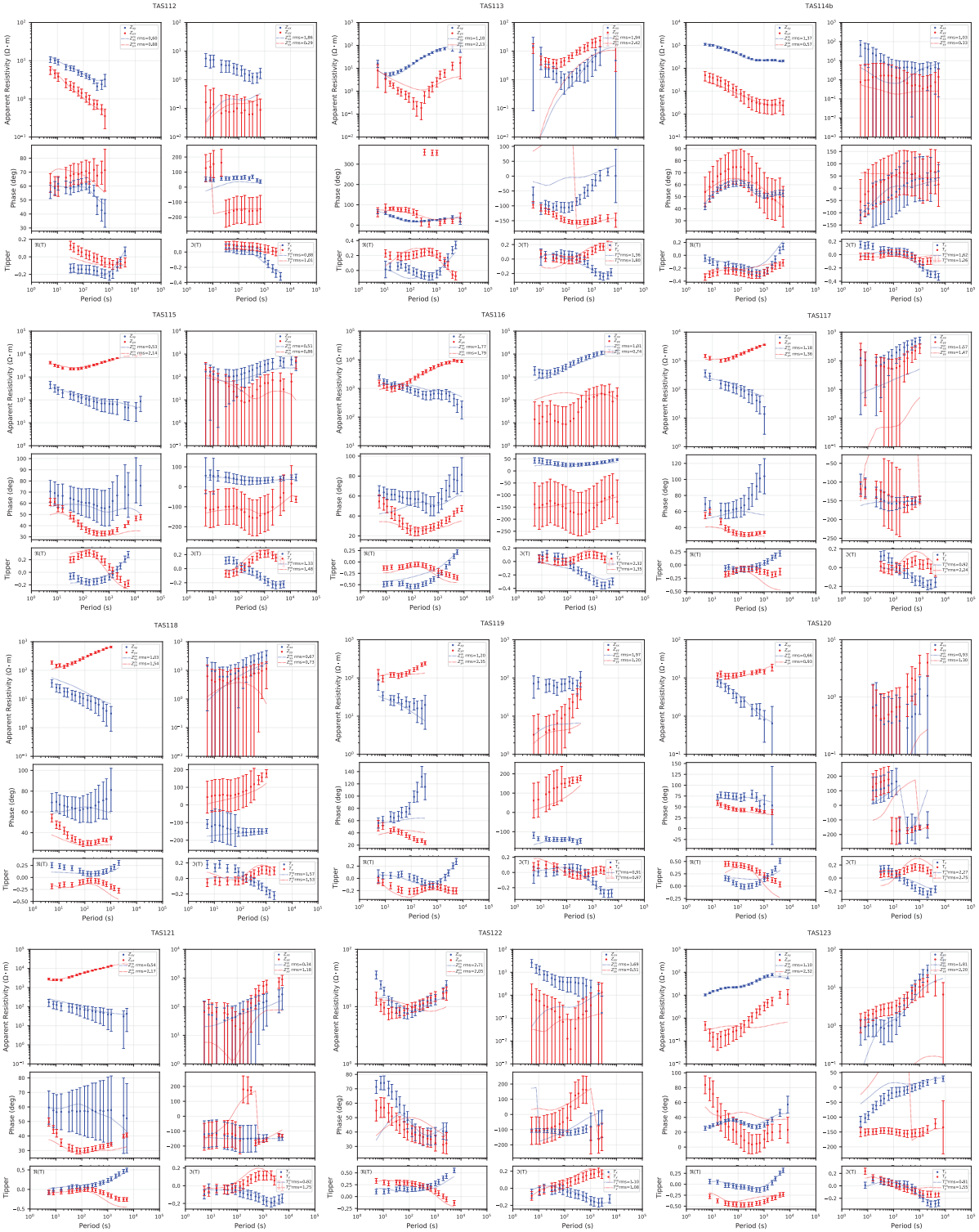
TAS112
TAS113
TAS114b
TAS115
TAS116
TAS117
TAS118
TAS119
TAS120
TAS121
TAS122
TAS123
Apparent Resistivity (Ω·m)
Phase (deg)
Tipper
Period (s)

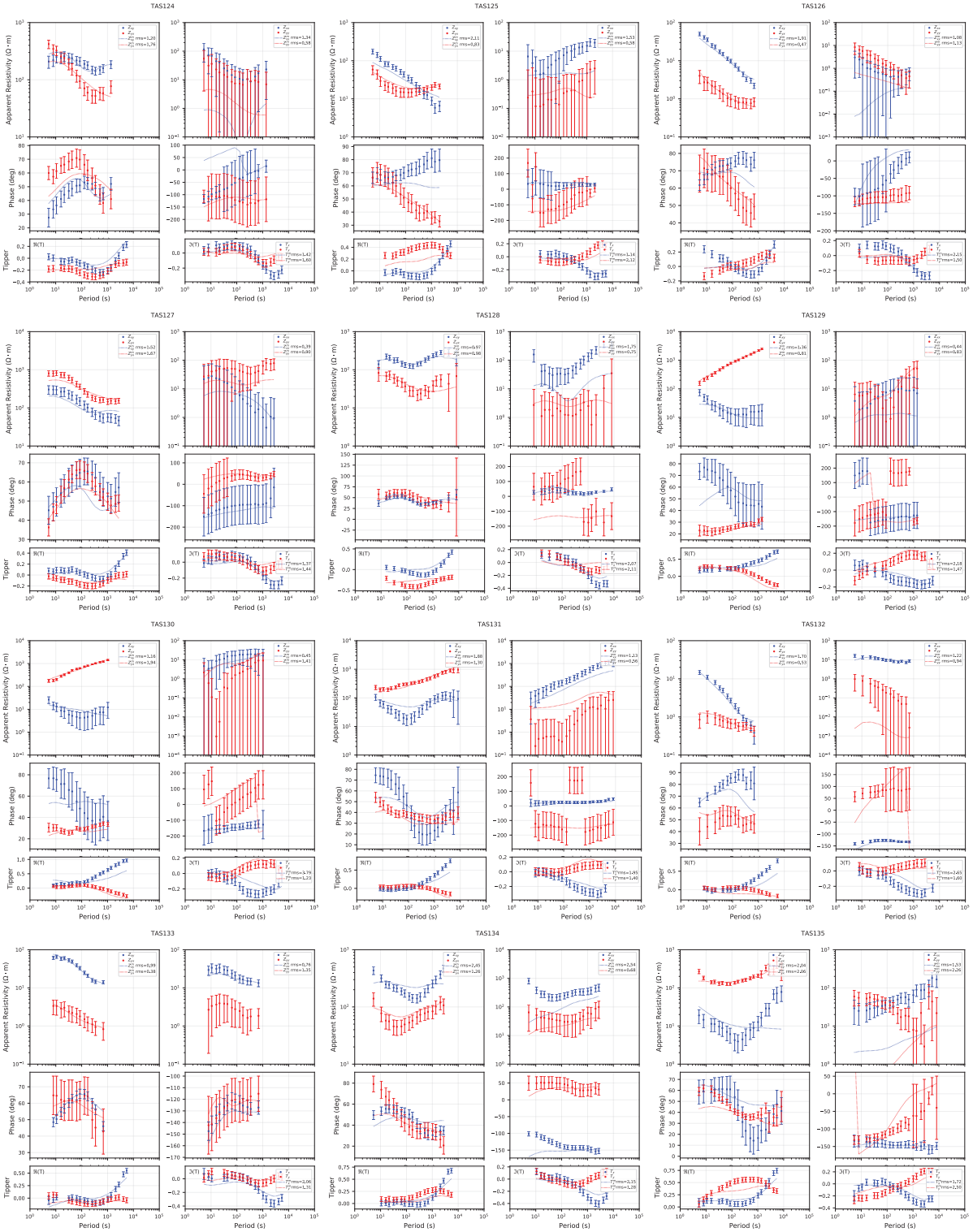
TAS124
TAS125
TAS126
TAS127
TAS128
TAS129
TAS130
TAS131
TAS132
TAS133
TAS134
TAS135
Apparent Resistivity (Ω·m)
Phase (deg)
Tipper
Period (s)

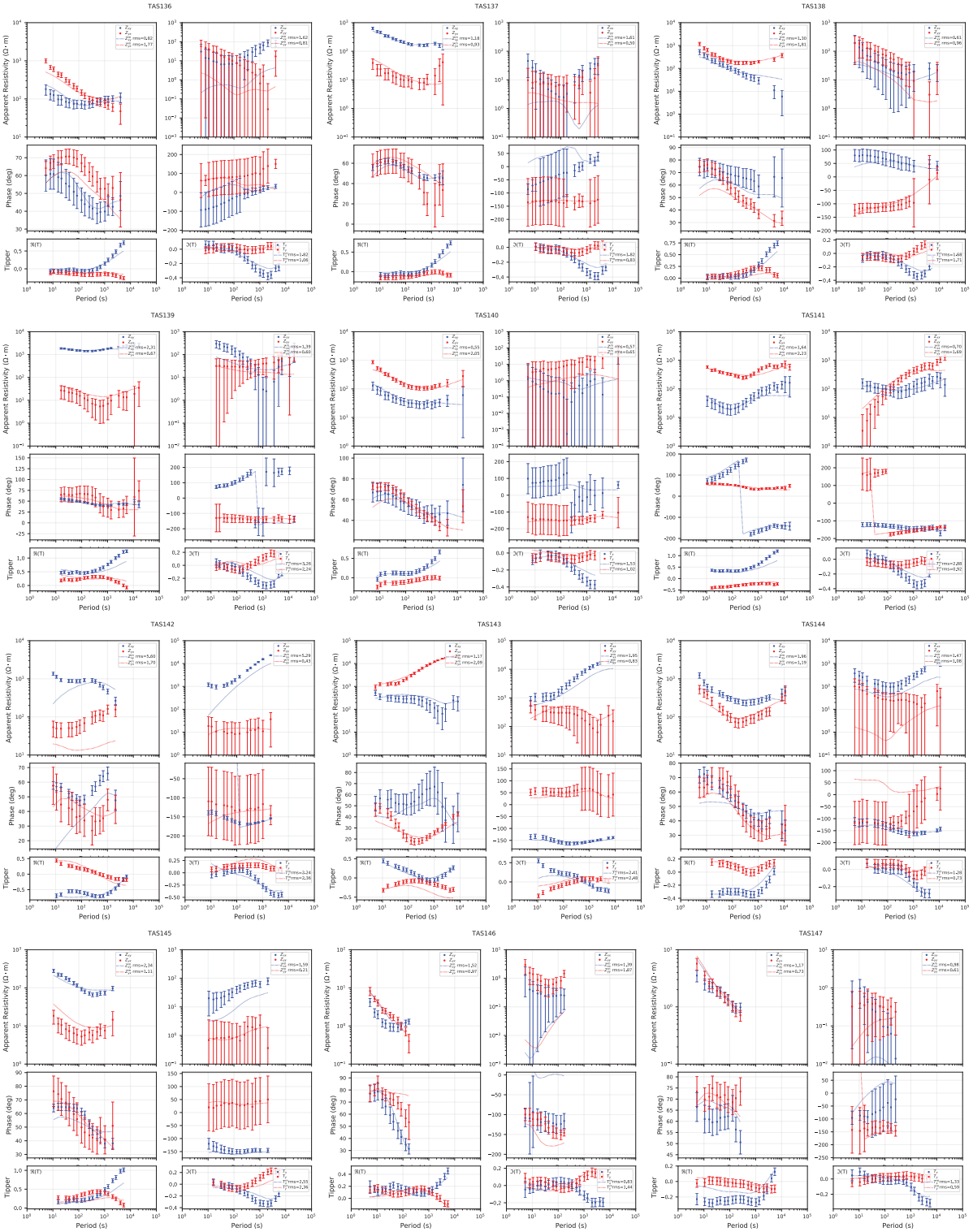
TAS136
TAS137
TAS138
TAS139
TAS140
TAS141
TAS142
TAS143
TAS144
TAS145
TAS146
TAS147
Apparent Resistivity (Ω·m)
Phase (deg)
Tipper
Period (s)

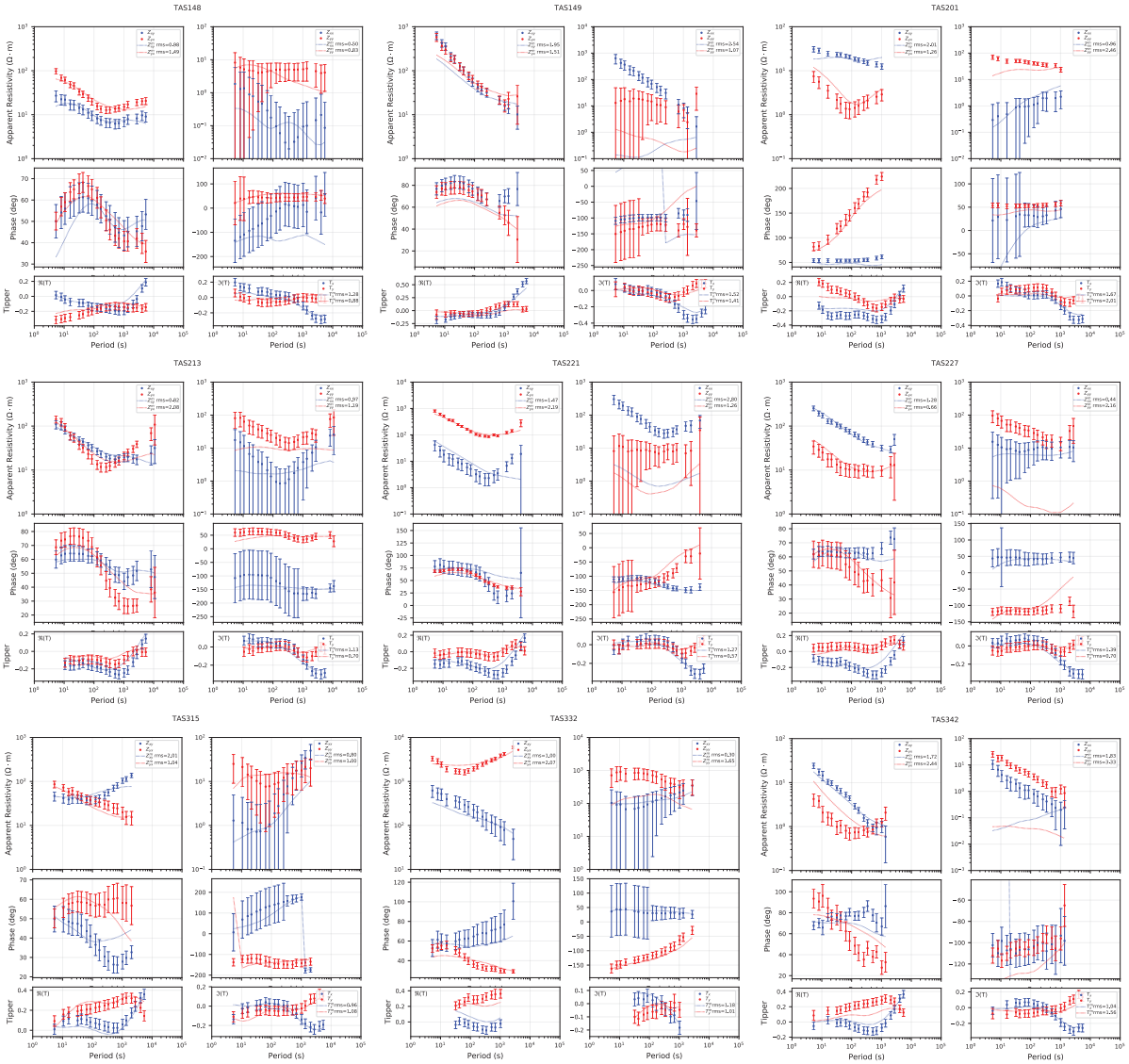
TAS148
TAS149
TAS201
TAS213
TAS221
TAS227
TAS315
TAS332
TAS342
Apparent Resistivity (Ω · m)
Phase (deg)
Tipper
Period (s)

Appendix C

3D Data Visualisation Digital Appendices

All 3D imagery presented in the thesis was captured from a Geoscience Analyst 3D project. Geoscience Analyst is a free geoscientific data viewing platform developed by Mira Geoscience and supported on Windows PC machines. To access this digital appendix, the reader is directed to the following links.

Geoscience Analyst software download page:
https://mirageoscience.com/mining-industry-software/geoscience-analyst/

Geoscience Analyst project containing all models presented in the thesis:
https://drive.google.com/file/d/1-E3ioGxU2pCPU0NxaA1DBjNMczEioMA5/view?usp=sharing

Appendix D

West Transect 2D Inverse Model Response Curves

Observed (points with error bars) and modelled (dashed lines) responses from the preferred 2D inverse model of the west transect broadband data set.

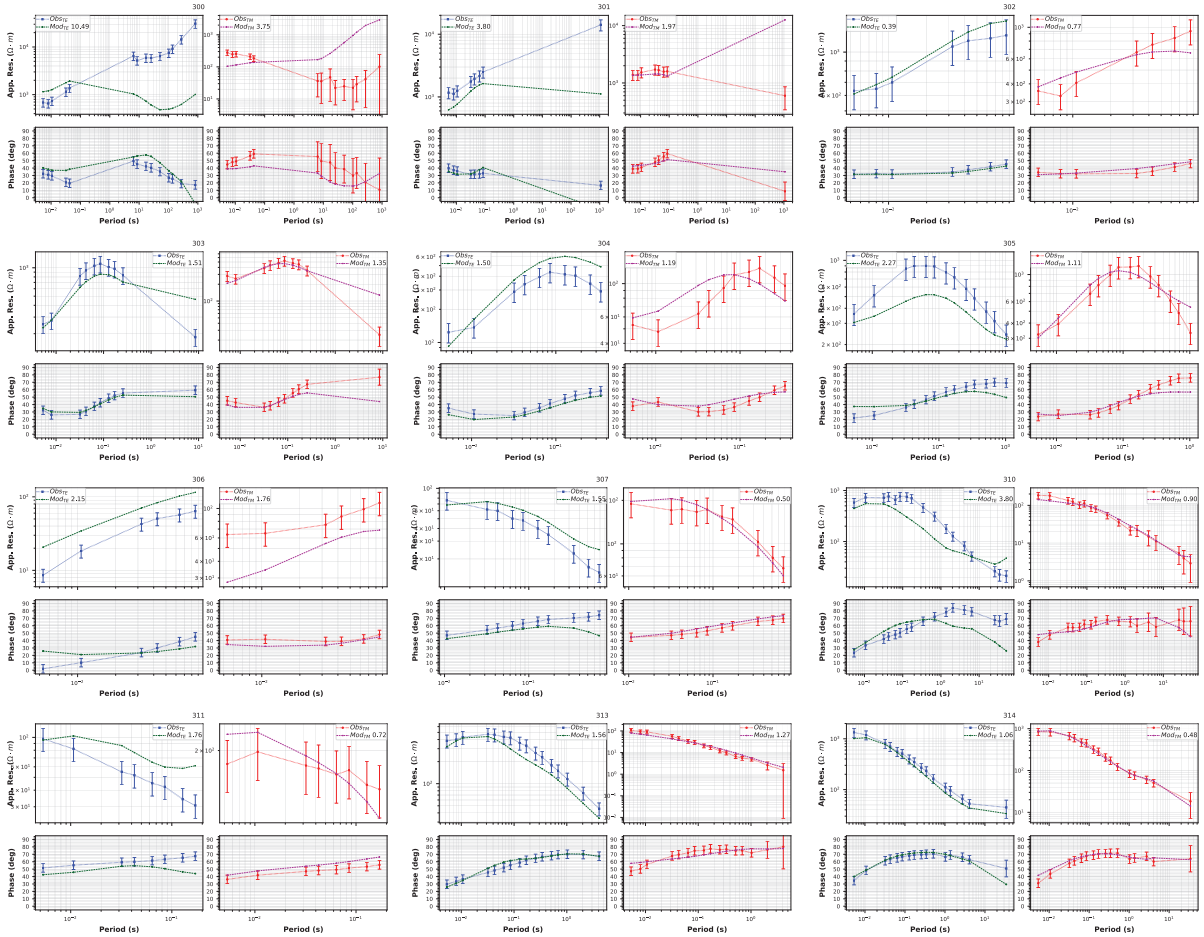

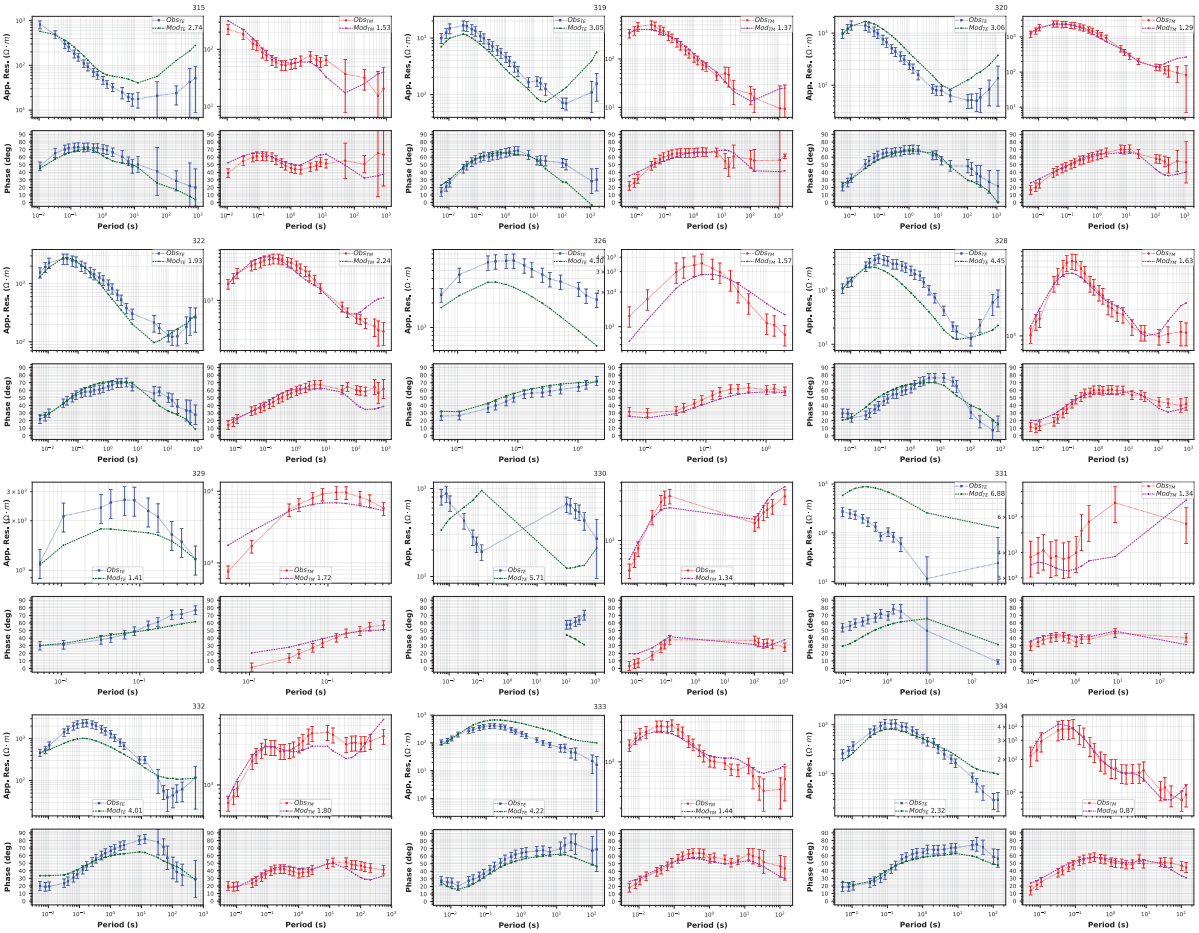
315
319
320
322
326
328
329
330
331
332
333
334
App. Res. (Ω · m)
Phase (deg)
Period (s)

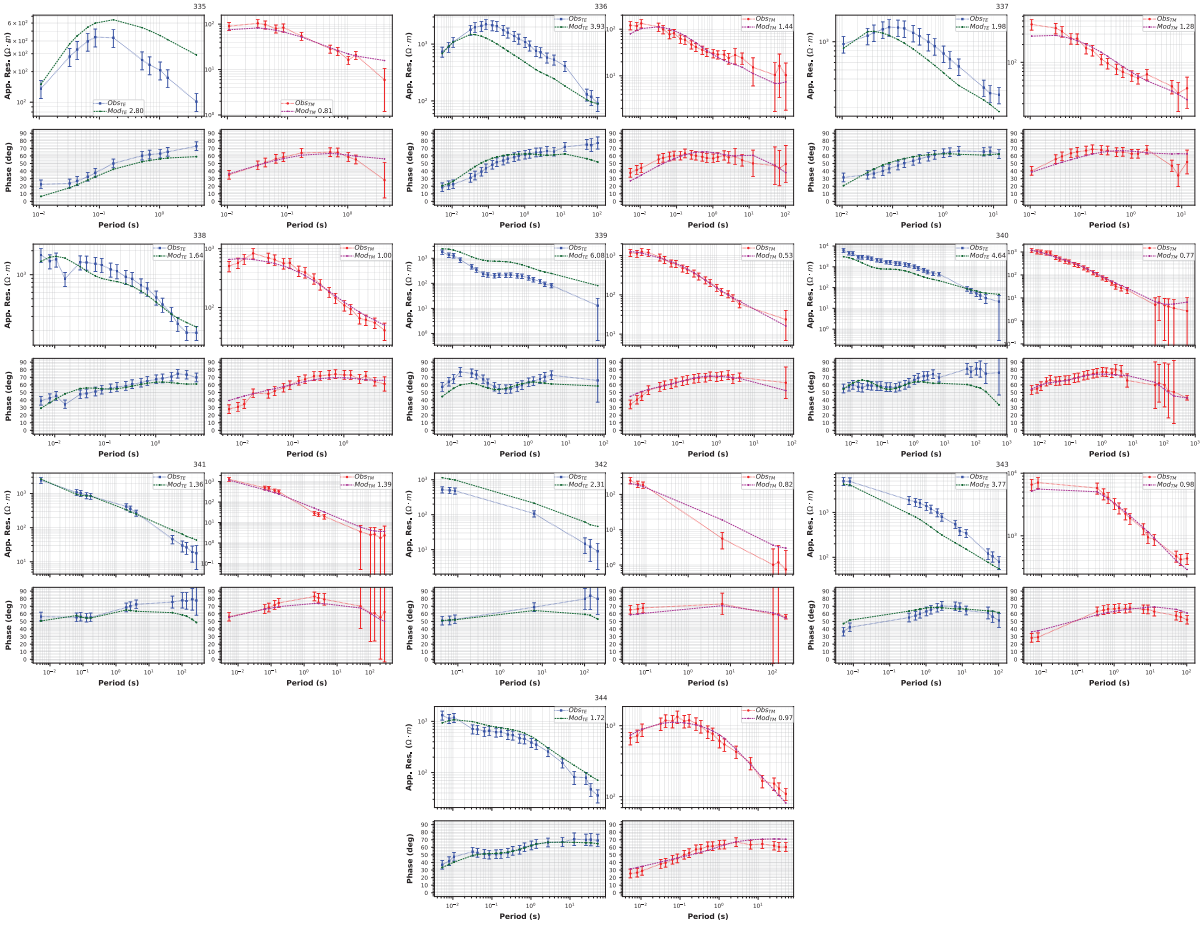
335
Obs_TE
Mod_TE 2.80
Obs_TM
Mod_TM 0.81
336
Obs_TE
Mod_TE 3.93
Obs_TM
Mod_TM 1.44
337
Obs_TE
Mod_TE 1.98
Obs_TM
Mod_TM 1.28
338
Obs_TE
Mod_TE 1.64
Obs_TM
Mod_TM 1.00
339
Obs_TE
Mod_TE 6.08
Obs_TM
Mod_TM 0.53
340
Obs_TE
Mod_TE 4.64
Obs_TM
Mod_TM 0.77
341
Obs_TE
Mod_TE 1.36
Obs_TM
Mod_TM 1.39
342
Obs_TE
Mod_TE 2.31
Obs_TM
Mod_TM 0.82
343
Obs_TE
Mod_TE 3.77
Obs_TM
Mod_TM 0.98
344
Obs_TE
Mod_TE 1.72
Obs_TM
Mod_TM 0.97
App. Res. (Ω · m)
Phase (deg)
Period (s)

Appendix E

KUTh Energy Combined Modelling Preferred Model Response Curves

Observed (points with error bars) and modelled (dashed lines) responses from the preferred 3D model from the combined broadband and long period MT inverse modelling investigation at Lemont, NE Tasmania.

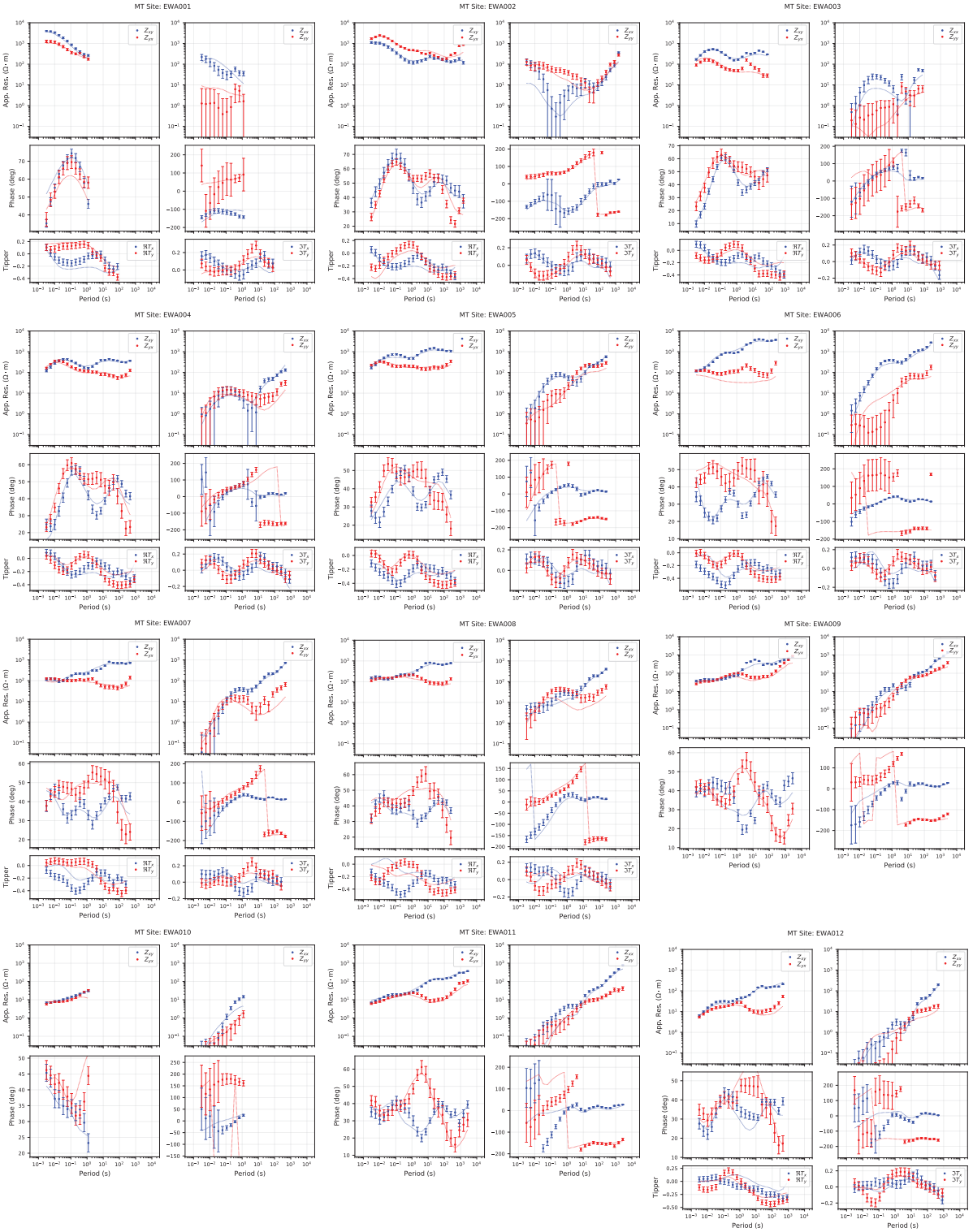
MT Site: EWA001
MT Site: EWA002
MT Site: EWA003
MT Site: EWA004
MT Site: EWA005
MT Site: EWA006
MT Site: EWA007
MT Site: EWA008
MT Site: EWA009
MT Site: EWA010
MT Site: EWA011
MT Site: EWA012
App. Res. (Ω·m)
Phase (deg)
Tipper
Period (s)

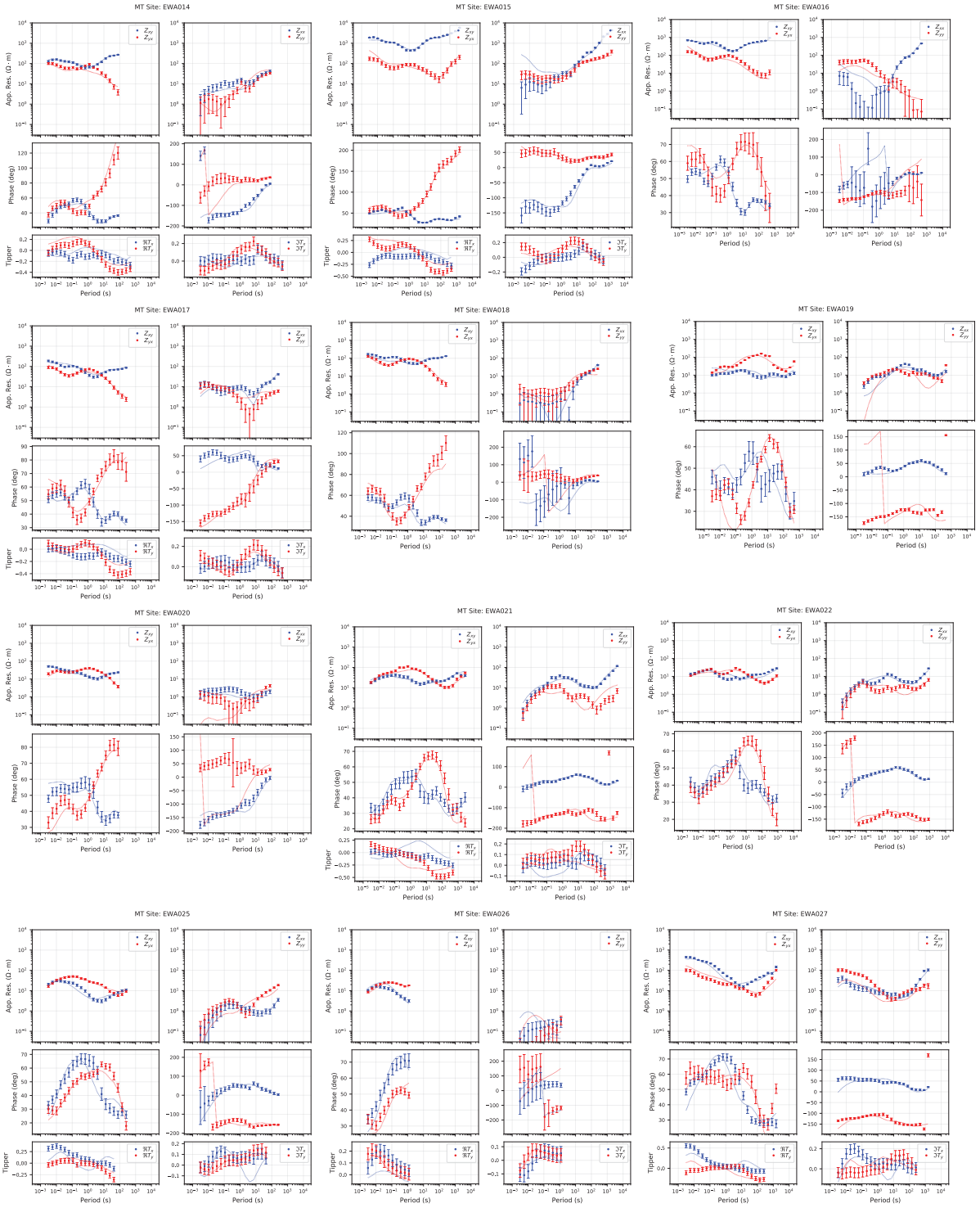
MT Site: EWA014
MT Site: EWA015
MT Site: EWA016
MT Site: EWA017
MT Site: EWA018
MT Site: EWA019
MT Site: EWA020
MT Site: EWA021
MT Site: EWA022
MT Site: EWA025
MT Site: EWA026
MT Site: EWA027
App. Res. (Ω · m)
Phase (deg)
Tipper
Period (s)

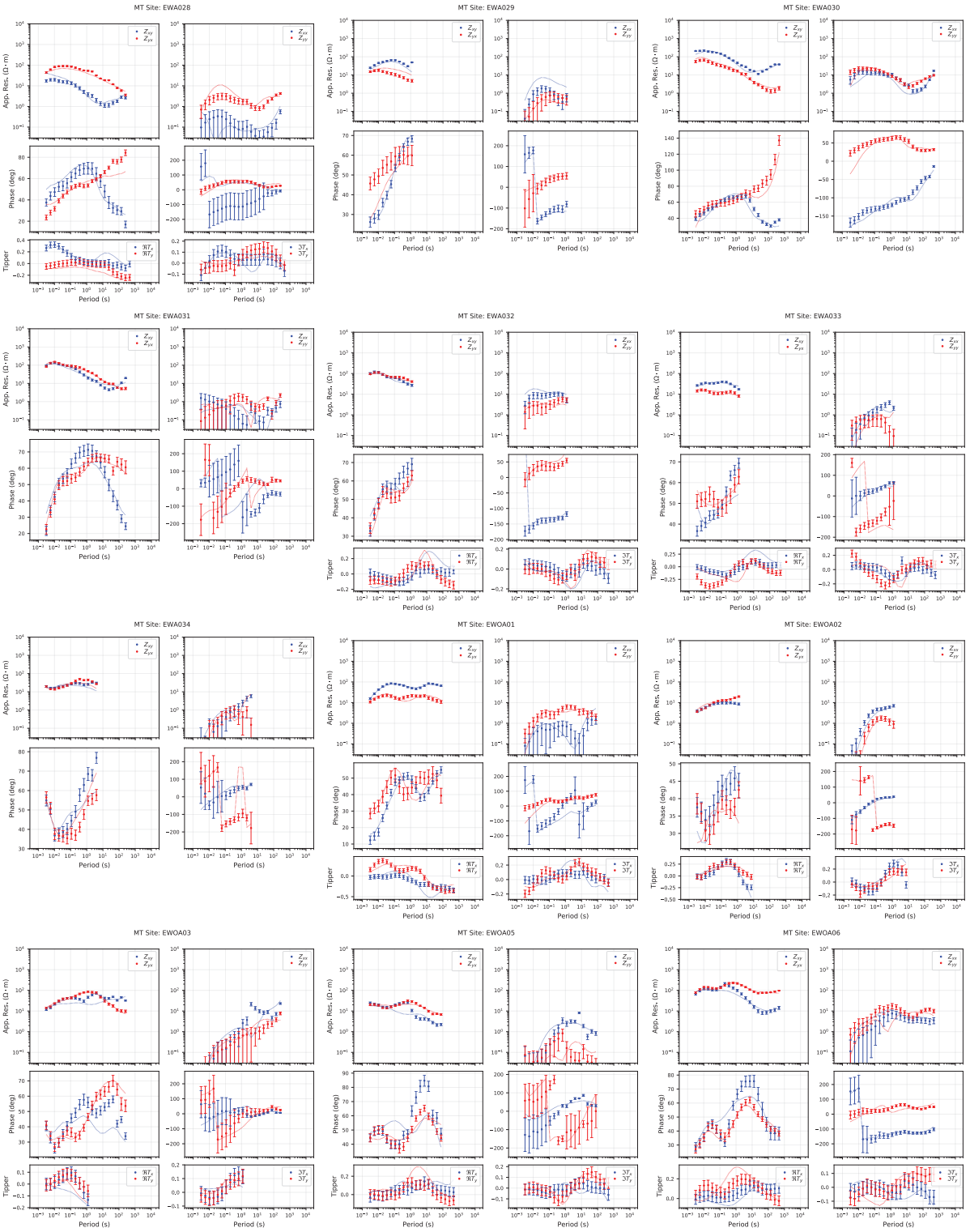
MT Site: EWA028
MT Site: EWA029
MT Site: EWA030
MT Site: EWA031
MT Site: EWA032
MT Site: EWA033
MT Site: EWA034
MT Site: EWOA01
MT Site: EWOA02
MT Site: EWOA03
MT Site: EWOA05
MT Site: EWOA06
App. Res. (Ω·m)
Phase (deg)
Tipper
Period (s)

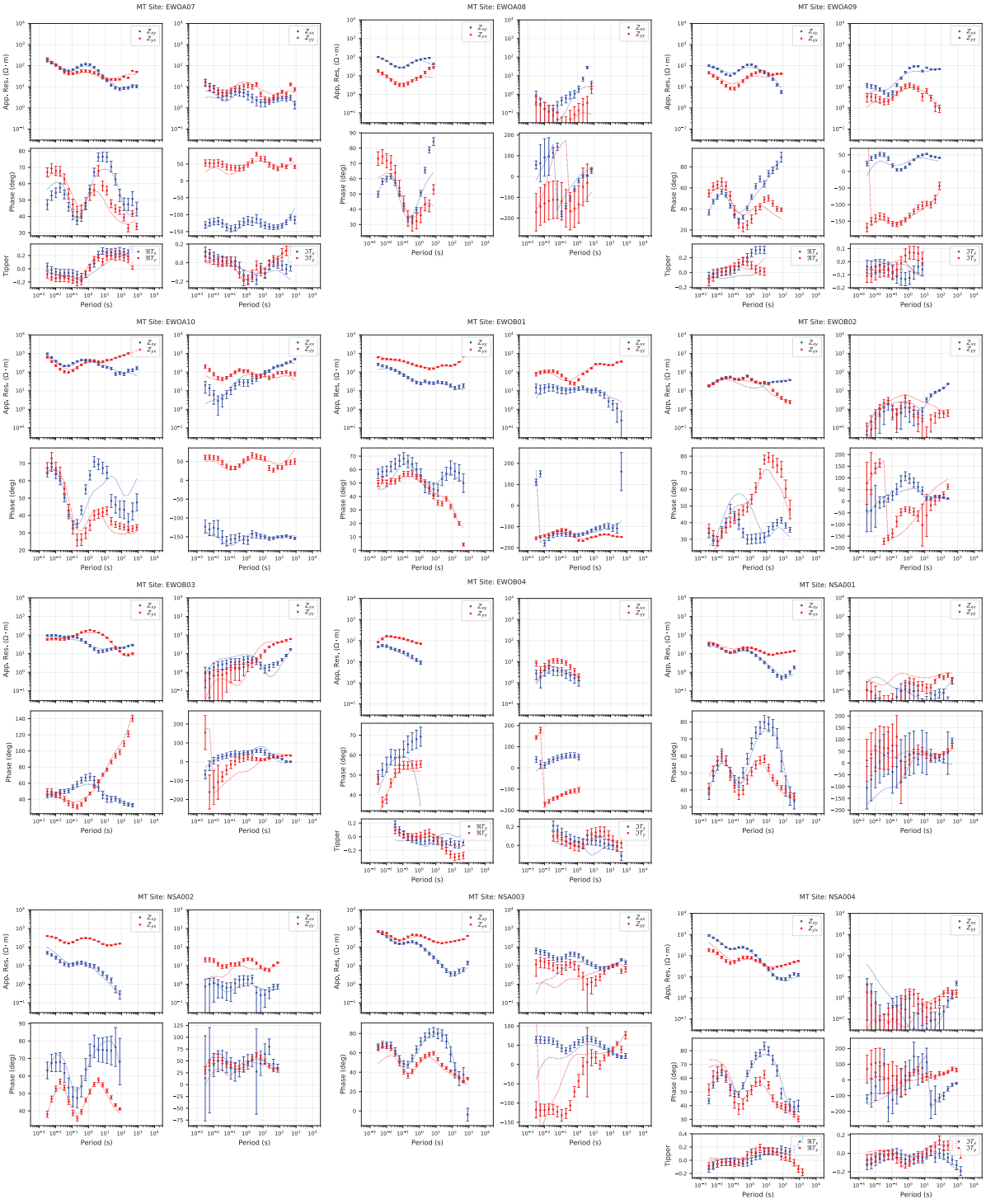
MT Site: EWOA07
MT Site: EWOA08
MT Site: EWOA09
MT Site: EWOA10
MT Site: EWOB01
MT Site: EWOB02
MT Site: EWOB03
MT Site: EWOB04
MT Site: NSA001
MT Site: NSA002
MT Site: NSA003
MT Site: NSA004
App. Res. (Ω·m)
Phase (deg)
Tipper
Period (s)

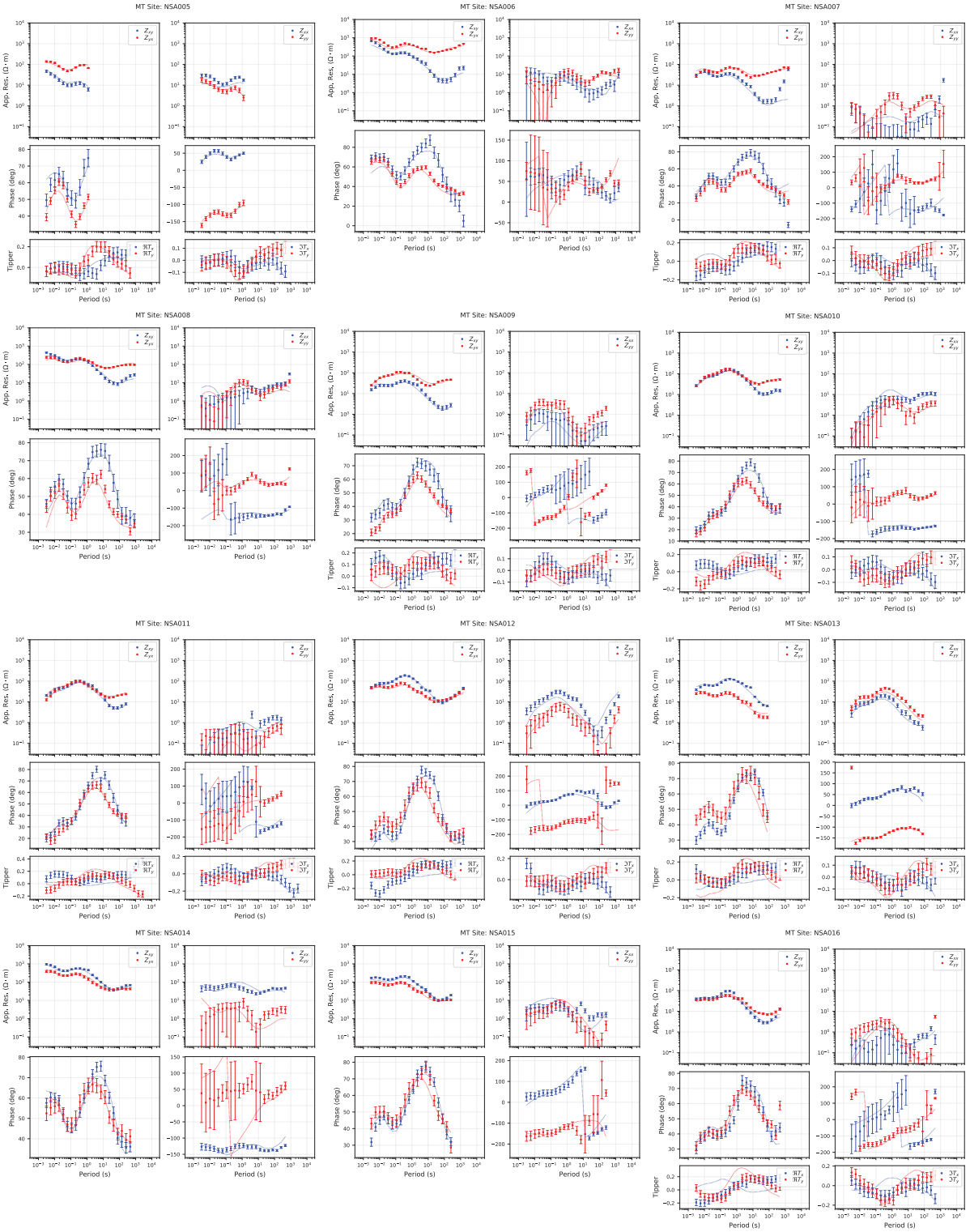
MT Site: NSA005
MT Site: NSA006
MT Site: NSA007
MT Site: NSA008
MT Site: NSA009
MT Site: NSA010
MT Site: NSA011
MT Site: NSA012
MT Site: NSA013
MT Site: NSA014
MT Site: NSA015
MT Site: NSA016
App. Res. (Ω·m)
Phase (deg)
Tipper
Period (s)

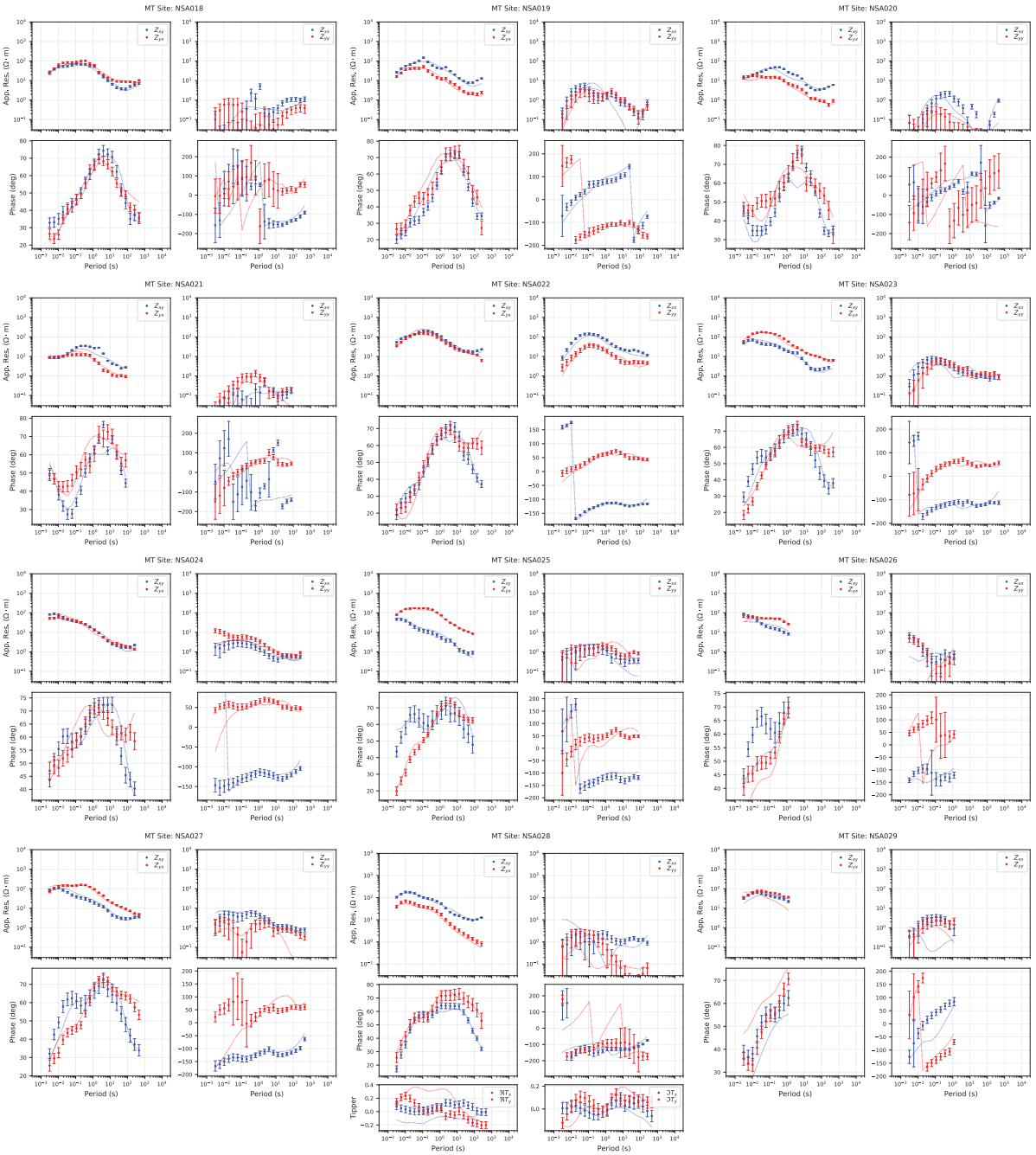
MT Site: NSA018
MT Site: NSA019
MT Site: NSA020
MT Site: NSA021
MT Site: NSA022
MT Site: NSA023
MT Site: NSA024
MT Site: NSA025
MT Site: NSA026
MT Site: NSA027
MT Site: NSA028
MT Site: NSA029
App. Res. (Ω·m)
Phase (deg)
Tipper
Period (s)

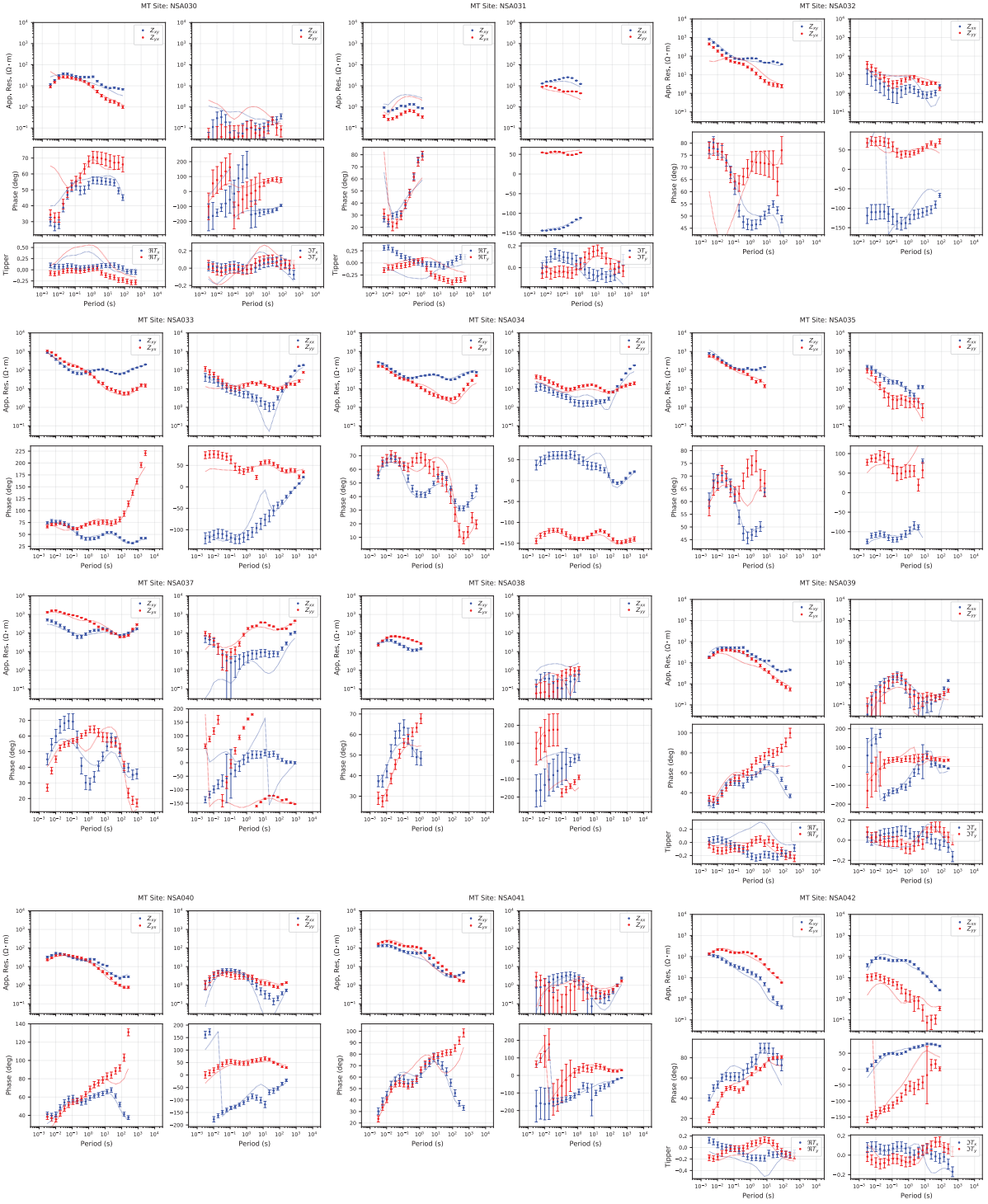
MT Site: NSA030
MT Site: NSA031
MT Site: NSA032
MT Site: NSA033
MT Site: NSA034
MT Site: NSA035
MT Site: NSA037
MT Site: NSA038
MT Site: NSA039
MT Site: NSA040
MT Site: NSA041
MT Site: NSA042
App. Res, (Ω·m)
Phase (deg)
Tipper
Period (s)

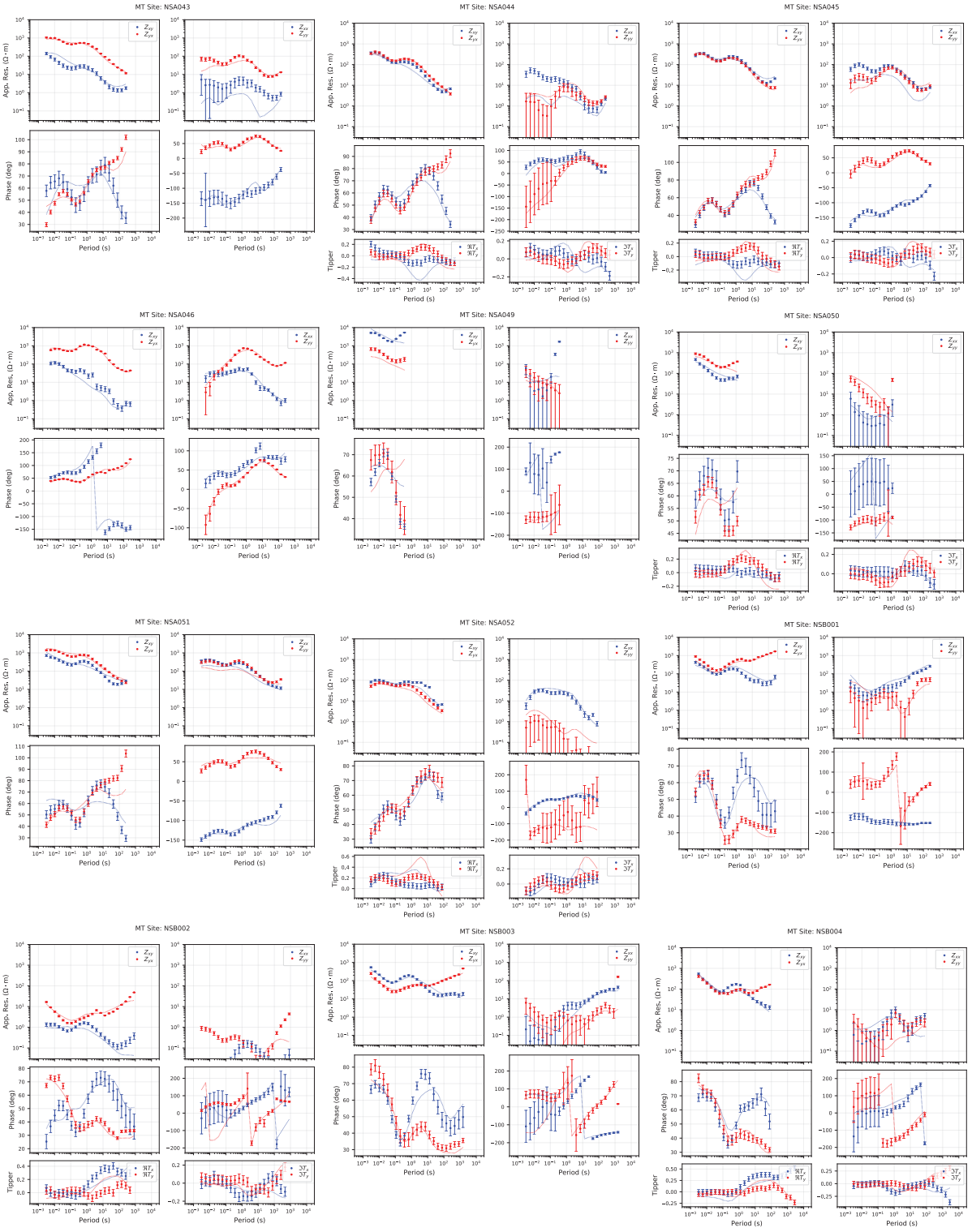
MT Site: NSA043
MT Site: NSA044
MT Site: NSA045
MT Site: NSA046
MT Site: NSA049
MT Site: NSA050
MT Site: NSA051
MT Site: NSA052
MT Site: NSB001
MT Site: NSB002
MT Site: NSB003
MT Site: NSB004
App. Res. (Ω·m)
Phase (deg)
Tipper
Period (s)

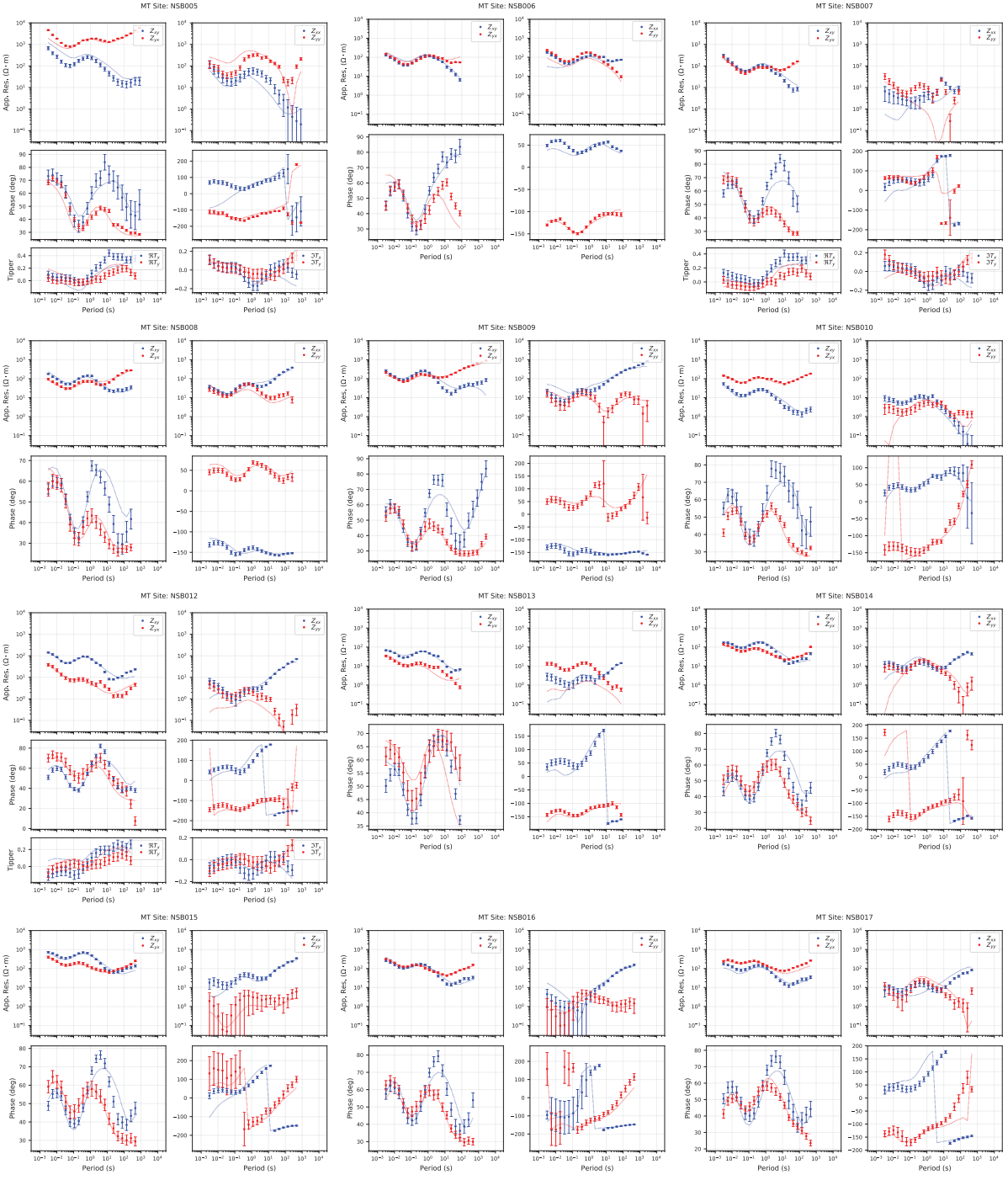
MT Site: NSB005
MT Site: NSB006
MT Site: NSB007
MT Site: NSB008
MT Site: NSB009
MT Site: NSB010
MT Site: NSB012
MT Site: NSB013
MT Site: NSB014
MT Site: NSB015
MT Site: NSB016
MT Site: NSB017
App. Res. (Ω·m)
Phase (deg)
Tipper
Period (s)

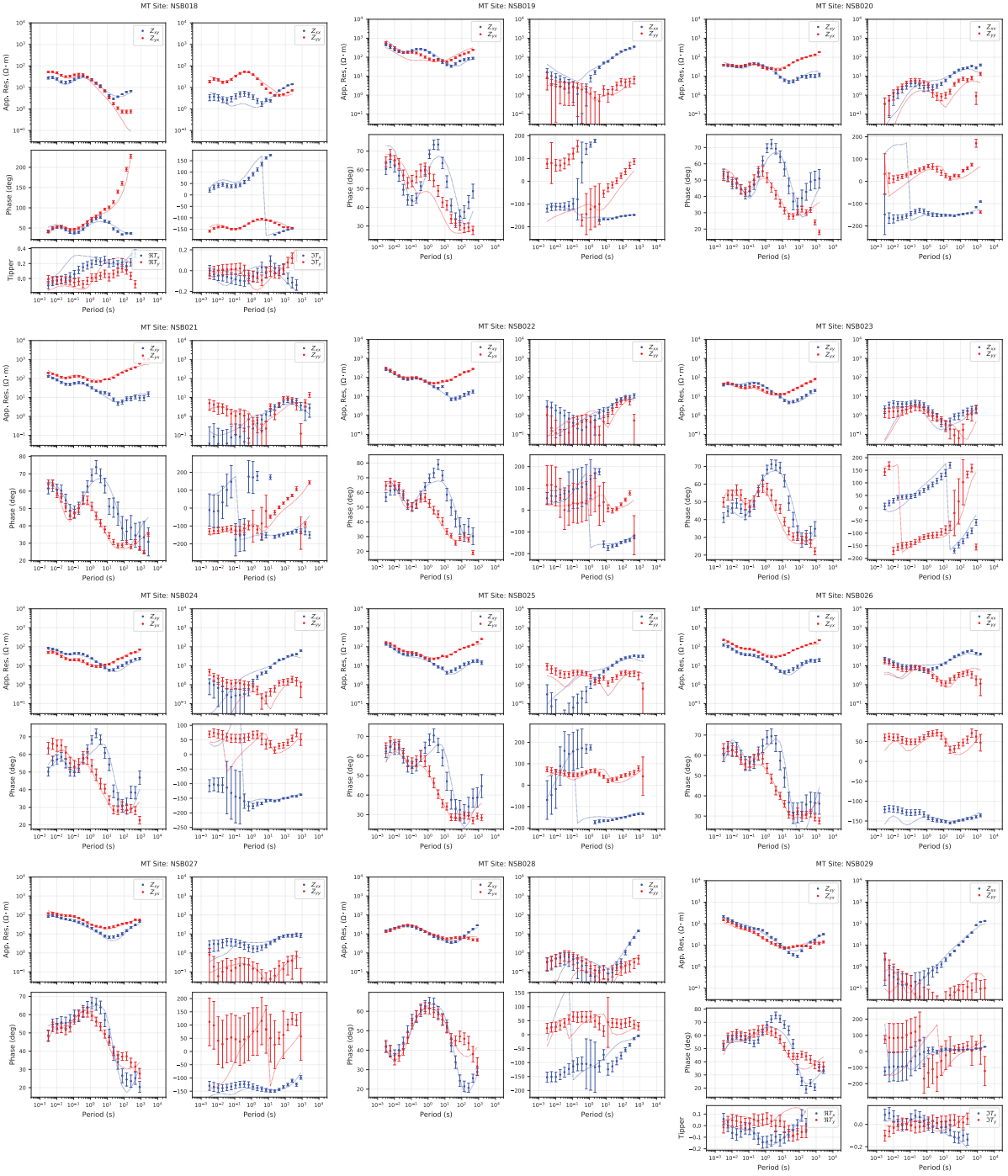
MT Site: NSB018
MT Site: NSB019
MT Site: NSB020
MT Site: NSB021
MT Site: NSB022
MT Site: NSB023
MT Site: NSB024
MT Site: NSB025
MT Site: NSB026
MT Site: NSB027
MT Site: NSB028
MT Site: NSB029
App. Res, (Ω·m)
Phase (deg)
Tipper
Period (s)

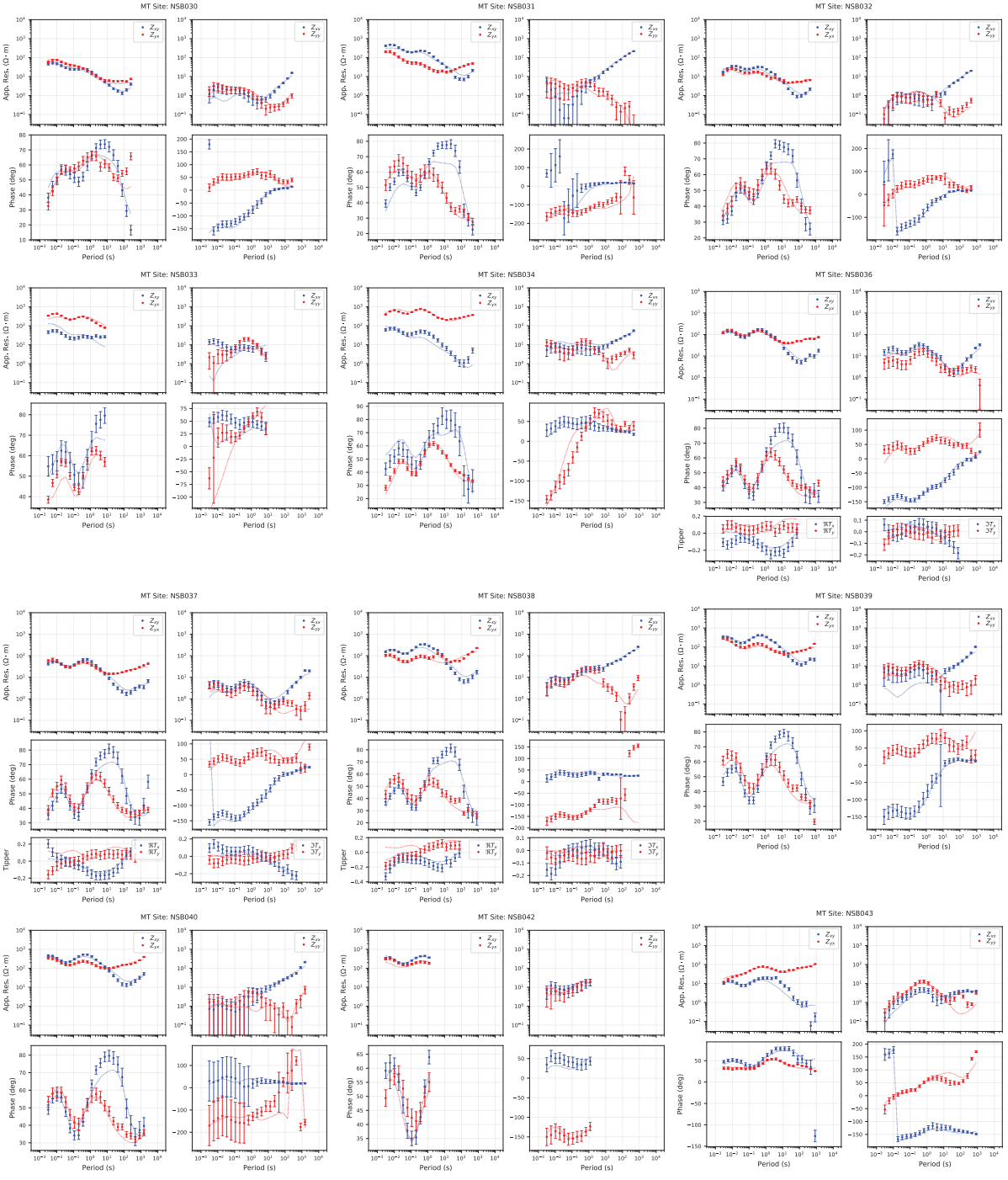
MT Site: NSB030
MT Site: NSB031
MT Site: NSB032
MT Site: NSB033
MT Site: NSB034
MT Site: NSB036
MT Site: NSB037
MT Site: NSB038
MT Site: NSB039
MT Site: NSB040
MT Site: NSB042
MT Site: NSB043
App. Res. (Ω·m)
Phase (deg)
Tipper
Period (s)

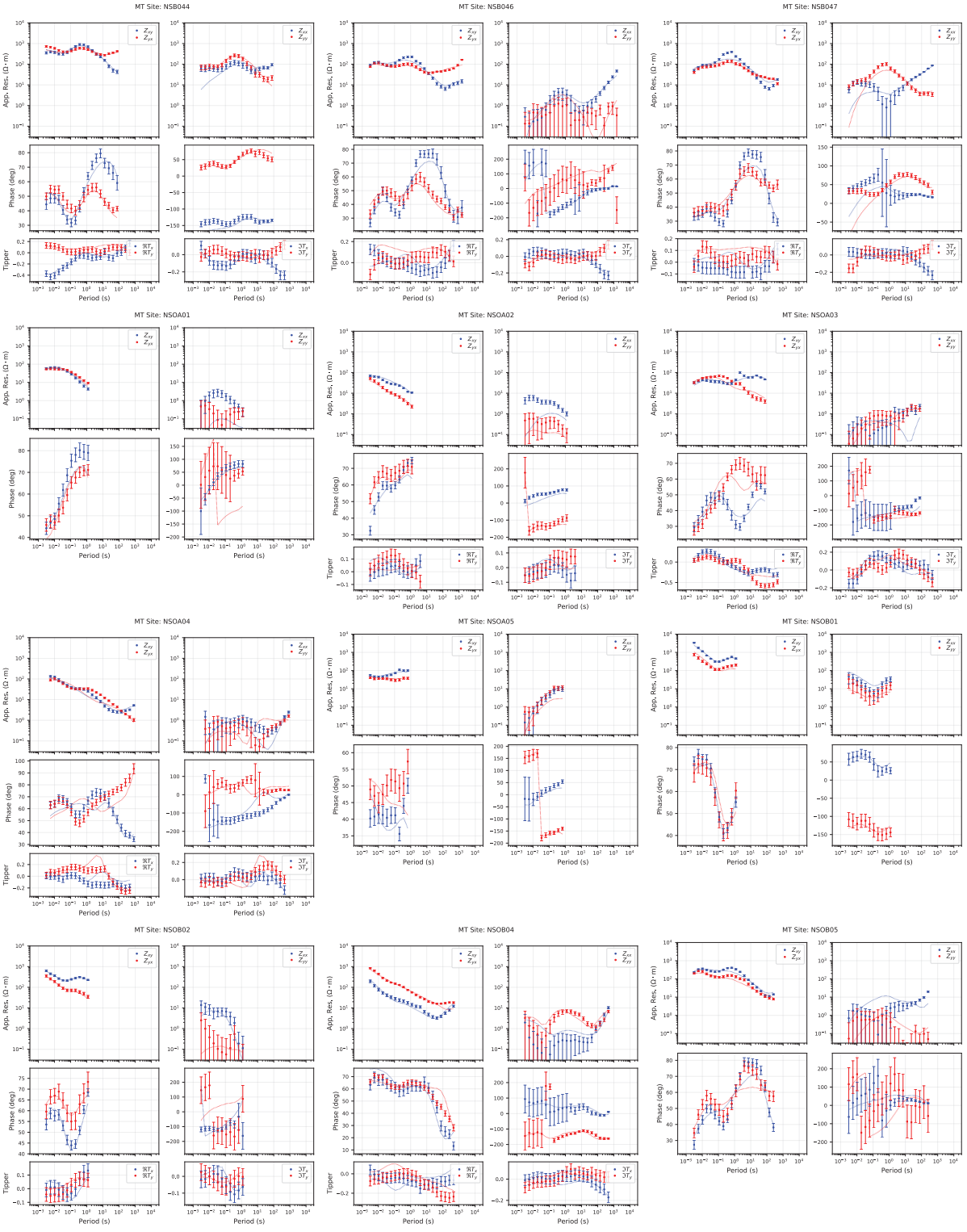
MT Site: NSB044
MT Site: NSB046
MT Site: NSB047
MT Site: NSOA01
MT Site: NSOA02
MT Site: NSOA03
MT Site: NSOA04
MT Site: NSOA05
MT Site: NSOB01
MT Site: NSOB02
MT Site: NSOB04
MT Site: NSOB05
App. Res. (Ω·m)
Phase (deg)
Tipper
Period (s)

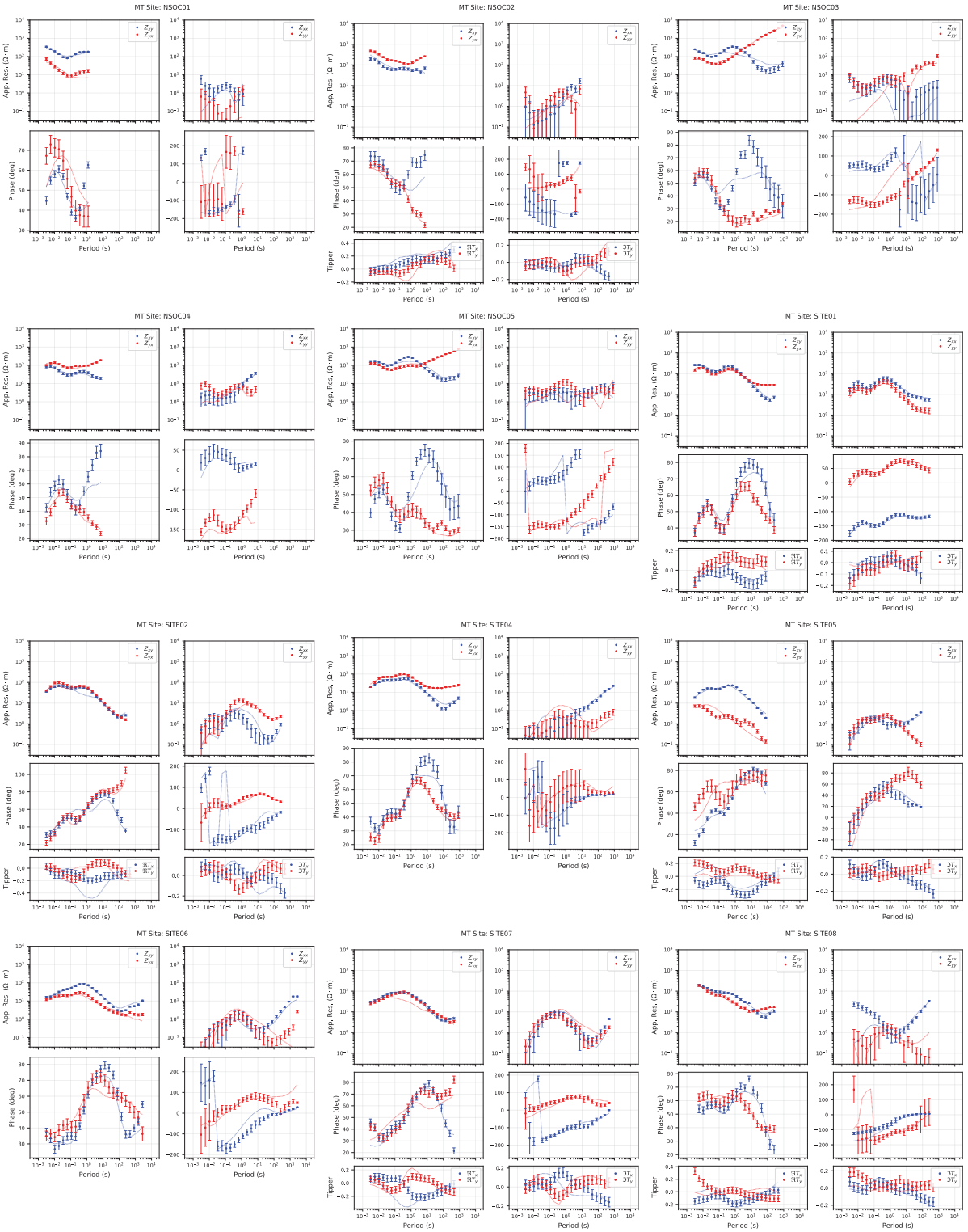
MT Site: NSOC01
MT Site: NSOC02
MT Site: NSOC03
MT Site: NSOC04
MT Site: NSOC05
MT Site: SITE01
MT Site: SITE02
MT Site: SITE04
MT Site: SITE05
MT Site: SITE06
MT Site: SITE07
MT Site: SITE08
App. Res. (Ω·m)
Phase (deg)
Tipper
Period (s)

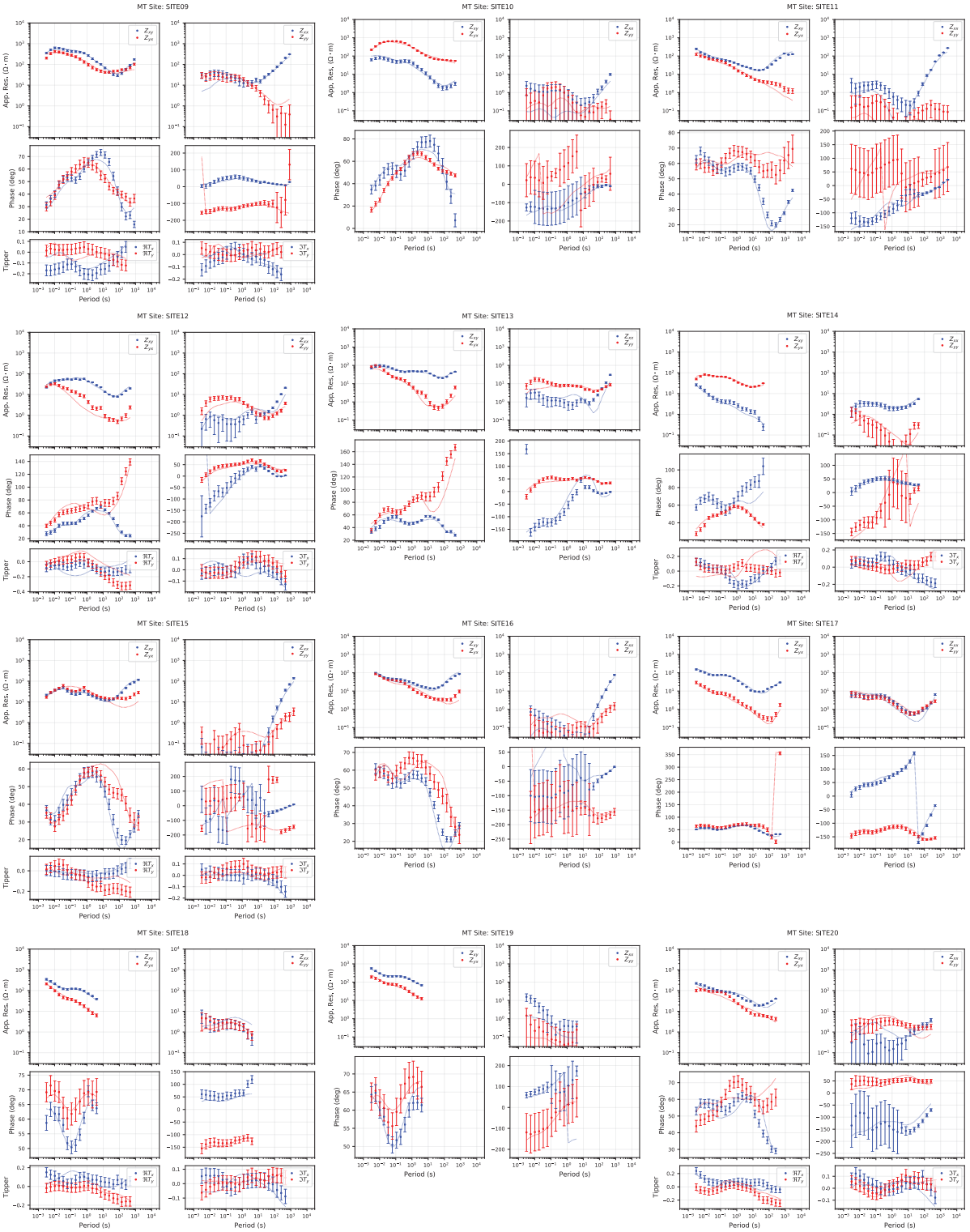
MT Site: SITE09
MT Site: SITE10
MT Site: SITE11
MT Site: SITE12
MT Site: SITE13
MT Site: SITE14
MT Site: SITE15
MT Site: SITE16
MT Site: SITE17
MT Site: SITE18
MT Site: SITE19
MT Site: SITE20
App. Res. (Ω·m)
Phase (deg)
Tipper
Period (s)

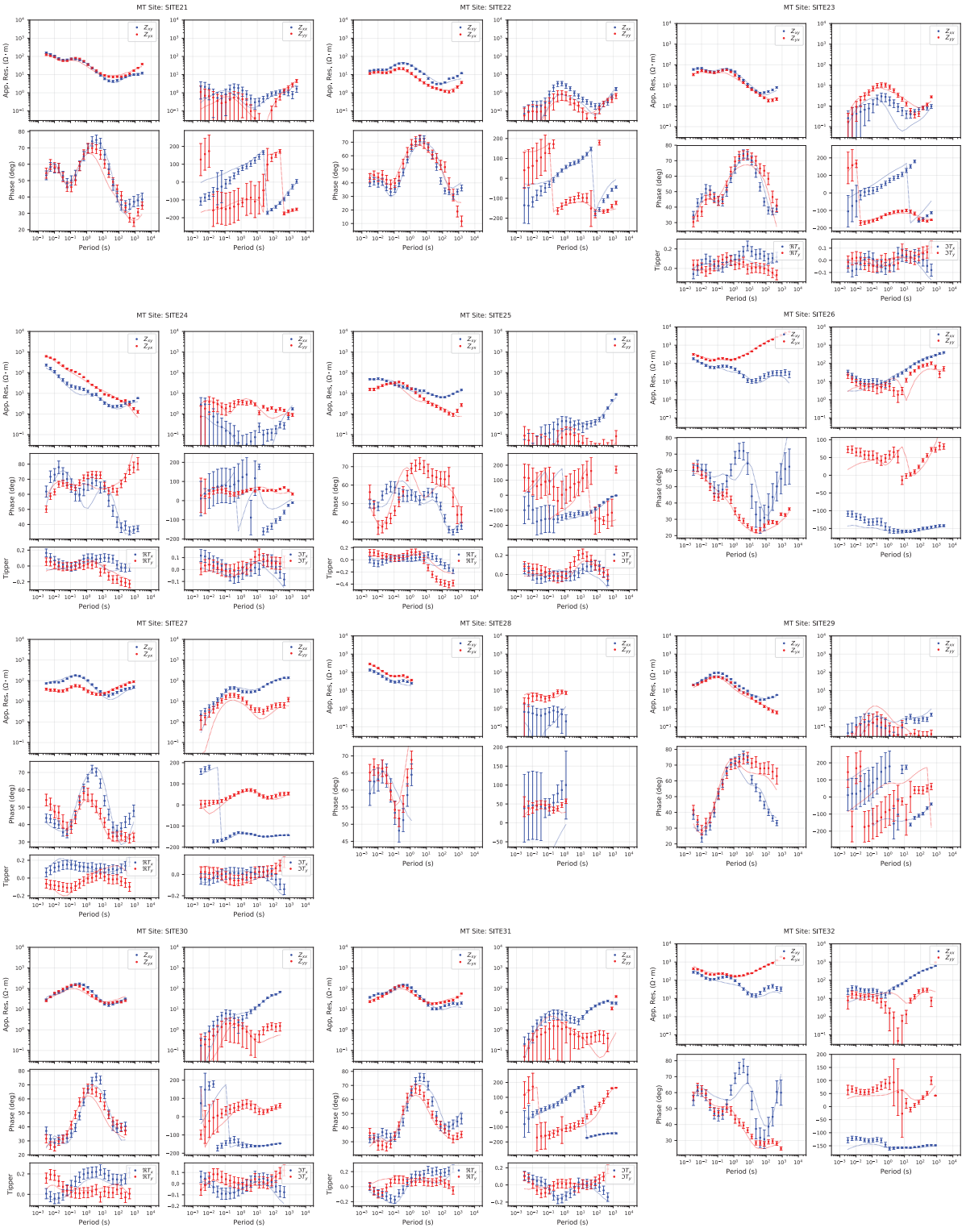
MT Site: SITE21
MT Site: SITE22
MT Site: SITE23
MT Site: SITE24
MT Site: SITE25
MT Site: SITE26
MT Site: SITE27
MT Site: SITE28
MT Site: SITE29
MT Site: SITE30
MT Site: SITE31
MT Site: SITE32
App. Res. (Ω·m)
Phase (deg)
Tipper
Period (s)

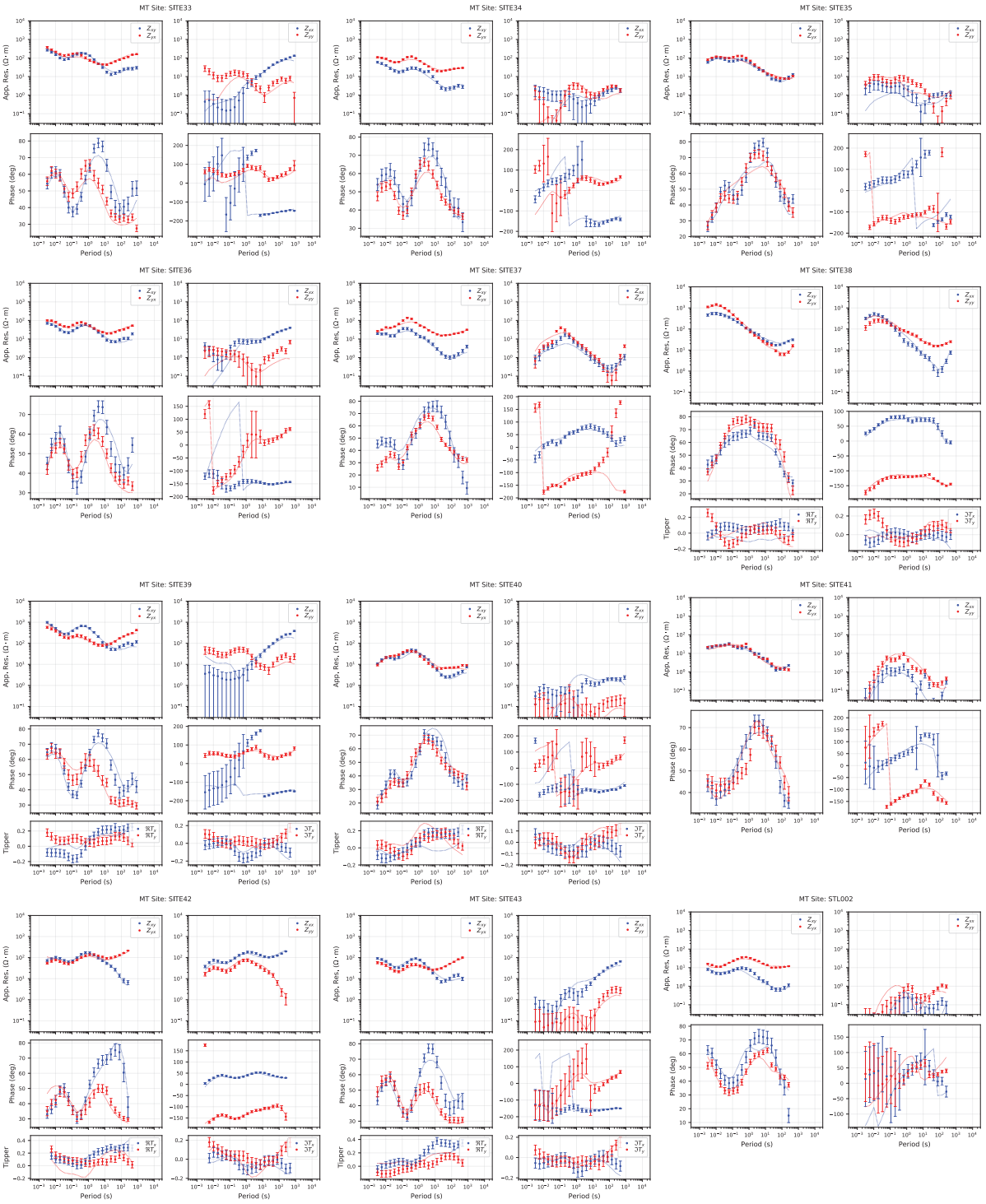
MT Site: SITE33
MT Site: SITE34
MT Site: SITE35
MT Site: SITE36
MT Site: SITE37
MT Site: SITE38
MT Site: SITE39
MT Site: SITE40
MT Site: SITE41
MT Site: SITE42
MT Site: SITE43
MT Site: STL002
App. Res. (Ω·m)
Phase (deg)
Tipper
Period (s)

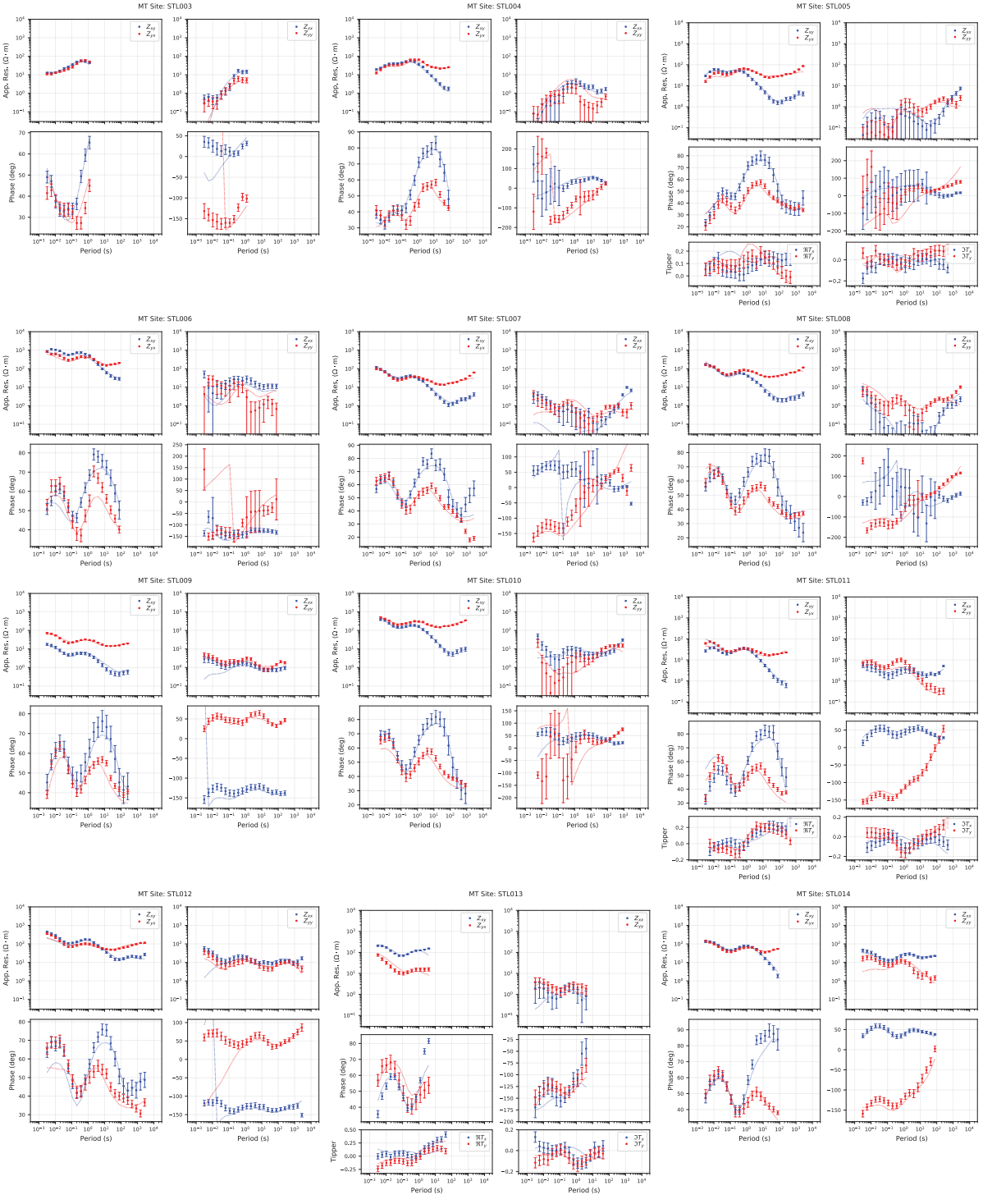
MT Site: STL003
MT Site: STL004
MT Site: STL005
MT Site: STL006
MT Site: STL007
MT Site: STL008
MT Site: STL009
MT Site: STL010
MT Site: STL011
MT Site: STL012
MT Site: STL013
MT Site: STL014
App. Res. (Ω·m)
Phase (deg)
Tipper
Period (s)

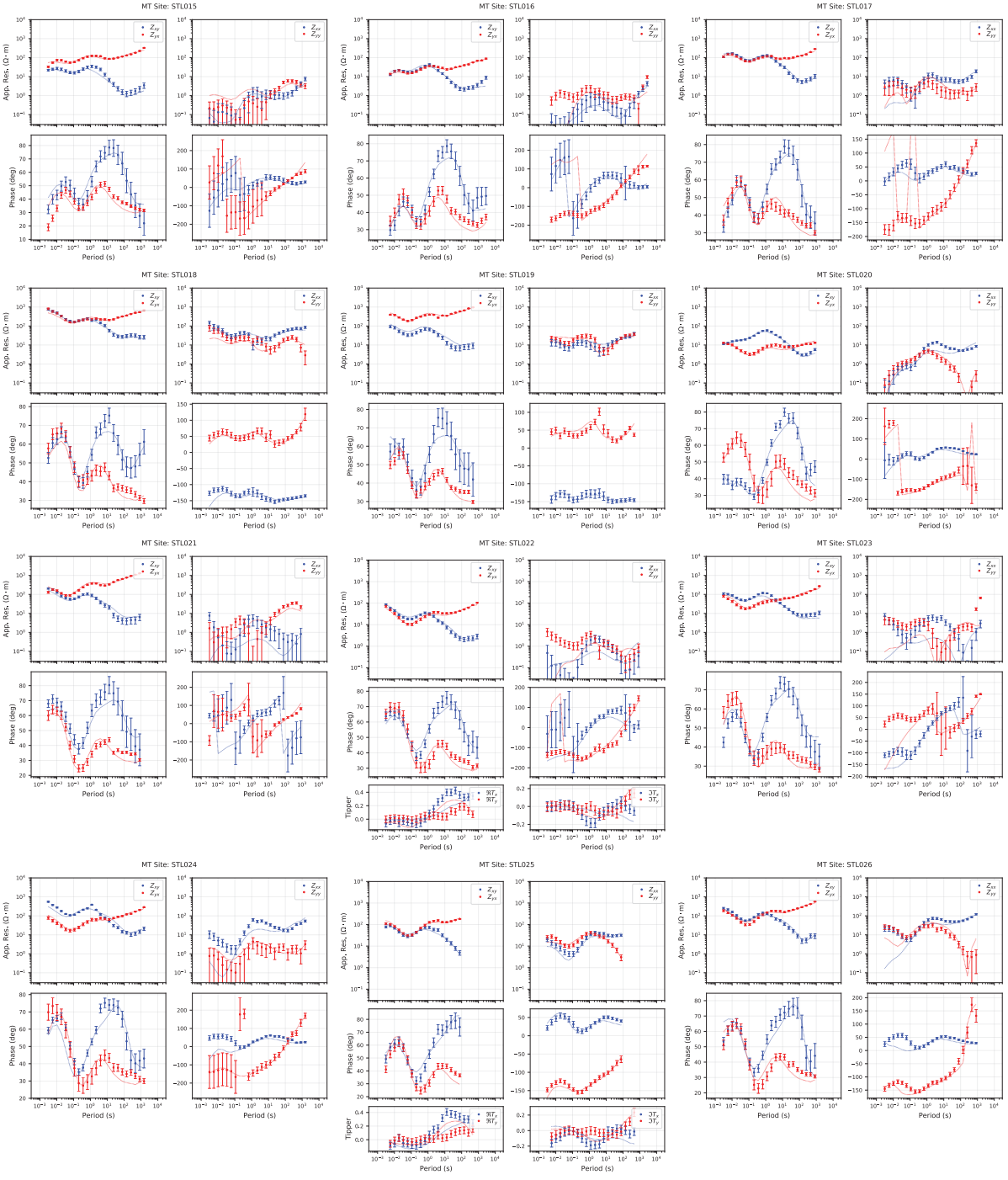
MT Site: STL015
MT Site: STL016
MT Site: STL017
MT Site: STL018
MT Site: STL019
MT Site: STL020
MT Site: STL021
MT Site: STL022
MT Site: STL023
MT Site: STL024
MT Site: STL025
MT Site: STL026
App. Res. (Ω·m)
Phase (deg)
Tipper
Period (s)

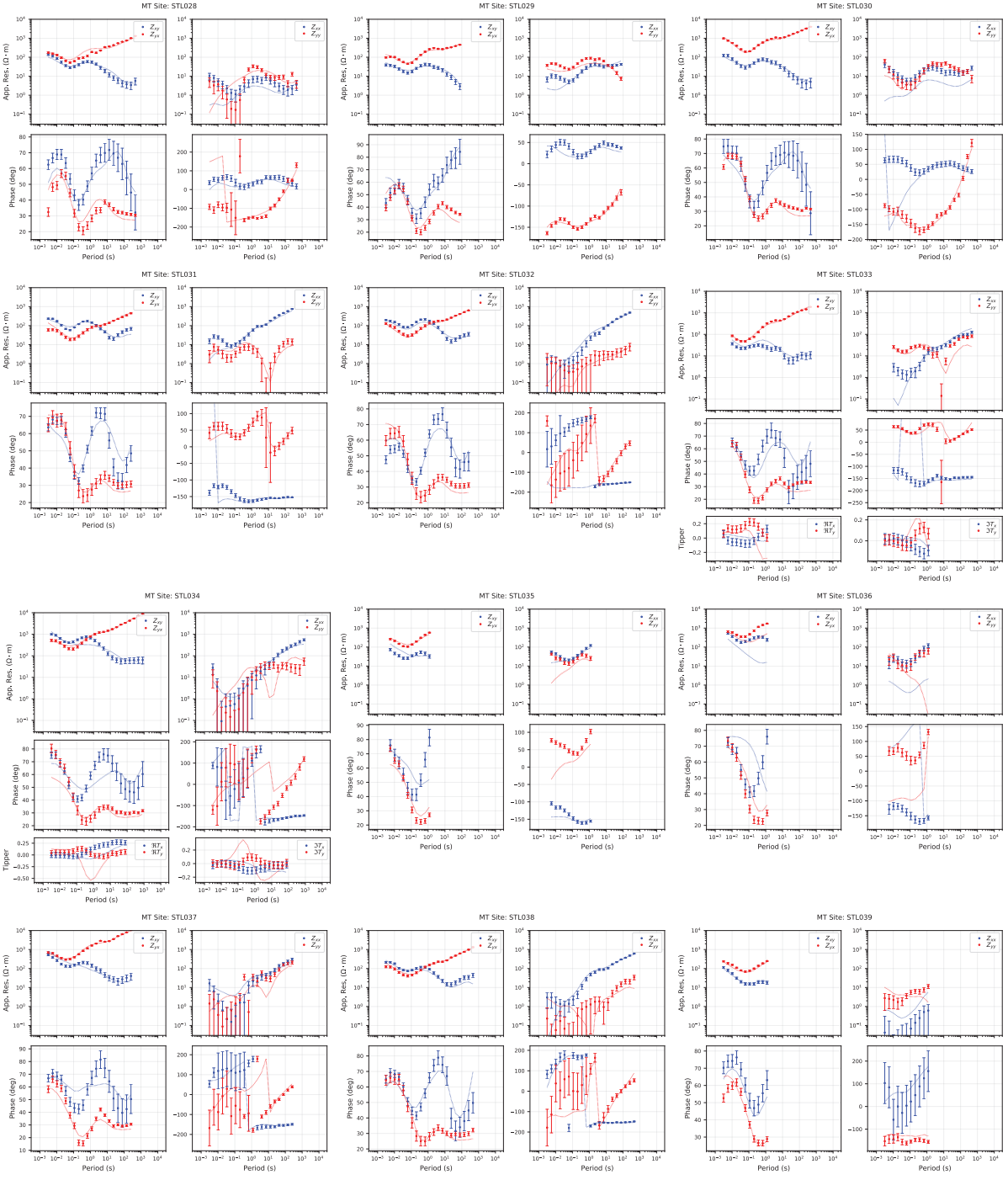
MT Site: STL028
MT Site: STL029
MT Site: STL030
MT Site: STL031
MT Site: STL032
MT Site: STL033
MT Site: STL034
MT Site: STL035
MT Site: STL036
MT Site: STL037
MT Site: STL038
MT Site: STL039
App. Res. (Ω·m)
Phase (deg)
Tipper
Period (s)

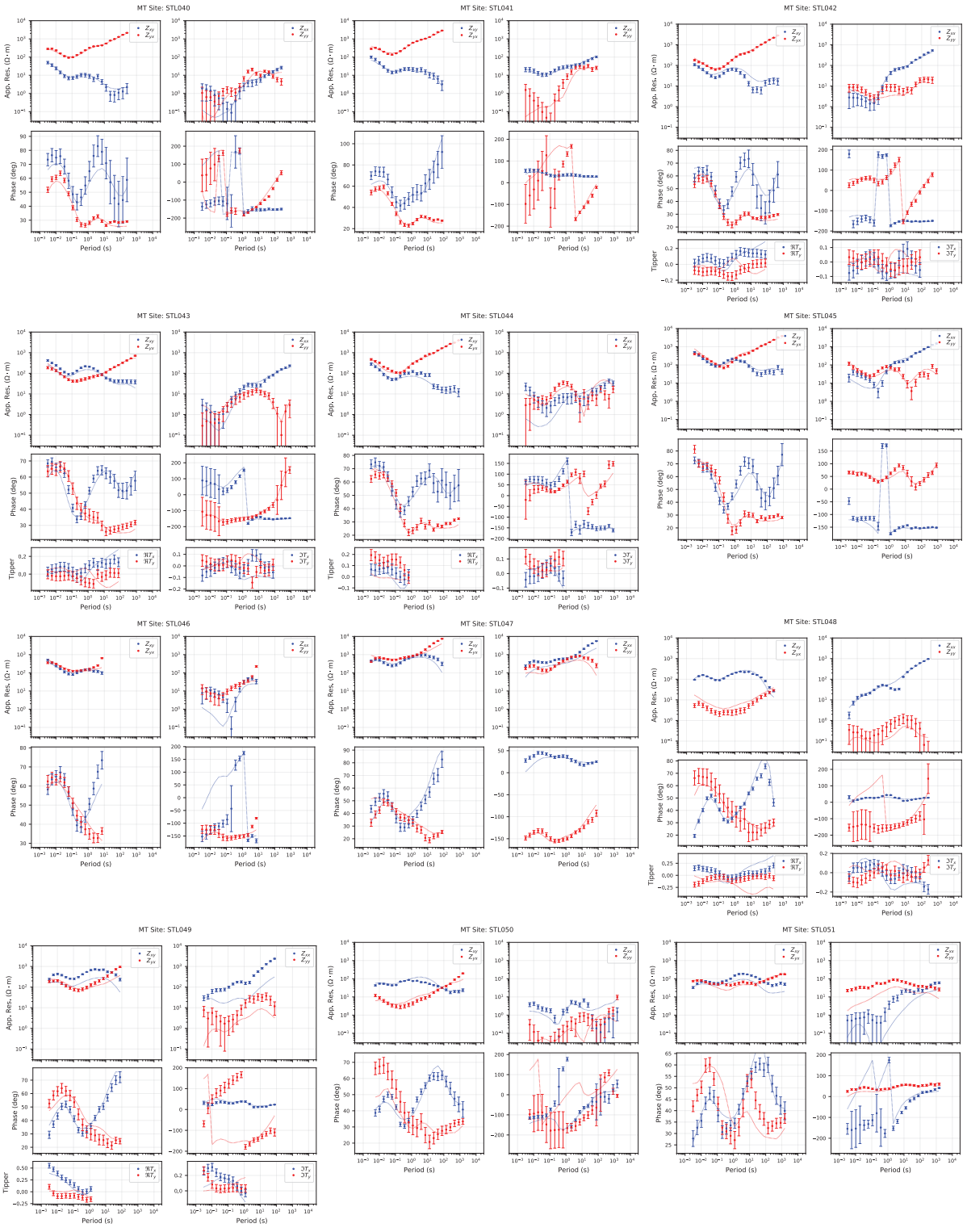
MT Site: STL040
MT Site: STL041
MT Site: STL042
MT Site: STL043
MT Site: STL044
MT Site: STL045
MT Site: STL046
MT Site: STL047
MT Site: STL048
MT Site: STL049
MT Site: STL050
MT Site: STL051
App. Res. (Ω·m)
Phase (deg)
Tipper
Period (s)

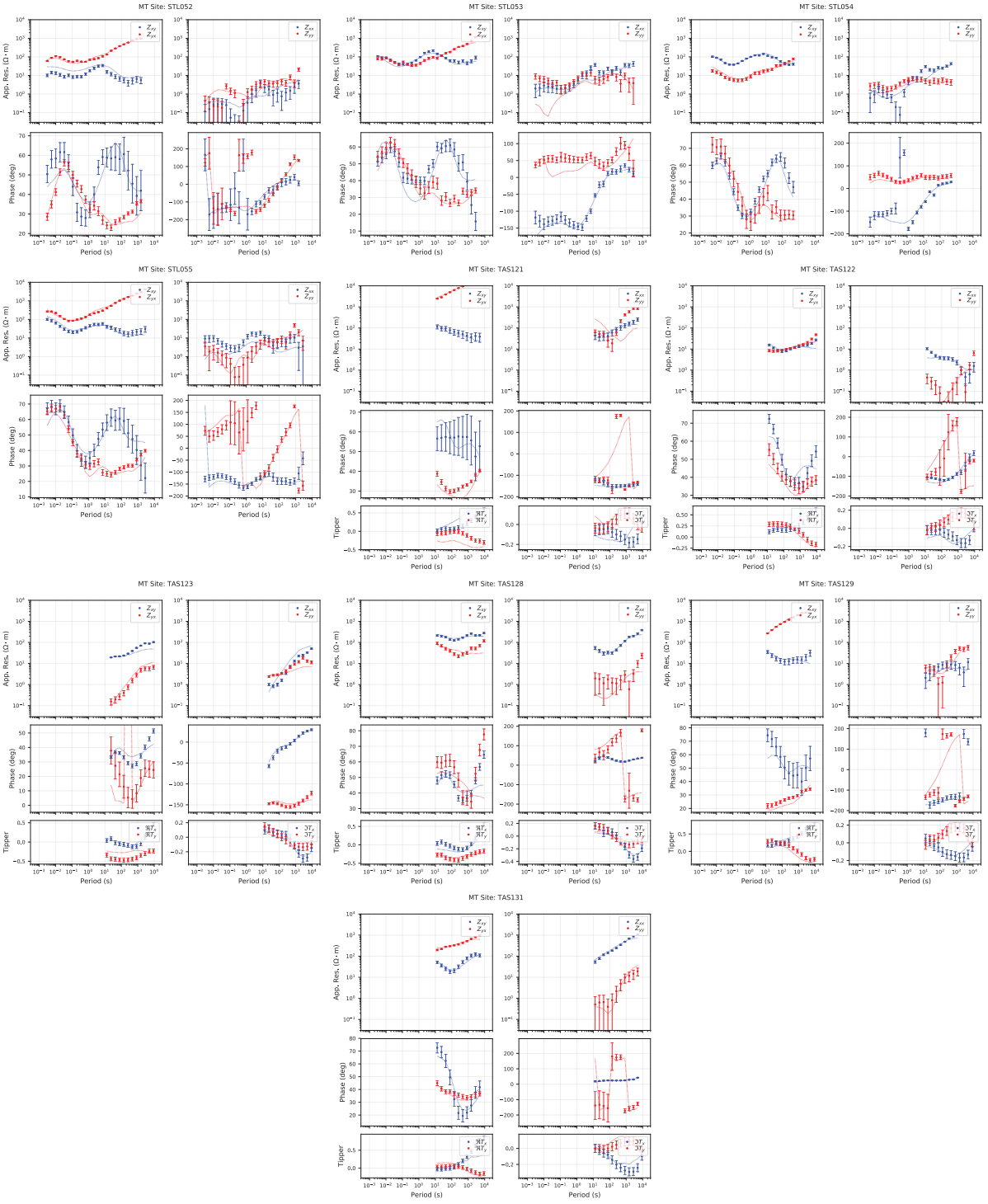
MT Site: STL052
MT Site: STL053
MT Site: STL054
MT Site: STL055
MT Site: TAS121
MT Site: TAS122
MT Site: TAS123
MT Site: TAS128
MT Site: TAS129
MT Site: TAS131
App. Res. (Ω · m)
Phase (deg)
Tipper
Period (s)